Towards Spin-Polarized Electron Beams from a Laser-Plasma Accelerator

Dissertation
zur Erlangung des Doktorgrades
an der Fakultät für Mathematik, Informatik und Naturwissenschaften
Fachbereich Physik
der Universität Hamburg

vorgelegt von
Felix Paul Georg Stehr

Hamburg
2025

Gutachter/innen der Dissertation:	Dr. Jenny List
	Prof. Dr. Gudrid Moortgat-Pick
Zusammensetzung der Prüfungskommission:	Dr. Jenny List
	Prof. Dr. Gudrid Moortgat-Pick
	Dr. Kristjan Põder
	Prof. Dr. Wolfgang Hillert
	Prof. Dr. Arwen Pearson
Vorsitzende/r der Prüfungskommission:	Prof. Dr. Arwen Pearson
Datum der Disputation:	19.05.2025
Vorsitzender Fach-Promotionsausschuss PHYSIK:	Prof. Dr. Wolfgang J. Parak
Leiter des Fachbereichs PHYSIK:	Prof. Dr. Markus Drescher
Dekan der Fakultät MIN:	Prof. Dr.-Ing. Norbert Ritter

Abstract

The LEAP (Laser Electron Acceleration with Polarization) project at DESY is a proof-of-principle experiment aiming to demonstrate the generation – thus also the transport – of spin-polarized electron beams from a laser-plasma accelerator (LPA). This is expected to be achieved using a pre-polarized plasma source, generated via the photodissociation of HCl molecules with an ultraviolet (UV) dissociation laser. Compton transmission polarimetry is envisioned for polarization measurements, inferring electron polarization from the transmission asymmetry of bremsstrahlung photons through magnetized iron. This thesis explores three key aspects of LEAP, focusing on development an experimental realization.

First, a feasibility study was conducted to generate the UV dissociation laser via cascaded second-harmonic generation in two beta-barium borate crystals directly from the LPA driver laser. A measured conversion efficiency of $\eta_{\omega\to 4\omega} \approx 0.8\,\%$ into the UV demonstrates the feasibility of this approach. Second, a homogeneous Cherenkov lead-glass calorimeter was built as an integral part of the LEAP Compton transmission polarimeter. Furthermore, it was tested and calibrated with single electrons at the DESY II Test Beam Facility. The derived calorimeter energy resolution of $\frac{\sigma_E}{\langle E\rangle} < 2\,\%$ at TeV-scale total energies meets the requirement for its application within the LEAP polarimeter. `GEANT4` simulations indicate a nonlinear calorimeter response to low-energy particles ($< 10\,\mathrm{MeV}$). The uncertainty of this response introduces a relative uncertainty of $\sim 1.5\,\%$ on the simulated analyzing power of the polarimeter. Finally, the full polarimeter setup, consisting of a solenoid magnet and the Cherenkov calorimeter, was commissioned at the FLARE facility using an unpolarized LPA electron beam. Initial system tests, beam charge and energy characterization, and operational polarization measurements were conducted. Simulations determined the analyzing power of the system to be $A = 11.74 \pm 0.18\,\%$ ($\frac{\Delta A}{A} = 1.6\,\%$) with the dominant uncertainty arising from the calorimeter response. The actual measurement was found to be primarily influenced by beam stability and control. In particular, observed asymmetries – unrelated to beam polarization – can be explained by potential energy drifts. Extrapolation to realistic polarization measurements indicates that shot-to-shot charge and energy stability must be provided at the $\leq 1\,\%$ level to enable reliable polarization measurements.

Zusammenfassung

Das LEAP-Projekt (Laser Electron Acceleration with Polarization) am DESY zielt darauf ab, erstmals die Erzeugung – und damit auch den Transport – von spinpolarisierten Elektronenstrahlen mittels eines Laser-Plasma Beschleunigers (LPA) zu demonstrieren. Dies soll durch die Verwendung einer vorpolarisierten Plasmaquelle erreicht werden, die mittels Photodissoziation von HCl-Molekülen mit einem ultravioletten (UV) Dissoziationslaser erzeugt wird. Die Polarisationsmessung basiert auf Compton-Transmissionspolarimetrie. Bei dieser Metode wird die Elektronenpolarisation aus der polarisationsabhängigen Asymmetrie der Transmission von von Bremsstrahlungsphotonen durch magnetisiertes Eisen bestimmt. In dieser Arbeit wurden drei zentrale Aspekte des LEAP-Projekts untersucht.
Erstens wurde eine Machbarkeitsstudie zur Erzeugung des UV-Dissoziationslasers durch kaskadierte Frequenzverdopplung des LPA-Treiberlasers mittels zweier Beta-Barium Borat Kristalle durchgeführt. Die gemessene Konversionseffizienz von etwa $\eta_{\omega\to 4\omega} \approx 0.8\,\%$ ins UV bestätigt die Umsetzbarkeit dieses Konzepts. Zweitens wurde ein homogenes Tscherenkow-Bleikristall-Kalorimeter als integraler Bestandteil des LEAP-Polarimeters konstruiert und mittels einzelner Elektronen vom DESY II Teststrahl getestet und kalibriert. Die ermittelte Energieauflösung von $\frac{\sigma_E}{\langle E\rangle} < 2\,\%$ bei TeV-Gesamtenergien erfüllt die Anforderungen für den Einsatz im LEAP-Polarimeter. `GEANT4`-Simulationen zeigen eine nichtlineare Kalorimeterantwort für niederenergetische Teilchen ($< 10\,\mathrm{MeV}$). Die Unsicherheiten dieser Kalorimeterantwort führen zu einer relativen Unsicherheit von etwa 1.5 % in der simulierten Analysierstärke des Polarimeters. Drittens wurde das vollständige Polarimeter, bestehend aus einem Solenoidmagneten und dem Tscherenkow-Kalorimeter, im FLARE Labor am DESY mit einem unpolarisierten LPA-Elektronenstrahl in Betrieb genommen. Dabei wurden erste Systemtests, Strahlcharakterisierungen und Polarisationsmessungen durchgeführt. Simulationen bestimmten die Analysierstärke des Systems zu $A = 11.74 \pm 0.18\,\%$ ($\frac{\Delta A}{A} = 1.6\,\%$), wobei die größte Unsicherheit aus der Kalorimeterantwort resultiert. Die eigentliche Messung wurde jedoch hauptsächlich durch Strahlstabilität und -kontrolle beeinflusst, insbesondere durch mutmaßliche Energiedrifts, die signifikante Schein-Asymmetrien erzeugten. Eine Extrapolation auf realistische Polarisationsmessungen zeigt, dass eine Schuss-zu-Schuss-Stabilität von Ladung und Energie von $\leq 1\,\%$ erreicht werden muss, um verlässliche Polarisationsmessungen zu ermöglichen.

Contents

Chapter 1.

Introduction

Polarized beams are an indispensable tool for many particle and nuclear physics experiments where spin-dependent processes are investigated. For instance, they are employed to study the nucleon spin structure via deep inelastic scattering experiments [1], and, when employed at high-energy e^+e^- colliders, they significantly enhance the capability to probe electroweak couplings and test the Standard Model in the search for physics beyond it [2].

The most commonly used sources of polarized electron beams include storage rings, where electrons acquire polarization via the Sokolov–Ternov effect [3], and gallium arsenide (GaAs) photocathodes within DC high-voltage photoguns [4, 5]. Further acceleration is conventionally achieved using radio-frequency (RF) technology. However, RF accelerators are constrained by material breakdown thresholds, limiting the achievable acceleration gradients. This limitation typically necessitates large experimental scales due to the extensive size of conventional accelerator systems.

Over the last few decades, plasma-based accelerators have shown great potential as a promising alternative, achieving acceleration gradients that are up to three orders of magnitude higher than those in conventional RF-based accelerators [6]. In plasma accelerators, electrons gain energy in the wakefield of a plasma wave, which can be driven either by a high-intensity laser pulse or a relativistic electron or proton bunch propagating through a plasma. Electron beams can reach energies of tens to hundreds of MeV within millimeter-scale distances, making plasma-based accelerators inherently compact.

This novel technology has the potential to enable more compact and cost-efficient accelerator designs, which is especially interesting for applications in high-energy experiments, as proposed by future plasma-based e^+e^- collider concepts such as HALHF [7]. However, the transport of polarized beams in plasma accelerators has so

far only been demonstrated in theory [8]. Moreover, several simulation studies have explored the feasibility of generating polarized beams directly using laser-plasma acceleration (LPA) [9–12]. The ability to generate polarized beams within compact LPAs would be highly attractive, as it could make polarized electron beams more affordable and accessible for small-scale, low-energy applications, thus facilitating a broader range of polarized-beam experiments.

Despite significant progress in plasma-based accelerator research, the experimental demonstration of polarized plasma acceleration still remains an open challenge. Addressing this gap is the central aim of the LEAP (Laser Electron Acceleration with Polarization) project at DESY. LEAP aims to serve as a proof-of-principle experiment to demonstrate, for the first time, the generation of spin-polarized electron beams from an LPA source and thus also the transport.

For the LEAP project, an LPA concept based on colliding pulse injection combined with a pre-polarized plasma source is envisaged [12]. In this approach, a circularly polarized ultraviolet (UV) laser pulse dissociates hydrogen halide molecules, producing spin-polarized electrons within the plasma source [13, 14]. These polarized electrons are subsequently injected into the wakefield of the LPA driver pulse using the colliding pulse injection technique and are accelerated within the wakefield. The resulting electron beam polarization is envisaged to be measured using Compton transmission polarimetry. This method, suitable for the expected beam energies in the tens of MeV range, leverages the polarization dependence of Compton scattering. Following this technique, the electron polarization can be retrieved by measuring the polarization-dependent transmission asymmetry of bremsstrahlung photons passing through a magnetized block of iron.

Within this thesis, three key aspects of the LEAP project have been addressed, focusing on the development and implementation of the experiment. The first topic involves a feasibility study to investigate the possibility of generating the required UV dissociation laser for the pre-polarization of the plasma source through cascaded second harmonic generation using beta-barium borate (BBO) crystals. The second topic focused on the design, construction, testing, and calibration of a homogeneous Cherenkov lead-glass calorimeter, which forms an integral part of the LEAP Compton transmission polarimeter for polarization measurement. Finally, the third topic involved the commissioning of the polarimeter setup under real experimental conditions, including performing a polarization measurement using an unpolarized LPA electron beam. This work encompassed initial system tests and an investigation of the leading systematic uncertainties in the polarization measurement, as well as the

identification of further experimental requirements to pave the way for an actual polarization measurement within the LEAP project.

This thesis is structured as follows. The first part of the thesis provides an overview of the basic physics and concepts relevant to the understanding of this work (Chap. 2). In Chapter 3, the specific methods used for the generation and measurement of polarized beams within the LEAP project are discussed, along with their anticipated experimental setups and expected parameters. Chapter 4 gives an overview of the experimental facilities, tools, and software that were applied at various stages throughout this thesis. The feasibility study for the generation of the UV dissociation laser required for the pre-polarization of the plasma source in the LEAP project is presented in Chap. 5. In Chapter 6, the design, construction, commissioning, and calibration of the homogeneous lead-glass Cherenkov calorimeter for the LEAP polarimeter are discussed. This chapter also includes a performance evaluation of the calorimeter through simulations based on the expected beam parameters within the LEAP experiment. Chapter 7 covers the commissioning of the complete LEAP polarimeter setup under real experimental conditions, including a polarization measurement using an unpolarized LPA electron beam. Finally, the results of this thesis are summarized in Chap. 8.

Chapter 2.

Experimental and Theoretical Foundations

In this chapter, the fundamental physics concepts relevant to this work will be introduced to provide a foundation for the subsequent discussions.

2.1. Polarization

This section discusses the concept of spin polarization of electron beams and a brief overview of photon polarization is provided. This section is primarily based on [15–17], where the reader is referred to for more detailed information.

2.1.1. Spin Polarization of Electron Beams

The spin of an elementary particle is a fundamental property. It is a quantized, inherent form of angular momentum carried by the particle, characterized by the quantum number s which can take integer (0, 1, 2, ...) or half-integer ($\frac{1}{2}$, $\frac{2}{3}$, ...) values. Particles with half-integer s values, such as electrons ($s = \frac{1}{2}$), are referred to as fermions. Particles with integer s values, such as photons ($s = 1$), are known as bosons. Unlike classical angular momentum, which arises from the physical rotation of an object, a particle's spin is a purely quantum-mechanical property with no classical analogue. The spin of an electron determines its magnetic moment and influences how electrons interact with magnetic fields. In classical mechanics the angular momentum can have any magnitude and can be oriented in any direction in space. In contrast, the spin

angular momentum has a fixed magnitude and only discrete orientations in space are allowed. In the case of the electron, only two orientations are possible, which are commonly referred to as the electron spin states.

In quantum mechanics, the spin is associated with the spin operator $\hat{\mathbf{S}}$. The spin state $|\psi\rangle$ of a particle with spin s is specified by the eigenvalues of the two commuting operators $\hat{\mathbf{S}}^2$ and $\hat{S}_z$. The eigenvalue of $\hat{\mathbf{S}}^2$ is given by $s(s+1)\,\hbar^2$ and the one of $\hat{S}_z$ is denoted by $m_s\,\hbar$, where m_s takes values from $-s$ to $+s$ in integer steps. For electrons, where $s = \frac{1}{2}$, the spin operator is explicitly given by $\hat{\mathbf{S}} = \frac{\hbar}{2}\boldsymbol{\sigma}$, where $\boldsymbol{\sigma} = (\sigma_x, \sigma_y, \sigma_z)$ denote the Pauli matrices. The square root of the eigenvalue of $\hat{\mathbf{S}}^2$ is associated with the total spin angular momentum, which gives a fixed value of $\sqrt{\frac{3}{4}}\,\hbar$ for electrons. Moreover, when measuring the projection of the electron spin along any axis yields only two possible values: $\pm\frac{\hbar}{2}$, which are the eigenvalues of $\hat{S}_z$. These two possible spin orientations are often labeled as "parallel" or "up" ($+\frac{\hbar}{2}$) and "antiparallel" or "down" ($-\frac{\hbar}{2}$).

The spin polarization P of an electron beam along a specific direction is defined as:

$$P = \frac{N^{\uparrow} - N^{\downarrow}}{N^{\uparrow} + N^{\downarrow}}, \tag{2.1}$$

where $N^{\uparrow}$ is the number of electrons with spin "up" (positive spin projection) and $N^{\downarrow}$ is the number of electrons with spin "down" (negative spin projection).

Equation 2.1 quantifies the net spin alignment within the beam along a specific direction. A value of $P = +1$ corresponds to a fully polarized beam with all spins aligned in the "parallel" direction, while $P = -1$ indicates a fully polarized beam with all spins aligned in the "antiparallel" direction. A value of $P = 0$ represents an unpolarized beam, where equal numbers of spins are aligned "parallel" and "antiparallel".

When discussing the polarization of an electron beam, one often distinguishes between longitudinal and transverse beam polarization. **Longitudinal polarization** refers to the case where the spin orientation of electrons is aligned with the beam's momentum direction. The spin can be oriented either parallel or antiparallel to the momentum. Transverse polarization refers to the case where the spin orientation lies perpendicular to the direction of motion of the electrons. Within the scope of this thesis, only longitudinal spin polarization is considered.

In practice, polarized electron beams are generated, for example, in storage rings, where transverse beam polarization builds up over time due to the Sokolov-Ternov effect [3, 18]. This mechanism has been employed, for example, in the $p/e^{\pm}$ collider

HERA at DESY [19], where spin rotators were used to convert the transverse polarization into longitudinal polarization, delivering beams with polarization levels of approximately 60 % to the experiments [20]. The most commonly used source for highly longitudinally spin-polarized electron beams is based on GaAs photocathodes within DC high-voltage photoguns. In this method, polarized electron beams are produced via polarized photoemission when the GaAs cathode is illuminated with circularly polarized laser light [4, 5]. This type of source was first applied in the SLAC parity-violation experiment E120 ($P \approx 40\,\%$) [21, 22] and has since been further developed and implemented at various laboratories, such as Mainz University [23], Bonn University [24], and CEBAF/Jefferson Lab [25], with polarization levels nearing 90 %. This type of source is also proposed for the polarized electron source of the International Linear Collider (ILC), which is expected to generate electron beams with 90 % polarization, nano-Coulomb bunch charges, nanosecond pulse lengths, and electron energies of approximately 200 keV [26], which are then further accelerated using RF acceleration technology.

2.1.2. Photon Polarization

In a picture of classical electrodynamics, light is described as an electromagnetic wave in which the electric and magnetic fields oscillate perpendicularly to each other and to the direction of propagation. In this classical picture, the polarization of light refers to the direction in which the electric field vector oscillates. One typically distinguishes:

- **Linear polarization**, where the electric field oscillates along a fixed axis.
- **Circular polarization**, where the electric field vector has a constant magnitude and rotates at a constant rate in plane perpendicular to the direction of propagation (right-handed or left-handed, depending on the sense of rotation).
- **Elliptical polarization**, a generalization of circular polarization in which the magnitude of the field changes during its rotation, causing the tip of the electric field vector to trace out an ellipse.

From a quantum-theoretical viewpoint, photons are spin-1 particles. Because photons are massless, they can only have two possible spin projections along the direction of motion ($\pm\hbar$) referred to as helicity: $+1$ (right-handed) or -1 (left-handed) [27]. In terms of polarization, a right-handed circularly polarized electromagnetic wave

consists of photons with helicity $+1$, while a left-handed circularly polarized wave consists of photons with helicity -1. Other polarization states, such as linear and elliptical, can be viewed as superpositions of these two circular states.

2.2. Laser Plasma Acceleration

When a high-intensity laser beam interacts with plasma, strong longitudinal electric fields can be generated, providing an ideal environment for electron acceleration.
The concept of laser-plasma acceleration (LPA) was initially proposed by Tajima and Dawson in 1979 [28] and became experimentally feasible with the advent of high-power, short-pulse laser systems. This was made possible by the development of chirped pulse amplification, a technique pioneered by Strickland and Mourou in 1985 [29]. Traditional accelerator technologies based on radio-frequency (RF) cavity systems are generally limited to acceleration gradients below 100 MV/m due to material breakdown limitations in their structures. In contrast, LPAs can sustain acceleration gradients that are three orders of magnitude higher [6] because they are not limited by material breakdown; the plasma itself is an ionized medium and thus unaffected by structural damage. With respect to plasma accelerators, a plasma is defined as a quasi-neutral gas of charged and neutral particles which exhibits collective behavior [30]. The following section provides an overview of the basic concepts, techniques, and key parameters of laser-plasma acceleration. For more detailed information, please refer to sources such as [6, 28, 31].
LPA requires high-intensity laser pulses, described by the laser strength parameter a_0 which is the peak amplitude of the normalized vector potential of the laser field $\mathbf{a} = \frac{e\mathbf{A}}{m_e c^2}$, where e, m_e and c are the electron charge, electron mass and the speed of light, respectively. Physically, a_0 represents the transverse momentum of plasma electrons in the laser field, normalized to the electron's rest mass momentum $m_\mathrm{e}c$. When $a_0 \geq 1$, the electron's motion becomes relativistic, marking the onset of nonlinear laser-plasma interactions. The laser strength parameter relates to the laser peak intensity I_0 by [6]:

$$a_0 \approx 0.85 \cdot \lambda[\mu\mathrm{m}] \cdot \sqrt{I_0[10^{18}\mathrm{W/cm}^2]} \tag{2.2}$$

where λ is the laser wavelength. For effective LPA, a laser strength of the order of one is typically required. In the case of a Titanium:sapphire (Ti:Sa) laser system ($\lambda = 800\,nm$), this corresponds to pulse intensities on the order of $I \approx 10^{18}\,\mathrm{W/cm}^2$.

A graphical illustration of an LPA setup is shown in Fig. 2.1 a), where a laser pulse is focused onto an LPA gas target, depicted here as a gas jet. The intense laser pulse ionizes the gas, creating plasma in situ. As the laser pulse propagates through the plasma, the plasma electrons expelled from regions of highest laser intensity by the ponderomotive force $\mathbf{F}_\mathrm{p}$ (see Fig. 2.1b)) which is proportional to the intensity gradient [6]:

$$\mathbf{F}_\mathrm{p} = -m_\mathrm{e}c^2\nabla a_0^2/2 \tag{2.3}$$

This force displaces the electrons radially outward, while the heavier ions remain largely immobile. Once the laser pulse passes, the displaced electrons experience a Coulomb restoring force due to the charge separation (see Fig. 2.1c)), causing them to oscillate at the characteristic electron plasma frequency ω_p [30]:

$$\omega_\mathrm{p} = \sqrt{\frac{e^2 n_\mathrm{e}}{m_\mathrm{e}\epsilon_0}} \tag{2.4}$$

where n_e is the plasma (electron) density. These oscillations form a wave-like structure behind the laser pulse, known as a plasma wave, with a phase velocity that matches the group velocity of the laser pulse as it propagates through the plasma. The wavelength of the plasma wave (length of the plasma cavity for $a << 1$) is given by the plasma wavelength $\lambda_\mathrm{p} = \frac{2\pi c}{\omega_\mathrm{p}}$, which depends on the plasma density.

$$\lambda_\mathrm{p}[\mu\mathrm{m}] \approx 33/\sqrt{n_\mathrm{e}[10^{18}\mathrm{cm}^{-3}]} \tag{2.5}$$

Due to charge separation in the plasma wave, strong longitudinal electric fields are generated. Electrons injected at the correct phase (at the back of the plasma cavity) can then be accelerated within the wakefield of the laser pulse (see Fig. 2.1d)). These fields can reach magnitudes in excess of $E_0 = \frac{m_\mathrm{e}\omega_\mathrm{p}c}{e}$, or equivalently [6]:

$$E_0[\mathrm{V/m}] \approx 96 \cdot \sqrt{n_\mathrm{e}[\mathrm{cm}^{-3}]} \tag{2.6}$$

which is referred to as the non-relativistic wave braking field [32]. This enables acceleration gradients exceeding 100 GV/m for plasma densities around $n_\mathrm{e} \approx 10^{18}\,\mathrm{cm}^{-3}$, surpassing conventional RF accelerator capabilities by orders of magnitude.
For lower laser intensities ($a_0 < 1$), the wakefield adopts a sinusoidal shape, a condition known as the linear regime. In this regime, only modest acceleration gradients

are achieved. In contrast, for higher laser intensities ($a_0 > 1$), the wakefield enters the non-linear regime, also referred to as the bubble regime [33]. In this regime, the intense ponderomotive force pushes nearly all electrons away from the axis, creating an electron-depleted cavity, or "bubble", which enables high accelerating gradients on the scale of E_0.

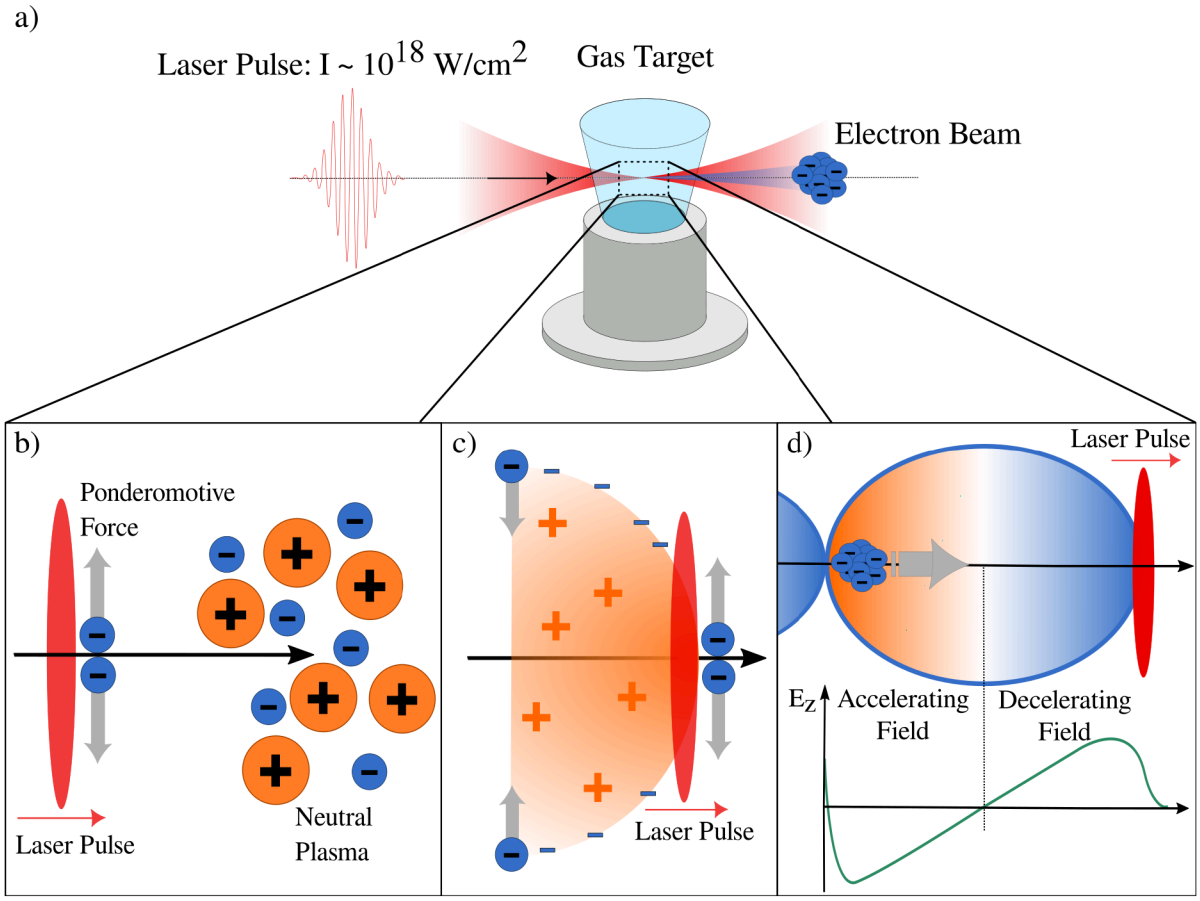

Figure 2.1.: a) Illustration of the LPA concept. An intense laser pulse is focused into a plasma source, ionizing the gas and creating plasma in situ. b) Electrons are radially expelled by the ponderomotive force from regions of highest laser intensity, while the heavier ions remain largely immobile due to their higher mass. c) After the laser pulse passes, the electrons are restored by the Coulomb force, causing them to oscillate and form a plasma wave. d) Longitudinal wakefield of the plasma wave, depicted for the first period (plasma bubble), with a deceleration phase at the front of the period and an acceleration phase at the back. Electrons injected (trapped) in the acceleration phase of the wakefield are subsequently accelerated (adapted from [34]).

Injection mechanism

For electrons to be accelerated within the plasma wakefield, they must be injected into the appropriate phase of the plasma wave. The following provides a brief overview of some commonly used injection techniques.

Self-injection: Electrons are spontaneously injected into the acceleration phase of the wakefield when, e.g., they are scattered from the back of the plasma bubble into the cavity. This is a highly stochastic process that occurs in strongly nonlinear regimes ($a_0 \gg 1$) where the wakefield is driven close to or beyond the wave-breaking threshold (Eq. 2.6) [35].

Ionization injection: Here, a gas mixture with two species of differing ionization thresholds is typically used. Electrons from lower ionization states form a background plasma, while those from higher ionization states are released only when the pulse reaches peak intensity, making them more likely to be trapped in the wakefield [36]. This technique is employed in the LPA setup discussed in Sec. 7.2, using helium and nitrogen.

Shock-front injection: The injection is based on a sharp density down-ramp transition within the plasma source density profile [37, 38]. Electrons are injected at the density down-ramp, as the plasma density decreases, the wakefield lengthens, enabling electrons at the back of the bubble to become trapped and accelerated.

Colliding-pulse injection: The colliding pulse injection employs an additional laser pulse counter-propagating to the LPA driver, forming a standing wave that enables trapping of background electrons near their collision point [39, 40].

Limitations

Despite the large accelerating fields within the plasma, the energy gain of electrons in a single LPA stage is constrained by factors such as pump depletion and electron dephasing [6]. Pump depletion occurs as the LPA driver pulse loses energy while driving the plasma wakefield. Once most of the pulse energy has been transferred to the plasma wakefield, further acceleration of electrons is no longer possible, effectively limiting the acceleration length. Electron dephasing also limits the achievable acceleration length. This occurs because the phase velocity of the wakefield in the plasma is slower than the speed of light. As electrons are accelerated to relativistic energies

close to the speed of light, they eventually overtake the wakefield, transitioning from an accelerating phase to a decelerating phase.

2.3. Passage of Particles through Matter

When particles pass through matter, they interact with the electrons and nuclei of the surrounding atoms, losing energy and eventually becoming absorbed. The probability and nature of these interaction processes depend strongly on the type of particle and its properties (such as charge, mass, and energy), as well as on the characteristics of the material, particularly its atomic number Z.
From an experimental perspective, these interaction processes can be leveraged for determining the physical properties of particles, such as their energy (e.g., in calorimetry, see Sec. 2.4), or for inferring specific characteristics like their polarization degree by exploiting spin-dependent reactions (see Sec. 2.5).
In this section, an overview of the most relevant interactions of photons (γ) and electrons (including positrons) as they pass through matter is provided. The content is based on [41–43], where more detailed information can be found.

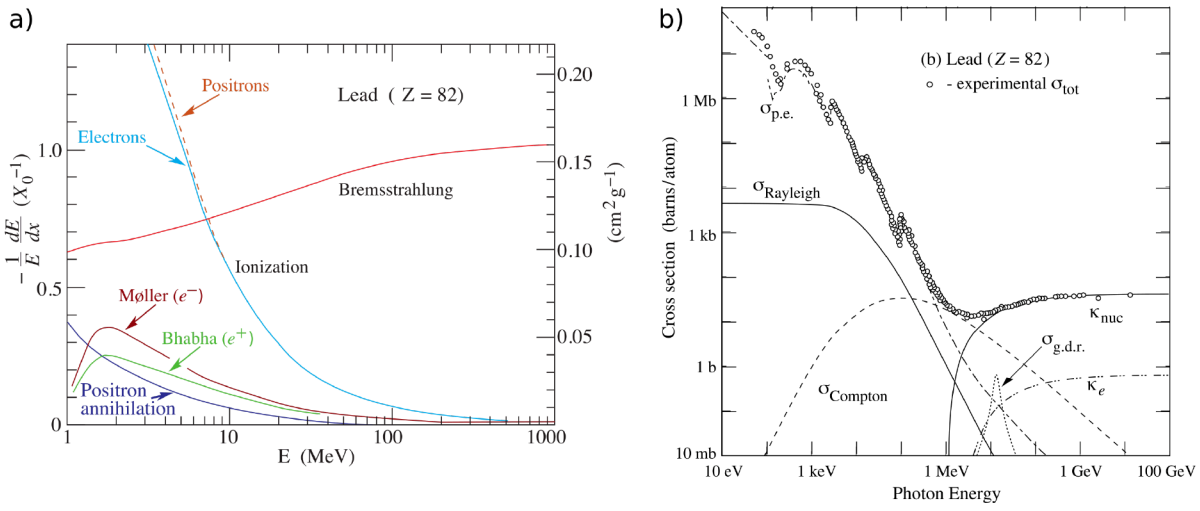

Figure 2.2.: a) Fractional energy loss per radiation length for electrons and positrons in lead as a function of energy, illustrating contributions from different energy loss processes. b) Total experimental photon cross-section as a function of energy in lead, showing contributions from various processes: the photoelectric effect ($\sigma_{\text{p.e.}}$), Rayleigh scattering(σ_{Rayleigh}), Compton scattering (σ_{Compton}) and electron-positron pair production in the Coulomb field of a nucleus (κ_{nuc}) and an electron (κ_{e}). $\sigma_{\text{g.d.r}}$ indicates the cross-section of photo-nuclear interactions (great dipole resonance) [41].

2.3.1. Electron and Positron Interactions

When a charged particle, such as an electron or positron, traverses matter, it loses energy through a continuous series of interactions, including ionization of atoms and the radiation of photons. The energy loss contributions from different interaction processes for electrons are exemplarily shown for lead in Fig. 2.2 a).
At lower energies (up to the order of 10 MeV), electrons and positrons primarily lose their energy through **ionization** of atoms along their path. In addition to ionization, other processes contribute to the total energy loss in this energy regime, albeit not dominantly. These processes include **Møller scattering** (for electrons) and **Bhabha scattering** (for positrons), where particles scatter off atomic electrons, as well as **positron annihilation**, where a positron captures and annihilates with an electron from the traversed material, resulting in the production of two photons, each with an energy of 511 keV. The cross sections for Møller and Bhabha scattering are spin-dependent which can be utilized in polarization measurements (see Sec. 2.5).
At higher energies (above $\sim$10 MeV for lead), the main contributor to the energy loss is **bremsstrahlung**, where the electrons and positions radiate photons due to the Coulomb interaction with the electric field of the nucleus. The energy spectrum of bremsstrahlung photons scales as $1/E$ and, in principle, can extend up to the energy of the radiating particle. Circularly polarized bremsstrahlung photons can be produced from polarized electrons. In the case of longitudinally polarized electrons with energies $E_{e^-} \geq 2$ MeV, if the emitted photon has energy $E_\gamma = E_{e^-}$ and is emitted in the forward direction, the polarization transfer to the photon is nearly complete [44–46]. The polarization transfer becomes important in later sections of this thesis (see Sec. 3.2).
The energy at which the contributions to the total energy loss from ionization and bremsstrahlung are equal is defined as the critical energy (E_c), which is highly material-dependent. For solid materials, it can be parameterized based on the atomic number Z as:

$$E_c = \frac{610}{Z}\,[MeV] \tag{2.7}$$

In addition to the primary energy loss mechanisms mentioned above, other processes result in the emission of optical photons, which are significant for applications such as calorimetry (see Sec. 2.4) and other electron beam diagnostics (see Sec. 4.2.2). These processes include:

- **Scintillation**: Atoms or molecules in the material are excited by the charged particle without being ionized. As the excited states de-excite to their ground state, the energy is released as one or more optical photons (scintillation light).
- **Cherenkov Radiation**: When a charged particle travels faster than the speed of light in a medium ($v > c/n$, where n is the refractive index of the medium) the particle loses energy through the emission of Cherenkov radiation. The number of photons produced per unit path length and per unit wavelength interval for a charged particle is given by [41]:

$$\frac{d^2N}{dx\,d\lambda} = \frac{2\pi\alpha z^2}{\lambda^2}\left(1 - \frac{c^2}{v^2 n^2(\lambda)}\right) \tag{2.8}$$

  where z is the charge of the particle in electron charges (e), α is fine-structure constant and λ the wavelength of the radiation. The characteristic $1/\lambda$ dependence of Cherenkov radiation results in its intensity being highest in the ultraviolet (UV) spectral range.

The emission of Cherenkov radiation requires the particle to exceed the speed of light in the medium, imposing a minimum threshold on its kinetic energy, known as the Cherenkov threshold. This threshold energy ($E_{\text{kin,min}}$) can be expressed as:

$$\begin{aligned} E_{\text{kin,min}} &= mc^2(\gamma - 1) \\ &= mc^2\left(\frac{1}{\sqrt{1 - \frac{v_{\text{min}}^2}{c^2}}} - 1\right) \overset{v_{\text{min}} = c/n}{=} mc^2\left(\frac{1}{\sqrt{1 - \frac{1}{n^2}}} - 1\right) = mc^2\left(\frac{n}{\sqrt{n^2 - 1}} - 1\right). \end{aligned} \tag{2.9}$$

Here, γ is the relativistic Lorentz factor, m is the rest mass of the particle, c is the speed of light in a vacuum, and n is the refractive index of the material.

2.3.2. Photon Interactions

The four predominant interactions of photons when passing through matter are the photoelectric effect, Rayleigh scattering, Compton scattering, and electron-positron pair production. The cross sections of these processes are exemplarily shown for lead as a function of photon energy in Fig. 2.2 b) and are explained as follows:

1. **Photoelectric Effect**: The photoelectric (absorption) effect dominates at low photon energies. In this process, the photon is absorbed by an atom, resulting in the ejection of a photoelectron from one of its bound shells, provided the photon energy exceeds the binding energy of the electron. The atom which is left in an excited state, de-excites as an electron from a higher shell fills the vacancy in the inner shell, emitting either X-rays or an Auger electron. The cross-section for the photoelectric effect scales with the atomic number Z of the absorber material and the photon energy as Z^n/E^3, where n is typically between 4 and 5. Due to this strong energy dependence, the importance of this process decreases rapidly as photon energy increases.

2. **Rayleigh Scattering**: Rayleigh scattering (coherent scattering) occurs when the photon is deflected by atomic electrons without a loss of energy. This process is significant at low photon energies. While the photon retains its original energy, Rayleigh scattering does not excite or ionize atoms and thus does not contribute directly to energy deposition. However, it does affect the spatial distribution of energy deposition.

3. **Compton Scattering**: Compton scattering occurs when a photon is scattered by an atomic electron. This process dominates in the energy range of a few hundred keV to $\sim 5\,MeV$ for most materials. During Compton scattering, energy and momentum are transferred to the scattered electron, with the energy transfer varying between 0 and a large fraction of the photon's initial energy. While photons can scatter in any direction, the probability of forward scattering increases with photon energy. The probability of Compton scattering is proportional to the number of available target electrons, which scales linearly with the atomic number Z of the material. The cross-section decreases with increasing photon energy (scaling as $\sim 1/E$).
   The Compton cross-section also has a spin-dependent component [47, 48], as shown in Fig. 3.4, which can be leveraged for polarimetry measurements and will be discussed further in this thesis in Sec. 3.2.

4. **Pair Production**: Pair production becomes possible when the photon energy exceeds twice the rest mass of an electron ($E = 2 \cdot 511\,\text{keV}$) and becomes the dominant process in the multi-MeV energy range. In this process, the photon interacts with the electromagnetic field of a nucleus or an atomic electron, creating an electron-positron pair.

2.3.3. Electromagnetic Cascades

When a high-energy electron, positron, or photon traverses dense matter, it can trigger a cascade-like process, referred to as an **electromagnetic shower** (cascade). In such a process, various interactions, as previously introduced, contribute to the development of the shower. For instance, when a high-energy electron enters a material, it primarily loses energy through bremsstrahlung radiation, emitting numerous photons. The behavior of these photons depends on their energy. Low-energy photons lose energy through Compton scattering or the photoelectric effect, while high-energy photons may undergo pair production, generating secondary energetic electrons and positrons. These secondary particles, in turn, deposit energy into the material and can initiate further interactions, repeating the same mechanisms. This results in a cascade of particles with progressively decreasing energy as the shower develops.

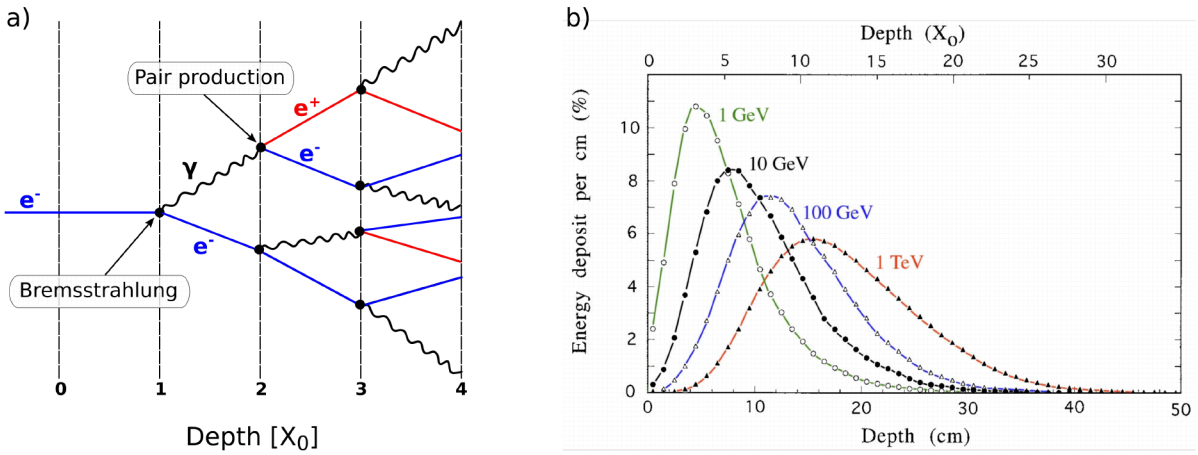

Figure 2.3.: a) Illustration of the development of an electromagnetic shower in a simplified model. b) Energy deposition as a function of depth for electromagnetic showers initiated by particles with energies of 1, 10, 100, and 1000 GeV, developing in a block of copper. Results are based on EGS4 [49] simulations (taken from [43]).

As the cascade progresses, the energy deposited within the material increases with depth due to the particle multiplication processes described above. This growth continues until the average energy of the shower particles falls below the critical energy, E_c (see Eq. 2.7), at which point particle multiplication diminishes. The depth where the number of shower particles reaches its maximum is called the shower maximum. Beyond this point, the number of particles and the energy deposition per unit depth decreases gradually, as energy loss occurs predominantly through ionization and excitation rather than further particle multiplication (see Fig. 2.3). Because the dominant shower processes are bremsstrahlung and pair production,

the longitudinal and lateral development of the shower is parameterized using the radiation length, X_0. The radiation length is defined as the distance over which a high-energy electron (or positron) loses $(1 - e^{-1}) = 63.2\,\%$ of its initial energy through bremsstrahlung. The value of X_0 depends on the properties of the absorber material and can be calculated using [41]:

$$X_0 \left[\frac{\mathrm{g}}{\mathrm{cm}^2}\right] = \frac{716\,A}{Z(Z+1)\,\ln\left(287/\sqrt{Z}\right)} \tag{2.10}$$

where Z and A are the atomic number and weight of the material, respectively. Unlike electrons or positrons, photons do not lose energy continuously but instead interact probabilistically. For photons, the concept of the mean free path length, λ_γ, is used to describe the average distance a photon can travel before undergoing pair production. The radiation length is related to the mean free path by:

$$\lambda_\gamma = \frac{9}{7} X_0 \tag{2.11}$$

The qualitative behavior of an electromagnetic shower can be understood through a simplified approach known as Heitler's model [50]. Assuming that bremsstrahlung and pair production interactions always occur after a fixed distance equal to one radiation length, X_0, creating exactly two outgoing particles (photon-electron or electron-positron), where the energy of the initial particle is equally shared between them. This simplified cascade is illustrated in Fig. 2.3 a). Under this assumption, the number of particles after t radiation lengths is given by:

$$N(t) = 2^t \tag{2.12}$$

The energy per particle at this stage is then:

$$E(t) = \frac{E_0}{2^t} \tag{2.13}$$

where E_0 is the initial energy of the primary particle. The cascade (or particle multiplication) is assumed to stop when the energy of individual shower particles reaches the critical energy, E_c. At this point, the shower reaches its maximum, occurring at a depth

$t_{\max}$. Following Eq. 2.13, $t_{\max}$ depends logarithmically on the initial particle energy:

$$t_{\max} \propto \log\left(\frac{E_0}{E_c}\right) \tag{2.14}$$

This simple model reveals the logarithmic scaling of the shower length with the energy of the primary particle.
A more quantitative description of electromagnetic shower development can be achieved through Monte Carlo simulations, which have shown that the shower maximum can be described by the empirical formula [41]:

$$t_{\max} = \ln\frac{E}{E_c} + f \tag{2.15}$$

Here, f is -0.5 for electrons and 0.5 for photons. This small difference arises from the distinct nature of the initial interaction processes. In Fig. 2.3 a), the energy deposition of an electromagnetic shower as a function of depth is exemplified for a block of copper, with initial electron energies of 1, 10, 100, and 1000 GeV, illustrating the logarithmic scaling of the longitudinal shower depth [43]. It should be noted that the development of an electromagnetic shower is approximately material-independent, scaling with X_0, although not perfectly. For high-Z materials, where the critical energy E_c is lower (Eq. 2.7), the multiplication process continues for a longer distance, causing the shower maximum to occur at a greater depth in terms of X_0 (see Eg. 2.15). Additionally, beyond the shower maximum, the shower decays more slowly in high-Z materials [43].
The lateral size of an electromagnetic shower is roughly independent of the beam energy and can be described by the Molière radius, R_M. Typically, about 90 % of the shower's energy is contained within a cylinder of radius R_M around the shower axis. The Molière radius can be parameterized as [43]:

$$R_M\left[\frac{\mathrm{g}}{\mathrm{cm}^2}\right] = \frac{21\,\mathrm{MeV}}{E_c[\mathrm{MeV}]} \cdot X_0 \tag{2.16}$$

2.4. Calorimetry for Energy Measurement

Calorimetry, in its broadest sense, refers to the measurement of heat, as it was originally developed in the context of thermodynamics. In particle physics, however, calorimeters are fundamental detector systems used to measure the energy of particles.

These detectors operate by stopping (absorbing) particles in a material, where the deposited energy is converted into measurable signals.
In high-energy physics, calorimeters are broadly classified into electromagnetic and hadronic calorimeters, depending on the type of particles they are optimized to measure. Within the scope of this thesis, only electromagnetic calorimeters are relevant. These detectors are specifically designed to measure the energy of particles such as electrons, positrons, and photons.
A key performance metric of any calorimeter is its energy resolution, which quantifies the precision with which the energy of a particle or particle bunch can be measured. Typically, the energy resolution of a calorimeter improves with increasing particle energy and depends on several factors, whose parametrization will be discussed in a subsequent section.

2.4.1. Energy Resolution

A primary quality criterion for calorimeters is their energy resolution. The energy resolution of most calorimeters is determined by the stochastic fluctuations in the number of charged particles N in the shower. If N is proportional to the initial particle energy E and follows Poisson statistics, the energy resolution can be expressed as:

$$\frac{\sigma_E}{E} \propto \frac{\sqrt{N}}{N} = \frac{1}{\sqrt{N}} \propto \frac{1}{\sqrt{E}} \tag{2.17}$$

In practice, in addition to stochastic terms, there are additional contributions with different energy dependencies. Generally, the energy resolution can be parameterized with three terms added quadratically:

$$\frac{\sigma_E}{E} = \frac{a}{\sqrt{E}} \oplus \frac{b}{E} \oplus c \tag{2.18}$$

The first term, scaling with $\frac{1}{\sqrt{E}}$, accounts for the contribution of stochastic shower fluctuations as mentioned above. The noise term b, whose absolute fluctuations are energy-independent, contributes as $\frac{1}{E}$ to the total relative energy resolution. This term is mostly due to the electronic noise of the readout electronics and is dominant at lower total energies.
The last term c represents a constant contribution, reflecting the maximum achievable relative energy resolution, typically on the order of a few percent. It dominates at

high energies where the effects of a and b become negligible. The constant term c is limited by the quality of the hardware and calibration procedures. It includes contributions from inhomogeneities, calibration imperfections, dimensional variations in the calorimeter construction, nonlinearities in the readout electronics, and fluctuations in leakage losses [51].

2.4.2. Basic Concepts of Electromagnetic Calorimeters

This section briefly introduces typical concepts of electromagnetic calorimeters as applied in particle physics. For more detailed information, refer to [43, 52].
Calorimeters generally consist of a large, instrumented volume of specific material in which a traversing particle deposits its energy, converting it to a measurable signal, such as scintillation light or Cherenkov radiation. These signals are then detected using photon sensors, such as photomultiplier tubes (PMT, see Sec. 4.4).
Electromagnetic calorimeters commonly used in particle physics are categorized into two main designs: homogeneous calorimeters and sampling calorimeters.

Sampling Calorimeters

In sampling calorimeters, the processes of energy absorption and signal generation occur in distinct materials, referred to as passive and active materials, respectively. The absorber (passive material), typically a dense material such as lead or iron, stops and absorbs the particle's energy, while the active material, such as plastic scintillators, generates the detectable signal. These materials are typically arranged in a sandwich-like structure, where high-Z absorber layers induce particle showers, and the resulting secondary particles produce signals in the active layers.
Sampling calorimeters offer compact designs due to the use of high-density absorber materials, such as lead, which are cost-effective. Additionally, the segmented structure provides lateral and transverse information about the particle shower. However, sampling calorimeters typically exhibit moderate energy resolution because only a fraction of the particle (shower) energy is deposited in the active material, which is referred to as sampling fraction f_{samp} (relative fraction). Consequently, the fluctuations are amplified when scaling to the full energy. Thus, the stochastic term of the energy resolution (see Eq. 2.18) of sampling calorimeters scales with $\frac{1}{\sqrt{f_{\text{samp}}}}$ and exhibits typical values of $\sim \frac{10\%}{\sqrt{E/GeV}}$ [43].

Homogeneous Calorimeters

Homogeneous calorimeters, more relevant to the scope of this thesis, consist entirely of an active material. In these devices, the entire instrumented volume absorbs the particle energy and generates the detectable signal. Commonly used materials include scintillating crystals (e.g., $PbWO_4$, BGO, CsI(Tl)) and lead glass, which produce scintillation or Cherenkov light, respectively.
Homogeneous calorimeters are particularly valued for their intrinsically good energy resolution, as the total energy of the particle shower is contained within the active material which leads to smaller fluctuations due to higher statistics. The stochastic term of the energy resolution of homogeneous electromagnetic calorimeters is typically on the order of a few $\frac{\%}{\sqrt{E/GeV}}$ [43]. However, in contrast to sampling calorimeters, homogeneous calorimeters typically lack detailed spatial information about the shower development.
Figure 2.4 illustrates a simple design concept for a homogeneous Cherenkov calorimeter, utilizing lead glass as the active material and a PMT for signal readout. A photon traversing the lead glass undergoes pair production, creating an electron-positron pair. If these charged particles exceed the speed of light in the material, they emit Cherenkov radiation. The Cherenkov photons are then detected by the photomultiplier tube, which converts the optical signal into an electrical signal proportional to the particle's energy.

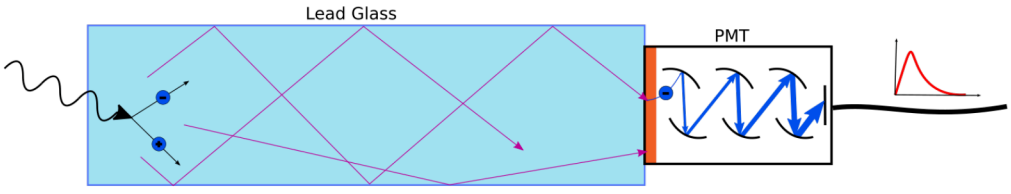

Figure 2.4.: Simplified concept of a homogeneous lead-glass Cherenkov calorimeter. A photon traversing the calorimeter undergoes pair production, emitting Cherenkov radiation that is detected by a photomultiplier tube, resulting in a signal proportional to the particle's energy.

2.5. Electron Polarimetry Methods

The most commonly used methods for measuring electron beam polarization are based on electron scattering processes with spin-dependent scattering cross-sections. The primary physical processes exploited include Mott and Møller scattering, as well as (laser) Compton scattering, where the polarized electron beam interacts with unpolarized nuclei, polarized atomic electrons, or polarized photons, respectively. In all polarimeter techniques, the polarization is determined by measuring the asymmetry in the scattering rates between two possible polarization states. A brief overview of these polarimetry methods is provided below; for more detailed information, please refer to [16, 53, 54].

Mott Polarimetry This method utilizes the elastic scattering of polarized electrons by the Coulomb field of an unpolarized heavy nucleus. Thin unpolarized foils, such as gold, are typically used as scattering targets. The scattering exhibits an asymmetry with respect to the transverse polarization of the electrons due to spin-orbit interactions between the electron and the electrostatic field of the nucleus. Mott scattering is sensitive only to transverse beam polarization and is effective for low beam energies (below 10 MeV).

Møller Polarimetry In this technique, polarized beam electrons scatter from other polarized electrons in a target. Magnetized ferromagnetic foils are commonly used as targets. Asymmetries in the scattering rates are proportional to the polarization of both the beam and the target. This method is effective across a wide energy range, from MeV up to several GeV. However, its use is limited to low electron beam currents (a few μA) due to the degradation of target magnetization caused by beam heating.

Laser Compton Polarimetry This method involves the scattering of high-energy electrons from laser photons. A circularly polarized laser typically collides nearly head-on with the polarized high-energy electron beam. The polarization-dependent asymmetry can be measured using either the back scattered photons or the scattered electrons. This technique is non-destructive and particularly suitable for energies above approximately 1 GeV.

Given the expected parameters for the LEAP experiment (see Sec. 3.1.2), with beam energies ranging from 30 MeV to 80 MeV and beam peak currents on the order of kA, none of the above polarimetry techniques is particularly suitable for measuring

the longitudinal spin-polarization. Instead, **Compton transmission polarimetry** is envisaged as a viable method for polarization measurement in LEAP. This established technique will be described in detail in Sec. 3.2.

Chapter 3.

The LEAP Project: Conceptional Design and Methods

The LEAP (Laser Electron Acceleration with Polarization) project at DESY is a proof-of-principle experiment aimed at demonstrating, for the first time, the generation of spin-polarized electron beams from an LPA source, thereby proving the feasibility of polarization-preserving plasma acceleration.
For the generation of polarized electron beams, the envisaged LPA concept in LEAP is based on colliding pulse injection combined with a pre-polarized plasma source. While the production of polarized beams is one key aspect of the project, equally important is the precise measurement of the achieved polarization degree. Within LEAP, the polarization measurement of the generated LPA beams is planned to be performed using Compton transmission polarimetry.
In the following chapter, the anticipated LPA concept will be discussed, along with the expected beam parameters. Furthermore, the concept of Compton transmission polarimetry will be introduced. Additionally, the results of a simulation-based design study for the envisaged Compton transmission polarimeter for LEAP, including the requirements for its components, will be presented.

3.1. Generation of Polarized Electron Beams with an LPA

While multiple plasma-based methods to generate polarized electron beams have been proposed [55] the most promising method for generating polarized beams using plasma-based accelerators involves the use of a pre-polarized plasma source [9, 14]. At

first glance, this concept appears straightforward: pre-polarized electrons are injected and subsequently accelerated within the wakefield generated by the LPA driver pulse. However, this approach encounters two primary challenges. The first is the availability of a suitable pre-polarized plasma source for LPAs. The second is ensuring that the electron polarization is preserved during the acceleration process.
The polarized plasma source could potentially be prepared through the molecular photodissociation of hydrogen halides using circularly polarized ultraviolet (UV) laser pulses [13, 14, 56–60] which is a well-studied process enabling the production of $> 10^{19}\,\mathrm{cm}^{-3}$ densities of polarized hydrogen. This approach will be discussed in the next section.
In the context of accelerating spin-polarized electrons, spin depolarization primarily occurs during the injection phase of the LPA process [8]. Several LPA concepts using a pre-polarized plasma source have been proposed, including density down-ramp injection [9], self-injection [10], Laguerre-Gaussian laser beams [11], and colliding pulse injection [12]. Among these, the first three approaches face significant practical limitations, such as the requirement for unrealistic plasma density profiles. However, the concept of colliding pulse injection proposed by Bohlen et al. shows the greatest potential. This injection method provides precise control over electron spin evolution during injection due to the numerous adjustable properties of the colliding laser pulses. Assuming a fully polarized plasma source, their simulation studies demonstrate that colliding pulse injection can produce polarized electron beams with polarization exceeding 90 %, high beam charges in the tens of pC, low normalized beam emittance ($< 1\,\mathrm{mm\,mrad}$) and energy spreads at the percent level [12]. This method is envisioned to be implemented within the LEAP project.

3.1.1. Pre-Polarization of the Plasma Source

The preparation of a pre-polarized plasma target has been proposed utilizing the molecular photo-dissociation of hydrogen halides [11, 13, 14]. The concept, illustrated in Fig. 3.1, involves three sequential steps.
First, the molecular bonds of the diatomic halide molecules are aligned using the electric field of a linearly polarized infrared (IR) laser pulse [61].
In the second step, the aligned molecules are dissociated by a circularly polarized ultraviolet (UV) laser pulse. Choosing the correct wavelength of the dissociation laser enables dissociation through a single channel, which leads to a polarization of

the two valence electrons from the hydrogen-halide bond. The polarization arises because the electronic angular momentum projection (along the molecular bond axis) of the particular molecular state is conserved [60]. For HCl molecules that has been demonstrated at UV wavelengths at around 200 nm [13, 62].
In the third step, the atoms are ionized by the LPA driver pulse, and the resulting free electrons are injected into the plasma wakefield for acceleration. To preserve the electron polarization for plasma acceleration, this ionization process must occur on a timescale much shorter than the hyperfine coupling. Hyperfine coupling transfers the electron spin polarization to the nuclei after the dissociation process, occurring on a timescale of approximately 350 ps for hydrogen [62].
The degree of polarization achievable in the plasma electrons is influenced by the choice of the precursor gas. The maximum fraction of polarized electrons is fundamentally constrained by the fact that only the electrons within the dissociated molecular bond can be pre-polarized. Halides contain numerous unpolarized outer-shell electrons that are easily ionized by the high intensity of the LPA driver pulse, thereby diluting the overall polarization of the plasma electrons. For hydrogen halides, this dilution limits the maximum achievable polarization to 25 % if all outer-shell electrons are ionized.
In contrast, nearly 100 % polarization of the plasma source electrons could theoretically be achieved using molecular hydrogen. However, the photo-dissociation of molecular hydrogen requires UV wavelengths shorter than 100 nm [63], which are challenging to produce with current laser technology and, therefore, remain impractical at present [64].

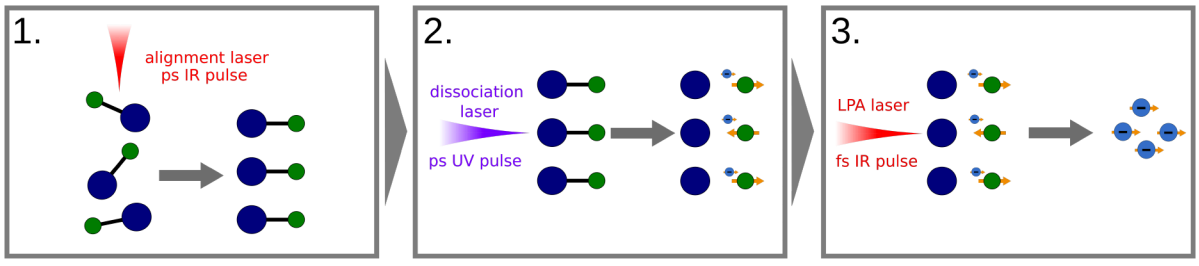

Figure 3.1.: Schematic depiction of the pre-polarization process for a plasma source in three steps: (1.) Alignment of the diatomic molecular bonds using a linearly polarized IR laser pulse. (2.) Photo-dissociation of the molecules with a circularly polarized UV laser pulse. (3.) Ionization of the atoms to create the plasma, followed by electron acceleration within the LPA wakefield.

3.1.2. LEAP Conceptional Design

The LEAP project will be built upon an existing LPA setup, utilizing a 10 Hz, 25 TW Titanium:sapphire (Ti:Sa) laser system, where stable acceleration of electron bunches over several hours has been demonstrated [65]. This system is planned to be adapted to facilitate polarized LPA through colliding pulse injection, employing a pre-polarized HCl gas target [12]. Figure 3.2 illustrates the anticipated LPA setup, showing all laser beams involved in the process. The laser for aligning the HCl molecules, as well as

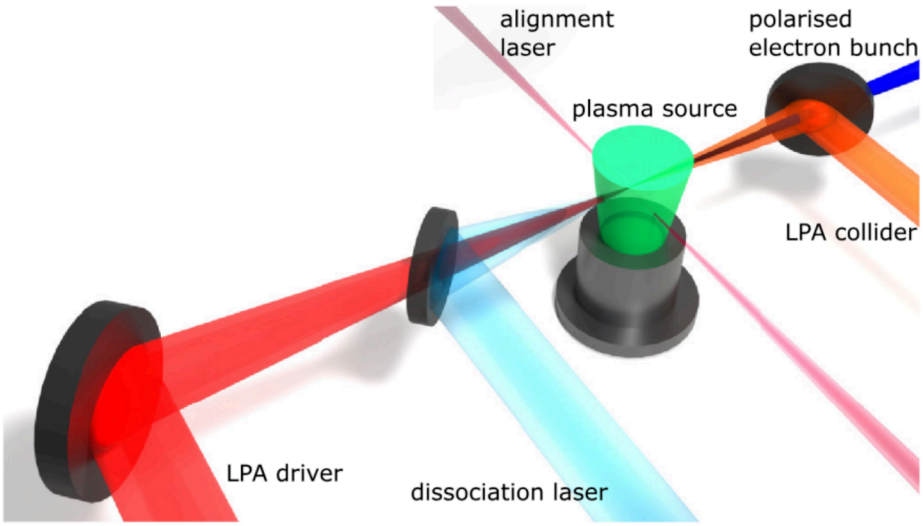

Figure 3.2.: Schematic of the conceptual design of an LPA employing colliding pulse injection for generating spin-polarized electron beams from a pre-polarized plasma source, as anticipated within the LEAP project (sketch adapted from [12]).

the LPA colliding laser for electron injection, will be created directly from split-offs of the main LPA pulse. The UV dissociation laser will be realized via fourth harmonic generation (FHG) from the fundamental 800 nm Ti:Sa system, utilizing cascading second harmonic generation (SHG) in two BBO crystals. This approach, which ensures the LPA driver and dissociation laser are inherently synchronized, will be discussed in detail in Chap. 5.

Given the experimental setup within the LEAP project, polarized electron beams with an overall polarization of approximately 10 %, a bunch charge of about 3 pC, and beam energies ranging from 30 MeV to 80 MeV are expected. It is important to note that the LEAP project is a proof-of-principle experiment, aiming to demonstrate the generation of polarized electron beams from an LPA for the first time, rather than achieving the highest possible polarization or energy levels.

Producing polarized beams is one aspect, but accurately determining their degree of polarization is just as crucial. The polarization measurement concept within the LEAP project, which is an integral part of achieving polarization, will be discussed in the following sections.

3.2. Compton Transmission Polarimetry

In the energy range where Compton scattering is the predominant interaction of photons with matter (see Fig. 2.2), the circular polarization of photons can be effectively determined by measuring the asymmetry in their transmission through a block of magnetized iron, with respect to the polarity of the magnetization [47, 48]. This method leverages the polarization dependence of Compton scattering.
The technique can be used to retrieve the longitudinal polarization of electrons (or positrons) by first converting them into circularly polarized photons via bremsstrahlung in a converter target. For longitudinally polarized electrons with energies $E_{e^-} \geq 2\,\mathrm{MeV}$ the polarization transfer can be almost complete for bremsstrahlung photons with $E_\gamma = E_{e^-}$ emitted in the forward direction [44–46]. By measuring the transmission rates of the polarized photons through magnetized iron, with the magnetic field oriented parallel and antiparallel to the electron (or positron) momentum vector, the longitudinal spin polarization of the original particle can be inferred. The transmission asymmetry can be measured with a calorimeter, as illustrated in Fig. 3.3.

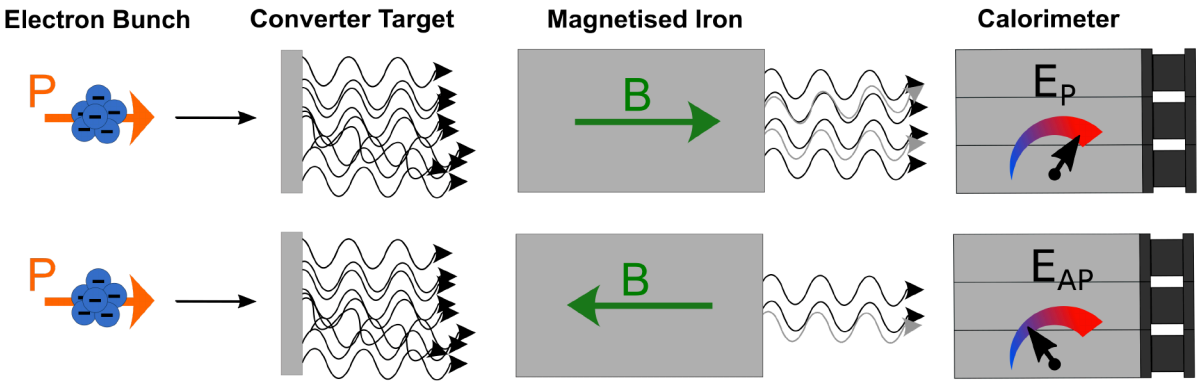

Figure 3.3.: Schematic depiction of the Compton transmission polarimeter concept.

This method can be applied over a wide range of beam energies, extending from a few up to several hundred MeV [46, 66–70]. For example, it was employed in the E166 experiment at SLAC [66] to measure the polarization of positrons with energies between

4 MeV and 8 MeV. In this experiment, a polarization of about 80 % was measured, with a relative measurement error of approximately 10–15 %. The following sections will provide a more detailed explanation of the technique and measurement.

3.2.1. Polarization dependent Photon Transmission

This section closely follows the explanation provided by [66]. The Compton scattering cross-section for photons interacting with free electrons can be expressed as:

$$\sigma = \sigma_0 + P_{e^-}^{\mathrm{Fe}} P_\gamma \sigma_1, \tag{3.1}$$

where σ_0 represents the unpolarized (Klein-Nishina) cross-section, and σ_1 the spin-dependent part of the cross-section [47, 48]. Here, P_γ is the circular polarization of the photons, and $P_{e^-}^{\mathrm{Fe}}$ is the net longitudinal polarization of the atomic electrons (in the iron absorber). Figure 3.4 illustrates the energy dependence of the cross-sections terms σ_0 and σ_1. $P_{e^-}^{\mathrm{Fe}}$ can be related to the average magnetization M and, therefore, to the

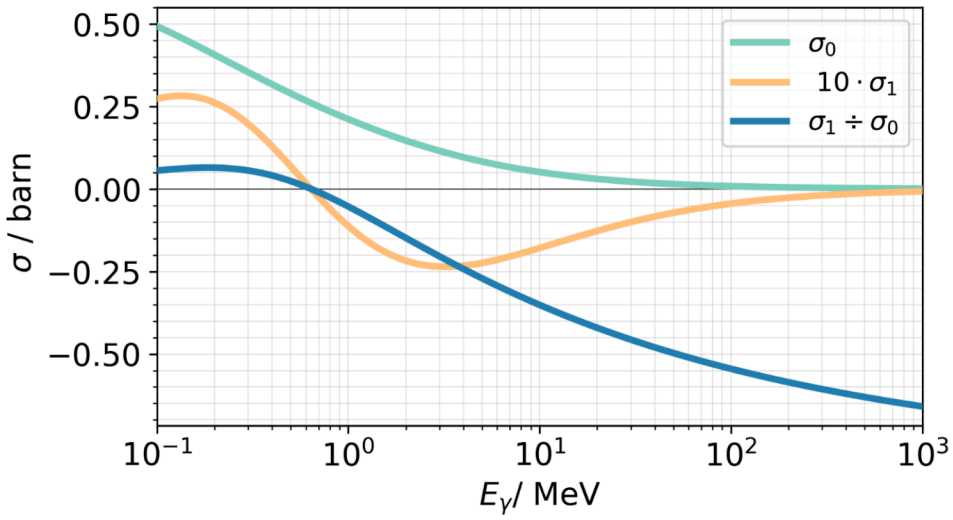

Figure 3.4.: The total cross-section terms σ and σ_1 for Compton scattering of circularly polarized photons with energy E_γ off unpolarized and longitudinally polarized electrons, respectively (taken from [34]).

average (longitudinal) magnetic field $\langle B - B_0 \rangle$ of the iron. Here B_0 is the "air field", the part of the total magnetic field B which is directly due to the current flow in the

coils and would be present in the absence of the iron core. This relation is given by:

$$P_{e^-}^{\mathrm{Fe}} = 2 \cdot \frac{g' - 1}{g'} \cdot \frac{M}{n_{e^-}\mu_B} = 0.03727 \langle B[T] - B_0[T] \rangle \,, \tag{3.2}$$

where M is the magnetization, $g' = 1.919 \pm 0.002$ is the magneto-mechanical factor, n_{e^-} is the electron number density and μ_B is the Bohr magneton. For fully magnetized (saturated) iron, $P_{e^-}^{\mathrm{Fe}}$ is naively estimated to be $\pm 2/26$.
The transmission probability $T(E, L)$ for photons of energy E and polarization P_γ passing through a block of magnetized iron of length L and longitudinal polarization $P_{e^-}^{\mathrm{Fe}}$ can be expressed as:

$$T(E, L) = e^{-n_{e^-}^{\mathrm{Fe}} L \sigma} = e^{-n_{e^-}^{\mathrm{Fe}} L (\sigma_0 + \sigma_{\mathrm{photo}} + \sigma_{\mathrm{pair}})} e^{-n_{e^-}^{\mathrm{Fe}} L P_{e^-}^{\mathrm{Fe}} P_\gamma \sigma_1}, \tag{3.3}$$

where σ_{photo} is the cross-section for the photoelectric effect, and σ_{pair} is the cross-section for pair production.

3.2.2. Asymmetry, Analyzing Power and Polarization Measurement

Using the definition of the transmission T in Eq. 3.3, the transmission asymmetry δ can be defined as:

$$\delta = \frac{T_{\mathrm{P}} - T_{\mathrm{AP}}}{T_{\mathrm{P}} + T_{\mathrm{AP}}}, \tag{3.4}$$

where T_{P} (T_{AP}) denotes the case where the photon polarization P_γ is parallel (anti-parallel) with respect to the target electrons' polarization $P_{e^-}^{\mathrm{Fe}}$. This convention in Eq. 3.4 is chosen to result in a positive asymmetry δ when the polarization-dependent Compton scattering cross-section term σ_1 is negative, which is expected for the energies in the LEAP project. For small values of $-n_{e^-}^{\mathrm{Fe}} L \sigma_1$, the asymmetry δ can be approximated by:

$$\delta = \tanh(-n_{e^-}^{\mathrm{Fe}} L P_{e^-}^{\mathrm{Fe}} P_\gamma \sigma_1) \approx -n_{e^-}^{\mathrm{Fe}} L P_{e^-}^{\mathrm{Fe}} P_\gamma \sigma_1. \tag{3.5}$$

Using this, the analyzing power of the system can be defined as:

$$A_\gamma = -n_{e^-}^{\mathrm{Fe}} L \sigma_1 = \frac{\delta}{P_{e^-}^{\mathrm{Fe}} P_\gamma}. \tag{3.6}$$

In other words, the analyzing power A_γ can be seen as the asymmetry δ for the ideal case where the polarization of both the photons P_γ and the electrons in the iron absorber $P_{e^-}^{\mathrm{Fe}}$ are 1. Consequently, the initial photon polarization P_γ can be retrieved by measuring the asymmetry δ, provided A_γ and $P_{e^-}^{\mathrm{Fe}}$ are known:

$$P_\gamma = \frac{\delta}{A_\gamma \cdot P_{e^-}^{\mathrm{Fe}}}. \tag{3.7}$$

The analyzing power of the polarimeter A_γ needs to be determined in practice using Monte Carlo simulations. Because of its energy dependence, it must be convoluted over the incoming photon spectrum [71]. This analyzing power must be simulated for the exact experimental setup and beam conditions. For the measurement of polarized electrons (positrons), the analyzing power $A_{e^\pm}$ must be determined through simulations that combine the processes of polarization transfer from electrons (positrons) to photons and their transmission through the magnetized iron block. The polarization is then calculated using Eq. 3.8:

$$P_{e^\pm} = \frac{\delta}{A_{e^\pm} \cdot P_{e^-}^{\mathrm{Fe}}}. \tag{3.8}$$

In practice, the asymmetry measurement – and consequently the polarization measurement – will be performed using a calorimeter. Here, the transmitted energy sums are measured when the polarization of the electrons (positrons) $P_{e^\pm}$ is parallel (E_P) and anti-parallel (E_AP) to the polarization of the electrons in the iron $P_{e^-}^{\mathrm{Fe}}$. This can be achieved by flipping the magnetic field in the iron absorber. The asymmetry is then given by:

$$\delta = \frac{E_\mathrm{P} - E_\mathrm{AP}}{E_\mathrm{P} + E_\mathrm{AP}}. \tag{3.9}$$

The statistical uncertainty in the asymmetry can be calculated following statistical error propagation and is expressed as:

$$\Delta\delta = \frac{2E_\mathrm{P} \cdot E_\mathrm{AP}}{(E_\mathrm{P} + E_\mathrm{AP})^2} \cdot \sqrt{\left(\frac{\Delta E_\mathrm{P}}{E_\mathrm{P}}\right)^2 + \left(\frac{\Delta E_\mathrm{AP}}{E_\mathrm{AP}}\right)^2} \tag{3.10}$$

3.3. LEAP-Specific Polarimeter Design

A Compton transmission polarimeter is proposed for the polarization measurement within LEAP. This type of polarimeter has been utilized in various experiments for beam energies in the range of a few MeV [46, 66–68] as well as for beam energies in the hundreds of MeV range [69, 70]. To evaluate the design – particularly the key parameter, the analyzing power A – of a Compton transmission polarimeter suitable for the tens of MeV energy range as expected for LEAP, an initial design study was conducted using `GEANT4` Monte Carlo simulations [34]. The simulation framework, `leap_sims`, used for the polarimeter design study, is introduced in Sec. 4.5. For additional details, refer to [34]. The following provides an overview of the design study, along with the primary results relevant to this thesis. This includes the influence of different polarimeter components on the analyzing power and the resulting requirements for the calorimeter.

3.3.1. Overview of the Polarimeter Design Study

For the design study, a simplified solenoid magnet with an iron core was assumed to serve as the analyzer for the polarimeter. A schematic of the magnet, as implemented in `GEANT4`, is shown in Fig. 3.5 a). The simulated magnet consists of an iron yoke, copper coils (modeled as solid copper bulk), a central cylindrical iron core serving as the analyzing absorber target, and a tungsten converter target positioned in front of the iron core. The initial design of the polarimeter's analyzing magnet was based on the solenoid magnet used in the positron line of the E166 experiment [66], featuring an aperture diameter of 50 mm. More detailed information about the dimensions of the relevant components will be provided throughout this section and additional information can be found in [34].
The design study aimed to investigate and optimize the analyzing power of the system for the tens of MeV electron energy range anticipated in LEAP. The optimization focused on two key geometric parameters of the polarimeter design: the length of the iron absorber and the thickness of the tungsten converter target. All simulation results presented here were conducted assuming monoenergetic, idealized electron bunches with a constant electron number of 5×10^5 (~ 0.08 pC) or 1×10^6 (~ 0.16 pC) which represents a fraction of the expected bunch charge for LEAP of 3 pC ($\sim 1.9 \times 10^7$ electrons per bunch). Simulating the full bunch charge would have been computationally

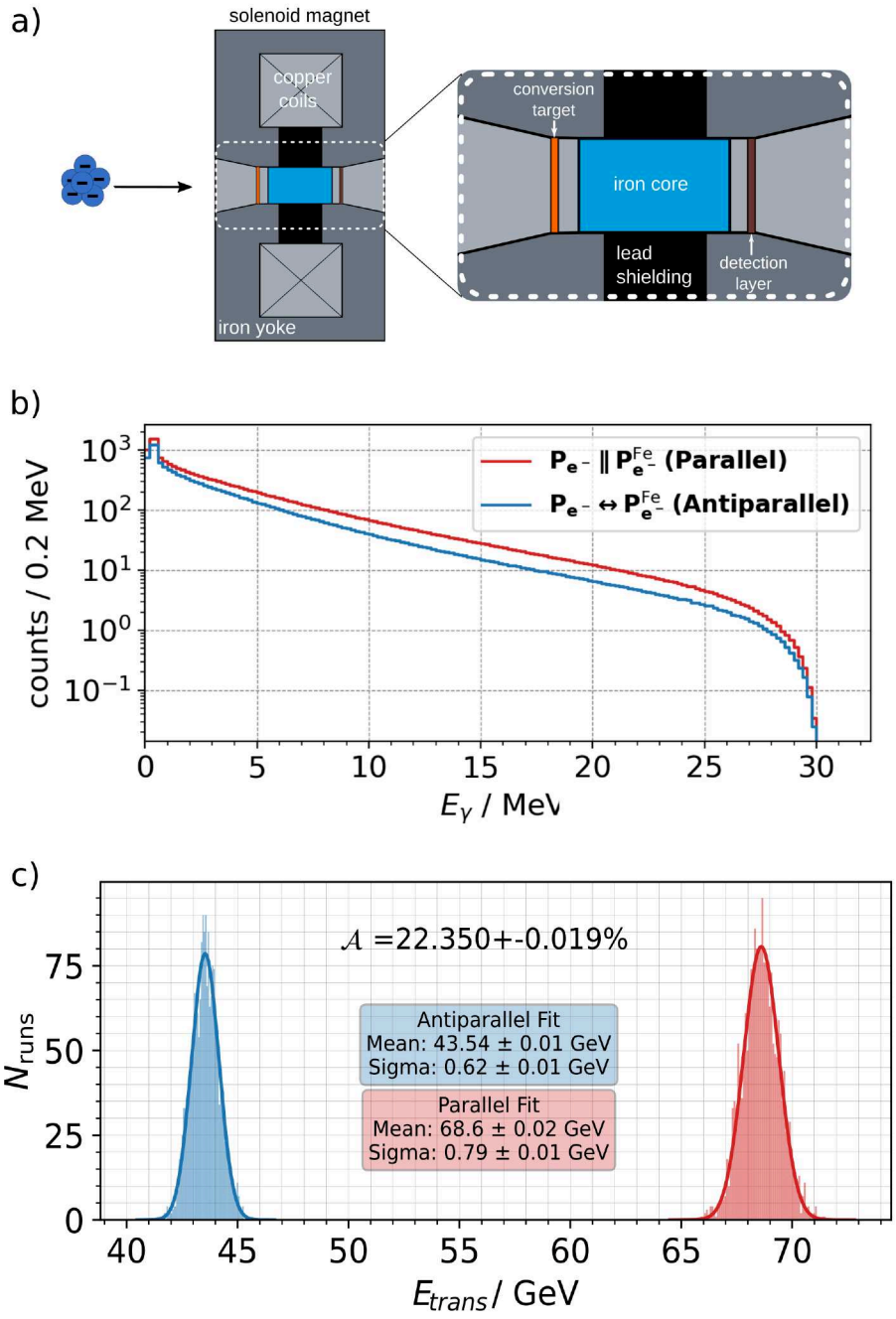

Figure 3.5.: a) Schematic of the simplified solenoid magnet geometry used in the design study for the LEAP polarimeter (adapted from [34]). b) Simulated transmitted photon spectra as expected for an idealized 30 MeV electron beam with a polarization of $|P_{e^-}^{Fe}| = 1$, where the electron polarization is parallel and antiparallel to the polarization of the electrons in the iron absorber ($|P_{e^-}^{Fe}| = 1$), shown in red and blue, respectively. c) Distribution of the transmitted photon energy sums (summed spectra from b)) for the parallel and antiparallel cases (taken from [34]).

expensive. Furthermore, the simulations assumed a vacuum, excluding additional scattering effects in air.

The analyzing power of the polarimeter is defined as the asymmetry observed (Eq. 3.9) for a fully (100 %) polarized electron beam ($|P_{e^-}| = 1$) and 100 % polarization of the electrons in the iron absorber ($|P_{e^-}^{\mathrm{Fe}}| = 1$), where the polarization of either the beam or the absorber is flipped (see Sec. 3.2.2). In the following, the simulation procedure for determining the analyzing power will be exemplified.

Figure 3.5 shows the photon transmission spectrum detected after the iron absorber (see panel a)), obtained for 2000 simulated electron bunches of monoenergetic 30 MeV electrons. Two cases were considered: one where the polarization of the electrons in the bunch is parallel (red curve) to the iron core polarization and one where it is antiparallel (blue curve). In the simulation, the polarization of the iron core was kept constant ($P_{e^-}^{\mathrm{Fe}} = 1$) while the polarization of the electron bunch alternated between $P_{e^-} = \pm 1$. A tungsten converter target of 1.75 mm thickness was used, and the iron core length was set to 150 mm.

The photon transmission spectra extend up to the total electron energy of 30 MeV. More photons are transmitted through the absorber in the parallel case due to the lower probability of Compton scattering. In Fig. 3.5 c) The distribution of the transmitted photon energy sums is shown as red and blue histograms for the parallel and antiparallel cases, respectively. Each entry in the histograms corresponds to the total photon energy sum (i.e., the sum of the transmitted photon spectrum) recorded for one of the 2000 simulated bunches per polarization direction. The histograms were fitted with Gaussian functions to extract the mean and standard deviation of each distribution. Using this data, the analyzing power (asymmetry) can be calculated with Eq. 3.9, where E_{P} and E_{AP} represent the mean values of the distributions for the parallel and antiparallel cases, respectively. For this specific setup, the analyzing power was calculated to be $A = 22.350 \pm 0.019\,\%$. The error corresponds to the statistical uncertainty of the simulation, calculated using Eq. 3.10, which incorporates the standard error of the mean $\sigma/\sqrt{N}$, where N is the number of simulated shots per distribution.

3.3.2. Design Study Results

The following section summarizes the results of the initial design study for the LEAP polarimeter [34].

Figure 3.6 a) illustrates the simulated analyzing power for the simplified detector setup discussed previously, using a monoenergetic 25 MeV electron bunch containing 10^6 electrons (~ 0.16 pC). The thickness of the tungsten converter target was fixed at 1.75 mm corresponding to half the radiation length for tungsten. The analyzing power is shown as a function of the absorber target length, which was varied up to 400 mm. While A increases linearly with the absorber length, the number of transmitted photons decreases exponentially, resulting in higher statistical uncertainty in the simulated analyzing power for longer cores, as shown in the lower panel. Nevertheless, because the electron bunches at LEAP have a significantly higher intensity (3 pC) compared to the simulation, the transmission rate is not a limiting factor [34]. Therefore, a longer absorber core is preferable for the LEAP polarimeter to maximize the analyzing power. In Fig. 3.6 b), the analyzing power is shown as a function of the electron energy, ranging from 1 MeV to 120 MeV, for three different lengths of the iron absorber target (magnet core): $L = 75$ mm, 150 mm, and 300 mm, represented by orange dots, triangles, and squares, respectively. The analyzing power decreases with increasing electron beam energy due to the energy dependence of the Compton cross-section (see Fig. 3.4). This energy dependence becomes less pronounced at higher beam energies. Therefore, for operation at the higher range of the expected beam energy at LEAP (~ 80 MeV), where the impact of energy variations are reduced, a longer core is preferred to enhance the analyzing power of the system.

Furthermore, Fig. 3.6 shows the analyzing power as a function of the thickness of the converter target, indicating that the thickness has no significant influence on the analyzing power. In the study, the converter target thickness was varied up to one radiation length for tungsten (3.5 mm). This independence of the converter target can be explained by the fact that the iron core itself acts as a converter, rendering the initial converter target unnecessary.

A solenoid magnet with an iron core length of 150 mm is already available from the E166 experiment [66], where it was used as a photon analyzer. This magnet, described in more detail in Sec. 7.1, will serve as the starting point for the LEAP polarimeter. Based on the design study results, the polarimeter's analyzing power featuring this 150 mm core is expected to be approximately $A = 22.4$ % at a beam energy of 30 MeV. Since the analyzing power depends on the exact beam energy, further investigations will be conducted to determine its behavior under the specific experimental conditions of the polarization measurement (see Sec. 7.7.4).

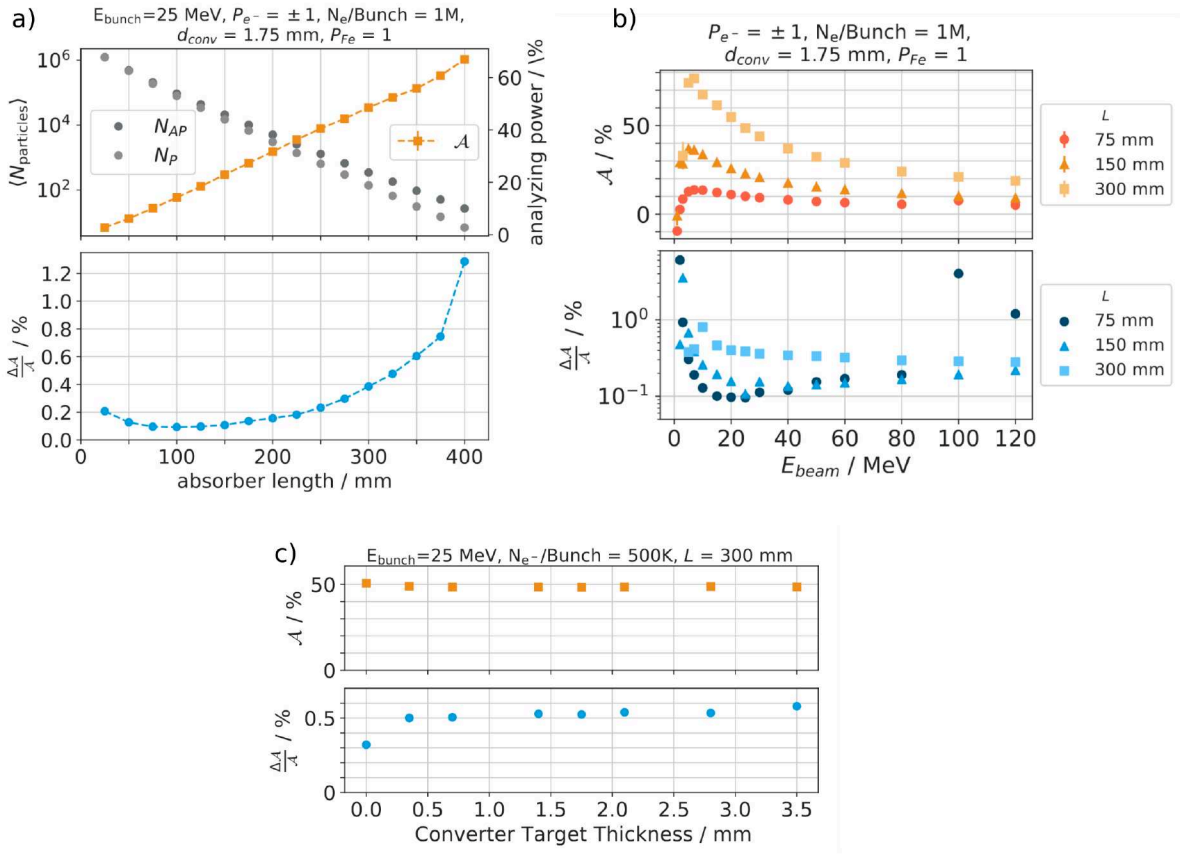

Figure 3.6.: a) Simulated analyzing power as a function of the absorber core length (orange squares), with the relative statistical uncertainty shown below. b) Analyzing power as a function of the electron energy for different absorber lengths: $L = 75\,\text{mm}$ (squares), 150 mm (triangles), and 300 mm (dots), together with the relative statistical uncertainty shown below. c) Analyzing power as a function of the converter target thickness, along with the relative statistical uncertainty [34]. Figures taken from [34].

3.3.3. Extrapolation of Observable Asymmetry and Calorimeter Requirements

In the previous section, the analyzing power of the polarimeter system was discussed, which essentially represents the scaling factor for how the initial beam polarization translates into an experimentally observable asymmetry and vice versa (see Eq. 3.8). This section provides a first extrapolation to the observable asymmetry under idealized conditions and discusses the measurement requirements, particularly the demands placed on the calorimeter.

Within the LEAP project, an electron polarization P_{e^-} of approximately 10 %. is expected. Furthermore, the polarization of the electrons within the solenoid iron core is

about $P_{e^-}^{\mathrm{Fe}} = 7.23\,\%$ when fully magnetized [66].
To explore the expected asymmetry δ, simulations were conducted [34] using the 150 mm core magnet (without the converter target), employing an idealized monoenergetic electron beam of 30 MeV with a constant charge of 0.08 pC (5×10^5 electrons). The polarization of the iron core was set to $P_{e^-}^{\mathrm{Fe}} = \pm 7.23\,\%$ while the beam polarization was set to $P_{e^-} = 10\,\%$ to mimic the expected polarization levels.

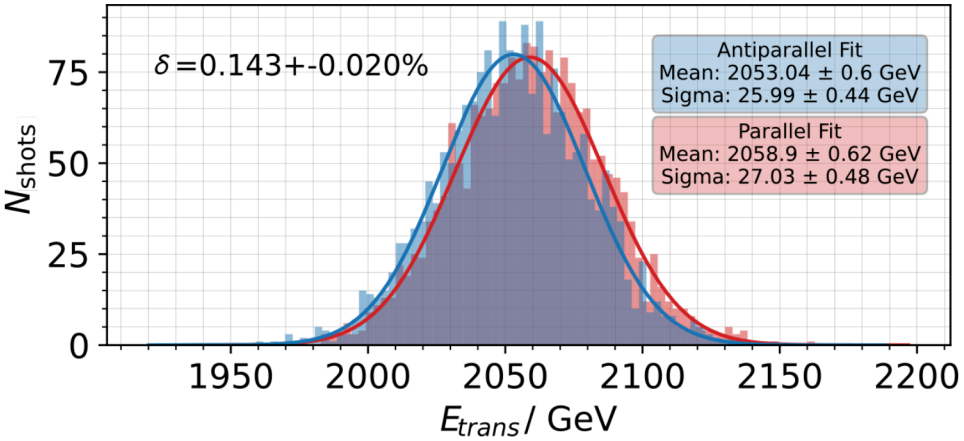

Figure 3.7.: Simulated transmitted energy through a 150 mm iron absorber for an idealized 30 MeV electron beam with a bunch charge of 3 pC, assuming an electron polarization of $P_{e^-} = 10\,\%$ and an iron core polarization of $P_{e^-}^{\mathrm{Fe}} = \pm 7.23\,\%$. The distributions where P_{e^-} and $P_{e^-}^{\mathrm{Fe}}$ are parallel and antiparallel are shown in red and blue, respectively (taken from [34]).

The distributions of the transmitted energy sums for 2000 simulated bunches are shown in Fig. 3.7. The simulation results were scaled to the full bunch charge of 3 pC, as expected for LEAP. The two cases, where P_{e^-} and $P_{e^-}^{\mathrm{Fe}}$ are parallel and antiparallel, are shown in red and blue, respectively. The total transmitted photon energy per bunch is expected to be in the TeV range and must be absorbed by the calorimeter. Consequently, the calorimeter must be capable of withstanding and accurately measuring such high energy levels. Compared to the simulations of the analyzing power shown earlier in Fig. 3.5 b), the distributions are much closer together, even overlapping, resulting in an asymmetry of $\delta = 0.14 \pm 0.02\%$, calculated using the mean and standard error of the mean along with Eqs. 3.9 and 3.10.
Notably, this simulation assumes a perfect detector with ideal energy resolution. However, in practical applications, the detector response will broaden the distributions, increasing the measurement error or the number of shots required to achieve the desired precision for these small, per-mille-level asymmetries.

Figure 3.8 shows the relative error of the measured asymmetry $\frac{\Delta\delta}{\delta}$, for the ideal beam conditions considered here. The relative error is displayed as a function of the total number of shots N_{shots} of which half of them are taken with parallel and the other half with anti parallel polarization setting, for four different calorimeter energy resolutions $\frac{\sigma_{\text{calo}}}{E}$. For the error calculations, Eqs. 3.9 and 3.10 were employed, with the relative error on the transmitted energy sums for E_{P} and E_{AP} given by:

$$\frac{\Delta E}{E} = \sqrt{\frac{(\frac{\sigma_{\text{sim}}}{E})^2 + (\frac{\sigma_{\text{calo}}}{E})^2}{N_{\text{shots}}/2}} \tag{3.11}$$

where σ_{sim} and E correspond to the mean and standard deviation of the respective distributions, as retrieved from the simulation shown in Fig. 3.7.

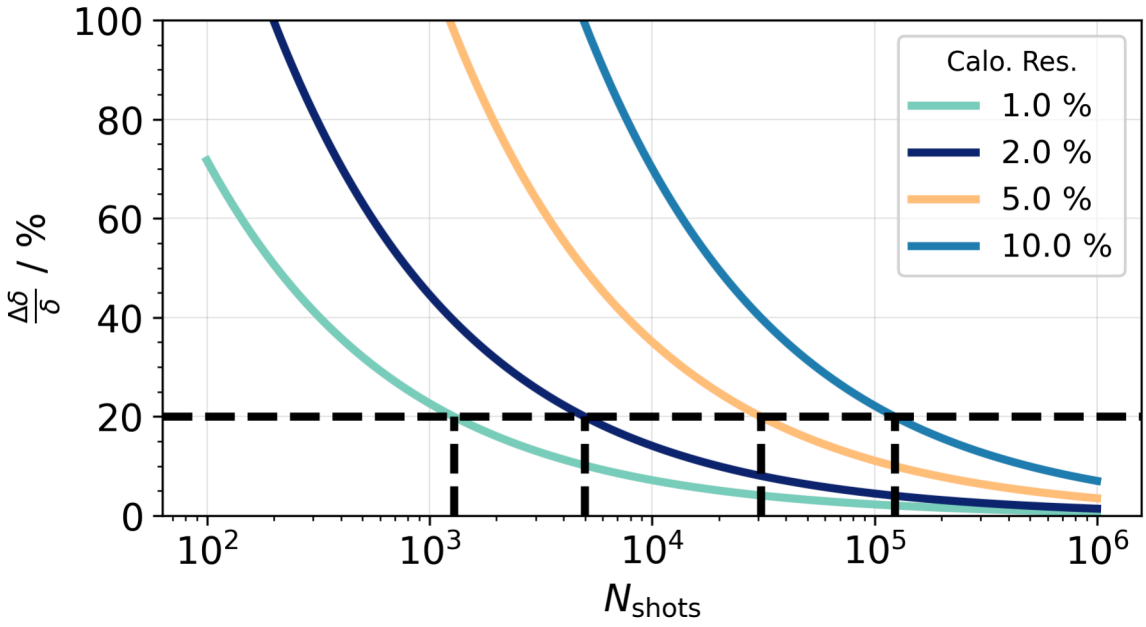

Figure 3.8.: Relative statistical uncertainty on the expected observable asymmetry as a function of the number of shots, shown for different calorimeter energy resolutions (taken from [34]).

Figure 3.8 indicates that more than 10000 shots are required for detector resolutions worse than 5 % to achieve a relative precision of 20 % in the measured asymmetry (marked by the black dashed line). This is impractical from an experimental perspective, as current accelerators have a repetition rate of only a few Hz, leading to unrealistically long measurement times. For a resolution of 2 %, the number of shots required to reach the same precision reduces to 5000, corresponding to a measurement

time of about 40 minutes assuming an accelerator repetition rate of 2 Hz. This begins to be experimentally more feasible. Further improving the resolution to 1 % reduces the required number of shots to around 1300, bringing the measurement time down to about 11 minutes, which would be even more favorable.
In this approach presented here for estimating the measurement uncertainty, the energy resolution can be regarded as a total resolution budget that also incorporates other effects that broaden the signals, such as fluctuations in beam charge and energy, which will be discussed later. Thus, a calorimeter with an energy resolution better than 2 % is required. The calorimeter must also be capable of absorbing large total photon energy sums in the TeV range without saturation. Therefore, a logical choice is to employ a homogeneous crystal calorimeter, which commonly offers an intrinsically high-energy resolution.

Another requirement for the calorimeter is its dimensions, which are vital for capturing all photons transmitted through the iron absorber, ensuring the energy is entirely deposited. Assuming the calorimeter is positioned immediately after the absorber, the aperture is primarily determined by the approximate diameter of the iron absorber, which is 50 mm. Therefore, the calorimeter should at least cover this area.
The calorimeter's length, specifically the crystals' length, should be sufficient to fully contain the electromagnetic shower and prevent longitudinal energy leakage. Since the level of shower energy containment in the longitudinal direction scales with the particle energy as $\ln(E)$ (see Sec. 2.3.3), calorimeters can be designed to be relatively compact. For instance, particles with GeV-level energies are stopped within ~ 10 radiation lengths X_0 (see Fig. 2.3). For lead glass, which is commonly used in homogeneous calorimeters and has an X_0 ranging from 1.7 cm to 3.1 cm [72, 73], this corresponds to a crystal length of about 20 cm to 30 cm. To emphasize, this length would already be sufficient for LEAP, as the energies of individual particles remain in the MeV range, while only the total energy sums are expected to reach the TeV range, as shown previously. The actual performance of the calorimeter, including its energy resolution and shower containment, will be assessed in a later section using `GEANT4` Monte Carlo simulations.

Chapter 4.

Experimental Facilities, Tools and Software

This chapter presents an overview of the experimental facilities, tools, and software utilized throughout this thesis, along with additional information on the diagnostics and methodologies employed in the experiments.

4.1. The DESY II Test Beam Facility

The DESY II Test Beam Facility [74], located on the DESY campus, provides users with access to multi-GeV electron and positron beams. Attached to the DESY II synchrotron, the facility operates three independent beamlines (T21, T22, T24) and offers selectable beam energies ranging from 1 to 6 GeV.

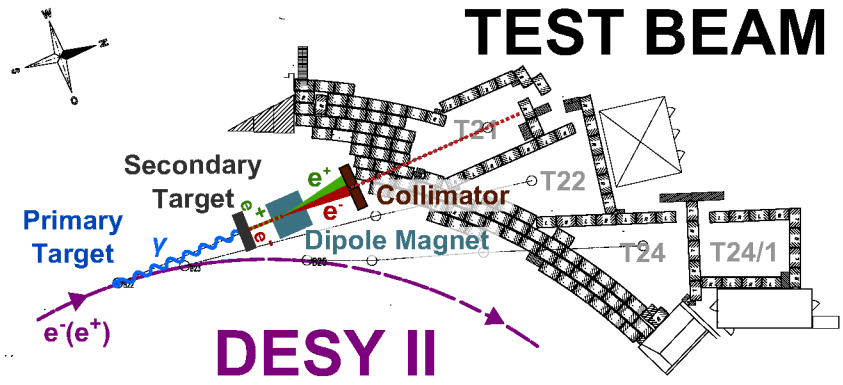

Figure 4.1.: Schematic of the DESY II Test Beam Facility and the beam generation process [74]

Figure 4.1 illustrates the layout of the facility, including its beamlines and the beam production mechanism. The beams are not derived directly from the primary DESY II beam (0.45 to 6.3 GeV electrons). Instead, they are produced through a double-conversion process.
A primary converter target (several μm thick carbon fiber) is installed in the DESY II beamline. When the DESY II beam interacts with this target, bremsstrahlung photons are generated with energies reaching up to the full beam energy of 6.3 GeV. These photons travel tangentially to the DESY II orbit and exit the vacuum system through an aluminum vacuum window. Afterwards, they propagate through up to 22 m of air before reaching the secondary converter target (several millimeters of copper or aluminum), where electrons and positrons are produced via pair production.
Subsequently, the electrons of a specific energy are selected using a dipole magnet and further collimated by a controllable (primary) collimator. Once the beam passes through the beam shutter, the particles exit the evacuated beam pipe and enter the respective test beam area. Here, an exchangeable, fixed-size (secondary) collimator is installed to provide additional beam collimation. Following the (secondary) collimator, the beam is made available for experimental use. The absolute energy spread of the beam remains constant across the full energy range and has been measured to be 158 ± 6 MeV [74] (measured at T21).
For more detailed information on the DESY II Testbeam Facility, please refer to [74].

4.2. The FLARE Facility

The FLARE facility, located at DESY, is a laboratory dedicated to research on laser plasma acceleration and its applications. The LEAP project is one of several projects hosted at the FLARE facility.

4.2.1. Laboratories and Laser System

The FLARE facility is divided into two primary areas: the laser laboratory and the experimental area, which is designated for laser-plasma acceleration experiments. This experimental area is referred to as the BOND (Beam Optimization and Novel Diagnostics) laboratory. Fig 4.2 shows the floor plan of both areas. The laser laboratory houses two main laser systems, whose beams are transferred via vacuum systems to

the BOND lab for use in their respective accelerator experiments. The laser system used throughout this thesis is the SPECTRE laser system, a 25 TW Titanium:Safire (Ti:Sa) laser with a central wavelength of 800 nm and a pulse duration of approximately 30 fs. This system allows for a maximum repetition rate of 10 Hz. The SPECTRE system generates the driver pulse for the LPA setup in the BOND lab, which was employed for the polarization measurement experiment discussed in this thesis (see Chap. 7). For a detailed description of the SPECTRE laser system and the general setup of the accelerator experiment in the BOND lab, the reader is referred to [75].

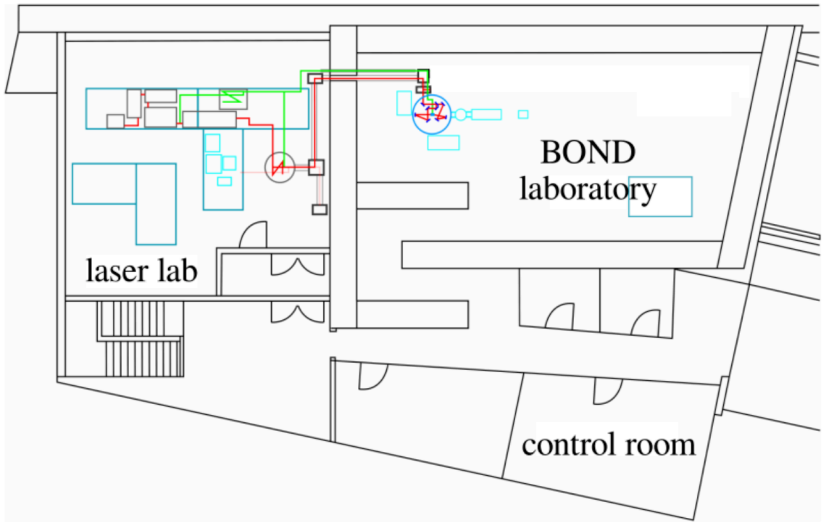

Figure 4.2.: Floor plan of the FLARE facility showing the laser laboratory, which hosts the SPECTRE laser system, and the BOND lab, where the LPA experiment is conducted. The control room, from which experiments are monitored and operated, is also shown (adapted from [75].)

4.2.2. Beam Diagnostics

This section introduces the electron beam diagnostics employed in the zero polarization measurement (see Sec. 7.2).

Beam Charge Measurement with Dark Current Monitor

The diagnostic used for a non-invasive measurement of the electrons bunch charge is the DaMon [75–77] which was initially developed as a dark current monitor for the European XFEL. The DaMon consist of a stainless steel cavity, as depicted in 4.3 a).

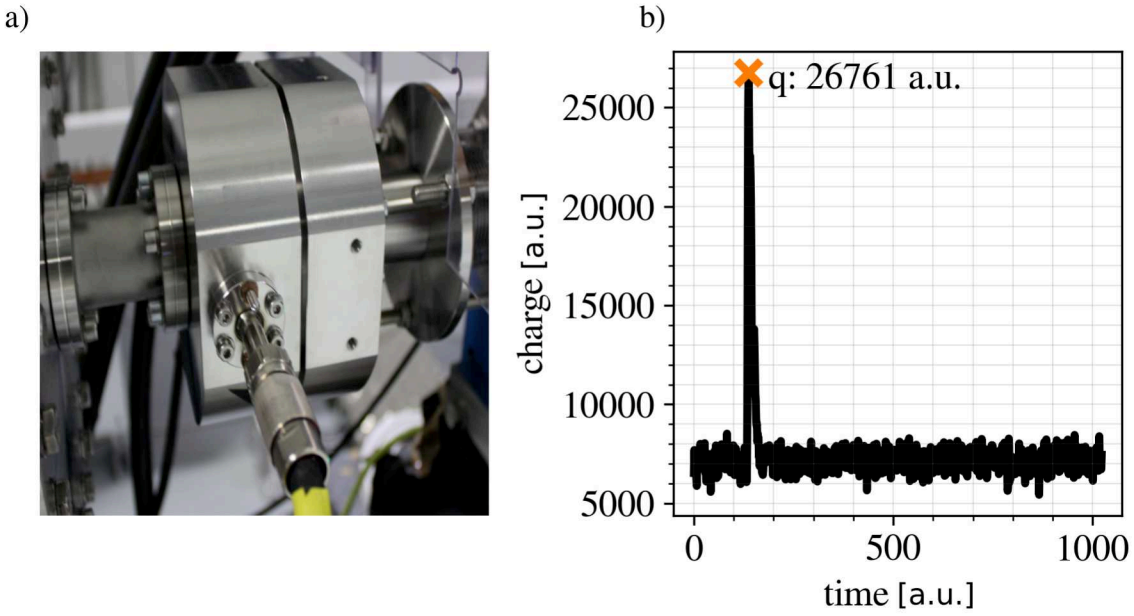

Figure 4.3.: a) Picture of the DaMon diagnostic. b) Exemplary DaMon trace to pictures the signal definition.

The cavity is designed to operate in the first transverse magnetic mode (TM01) at a resonant frequency of $f = 1.3\,\mathrm{GHz}$. A beam passing through the cavity excites the TM01 mode, generating a voltage described by:

$$U = U_0 \sin(\omega t) e^{-t/\tau} \tag{4.1}$$

with $\omega = 2\pi f$ and the decay time $\tau = \frac{Q_L}{\pi f}$, indicating how quickly the voltage decreases over time, and Q_L is the loaded qualify factor of the resonator, reflecting the cavity's efficiency in storing energy (i.e., the number of oscillations until the amplitude falls to $1/e$). The amplitude of this TM01 mode U_0 is proportional to the beam charge q via

$$U_0 = qS \tag{4.2}$$

where S is the sensitivity and is defined as $S = \pi f \sqrt{\frac{Z}{Q_{\mathrm{ext}}} \left(\frac{R}{Q}\right)}$. Here Z denotes the line impedance, which is the characteristic impedance of the transmission line. The term Q_{ext} refers to the external quality factor of the resonator, which is associated with energy losses due to external coupling mechanisms, the fraction $\left(\frac{R}{Q}\right)$ is the normalized shunt impedance, indicating the efficiency of the cavity in storing energy relative to

its losses and interaction with charged particles. The sensitivity is only defined by constants, and if they are known for the system, the bunch charge can be determined by measuring the amplitude of the TM01 mode. The TM01 mode is independent of the position of the electron bunch, which ensures consistent results regardless of the pointing of the electron beam. To measure the amplitude the mode is picked up by two antennas. The signal of the antennas is then directed to a dedicated electronics unit which filters the signal and converts the amplitude to a logarithmic value. This value is then measured with an ADC. The use of two antennas and the conversion to a logarithmic scale allows the DaMon to detect bunch charges over a wide dynamic range of seven orders of magnitude. The minimum detectable charge is about 50 fC, limited by electronic noise. In practice, the bunch charge can be calculated using the peak of the ADC trace, which was saved for each shot and can be seen as exemplary in Fig. 4.3 b). The peak of this ADC trace can be converted from arbitrary digital units to pC using the following formula:

$$q_{\text{damon}}[\text{pC}] = p_0 \times 10^{p_1 q[\text{a.u.}]+p_2} \tag{4.3}$$

With the calibration values for the system used in this experiment: $p_0 = 9.661 \times 10^{-5}$, $p_1 = 5.847 \times 10^{-5}$, and $p_2 = 3.209$. This formula, along with the respective calibration constants, was provided by Simon Bohlen (personal communication).

Beam Charge Monitoring with Scintillation Screen

To provide real-time visual feedback of the electron beam scintillation screens are commonly used. Within this thesis a DRZ-high [78] scintillation screen was installed to monitor the beam entering the LEAP polarimeter setup (see Sec. 7.2). This screen captures the spatial beam profile and fluctuations in beam intensity, complementing charge measurements from the DaMon diagnostic. The DRZ-high screen, distributed by MCI Optonix LLC / Mitsubishi Chemical Incorporated, consists of a luminescent material, a thin PET protective layer, and a plastic supporting layer. The luminescent material, Gd_2O_2S (Gadox), is doped with terbium, efficiently converting energy deposited by electrons into visible light, primarily through fluorescence at a wavelength of 545 nm [79]. When the electron beam passes through the screen, it deposits energy into the Gadox host lattice. This energy is transferred to the terbium ions, which are excited to higher energy levels. As the ions return to their ground state, they emit the absorbed energy as visible light, a process called fluorescence, first described by Stokes

in 1852 [80]. The fluorescence decay time is approximately 1 ms. The luminescent layer of the DRZ-high screen is only 310 μm thick [78], ensuring nearly constant energy deposition by electrons above 10 MeV [81]. Due to the high atomic numbers and densities of gadolinium and terbium, the DRZ-high screen exhibits high light yields, with a reported fluorescent efficiency of approximately 8 x 10^9 photons/sr/pC [81, 82]. In the experiment, the DRZ-high screen is imaged by a CCD camera, where the image intensity values directly correlate with the electron beam charge distribution, providing a visual representation of the beam's characteristics for each shot. The scintillator screen and imaging system can be calibrated for absolute charge measurements, as demonstrated in [82]. However, within this thesis, it was primarily planed to be used as a relative charge diagnostic rather than for absolute measurements.

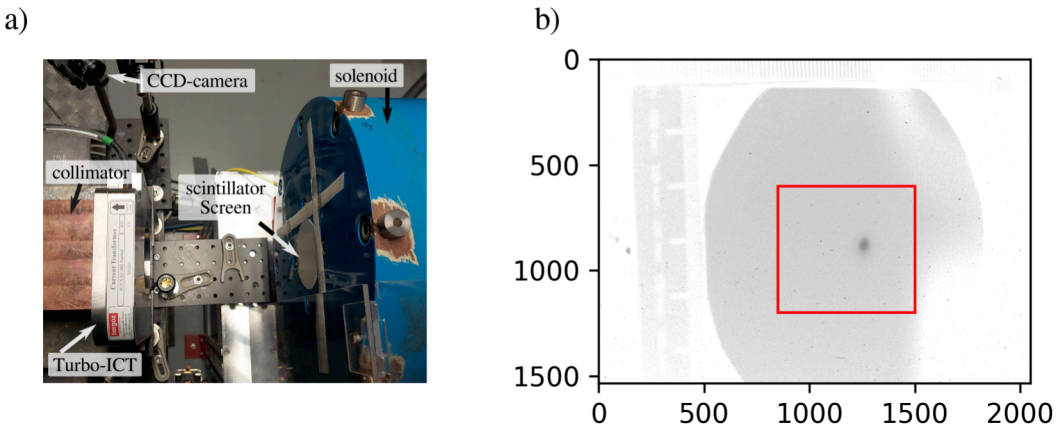

Figure 4.4.: a) Photograph of the DRZ-high scintillator screen and CCD camera as installed in the beamline. b) Example of a camera image showing the electron beam, visible as a dark spot. The red square indicates the region of interest (ROI), where the sum of pixel values is used to define the signal.

Figure 4.4 a) shows a photograph of the installed DRZ-high scintillator screen, which has a diameter of approximately 80 mm and is attached to the solenoid magnet opening, along with measuring tape used for absolute length calibration. The screen is imaged by a CCD camera as shown in the photograph. Figure 4.4 b) displays a camera image of the electron beam. A region of interest (ROI) is defined to analyze the image data, shown as a red square in the camera image. For the relative charge measurement, the signal from the DRZ-high screen is defined as the sum of all pixel values within the ROI:

$$S_{\text{scint}} = \sum N_{\text{ROI}} - \text{pedestal} \tag{4.4}$$

Here, N_{ROI} represents the pixel count value for each pixel within the ROI. The pedestal is determined by the mean sum of pixel values in the ROI during runs without an electron beam and is subtracted to eliminate the dark counts of the imaging system. During data acquisition, the imaging system and DRZ-high screen were covered with a black cloth to shield them from ambient light.

Dipole Electron Spectrometer

To measure the electron energy of the LPA beam, a single-shot dipole spectrometer is employed. The spectrometer operates based on the energy-dependent bending radii of electrons, which result from the Lorentz force in the dipole magnetic field. This process converts the electron energy spectrum into a spatial distribution. The dipole spectrometer method is widely used, and a comprehensive overview can be found in [83].
The spectrometer used in this experiment has been described and studied in previous works [75, 84, 85], and thus, its calibration was not part of this thesis. Consequently, only a brief explanation of the calibration will be provided. The dipole magnet of the spectrometer is positioned approximately 2.25 m downstream from the electron source, with a length of 500 mm and a maximum current of 311 A, producing a magnetic field strength of approximately 245 mT. To prevent electron scattering in air, the vacuum beam pipe extends into the magnet. A schematic of the spectrometer setup is shown in Fig. 4.5 a). Due to the Lorentz force, electron trajectories are bent based on their energy onto a DRZ-High screen [78], which is positioned at a 140-degree angle relative to the beam axis. This setup results in the energy-dependent deflection of the electron beam onto the screen. The screen is imaged via a mirror onto a CCD camera, enabling the detection of the energy-dispersed electron beam for single-shot energy measurements. A photograph of the electron spectrometer setup is shown in Fig. 4.5 c).
To extract the electron spectrum from the spatial intensity distributions on the screen (captured by the CCD camera), the spectrometer must be calibrated. The calibration consists of two main steps: first, converting the position on the screen to a corresponding energy for a given magnetic field; second, translating the pixel position on the images to an absolute position on the scintillation screen. To determine the energy-dependent position along the screen and the energy-dependent drift length of electrons originating from the plasma source, particle tracking simulations were conducted for centrally incoming electrons. In the experiment, a magnet current of 180 A was selected, for which precise magnetic field maps are available.

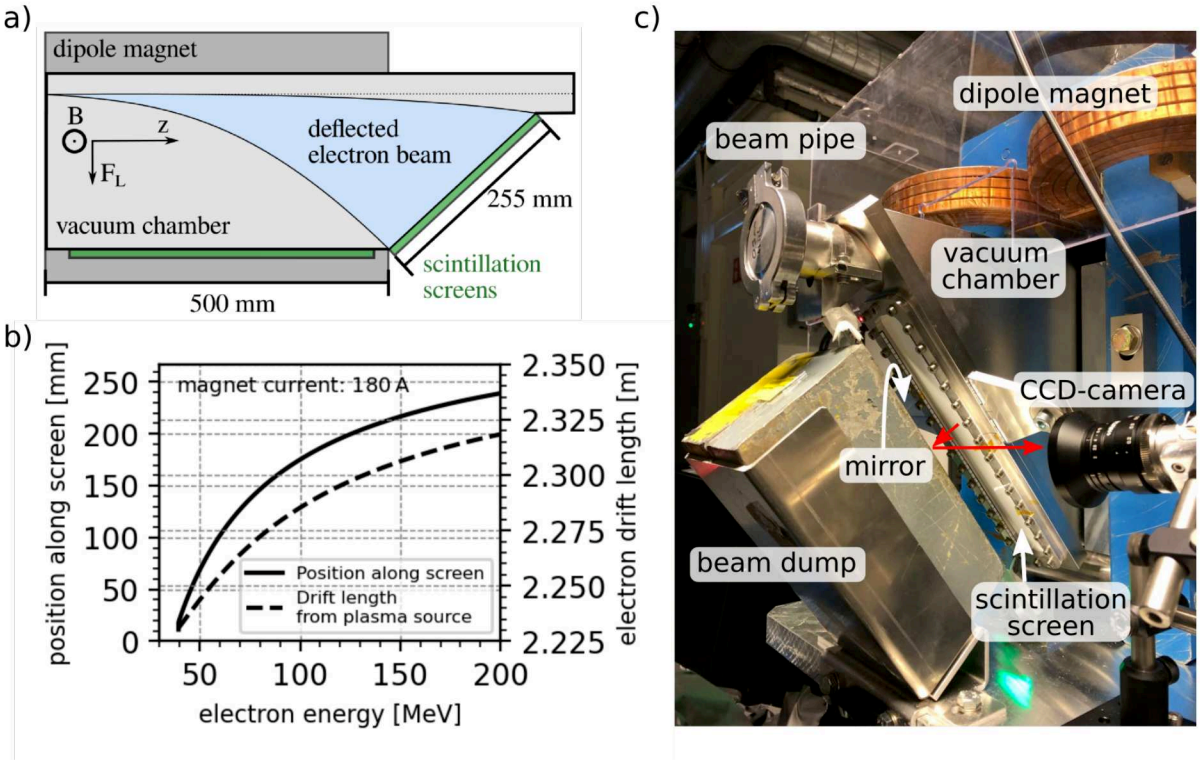

Figure 4.5.: a) Schematic of the electron spectrometer (adapted from [34]). b) Simulated energy-dependent track length and position on the scintillating screen for a magnet current of 180 A. c) Photograph of the electron spectrometer, scintillation screen, and imaging system. The red arrows indicate the reflection from the mirror.

Figure 4.5 b) shows the energy-dependent drift length and position on the screen for a magnet current of 180 A. The screen's position is measured from its lower edge. Higher-energy electrons appear higher on the screen due to their larger bending radius in the dipole fields. Additionally, higher-energy electrons undergo a longer drift than lower-energy electrons because of the angled orientation of the electron spectrometer screen. With this information, combined with the calibration of the CCD camera pixels to absolute positions on the screen (achieved by imaging a physical scale placed on the screen), the energy spectrum can be retrieved [84].

Within this work, the Python tool `espec_analysis_tool` [86], developed by Rob Shallo, was used to extract the single-shot electron spectrum from the raw CCD camera images recorded during the experiment. For a more technical explanation of the calibration procedure and spectrum retrieval, please refer to [84].

4.2.3. DAQ and Slow Control

The FLARE Facility uses the DOOCS (Distributed Object-Oriented Control System) [87] which is a control system framework developed and commonly used by DESY for operating complex scientific instruments, such as particle accelerators. The DOOCS control system can be interfaces using the graphical user interface JDDD (Java DOOCS Data Display) [87, 88]. It is used to create and display control panels that allow to interact with and monitor the status of different components within the accelerator or experiment.

4.3. Active Plasma Lens (APL)

This section explains the concept of the active plasma lens (APL) and presents beam transport calculations using matrix formalism. Additionally, detailed information is provided on the APL device used in the experimental setup for the zero polarization measurement (see Sec. 7.2).

4.3.1. Basic Concept of an APL

An APL [89–92] is a device used to focus charged particles by utilizing the azimuthal magnetic fields generated by an externally applied, radially uniform longitudinal current within a plasma. The concept of an APL was first discussed and applied by Panofsky and Baker in 1950 [89]. In 2015, J. van Tilborg et al. [90] utilized an APL for the first time to focus relativistic electron beams from a laser plasma accelerator.
The basic working principle of an APL is shown in Fig. 4.6. An APL mainly consists of a thin, gas-filled cylindrical capillary with a radius R, with two high-voltage electrodes at both ends to supply the external discharge current. When the gas is discharged, a plasma channel is formed within the capillary that conducts the current. For an ideal lens, the density of the longitudinal current is uniform and can be expressed as $J = \frac{I_0}{\pi R^2}$ where I_0 is the current and R is the radius of the capillary, similar to a straight conductor. According to Ampère's law, the current generates an azimuthal magnetic field that increases linearly with the radius r within the aperture ($r < R$), given by:

$$B_\Phi = \frac{\mu_0}{2\pi} \frac{r}{R^2} \tag{4.5}$$

where μ_0 is the vacuum permeability. An electron beam passing through the plasma, and hence the magnetic field, experiences a Lorentz force that radially focuses it toward the beam axis. To focus the negatively charged electron beam, the technical current flow and the electron beam must be counter-propagating, as sketched in Fig. 4.6.

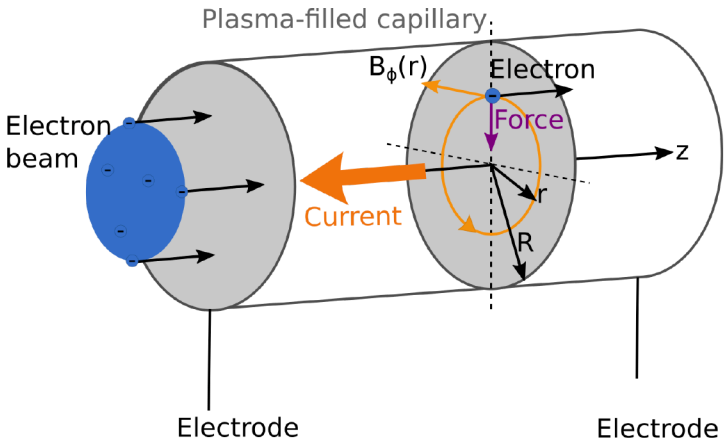

Figure 4.6.: Schematic of the operating principle of an active plasma lens: A current flowing between two electrodes generates an azimuthal magnetic field that increases linearly with radius. An electron beam experiences a radial focusing force as it propagates through the plasma. The schematic is adapted from [90].

The focusing strength of an APL, k_{APL}, is given by:

$$k_{\mathrm{APL}} = \frac{e}{m_0 \gamma_r c} \cdot \frac{\partial B_\phi}{\partial r} = \frac{e}{m_0 \gamma_r c} \cdot \frac{\mu_0 I_0}{2\pi R^2} = \frac{ec}{E_{e^-}} \cdot \frac{\mu_0 I_0}{2\pi R^2} \tag{4.6}$$

where e is the electron charge, m_0 is the electron rest mass, γ_r is the Lorentz factor, c is the speed of light, and E_{e^-} is the electron energy. The focusing strength depends on the electron energy, leading to different focal lengths for different electron energies. The exact focal lengths can be adjusted experimentally by tuning the applied current I_0 flowing through the APL. Under the thin lens approximation ($k_{\mathrm{APL}} L_{\mathrm{APL}} << 1$), which is often applicable, the focal length of an APL is given as:

$$f_{\mathrm{APl}} \approx \frac{1}{k_{\mathrm{APL}} L_{\mathrm{APL}}} \tag{4.7}$$

where L_{APL} is the length of the discharge capillary.

4.3.2. Beam Parameters and Transport

To describe the beam transport and focusing of the APL, the transfer matrix formalism will be employed, incorporating the parametrization of the beam using the Courant-Snyder parameters (Twiss parameters) [93], which will be briefly introduced in the following. This overview is based on [94], which provides detailed information on linear beam dynamics.

The transfer matrix formalism is a widely used method for describing the transverse motion of particles in an accelerator or other optical systems. It is based on the linearization of the equations of motion (Hill's equation) and enables straightforward analysis and calculations of beam dynamics. A particle is described, with respect to its reference (ideal) orbit, by its transverse phase space coordinates u (x or y) which is its position, and the transverse momentum $u' = \frac{\delta u}{\delta s}$ (either x' or y'), where s is the arc length along the reference trajectory. The effect of beam line elements such as, dipole magnets, quadrupole magnets, drift section or an APL on the phase space coordinates of the particle can be described by a 2x2 matrix R transforms the state of the particle at position s_0 to s:

$$\begin{pmatrix} u(s) \\ u'(s) \end{pmatrix} = \begin{pmatrix} R_{11} & R_{12} \\ R_{21} & R_{22} \end{pmatrix} \cdot \begin{pmatrix} u(s_0) \\ u'(s_0) \end{pmatrix} \tag{4.8}$$

For a sequence of beam line elements, the overall effect ca be determined by multiplying the individual transfer matrices:

$$R_{\text{total}} = R_{\text{N}} + R_{\text{N}-1} ... R_2 R_1 \tag{4.9}$$

For example, the transfer matrix that describes a drift of length d is written as:

$$R_{dift} = \begin{pmatrix} 1 & d \\ 0 & 0 \end{pmatrix} \tag{4.10}$$

The transfer matrix that describes the focusing of the APL is given by:

$$R_{APL} = \begin{pmatrix} \cos\left(\sqrt{k} L_{\text{APL}}\right) & \frac{1}{\sqrt{k}} \sin\left(\sqrt{k} L_{\text{APL}}\right) \\ -\sqrt{k} \sin\left(\sqrt{k} L_{\text{APL}}\right) & \cos\left(\sqrt{k} L_{\text{APL}}\right) \end{pmatrix} \tag{4.11}$$

where k (>0) is the focusing strength, as defined in Eq. 4.6, and L_{APL} the length of the APL discharge capillary. This matrix is adapted from the transfer matrix of a quadrupole magnet focusing plane [85, 94].
So far, the transport equations have been valid for single particles. However, in reality, we deal with a particle distribution or a particle beam. The particle beam describes an ellipse in phase space, which can be written as:

$$\varepsilon = \gamma u^2 + 2\alpha u u' + \beta u'^2 \tag{4.12}$$

Here α, β and $\gamma = \frac{1+\alpha^2}{\beta}$ are the Courant-Snyder parameters (or Twiss parameters) α is related to the beam tilt, while β is related to the shape and size of the beam. The beam emittance (geometric beam emittance) ε describes the phase space area of the beam, $A = \pi\varepsilon$ and is a parameter often used to gauge beam quality. In accelerator physics, the normalized beam emittance is often preferred and reported because it is energy-independent, allowing for consistent comparisons across different beam energies. The normalized emittance, $\varepsilon_{\mathrm{norm}}$, is related to the geometric emittance ε according to:

$$\varepsilon_{\mathrm{norm}} = \frac{p}{m_0 c} \cdot \varepsilon = \gamma_r \cdot \beta_r \cdot \varepsilon\,, \tag{4.13}$$

where γ_r is the relativistic Lorentz factor and $\beta_r = \frac{v}{c}$ represents the velocity of the particles normalized to the speed of light.
Since real beam distributions are usually not uniform in phase space, the RMS-size of the beam is often used to describe it. For a beam with N particles, the RMS-size is given by:

$$\langle u \rangle = \sqrt{\frac{1}{N}\sum_{i}^{N} (u_i - u_{\mathrm{avg}})^2} \tag{4.14}$$

Similarly, the RMS momentum spread $\langle u' \rangle$ is calculated in the same manner. The RMS values of the beam are related to the Courant-Snyder parameters as follows:

$$\beta = \frac{\langle u^2 \rangle}{\varepsilon}, \quad \gamma = \frac{\langle u'^2 \rangle}{\varepsilon}, \quad \alpha = \frac{\langle u u' \rangle}{\varepsilon} \tag{4.15}$$

According to Liouville's theorem, the phase space area of a beam is conserved under linear transformations, and therefore the beam emittance is conserved. As a result, all

phase space evolutions, which result in changes in beam sizes and divergences, are equivalent to ellipse transformations.
The Courant-Snyder parameters, which describe the beam, can be propagated using the transfer matrix formalism as follows:

$$\begin{pmatrix} \beta(s) \\ \alpha(s) \\ \gamma(s) \end{pmatrix} = \begin{pmatrix} R_{11}^2 & -2R_{11}R_{12} & R_{12}^2 \\ -R_{11}R_{21} & R_{12}R_{21} + R_{11}R_{22} & -R_{12}R_{22} \\ R_{21}^2 & -2R_{21}R_{22} & R_{22}^2 \end{pmatrix} \begin{pmatrix} \beta(s_0) \\ \alpha(s_0) \\ \gamma(s_0) \end{pmatrix} \tag{4.16}$$

where R_{ij} are the matrix elements of the transfer matrices R. Using Eq. 4.15 and 4.16, the beam size $\langle u \rangle$ (either $\langle x \rangle$ or $\langle y \rangle$) at position s can be calculated as:

$$\langle u_s^2 \rangle = R_{11}^2 \beta_{s_0} \varepsilon - 2R_{11}R_{12}\alpha_{s_0}\varepsilon + R_{12}^2 \gamma_{s_0}\varepsilon \tag{4.17}$$

This equation will be used later on to calculate the beam transport within the APL.

4.3.3. APL Device: Design and Operation

The APL utilized within this thesis (see Sec. 7.2) was originally designed, characterized, and employed by Martin Meisel to investigate the emittance of an LPA electron beam source [85].

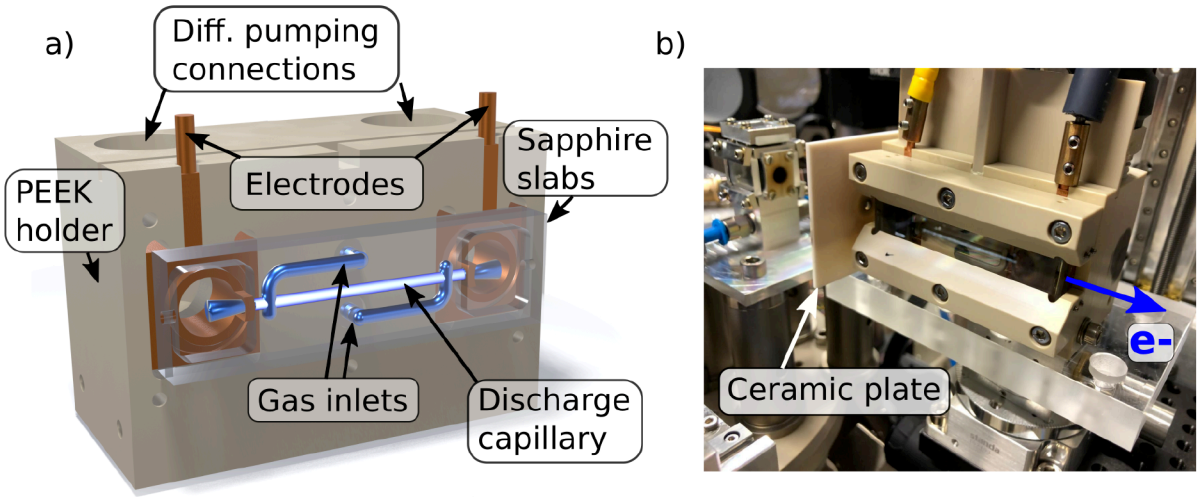

Figure 4.7.: a) Schematic representation of the APL, illustrating all major components (adapted from [85]). b) Photograph of the APL as installed into the beamline.

Figure 4.7 illustrates the APL, with panel a) showing a schematic of its main components and panel b) a photograph of the APL installed in the LPA beamline. The APL features a sealed design comprising a cylindrical discharge capillary with a length of 40 mm and a diameter of 2 mm. Two sapphire slabs form the capillary, each measuring 70 mm x 20 mm x 4 mm and machined with a half-cylindrical channel on their inner surfaces. The capillary is equipped with two gas inlets at the front and back, both connected to the gas supply. Argon is chosen as the working gas, which will be ionized to form the plasma and carry the current through the confined channel. Argon was selected because it is the only gas species confirmed to provide a linear focusing field that preserves the beam emittance [91]. Copper electrodes, each with a 2.5 mm aperture to allow the electron beam to pass through, are positioned at both ends of the capillary to conduct the discharge current through the plasma. The discharge is triggered by a high-voltage pulser system, described in detail in [85, 95]. The setup generates a positive pulse with a voltage of up to 25 kV, which is applied to the anode at the downstream end of the APL while the upstream electrode is connected to the ground. This polarity enables the focusing of negative particles. The current passing through the APL is measured using an inductive coil on the ground side of the capillary. The signal is attenuated and sent to an analog-to-digital converter (ADC) for data acquisition. The APL operates with a constant gas flow regulated by a mass flow controller, allowing it to function at the laser system's maximum repetition rate of 10 Hz. The exhaust gases are differentially pumped through the electrodes and the openings in the support structure. The support structure, which holds the sapphire slabs, electrodes, gas connectors, and pumping system, is made from PEEK, a thermoplastic known for its excellent mechanical and chemical resistance properties. A ceramic plate with a 3 mm aperture was also installed to protect the APL mount and sapphire slabs from potential laser damage. To align the APL with the electron beam axis, it was mounted on a motorized X-Y-Z stage, complemented by manual tilt and rotation stages.

4.4. Photomultiplier Tube (PMT)

Photomultiplier tubes (PMTs) are widely used photon detectors in physics experiments and applications, such as in calorimeters, and will be employed in the LEAP calorimeter discussed in this thesis (see Sec. 6.1.2). Therefore, this section introduces the basic working principle of PMTs and their key performance parameters. The

discussion is primarily based on [51, 96, 97] where further details can be found.
The basic working principle of a PMT is illustrated in Fig. 4.8. The PMT utilizes the photoelectric effect to convert incoming photons into amplified electrical signals, which can then be further processed experimentally. The PMT consists of an evacuated glass tube with a photocathode, often deposited on the inner surface of the entrance window. When an incoming photon passes through the entrance window and strikes the photocathode, it may release a photoelectron via the photoelectric effect, which is subsequently emitted into the vacuum tube. Inside the PMT, a series of electrodes, called dynodes, are arranged to generate an electric field when a supply voltage is applied, accelerating and multiplying the emitted photo electrons. An initial photo electron is directed toward the first dynode, where it strikes the surface, releasing several secondary electrons. These secondary electrons are then accelerated toward the next dynode, where further multiplication occurs. This cascading process repeats at each dynode stage, resulting in a large number of electrons. The electrons are collected at the PMT anode, where the amplified electrical signal is extracted for further processing.

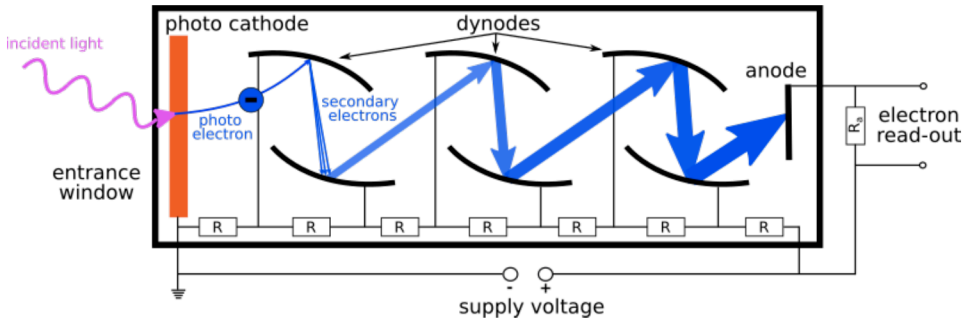

Figure 4.8.: Schematic of a photomultiplier tube (PMT).

One of the key characteristics of a PMT is its gain (μ_{PMT}), which refers to the current amplification achieved from the initial photocathode current to the final anode current. The gain is typically very high, ranging from 10^5 to 10^7 [51], enabling the detection of extremely low light intensities, including single-photon events. The gain is highly sensitive to the supply voltage V, which is typically in the range of 1 kV. The relation between the gain and the supply voltage can be expressed as follows [97]:

$$\mu_{\text{PMT}} = A \cdot V^{\alpha} \tag{4.18}$$

Here, A and α are PMT-specific constants. It can be seen that the gain is proportional to the α exponential power of the supply voltage V. The parameter α corresponds to

the number of dynodes in the PMT multiplied by a factor typically ranging from 0.7 to 0.8, depending on the dynode material and geometry [97].
Another important parameter of the PMT is the quantum efficiency (QE), which describes the wavelength-dependent sensitivity of the photo cathode. The QE is defined as the ratio of emitted photo electrons to the number of incident photons striking the PMT's entrance window [96]. Typical quantum efficiencies of PMTs are around 25 %, with peak sensitivity usually in the wavelength range of 300 nm to 600 nm, depending on the specific photo cathode material and entrance window transmission properties [51].
For the LEAP calorimeter, PMTs with enhanced sensitivity in the ultraviolet region will be utilized. The selection of these PMTs and their specific characteristics are discussed in more detail in Sec. 6.1.2.

4.5. `leap_sims`: A Simulation Framework for Polarimeter Studies

`leap_sims` [98] is a simulation framework specifically designed to study the performance of the LEAP polarimeter. The framework was primarily developed by Jennifer Popp, with contributions from the author of this thesis. A comprehensive technical description and detailed information about `leap_sims` can be found in Jennifer Popp's thesis [34]. In this section, a general overview of `leap_sims` is provided.
At its core, `leap_sims` is a `GEANT4` [99–101] application that simulates the passage of particles through the diagnostic system, modeling the relevant physical processes. `GEANT4` is a widely used toolkit for simulating particle interactions with matter, using Monte Carlo methods to model physical processes across a wide range of energies [102]. While `leap_sims` builds on `GEANT4`'s capabilities, it incorporates additional layers of customization and automation to support extensive polarimeter simulation campaigns. The framework is designed with a modular architecture, allowing users to customize the simulation setup via a configuration file. This modularity enables the dynamic configuration of detector components, geometry, and physical processes, making the framework versatile for a wide range of simulation needs.

4.5.1. Core Features and Configurations

The setup of each simulation in `leap_sims` is handled through a configuration file that defines key parameters, such as the geometry, detector components, particle types, and physics models to be used which enables users to tailor simulations to their specific requirements. Key configurable options include:

Physics Processes and Polarization: The configuration file allows users to choose whether to include polarization in the simulation of particle interactions. Users can select between `PhysListEMPolarized`, a customized polarized electromagnetic physics list, or the standard `GEANT4` module `G4EmStandardPhysics` [103], which simulates unpolarized electromagnetic processes. The customized `leap_sims` module, used as the default unless otherwise specified, supports polarized materials and particles, enabling the simulation of processes such as the polarized photoelectric effect, Compton scattering, γ-conversion, ionization, bremsstrahlung, and positron annihilation.

A key parameter influencing simulation accuracy is the `StepFunction` for charged particles which controls step length based on the energy loss fraction (`dRoverRange`) and a minimum step size (`finalRange`). In `leap_sims`, `finalRange` was reduced from the default value of 1 mm to 0.01 mm to enhance the precision of energy deposition modeling, particularly in calorimeter regions. This adjustment ensures that fine-scale energy deposition effects, such as the Cherenkov radiation threshold, are captured more accurately (see Sec. 6.2.3). While this increases the number of computational steps and overall simulation time, it was found to be essential for improving accuracy. Consequently, all `leap_sims` simulations presented in this thesis adopt this optimized step size setting.

Beam Parameters: The configuration file also defines the characteristics of the particle beam. Users can specify parameters such as particle type (e.g., electrons), beam energy, beam spot size, spatial distribution, divergence, and degree of polarization. Both mono-energetic beams and more complex energy distributions are supported.

Detector Geometry and Materials: The modular architecture of `leap_sims` enables users to define a wide range of detector configurations. Key components of the diagnostic system, such as the solenoid, calorimeter, and specific beamline components, can be included or excluded as required by the simulation. Additionally, the positioning of the detector components and the particle gun can

be adjusted to match different experimental conditions. The framework also allows users to specify the simulation environment, such as whether it takes place in air or vacuum. Furthermore, a homogeneous solenoidal magnetic field with adjustable field strength can be activated within the region of the solenoid's iron core. In Fig. 4.9 illustrates the detector geometry setup within `leap_sims`. The exact setup geometries, as implemented in the `GENT4` application, are described in greater detail throughout the thesis in the respective sections where the simulations are applied.

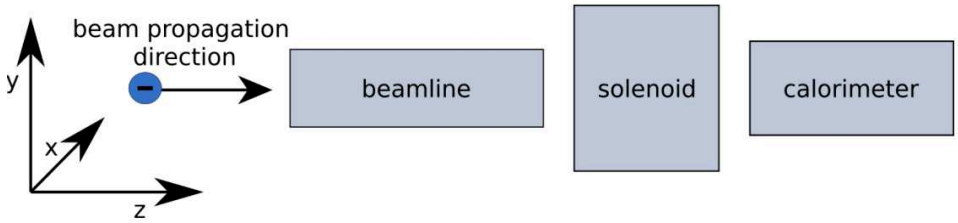

Figure 4.9.: Modules of the `leap_sims` detector geometry [34].

Sensitive Detectors and Output: `GEANT4` sensitive detectors [104] are used to record information about particles as they pass through different components of the system. In `leap_sims`, virtual volumes function as ideal detectors, gathering either summary data (such as energy deposition and particle counts) or detailed information on each interaction, including particle position and momentum. In the case of the calorimeter, the entire crystal material is defined as a sensitive detector. Users can specify which sensitive detectors within the geometry will collect data, and whether summary or detailed information should be stored. The simulation output is saved in ROOT files as TTrees, a tree-like data structure, along with the simulation parameters from the configuration file. ROOT [105, 106] is a framework for large scale data analysis, originally developed at CERN [107] to handle the enormous amounts of data generated by high-energy physics experiments.

4.5.2. General Workflow with `leap_sims`

A brief overview of the general workflow for using `leap_sims` for polarimeter simulations is provided here, with more detailed information available in [34, 98]. The simulation process begins with the user defining the necessary parameters in the

configuration file. This file is then passed to the `leap_sims` application using the command: `leap_sims -c [configuration file]`. Additionally, the simulation can be run interactively with a visualization of the detector setup by using the flag `-v 1`, which enables event displays or simply visualizes the geometry.
Running large simulation campaigns, which are computationally expensive due to the need to simulate thousands of particles per electron bunch and track each particle through the system, typically requires the use of a computing cluster. For this thesis, the National Analysis Facility (NAF) [108] at DESY was utilized. The NAF is a multi-purpose batch cluster optimized for high-throughput computing, using HTCondor [109] as the scheduling system. Simulations are typically split into smaller tasks and run in batch mode.
To submit simulation jobs to the cluster, a submission script is used to define the number of jobs and specify the varying simulation parameters, which can be modified from those already present in the `leap_sims` configuration file. For example, if a simulation requires varying beam energies, the desired energy values would be listed in the submission file, and the number of jobs to be run for each energy setting would be defined. The scheduling system then distributes the jobs across different working nodes of the computing cluster. For each job, a bash script modifies the configuration file based on the input parameters (e.g., energy) specified in the submission script. The bash script then executes the `leap_sims GEANT4` application using the updated configuration file. Each job generates a single ROOT output file. Once the simulations are completed, all output files corresponding to the same set of simulation parameters can be merged into a single file.

Chapter 5.

Towards a Dissociation Laser for LEAP

A UV laser is required for the photodissociation of HCl molecules for the preparation of the pre-polarized plasma source in LEAP (see Sec. 3.1.1). The production of spin-polarized hydrogen, and consequently spin-polarized electrons, through the photodissociation of HCl has been successfully demonstrated at specific UV wavelengths, where powerful laser sources exist, such as 193 nm and 213 nm [13, 60, 62]. However, using a separate laser source for the pre-polarization of the plasma presents a challenge due to the need for precise synchronization with the LPA driver laser.
Synchronization is essential to prevent the loss of electron polarization through spin transfer via hyperfine coupling to the nuclei, which occurs on a timescale of about 350 ps for hydrogen [62]. Achieving synchronization with the necessary picosecond precision is feasible using state-of-the-art laser technologies [110–112]. However, such solutions are highly complex and expensive, making them unsuitable for implementation within the scope of the LEAP project. To address the synchronization issue, the dissociation laser for LEAP is proposed to be generated through the fourth harmonic of the fundamental 800 nm Ti:Sa laser. This method inherently ensures synchronization between the LPA driver and the dissociation laser, as both are generated from the same laser source.
The most straightforward method of fourth harmonic generation (FHG) from a Ti:Sa laser is applying cascaded second harmonic generation (SHG) which will be introduced in Sec. 5.1. This method involves frequency doubling in two sequential stages. In the first stage, the second harmonic (2ω) of the fundamental laser wavelength (ω) is generated. This output is then directed into a second nonlinear medium, where the frequency is doubled again, producing the fourth harmonic (4ω).
With regard to the wavelength of the dissociation laser – where the photodissociation of HCl has been successfully demonstrated – a wavelength near 193 nm is particularly

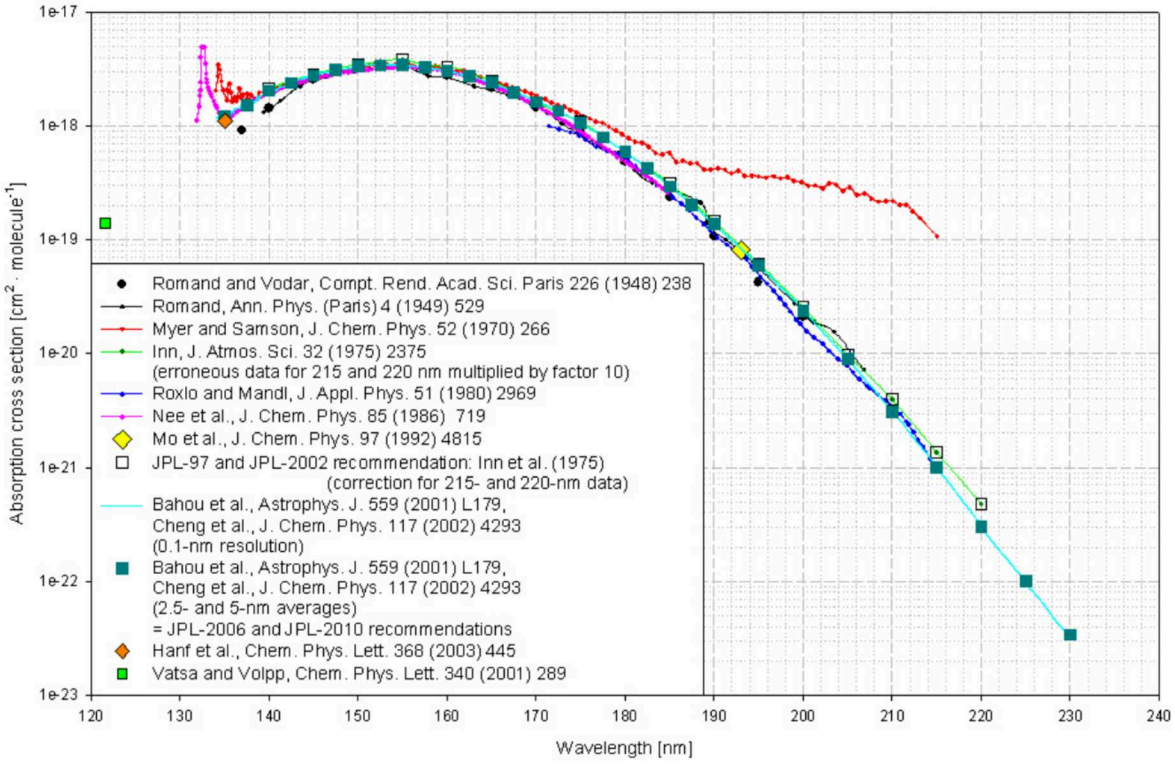

Figure 5.1.: Absorption cross sections of hydrogen chloride HCl at 298 K (taken from [113]).

desirable. At this wavelength, the absorption cross-section for HCl molecules is approximately 40 times higher than at 213 nm (see Fig. 5.1). From a practical perspective, this means that significantly less laser energy would be required to achieve efficient photodissociation.

For wavelengths below 200 nm, the only nonlinear medium that supports SHG with the necessary phase matching is the $KBe_2BO_3F_2$ (KBBF) crystal [114]. When used in a prism-coupled device (KBBF-PCD), where KBBF crystals are sandwiched between CaF_2 or SiO_2 prisms to avoid cutting the thin crystal at the phase-matching angle (52.5° for 400 nm), these crystals have demonstrated high conversion efficiencies of up to $\sim 10\,\%$ (ω to 4ω) for generating the fourth harmonic of the Ti:Sa laser at 200 nm [114]. Additionally, a wide tunable range from 175 nm to 235 nm has been shown [115–117]. However, due to a Chinese export embargo on KBBF crystals [118], their use is impractical for LEAP, though it remains a future option.

With more commonly available nonlinear crystals like beta-barium borate (BBO) [119], FHG using cascaded SHG is limited to wavelengths above 205 nm. This is because SHG becomes unattainable for wavelengths below 410 nm due to the phase matching

angle exceeding 90° [120]. To generate wavelengths of 200 nm and below using BBO, sum frequency generation (SFG) can be applied [121]. In this approach, the third harmonic of the Ti:Sa laser (266 nm) is mixed with the fundamental wavelength (800 nm) to generate the fourth harmonic at 200 nm. However, this method involves a more complex setup, as the laser pulses must be precisely overlapped both spatially and temporally within the nonlinear medium. Additionally, the need for multiple SFG steps reduces the overall conversion efficiency.
Given these considerations, the feasibility of generating the UV dissociation laser for LEAP through cascaded SHG using two BBO crystals will be explored. The focus will be on the practical aspects, particularly the achievable conversion efficiencies from the fundamental to the fourth harmonic ($\eta_{\omega\to 4\omega}$) near the wavelength limit of ~ 205 nm for BBO crystals.

5.1. Second Harmonic Generation

This section provides a brief overview of the principles and physics underlying second harmonic generation (SHG). For more detailed information, the reader is referred to [122], which serves as the primary reference for this section.
The propagation of light in an optical medium is governed by a driven wave equation, derived from Maxwell's equations:

$$\nabla^2\mathbf{E} - \frac{1}{c^2}\frac{\partial^2\mathbf{E}}{\partial t^2} = \mu_0\frac{\partial^2\mathbf{P}}{\partial t^2} \tag{5.1}$$

Here, **P** represents the material's polarization response to the applied electric field **E** (from the incident laser light), acting as a source term in the wave equation.
SHG is a second-order nonlinear optical process in which the polarization P of a material responds in a nonlinear way to an applied electric field. This effect becomes significant at high electric field strengths. For a second-order process, this relation is:

$$\mathbf{P} = \varepsilon_0\left(\chi^{(1)}\mathbf{E} + \chi^{(2)}\mathbf{E}\mathbf{E}\right) \tag{5.2}$$

where ε_0 is the vacuum permittivity, $\chi^{(1)}$ is the linear susceptibility tensor and $\chi^{(2)}$ is the second-order nonlinear susceptibility tensor of the material. The nonlinear term $\chi^{(2)}\mathbf{E}\mathbf{E}$ leads to a polarization oscillating at twice the frequency of the input electric field, effectively creating a new electric field at frequency 2ω. In physical terms, the

SHG process can be visualized as two photons of frequency ω combining to form a single photon with frequency 2ω.
The SHG process must satisfy both energy and momentum conservation, the latter of which can be expressed as:

$$\hbar(k_{2\omega} - 2k_{\omega}) = 0 \tag{5.3}$$

for a collinear geometry, where $k_{\omega} = \frac{2\pi n_{\omega}}{\lambda_{\omega}}$ and $k_{2\omega} = \frac{2\pi n_{2\omega}}{\lambda_{2\omega}}$ are the wave numbers of the fundamental and second harmonic waves, respectively. This condition is met when the phase velocity of the fundamental wave matches that of the second harmonic in the medium, referred to as **phase matching**.
In SHG applications, **nonlinear birefringent crystals**, such as Beta-Barium Borate (BBO), are commonly used. The phase matching can be achieved in birefringent crystals, where the refractive index n depends not only on the frequency but also on the polarization and the angle θ, relative to the crystal's characteristic direction, known as the optical axis. Radiation polarized perpendicular to the plane defined by the optical axis and the propagation direction experiences the ordinary refractive index n_{o} which is independent of θ. In contrast, radiation polarized parallel to this plane experiences the extraordinary refractive index n_{eo} which varies with θ (see Fig. 5.2).
In the SHG process, the waves at frequencies ω and 2ω are typically orthogonally polarized.
For negative uniaxial birefringent crystals, such as BBO, where $n_{\mathrm{eo}} < n_{\mathrm{o}}$, the phase matching condition is fulfilled when:

$$n_{\mathrm{o}}(\omega) = n_{\mathrm{eo}}(2\omega, \theta) \tag{5.4}$$

This is referred to as Type-I phase matching as two photons of the fundamental frequency ω with ordinary polarization are combined into one photon of the second harmonic 2ω with extraordinary polarization.
The phase matching is graphically illustrated in Fig. 5.2. Figure 5.2 a) depicts the refractive index surfaces for ω and 2ω: the ordinary refractive index is represented as a circle, while the extraordinary refractive index is shown as an ellipse. The phase matching condition is satisfied at the angle θ, where the circle corresponding to ω intersects the ellipse corresponding to 2ω. In general SHG applications, crystals are cut to fulfill the phase matching condition for a specific wavelength, as shown in Fig. 5.2 b). In practical applications, phase mismatch, defined as $\Delta k = k_{2\omega} - 2k_{\omega}$, can occur due to deviations in the phase matching angle – which can be fine-tuned, for

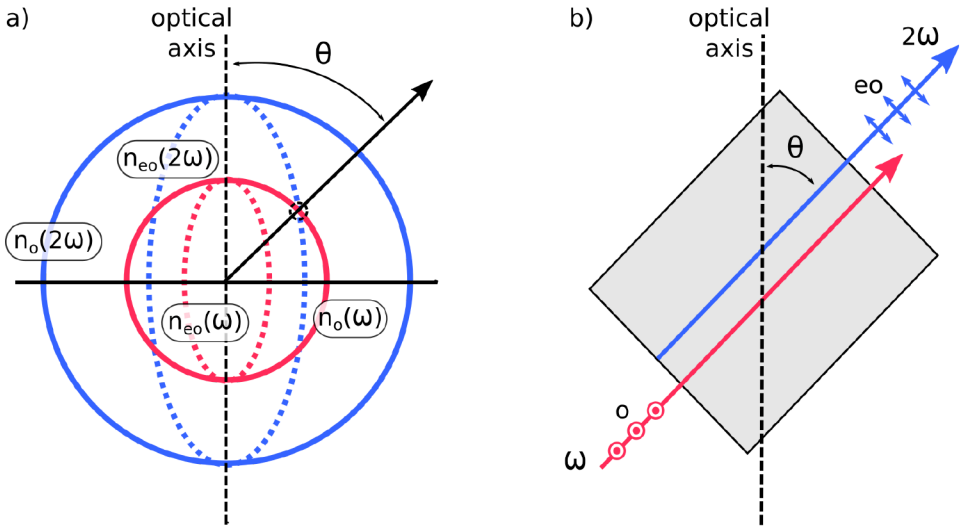

Figure 5.2.: Phase matching. a) Refractive index surfaces for a negative uniaxial birefringent crystal, showing the ordinary (n_o) and extraordinary (n_{eo}) indices for ω (red) and 2ω (blue). b) Illustration of the nonlinear crystal, where the fundamental wave (ω) experiences the ordinary refractive index, and the SHG wave (2ω) experiences the extraordinary refractive index. Phase matching is achieved by adjusting the angle θ which corresponds to the propagation angle with respect to the crystal's optical axis.

example, by rotating the crystal – or due to material dispersion. Such mismatches lead to destructive interference, reducing the efficiency of the SHG process.
The SHG efficiency depends on several factors, including the input intensity I_ω, the nonlinear coefficient of the material $\chi^{(2)}$, the crystal length L, and the phase matching. The intensity of the generated second harmonic wave, $I_{2\omega}$, is proportional to:

$$I_{2\omega} \propto L^2 I_\omega^2 \mathrm{sinc}^2\left(\frac{\Delta k L}{2}\right) \tag{5.5}$$

5.2. UV Energy Requirement

Besides the wavelength and synchronization requirements, another critical factor is the energy, or the amount of UV photons, needed for the photodissociation of the HCl gas target in LEAP. To inject and accelerate polarized electrons, it is essential that the spatial region where the electrons are injected into the plasma bubble of the LPA is fully dissociated and therefore polarized. This suppresses the injection of unpolarized electrons, which would otherwise dilute the overall polarization. In this section, the required energy of the UV laser will be estimated to ensure complete dissociation of

a sufficient gas volume, with a diameter approximately equal to that of the plasma bubble (10 µm). This estimation will be done using an absorption model for HCl, detailed in [62], assuming an absorption cross-section of $\approx 9 \cdot 10^{-21}$ cm^2 at 205 nm (see Fig. 5.1).

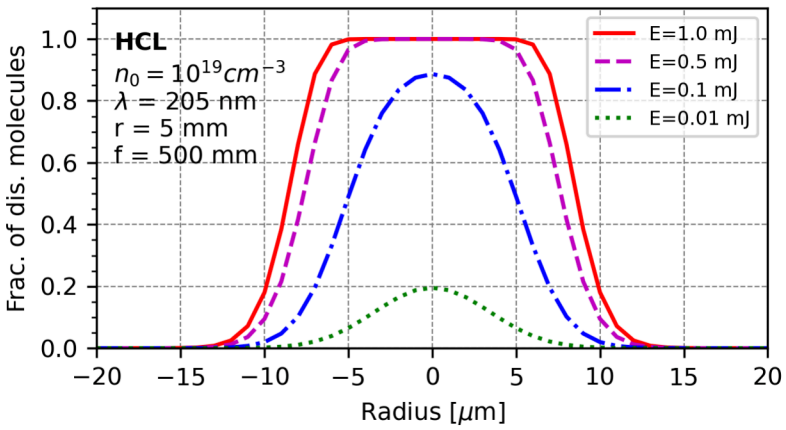

Figure 5.3.: Fraction of dissociated HCl molecules across the beam waist of the focused UV dissociation laser for a realistic set of parameters and different beam energies. The calculations are based on the absorption model for HCl from [62].

In Fig. 5.3, the fraction of dissociated HCl molecules is shown across the beam waist of the dissociation laser when focused in HCl gas, for a realistic set of experimental parameters: a gas density of $n_0 = 10^{19}$cm^{-3}, a UV laser wavelength of $\lambda = 205$ nm, a beam radius of 5 mm, and a lens with a focal length of 500 mm, for different total beam energies. It can be seen that a UV pulse of 0.5 mJ is sufficient to fully dissociate a gas volume with a diameter of approximately 10 µm, which corresponds to the plasma wavelength at a density of $n_0 = 10^{19}$cm^{-3}.
Fundamental laser energy of approximately 200 mJ is available for generating the dissociation laser. To achieve a UV pulse energy of 0.5 mJ (on target), an overall efficiency of $T = 0.25\,\%$ is required. This efficiency can be understood as the product of different contributing factors, including the conversion efficiency from the fundamental wave to the fourth harmonic $\eta_{\omega\to 4\omega}$ which is given by:

$$\eta_{\omega\to 4\omega} = \frac{E_{4\omega}}{E_\omega} \tag{5.6}$$

where E_ω and $E_{4\omega}$ are the energies of the fundamental and fourth harmonic pulses, respectively, as well as other efficiency factors associated with additional energy losses, such as those arising from beam transport to the interaction point.

Additionally, the dissociation laser pulse needs to be shorter than $\sim 350\,\text{ps}$ to provide dissociation while ensuring electron polarization. However, it is crucial not to ionize the HCl molecules during dissociation, which also sets a lower limit on the pulse duration.
The intensity I required for barrier suppression ionization (BSI) – where the oscillating laser field suppresses the Coulomb potential of the nucleus – at a specific ionization level (Z_{ion}) for the elements can be estimated from their binding energies (E_{bind}) using [75, 123]:

$$I\left[\frac{\text{W}}{\text{cm}^2}\right] = 4 \times 10^9 \frac{E_{\text{bind}}^4\,[eV]}{Z_{\text{ion}}^2}. \tag{5.7}$$

The binding energies for the first ionization stage of H and Cl are 13.6 eV and 13 eV, respectively [124]. Substituting these values into Eq. 5.7 gives ionization intensities of $1.4 \cdot 10^{14}\,\frac{\text{W}}{\text{cm}^2}$ for H and $1.1 \cdot 10^{14}\,\frac{\text{W}}{\text{cm}^2}$ for Cl. Taking the BSI threshold for Cl as the lower bound, this corresponds to a pulse duration of approximately 6 ps (FWHM) for the given parameters, setting the threshold to avoid barrier suppression ionization of the gas. It should be noted, however, that ionization is a complex process and can occur at lower intensities via multiphoton or tunneling ionization. Therefore, the 6 ps represents only a lower bound estimate, and the pulse duration of the dissociation laser may need to be longer to reliably prevent ionization.

5.3. FHG Efficiency Measurement

To investigate the feasibility of cascaded SHG for the generation of the UV laser for the LEAP project, initial experimental measurements were conducted using two BBO crystals to characterize the conversion efficiency from the fundamental near-infrared femtosecond Ti:Sa laser to its fourth harmonic. The SHG process is a nonlinear optical phenomenon proportional to the fundamental laser intensity. However, the conversion efficiency is limited by the damage threshold of the BBO crystals, which is in the range of several $100\,\frac{\text{GW}}{\text{cm}^2}$ for femtosecond laser pulses at a wavelength of 800 nm [120, 125]. The aim is to convert as much energy as possible into UV light while ensuring that the BBO crystals remain undamaged. For this feasibility test, two BBO crystals with type-I phase matching, each with a 5-mm aperture, were employed. The first crystal, used for SHG, is 0.5 mm thick and is phase-matched for a wavelength of 824 nm. The

second BBO crystal, designated for FHG, is 0.75 mm thick and is phase-matched for a wavelength of 412 nm.
One further consideration is to apply a spectral clip to the broad spectrum from the initial Ti:Sa laser to narrow it down. This spectral clipping eliminates frequency components of the initial spectrum that do not fulfill the phase-matching condition in the crystal, thereby reducing the flux the crystal must sustain.

5.3.1. Experimental Setup and Diagnostics

In Fig. 5.4 a sketch of the experimental setup is depicted. The setup is all in air. The initial beam was picked off from the Ti:Sa system after the final amplifier where the beam is still uncompressed and can be tuned in energy. The beam is then passed to a gold grating compressor (air compressor, AC) to compress the amplified pulse again by removing the group delay dispersion (GDD). Within the air compressor, a beam clip can be applied to cut off parts of the spectrum from both sides, leading to a narrower spectrum and a longer pulse. After the AC, near field (NF) and far field (FF) diagnostics are installed, ensuring repeatability of beam alignment. By removing mirror M2, which is on a magnetic base, the beam can be guided to the WIZZLER [126, 127] diagnostic to measure its pulse shape. M2 is used to guide the beam to the FHG setup through a safety interlock shutter (IS).
First the beam size is reduced with a telescope which is set up with mirror M5 and M6 which are spherical mirrors with radii of R_{M5} = -1500 mm and R_{M6} = 600 mm corresponding to a focal length of f_{M5} = 750 mm and f_{M6} = -300 mm, respectively which are separated by $d = f_{M5} + f_{M6}$. This reduces the beam size by a factor of 2.5, generating a beam diameter of about 5 mm. M5 is mounted on a linear stage to fine-tune the separation of M5 and M6 to conserve the beam collimation.

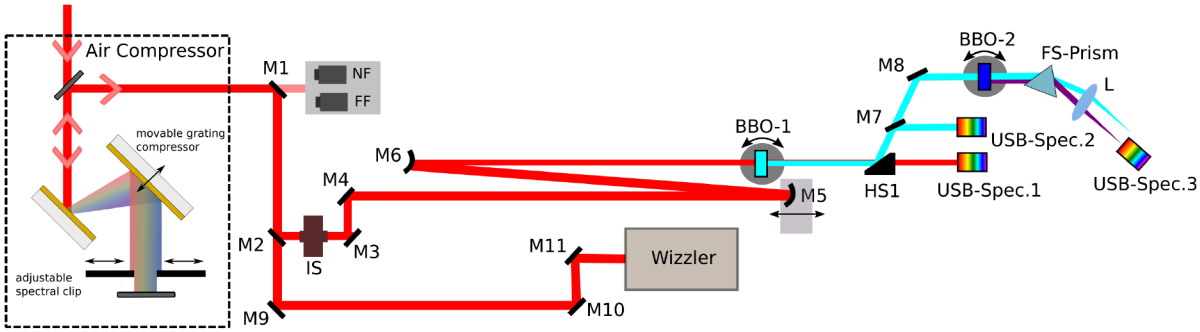

Figure 5.4.: Sketch of the FHG setup incorporating the main optics and diagnostics.

The beam is then passed to the first BBO crystal (BBO-1), optimized for SHG. The crystal is mounted in a rotation mount to adjust the ϕ angle, which describes the rotation around the beam axis, and on a motorized rotation stage to adjust the θ angle, which describes the tilt of the crystal surface with respect to the beam axis. The ϕ-rotation is used to align the crystal with the polarization of the incoming beam, ensuring it becomes the ordinary ray (Type-1 phase matching, see Sec. 5.1), while the θ rotation is essential for achieving phase matching. The fine-tuning both ϕ and θ is crucial for maximizing the efficiency of the harmonic generation process.
Subsequently, the second harmonic (2ω) and the fundamental (ω) signal are separated using a high harmonic separator beam splitter (HS1), which reflects the vertical polarized (s-polarized) second harmonic and transmits the horizontally polarized (p-polarized) fundamental signal. The fundamental spectrum can be detected with the spectrometer (USB-Spec.1). Mirror M7 can be flipped into the beam path to measure the 2ω spectrum with USB-Spec.2. M8 is employed to align the beam through the second BBO crystal (BBO-2) which is used to generate the fourth harmonic (4ω) at approximately 206 nm which again is p-polarized. This crystal is also mounted on rotation stages to allow for precise adjustments of both the θ and ϕ angles.

Label	**Description**	**Company / Product number**
BBO-1	BBO Type I, 28.36°, 5x5x0.5 mm, AR 760-840 nm + 380-420 nm	United Crystals
BBO-2	BBO Type I, 82.56°, 5x5x0.75 mm, AR 380-420 nm + 190-210 nm	United Crystals
FS-Prism	UV Fused silica Brewster Prism, H = 15 mm, t = 14.1 mm, apex angle = 69.25°	Altechna Co Ltd
L	Barium fluoride (BaF_2) lens, ø1", FL = 150 mm	EKSMA OPTICS
HS1	25 mm elliptical Low-GDD Beamsplitter for Second Harmonic of Ultrafast Ti:Sapphire Lasers, Reflects 360-440 nm, Transmits 700-900 nm	Thorlabs / UBS21
M1, M2	ø2" Broadband dielectric mirror, 750-1100 nm	Thorlabs / BB2-E03
M3, M4, M9, M10, M11	ø2" Protected silver mirror	Thorlabs / PF20-03-P01
M5	UV FS protected silver spherical mirror, ø1", Plano-concave, R = -1500 mm	EKSMA OPTICS / 092-3125R-1500
M6	UV FS protected silver spherical mirror, ø1", Plano-convex, R = +300 mm	EKSMA OPTICS / 092-3225R+600
M7, M8	ø1" Protected aluminum mirror	Thorlabs / PF10-03-G01
Energy detector	Pyroelectric detector, 7.8x7.8 mm, 0.193-20 μm, noise equivalent energy 50 nJ	gentec-eo / QE8SP-B-MT-D0
USB-Spec.1, USB-Spec.2	STS-UV miniature USB spectrometer , 186-667 nm	Ocean Insight / STS-UV-L-50-400-SMA
USB-Spec.3	USB2000+ USB spectrometer, 200-1100 nm	Ocean Insight / USB2000+
IS	ø15 mm Laser interlock shutter	lasermet / LS-10-12

Table 5.1.: Table of main optics and detectors used in the setup as shown in Fig. 5.4.

Within this setup, the 4ω and the ω signals are separated using a UV-enhanced fused silica prism. The incidence angle relative to the prism surface's normal is set to 60° which is approximately the Brewster angle for the fused silica prism. The Brewster angle corresponds to the angle at which no reflection occurs for a beam with parallel polarization [17]. As a result, reflection losses are negligible. After passing through the prism, the separated beams are focused using a BaF_2 lens (f=150 mm) and the 4ω spectrum is measured using the USB-Spec3 spectrometer. A pyroelectric energy detector (Gentec-EO, QE8SP-B-MT-D0) was used to measure the energy of the ω, 2ω and 4ω signals. This detector is sensitive in the UV range and features a low noise equivalent energy of 50 nJ.

5.3.2. Results

The uncompressed laser pulse of the final amplifier output of the laser system was first compressed with the grating compressor. Pulse compression was measured using the WIZZLER diagnostic. To fine-tune the pulse's spectral phase and, therefore, the pulse width, the DAZZLER [128, 129] in the laser front end was used. A feedback loop of the WIZZLER and the DAZZLER was used to optimize and flatten the spectral phase of the initial laser pulse to achieve maximum compression.
In Fig. 5.5 a), the initial averaged laser spectrum, measured over 100 shots using the WIZZLER, is shown in black, while the optimized spectral phase is represented by a red dashed line. The corresponding averaged temporal pulse shape, obtained through Fourier transformation, is displayed in panel b), with a FWHM of 25.8 ± 0.3 fs. The uncertainty corresponds to the standard deviation of the 100 measured shots.
The spectrum was narrowed down to concentrate on the wavelength which contribute to the SHG process by applying beam clips within the compressor as indicated in Fig. 5.4. The clipped spectrum is shown in panel c) in black together with its spectral phase shown as a red dashed line. The corresponding temporal profile is shown in panel d) with an increased pulse width 67.5 ± 0.2 fs. Due to the applied spectral clip, the pulse energy is reduced to $\sim 50\,\%$ of the initial unclipped pulse.
In Fig. 5.6 the spatial intensity profile of the fundamental pulse at the first BBO crystal is shown. The profile was measured using a diffuser which was imaged with a CCD camera. The pixel-wise intensity I_i was calculated from the image pixel values $I_{\mathrm{im},i}$

using:

$$I_i = I_{\mathrm{im},i} \cdot \frac{E}{A_{\mathrm{pix}} \cdot \tau \cdot \sum I_{\mathrm{im},i}} \tag{5.8}$$

where E is the total beam energy, τ the pulse width and A_{pix} the area represented by one pixel. The intensity was calibrated for a pulse width of 67.5 fs and a total energy of 1 mJ. The spatial profile fits well with the apertures of the BBO crystals used, and its peak intensity of about $\sim 100\,\frac{\mathrm{GW}}{\mathrm{cm}^2}$ is below the damage threshold of the BBO crystals. The measurement procedure for determining the conversion efficiencies, $\eta_{\omega\to 2\omega}$ and $\eta_{\omega\to 4\omega}$, during this initial test is outlined as follows: First, the conversion to the second harmonic signal was optimized by carefully adjusting the ϕ and θ angles in a manual and continuous manner using the crystal rotation mounts. The ϕ angle involves rotating the crystal around the beam axis to ensure that the BBO crystal's optical axis

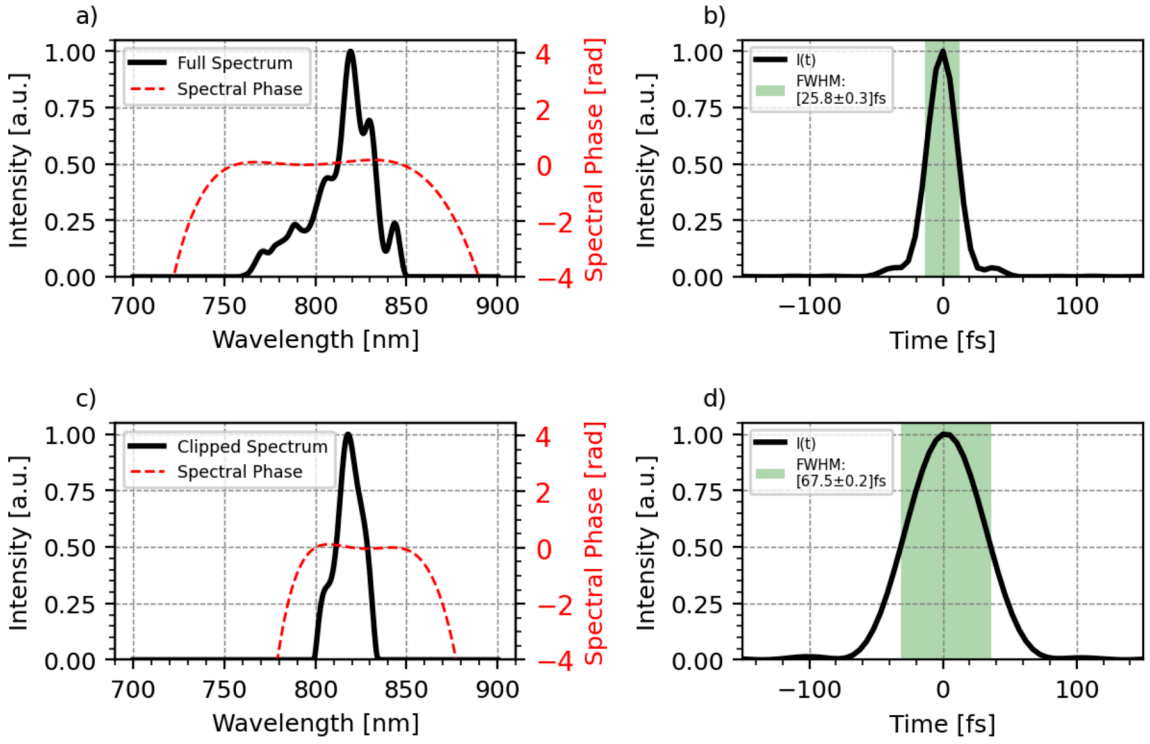

Figure 5.5.: a)The mean spectra and spectral phase of the initial laser pulse are displayed as a solid black line and a dashed red line, respectively, as measured over 100 shots with the WIZZLER. b) Temporal profile of the laser pulse calculated from the unclipped spectra and spectral phase as depicted in a). c) and d) same as a) and b) for an applied spectral clip.

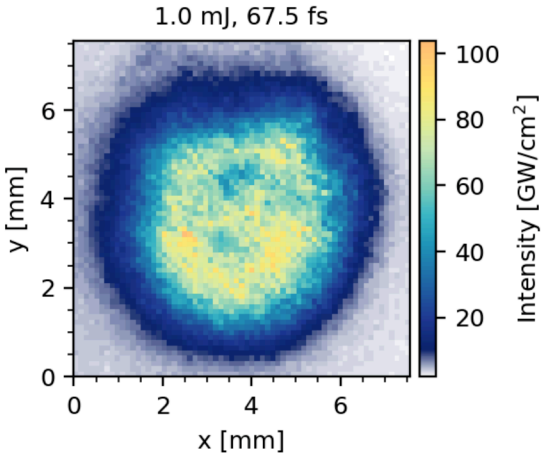

Figure 5.6.: Measurement of spatial intensity profile of the fundamental laser pulse before the first BBO crystal, calibrated assuming a total energy of 1 mJ and a temporal pulse width of 67.5 fs, as described in the text.

is perpendicular to the plane of polarization of the incident beam to experience the ordinary refractive index. The θ angle adjustment ensures proper phase matching, making the beam axis perpendicular to the surface of the crystal. This optimization was conducted in real-time by visually monitoring the second harmonic spectrum using USB-Spec.2, ensuring the central wavelength matched the expected value and the maximum spectral intensity was achieved. The same procedure was applied to optimize the conversion to the fourth harmonic by adjusting the ϕ and θ angles of the second BBO crystal (BBO-2), while monitoring the fourth harmonic spectrum using USB-Spec.3. For the measurement of $\eta_{\omega\to 2\omega}$ and $\eta_{\omega\to 4\omega}$, the energy detector was used (see Tab. 5.1). The energy of the fundamental near-infrared (NIR) pulse was measured before the first BBO crystal. The energy of the second harmonic signal was measured at the position of USB-Spec.2, and the energy of the fourth harmonic was measured at the position of USB-Spec.3, as shown in Fig. 5.4. For each energy measurement, pulse energies were averaged over 200 laser shots.

In Fig. 5.7, representative single-shot spectra of the fundamental, the second harmonic, and the fourth harmonic are presented for the optimized experimental setup. The spectrum of the second harmonic is centered around the expected wavelength of 412 nm. For the fourth harmonic, it becomes apparent that the spectral resolution of the USB2000+ (USB-Spec3) spectrometer, approximately 1 nm, is insufficient to

accurately resolve the precise shape of the narrow spectrum, which is anticipated to peak at approximately 206 nm. To achieve a more detailed characterization of the spectral shape in future measurements, a spectrometer with higher resolution should be employed.

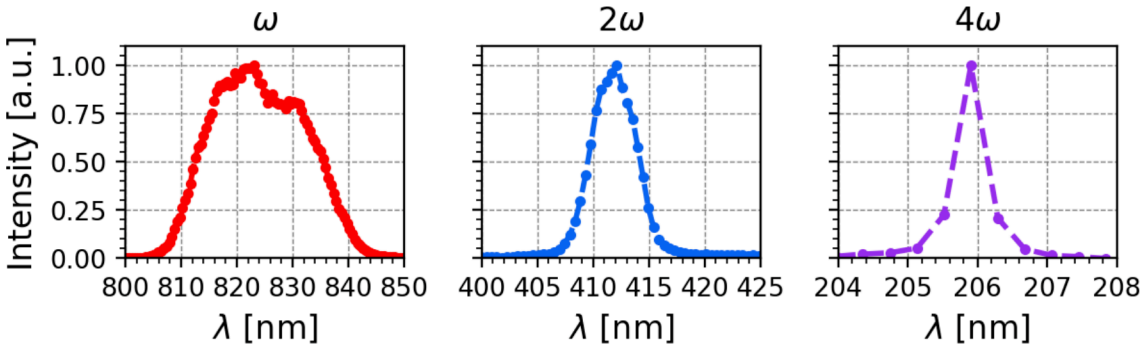

Figure 5.7.: Measured single shot spectra of the fundamental (ω), second harmonic (2ω), and fourth harmonic (4ω) for an optimized setup.

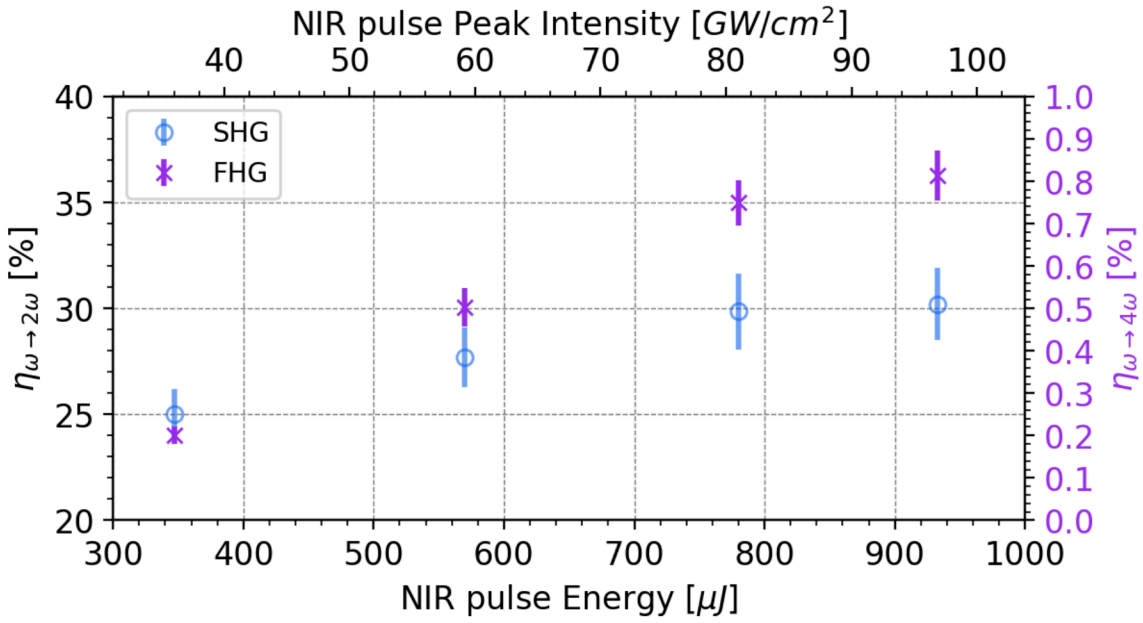

Figure 5.8.: First results of the SHG and FHG energy conversion efficiencies, $\eta_{\omega\to 2\omega}$ and $\eta_{\omega\to 4\omega}$, respectively, with respect to the fundamental NIR pulse energy.

The achieved energy conversion efficiencies, $\eta_{\omega\to 2\omega}$ and $\eta_{\omega\to 4\omega}$, with respect to the initial fundamental beam energy are displayed in Fig. 5.8. As expected, the conversion efficiency of both SHG and FHG increases with the fundamental energy due to the rise

in intensity. However, it begins to saturate at high fundamental beam energies. This saturation is attributed to the cubic non-linearity $\chi^{(3)}$ which leads to strong intensity modulation and re-conversion from the second harmonic to the fundamental waves [130].

This initial experiment achieved a conversion efficiency into the UV of up to $\eta_{\omega\to4\omega} \approx 0.8\,\%$ (8 µJ) with a peak intensity of around 95 $\frac{\mathrm{GW}}{\mathrm{cm}^2}$ which remains below the damage threshold of the BBO crystals. To note, $\eta_{\omega\to4\omega}$ is not simply $\eta^2_{\omega\to2\omega}$ but significantly smaller, as the intensity in the second conversion step is lower, e.g., due to energy depletion in the first step. The overall transmission efficiency from the initial Ti:Sa laser to the UV dissociation laser (on target) is expressed as $T = T_{\mathrm{clip}} \cdot \eta_{\omega\to4\omega} \cdot T_{\mathrm{UV}}$ where $T_{\mathrm{clip}} \approx 50\,\%$ accounts for energy loss due to spectral clipping of the initial Ti:Sa spectrum and T_{UV} represents the transmission efficiency of the UV beam transport to the interaction point. To achieve the required 0.5 mJ dissociation pulse energy, $T > 0.25\,\%$ is necessary, given the available 200 mJ of initial energy. With the currently demonstrated conversion efficiency of $\eta_{\omega\to4\omega} \approx 0.8\,\%$ it would be sufficient to generate the dissociation laser, provided that the beam transport achieves $T_{\mathrm{UV}} > 62.5\,\%$ which appears feasible.

Furthermore, for the dissociation laser, the setup needs to be scaled up to generate the required 0.5 mJ UV energy on target. A simple estimate of the scaling feasibility is provided below. Assuming that the experimental conditions (e.g., pulse length, spectral clip, etc.) remain the same as in the present experiment and considering a worst-case transmission efficiency of $T_{\mathrm{UV}} = 62.5\,\%$, the initial UV energy required to be generated is approximately 0.8 mJ. Compared to this experiment, this represents a factor of 100 increase over the demonstrated energy (8 µJ). Achieving this would require increasing the cross-section area of the beam and the BBO crystal aperture by a factor of 100. This corresponds to a beam diameter of 50 mm which is the size of a standard 2-inch optic. This demonstrates that scaling towards the full UV energy is realistic and becomes even more feasible with improved energy transmission (T_{UV}) and/or higher conversion efficiency $\eta_{\omega\to4\omega}$ which may be investigated in future work.

5.4. Conclusion

A conversion efficiency of $\eta_{\omega\to4\omega} \approx 0.8\,\%$ from the Ti:Sa laser into the fourth harmonic at 206 nm was demonstrated using two BBO crystals. This achieved conversion efficiency may already be sufficient to generate the 0.5 mJ dissociation laser required

for the LEAP project, provided that the UV beam transport to the interaction point achieves a transmission efficiency of $T_{\mathrm{UV}} > 62.5\,\%$.
Nevertheless, the conversion efficiency $\eta_{\omega \to 4\omega}$ could potentially be improved through further optimizations, such as refining the spectral width or the group delay dispersion (GDD) of the fundamental pulse. Furthermore, more detailed investigations through simulations could help optimize the setup, but these efforts are beyond the scope of this thesis.
This proof-of-principle study demonstrates that cascaded SHG generation using two BBO crystals is a promising method for generating the UV dissociation laser required for the LEAP project. As a next step toward achieving a pre-polarized plasma source, the dissociation of HCl molecules using the generated UV pulse at 206 nm needs to be demonstrated. This includes characterizing the pulse duration of the UV pulse, which may need to be stretched to avoid ionization of HCl molecules. The actual dissociation can then be measured by observing the hyperfine quantum beating of the H and Cl magnetization with a pickup coil, as described by Sofikitis et al. [59]. These objectives will be addressed in future studies.

Chapter 6.

Construction and Test of the LEAP Calorimeter

The Compton transmission polarimeter proposed for the LEAP project consists primarily of two components: a magnetized iron absorber, created using an iron-core solenoid magnet, and a calorimeter designed to measure the asymmetry in transmitted energy. The working principle of the polarimeter is detailed in Sec. 3.2, and an illustrative schematic of the setup is provided in Fig. 3.3. As discussed in Sec. 3.3.3, the calorimeter is required to achieve an energy resolution $\frac{\sigma_E}{E} < 2\,\%$ at a total energy deposition in the TeV range to meet the requirements of the LEAP project. Consequently, the use of a homogeneous lead-glass calorimeter is proposed.
In the following sections, the calorimeter for the LEAP polarimeter, as developed in this work, will be introduced. First, the design, contraction and the components used are discussed, followed by a description of the calorimeter as implemented within the `leap_sims` `GEANT4` framework. Additionally, the commissioning and calibration of the calorimeter at the DESY II Test Beam Facility will be presented. Furthermore, a performance evaluation of the calorimeter, based on simulations incorporating the expected beam parameters of the LEAP experiment, is provided.

6.1. Calorimeter Description

The LEAP calorimeter follows the geometry of the crystal calorimeter utilized in the E166 experiment [66], featuring nine identical calorimeter cells arranged in a 3x3 grid. The following section covers the description of the calorimeter and its components. It

is worth noting that a resource-saving approach was taken for the construction of the calorimeter, incorporating mainly recycled materials and components readily available in stock. This strategic choice aimed to optimize the project's time and cost factors. For the construction of the calorimeter, nine lead glass crystals of type TF1 with a dimension of 38x38x450 mm^3 were used as active material and nine UV sensitive PMTs (*XP-1911 UV*) were used for the signal readout. The PMTs and the crystals will be described in more detail in the following section. As well as the design and assembly of the calorimeter.

6.1.1. Crystal Selection

The crystals readily available in the inventory are lead glass crystals, likely remnants from the GAMS-2000 spectrometer [131]. These crystals measure 38x38x450 mm^3 and are illustrated in Fig. 6.1 a). The length of the crystals amounts to about $18X_0$ for this type of material, which is more than sufficient for photon energies below 100 MeV, as expected for LEAP. This is especially true considering the crystals have been designed to sustain photons with energies ranging from 10 to 20 GeV [131]. Each crystal initially had a cylindrical plastic mount for PMTs attached to one side, a feature which was later removed. Two distinct types of lead glass crystals, TF1-000 and TF1-101, are present, sharing nearly identical optical and physical properties such as a refractive index of $n_e = 1.65$ and a density of 3.86 g/cm^3. However, they differ slightly in chemical composition, detailed in Tab. 6.1. Further information can be found on the data sheet from the crystals manufacturer in A.3. The TF1-101 type of lead glass is

	TF1-000	TF101
Pb0	51.2%	51.2%
SiO_2	41.3%	41.5%
K_2O	7%	7%
As_2O_3	0.5%	
CeO_2		0.2%
Refractive index, n_e	1.65	1.65

Table 6.1.: The chemical structure and refractive index of the lead-glass crystals [73].

more resistant to radiation-induced darkening due to the presence of cerium oxide in its chemical composition [132]. The presence of cerium causes a yellowish tint

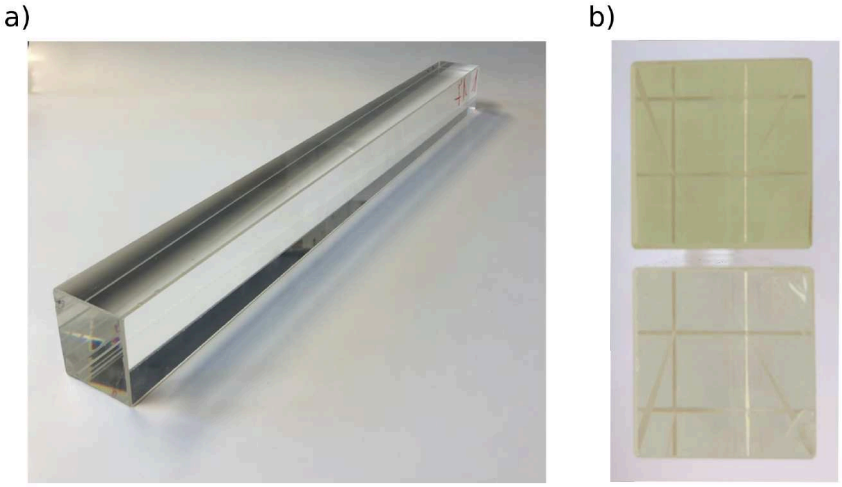

Figure 6.1.: a) Lead glass crystal for LEAP with dimensions of 38x38x450 mm^3. b) Color comparison of the two lead glass types: TF1-101 (on the top), exhibiting a yellowish tint, and TF1-000 (on the bottom), which is clearer in color.

to the glass [133], which can be used to distinguish between the two types, as the crystals were unlabeled. This color disparity is evident in Fig. 6.1 b), which presents cross-sectional views of both lead glass types, allowing a view through the crystal. The upper crystal, belonging to the TF1-101 type, exhibits a distinct yellowish tint compared to the TF1-100 type depicted below. The visible lines in the photograph correspond to reflections of the crystal's rear edges. Given the predominance of TF1-000 crystals in the inventory, we decided to use those to maintain the uniformity of the calorimeter cells. A selection of nine crystals were chosen based on criteria related to scratches and minor damages caused by the crystal's age. Unfortunately, no information is available regarding whether the crystals were previously exposed to radiation, e.g., used in an experiment before.

6.1.2. PMT Selection

For the detection of Cherenkov light, which peaks in intensity in the ultraviolet spectrum and is emitted by electromagnetic showers in the crystals, UV-sensitive PMTs will be used. The decision was made to re-purpose UV-PMTs of the type *XP-1911 UV*, which were already available in stock and initially utilized for the HERMES RICH detector [134]. These PMTs feature a cylindrical design with an active photocathode diameter of 15 mm. Figure 6.2 shows the dimensions, a photograph and the quantum efficiency of the PMTs, as provided in the data sheet [96].

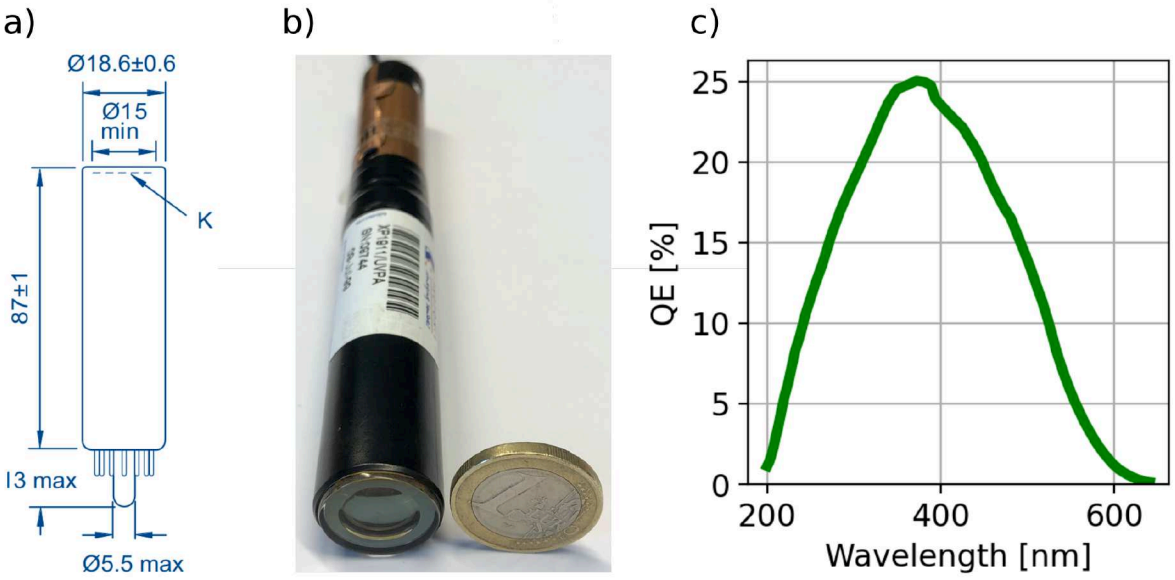

Figure 6.2.: a) Dimensions of the *XP-1911 UV* PMTs taken from the data sheet [96]. b) Photograph of a PMT. c) Quantum efficiency as provided in the data sheet.

To ensure the functionality of the recycled PMTs, tests were conducted in order to select the most similar nine of approximately 45 of them for the calorimeter. The PMTs were compared by their behavior with respect to the applied HV in the range of 800 V to 1300 V. The PMT signal Q can be expressed as the product of incident light intensity I, quantum efficiency QE, and gain μ_{PMT} described by $Q = I(\lambda) \cdot QE(\lambda) \cdot \mu_{\mathrm{PMT}}(V)$, where $\mu_{\mathrm{PMT}} = A \cdot V^{\alpha}$ (see Sec. 4.4). For a given intensity and wavelength of the incident light, the PMT signal can be written as $Q = b' \cdot V^{\alpha}$. Simplifying this expression by taking the logarithms results in a linear function:

$$\log(Q) = \log(b') + \alpha \cdot \log(V) \tag{6.1}$$

To confirm this characteristic, a UV LED emitting light with a central wavelength of approximately 380 nm was employed. The UV LED was pulsed using a 100 ns pulse generated by a pulse generator (*Tekronix AFG3102* [135]). The LED was fixed to a plastic lid, which fit onto the PMT's front. This construction ensured the light tightness and the equal position of the LED in front of the PMT's photocathode. To power the PMT a positive HV VME supply board (CAEN 6533M, [136]) was used. The PMT signal was measured with the VME QDC board CAEN V965 [137] as described in more detail in Sec. 6.1.4. A sketch of the experimental setup is shown in Fig. 6.3. For each PMT, a voltage scan was performed from 800 V to 1300 V in 50 V steps, collecting

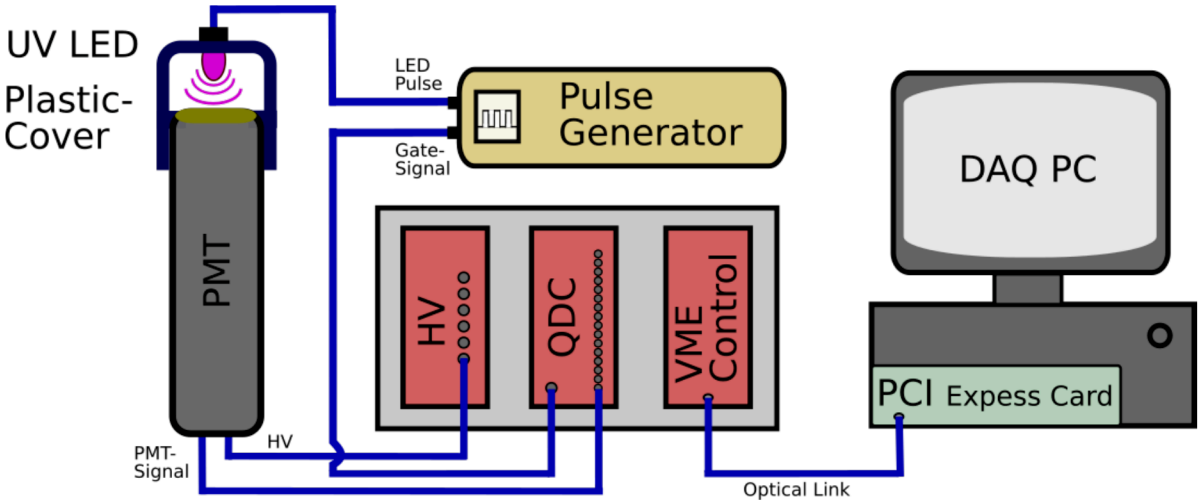

Figure 6.3.: Sketch of the PMT test setup.

20000 LED pulses every step. In addition, runs were conducted where the LED was off to get a pedestal of the measurements, which is caused by the dark current of the PMTs and the QDC channel itself.
The results of the PMT tests are illustrated in Fig. 6.4. Panel a) shows the voltage scan for PMT1, displaying a logarithmic representation of the PMT signal $\log(Q)$ over $\log(V)$ with a linear fit highlighted in red. This plot serves as an example, as all other tested PMTs exhibit very similar behavior. The resultant fit parameters a and b for the PMTs are depicted in Fig. 6.4 b) and c), respectively. The black dashed lines represent the mean of the obtained fit parameters, while the light grey band indicates the standard deviation σ. To ensure uniformity across the calorimeter cells to the greatest extent possible, PMTs demonstrating comparable behavior, where both fit parameters lie within the 1σ band, were considered. A total of 9 PMTs were pre-selected for the calorimeter highlighted in blue circles in panels a) and b). It is noteworthy that a more comprehensive comparison of the PMTs could involve measuring the absolute gain values using a single photon signal. However, this simplified test should be regarded merely as an initial sanity check of the PMT functionality. A more detailed calibration of the calorimeter cells will be described in a subsequent section.

6.1.3. HV-Power Supply

In order to power the PMTs for the calorimeter, a positive high voltage (HV) power supply with nine channels is needed. Due to a shortage of positive channels of the

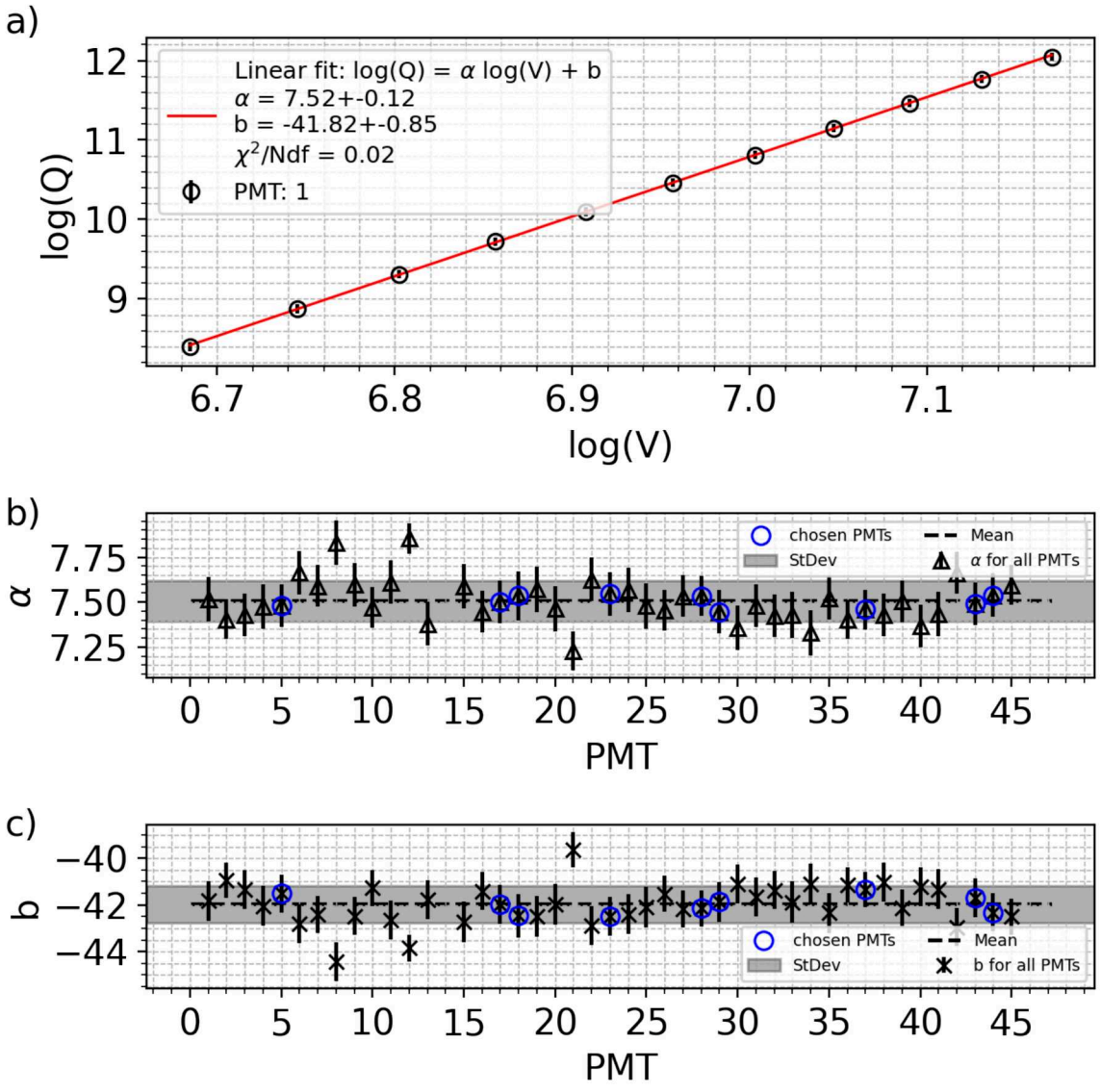

Figure 6.4.: Outcomes of the PMT tests. a) Voltage scan for PMT1: $\log Q$ over $\log(V)$ with linear fit. b) α parameter c) and b parameter for all tested PMTs. Blue circles: PMTs selected for the calorimeter.

HV VME supply board CAEN 6533M, a slightly older CAEN SY12 high voltage system [138] with three positive high-voltage models (*A100* [138]), each containing four channels as shown in Fig. 6.5 a) and b), was used. This configuration proved sufficient for the calorimeter PMTs, with some spare channels available. The power supply, connected to a PC via an RS-232 cable and controlled through the serial port, features both set and read-back values for each channel voltage. It has been observed that the set value V_{set} for each channel significantly deviates from the read-back

value V_{read} by more than three times the display resolution of 2 V, as provided in the technical information manual. Given the age of the devices, decalibration is likely. To better understand the actual voltage at the output of each channel and to address this discrepancy for the later analysis, the actual output voltage V_{out} was measured for each of the 12 channels at various set voltages ranging from 600 V to 1000 V in 50 V increments, using a digital multimeter (*FLUKE 79 SERIES II* [139]). Figure 6.5 c) shows the measured output voltage V_{out}, exemplary for HV-channel 1, as a function of the set voltage V_{set}. The technical information manual of the HV unit claims an accuracy and reproducibility of V_{out} better than $\pm 0.1\,\%$ [138]. Considering our measurement range from 600 V to 1000 V, the estimated error on V_{out} is on the order of ± 1 V, which is drawn but not visible in the data points. The data shows a linear behavior and was fitted using:

$$V_{out} = a \cdot V_{set} + b \tag{6.2}$$

The true output voltage exhibits a linear relation with the set voltage, with an intercept of approximately −6 V. This suggests that the actual voltage primarily differs from the set voltage by a constant voltage pedestal, a behavior consistent across all 12 HV-channels. Table 6.2 displays the fit parameters for each channel. Equation 6.2 will be used to calibrate V_{set} to the output voltage V_{out} for the later analysis.

HV-Channel	Slope	Intercept [V]	χ^2	Ndf
0	0.9917 ± 0.0026	-6.99 ± 2.09	0.21	7
1	0.9965 ± 0.0026	-6.18 ± 2.09	0.30	7
2	0.9958 ± 0.0026	-6.71 ± 2.09	0.35	7
3	0.9979 ± 0.0026	-6.31 ± 2.09	1.09	7
4	0.9979 ± 0.0026	-6.22 ± 2.09	0.16	7
5	0.9952 ± 0.0026	-5.87 ± 2.09	0.19	7
6	0.9954 ± 0.0026	-5.06 ± 2.09	0.70	7
7	0.9964 ± 0.0026	-6.28 ± 2.09	1.59	7
8	0.9975 ± 0.0026	-6.66 ± 2.09	0.51	7
9	0.9960 ± 0.0026	-5.67 ± 2.09	0.20	7
10	0.9969 ± 0.0026	-6.92 ± 2.09	0.70	7
11	0.9962 ± 0.0026	-5.63 ± 2.09	0.23	7

Table 6.2.: Fit parameters (Eq. 6.2) for the calibration of the 12 HV channels of the used power supply CAEN SY12.

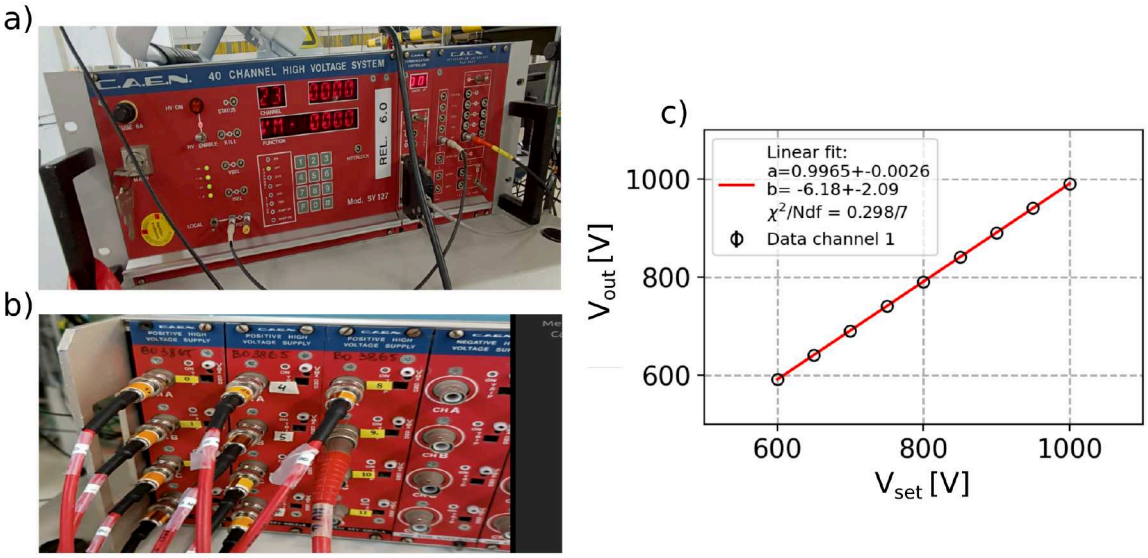

Figure 6.5.: a) Photograph of the front panel of the HV power supply CAEN SY127 [138]. b) Rear panel of the power supply, showing the high-voltage modules *A100* [138] and the 12 positive HV channels in use. c) Measured output voltage (V_{out}) as a function of the set voltage (V_{set}) for HV-channel 1, with the data fitted using a linear function.

6.1.4. Data Acquisition

To digitize the calorimeter PMT signals, a 16-channel charge-sensitive analogue-to-digital converter (QDC) module V965 from CAEN [137], was used. This module integrates and digitizes the current of negative inputs with a 12 bit resolution (equivalent to 4096 QDC bins). It offers two sensitivity ranges to accommodate a variety of signal strengths. The "low" range is suitable for signals up to 100 pC with a resolution of 25 fC, while the "high" range accommodates signals up to 800 pC with a resolution of 200 fC. This dual-range feature helps prevent saturation for higher charge pulses while enhancing resolution for smaller signals.
The cycle and integration time are steered by a gate signal (following the NIM standard), which needs to be provided to the QDC and typically has a duration on the order of 100 ns. The QDC module communicates via the VME computer bus standard and is controlled by a CAEN VME master module (V2718 [140]), which is connected via an optical link to a PCI Express card (CAEN A3818) of the DAQ computer.
Throughout the project, various DAQ software programs were employed for different setups, and more detailed descriptions of these will be provided in the respective sections.

6.1.5. Construction of the Calorimeter

In this section, the design and construction of the calorimeter will be described in detail.
Illustrated in Fig. 6.6 a) is the LEAP Calorimeter configuration, featuring nine lead glass crystals arranged in a 3x3 matrix and optically coupled with PMTs. The structural framework predominantly comprises two aluminum plates encapsulating the nine calorimeter cells. The frontal plate, fashioned from PEEK plastic, incorporates circular apertures with an diameter of 37 mm, centered on the crystals surfaces to minimize the absorptive material in front of the active medium. Adjacent to the crystals' rear facets are nine circular plastic housings installed, intended for PMT accommodation. In the plastic front, there are drill holes at the position of each crystal's corner. These holes serve as a feed trough for optical fibers attached to brass screws. The fibers can be connected to a UV LED, enabling light to shine onto the crystals for system checks. To accommodate the smaller photocathode area of the PMTs compared to the cross-section of the crystal, light guides were employed to increase the aperture of the PMTs, thereby enhancing the light yield. The light guides are plexiglass cones with a diameter of 32 mm at the thick end, covering $\approx 56\,\%$ of the crystal's back end. They are glued to the entrance window of the PMTs. Figure 6.7 a) shows a drawing of the PMT attached to the light guide, and Fig. 6.7 b) presents a photograph of the same. For the mounting of the PMT units in the provided plastic housings, a mounting structure is used, as depicted in Fig. 6.7, consisting of a spacer ring to center the PMT in the plastic tube and a spring at the back of the PMT. This system allows firm pressing of the PMT unit against the crystal surface, bypassing the use of optical grease. Power is supplied to each PMT through SHV cable and connector, while the anode signal is transmitted via a LEMO cable.
Figure 6.8 displays the calorimeter during the assembly process, with the first crystal placed in the support structure. Before assembly, all crystals were wrapped with aluminum-covered Mylar foil to increase reflectivity and with black vinyl tape to ensure the light tightness of each calorimeter cell. The back side of the crystal remained unwrapped to allow for the attachment of PMTs, and a small hole was poked in the front of the wrapping for the optical fiber.
Figure 6.9 showcases the finished calorimeter from different perspectives. The quadratic aperture of the active area is approximately $\approx 120\text{x}120\,\text{mm}^2$. The total dimensions of the calorimeter are $\approx 160\text{x}160\text{x}700\,\text{mm}^3$ with a weight of $\approx 35\,\text{kg}$.

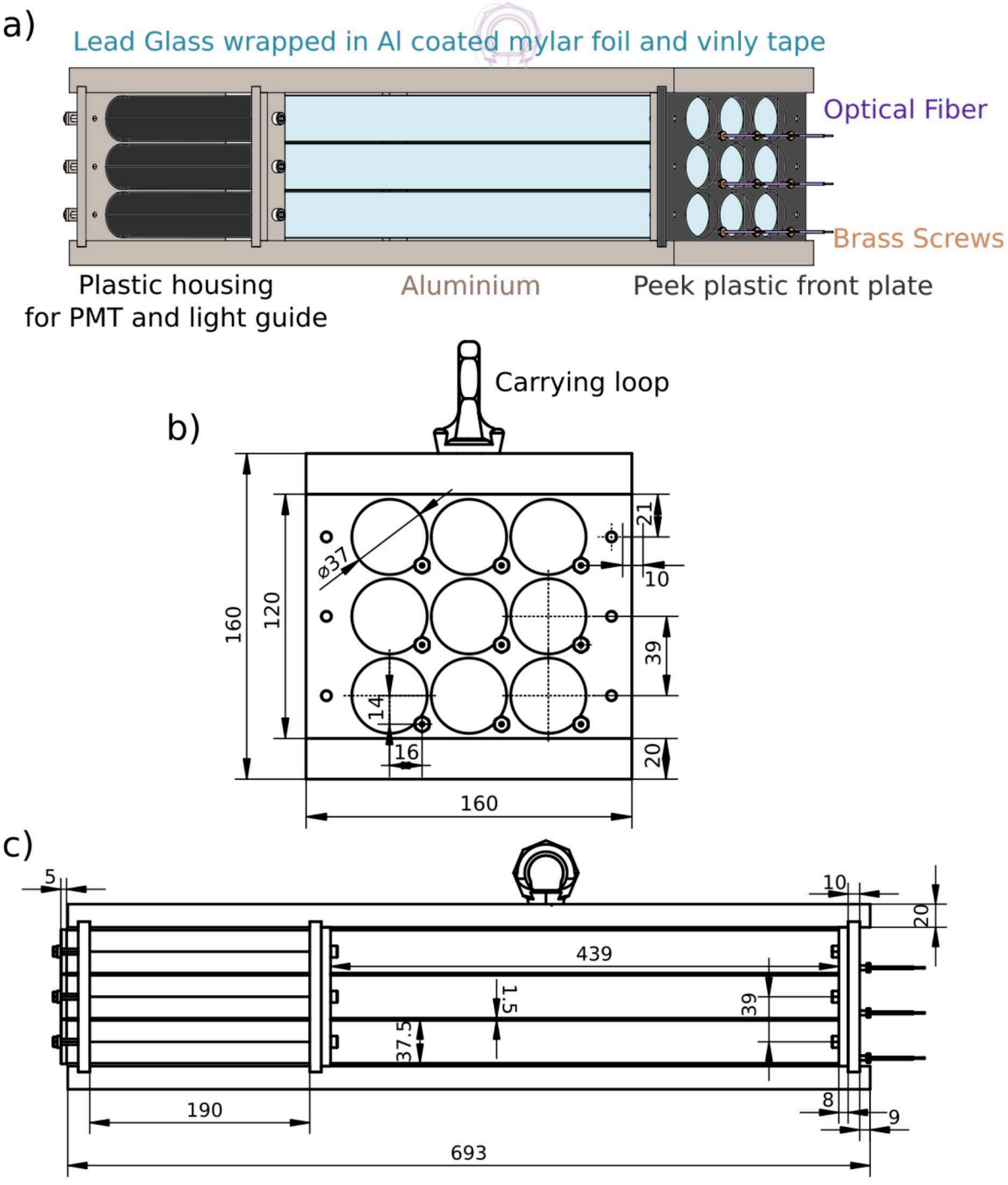

Figure 6.6.: a) Illustration of the LEAP calorimeter, comprising nine lead glass crystals arranged in a 3x3 grid and coupled with UV-sensitive PMTs. c) Technical drawing of the calorimeter (front view). c) Technical drawing of the calorimeter (side view).

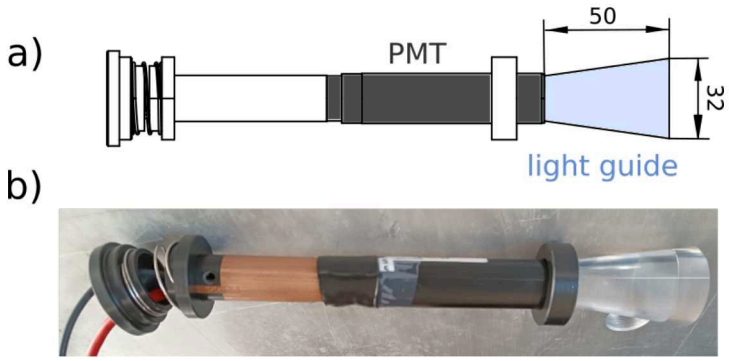

Figure 6.7.: a) Illustration of the PMT attached to the light guide and the mounting structure. b) Photograph of the PMT and light guide unit.

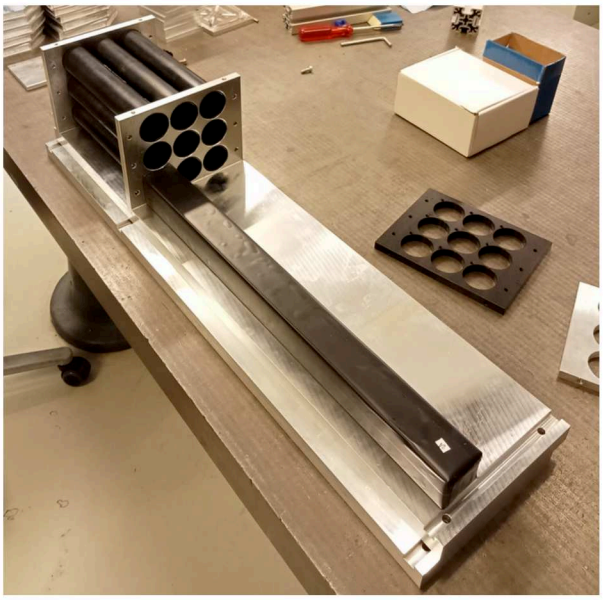

Figure 6.8.: Photograph of the calorimeter assembly

6.2. Calorimeter Simulations

The polarization measurement within the LEAP project relies on a good understanding of the polarimeter in simulations and, therefore, the calorimeter response for the expected beam parameters. The performance of the calorimeter will be investigated using `GEANT4` simulations. These simulations, are conducted using the simulation framework `leap_sims`, as described in Sec. 4.5, enable the modeling of particle behavior within the system. In this section the implementation of the LEAP calorimeter within the `leap_sims` `GEANT4` application will be discussed. Furthermore the expected response of the calorimeter system to particles from the MeV to the GeV range will be presented.

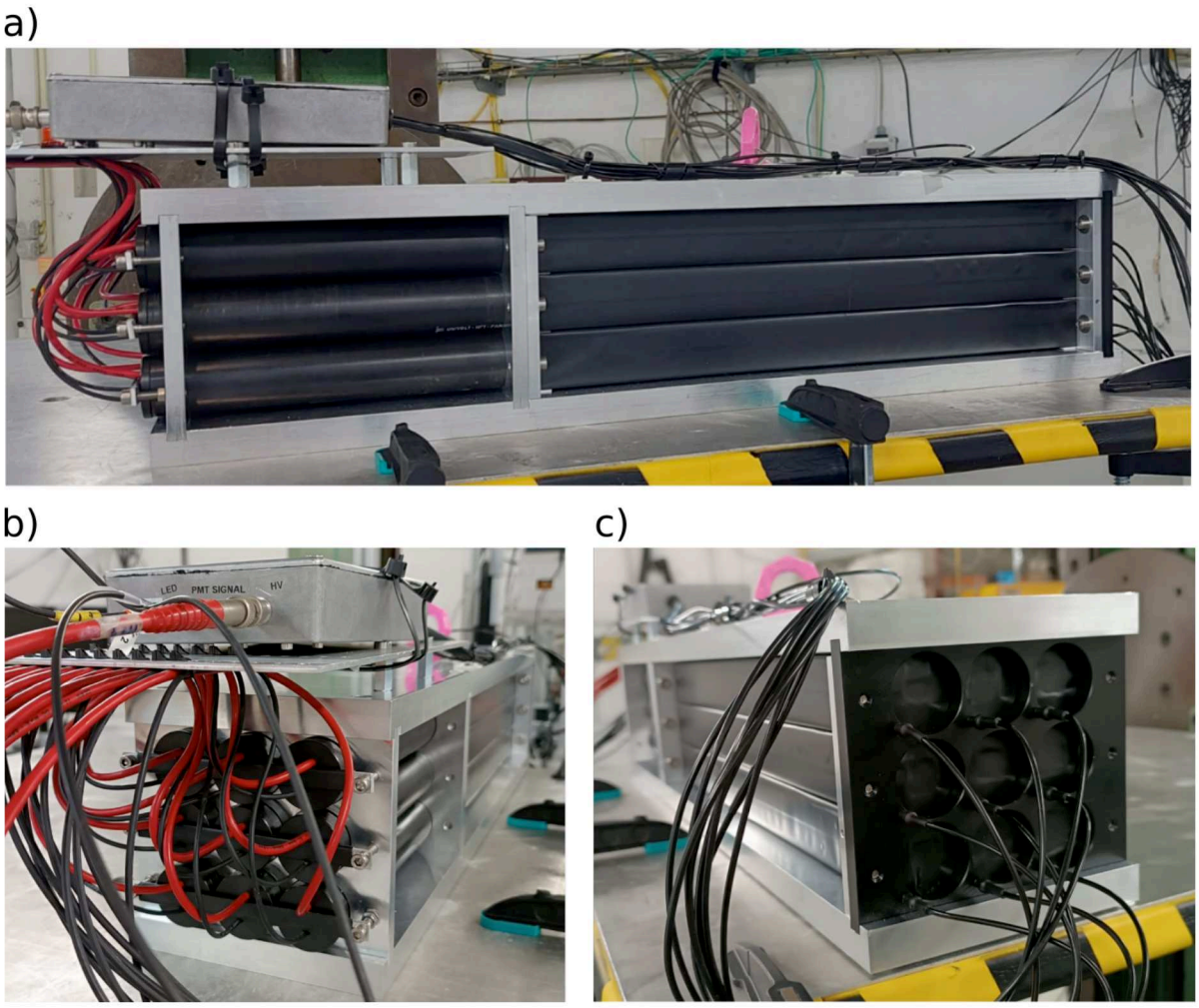

Figure 6.9.: Photograph of the side view a), back view b) and front view c) of the assembled LEAP calorimeter.

6.2.1. Calorimeter Geometry in GEANT4

The calorimeter is implemented in GEANT4 following the design and dimensions as described in Sec. 6.1.5. Fig. 6.10 a) depicts a display of the simulated calorimeter geometry. The calorimeter comprises nine TF1 lead glass bricks. The material is defined using the composition as shown in Tab. 6.1. The crystals are wrapped in thin aluminum foil including a thin air gab and arranged in a 3x3 matrix. The geometry includes the PEEK plastic front plate with the round apertures for each crystals as well as the the aluminum top and bottom plates of the support structure. The PMTs and PMT plastic mounts are not included in the geometry. The orange volumes in front and on the back of the calorimeter cells, visible in Fig. 6.10 b), are sensitive detector planes to detect the incoming particles and any leakage at the back of the

calorimeter. Furthermore, the crystals are defined as sensitive detector volumes to gather information on the electromagnetic showers within the system.

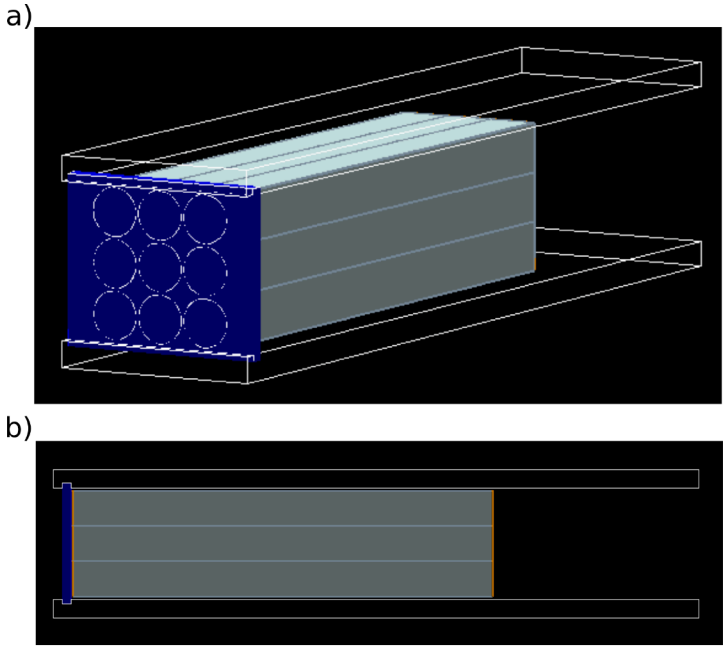

Figure 6.10.: a) Calorimeter geometry as implemented in `GEANT4`. b) Side view.

6.2.2. Preliminary Considerations and Signal Definition

First, it is essential to define what will be referred to as the simulated calorimeter signal, as there are multiple ways to do so. The concise objective is to have a value proportional to the energy of the incoming particles. The overarching goal is to define a value in the simulation that closely resembles the signal observed in reality.
To understand the signal generated in the crystal and detected by the PMTs, one must consider the underlying processes. When a particle enters the lead glass of the material, it undergoes an electromagnetic shower. Charged particles within this shower, which exceed the speed of light in the material (Cherenkov threshold), emit Cherenkov radiation (cf. Sec. 2.3). Those emitted photons may then strike the photocathode of the PMTs, generating photoelectrons according to the quantum efficiency of the cathode. These photoelectrons are subsequently multiplied within the PMT's dynodes, depending on the PMT's gain, and produce an anode current, which is then digitized using the QDC.

The most accurate simulation one can think of to estimate the calorimeter response is to simulate the hole signal chain, including the optical photon production. GEANT4 is capable of including optical physics processes [103]. Within this work it was envisaged to simulate the detector response on a level of the production of optical photons, including GEANT4 optical processes such as the Cherenkov effect, scintillation, absorption, rayleigh scattering processes and boundary processes.
To incorporate optical physics, detailed information on the optical properties of the material, such as absorption, refraction, reflection and surface properties, are required and need to be tweaked carefully to produce reliable results. While the production of Cherenkov photons with an accurate spectral shape was achieved, it appears that statistical fluctuations caused by optical transmission through the crystals were unnaturally large, far beyond what was observed in the calorimeter signal during the test beam campaign (Sec. 6.3). This issue warrants further investigation in future studies which are beyond the scope of this thesis. Consequently, it was decided not to continue with the optical simulations, which are also computationally expensive due to the huge amount of optical photons produced and tracked in the simulation.
The most straightforward approach to define a simulated signal proportional to the incoming energy is to use the energy deposited within the crystal, E_{dep}. One major drawback of this approach is the neglect of the kinetic energy threshold for charged particles required for the production of Cherenkov photons, as mentioned above. For the TF1 lead glass, assuming a refractive index of $n = 1.65$ (see Tab. 6.1), this energy Cherenkov threshold, on the kinetic energy of electrons and positrons, calculates as $E_{\text{treshold}} \approx 131\,\text{keV}$ using Eq. 2.9. Thus, this threshold becomes significant for low-energy particles which are of particular interest for the LEAP project. To address this in the definition of the calorimeter signal, the deposited energy in the crystal is only counted for electrons and positrons with kinetic energies above 131 keV. In the following, this definition of the simulated calorimeter signal will be used and will be referred to as E_{ct}.

6.2.3. Calorimeter Response

The calorimeter response will be investigated for photons and electrons over a broad energy range, from a few MeV to several GeV. This range is chosen to encompass the low-energy particles expected in polarization measurements for LEAP, as well as the GeV single electrons at the DESY II Test Beam Facility, which will be used for

the calorimeter calibration. For this this simulation study, the calorimeter geometry as depicted in Fig. 6.10 is used, employing the LEAP `PhysListEMPolarized` physics list to model the electromagnetic processes. The particle gun is configured as a monoenergetic point source aimed at the center of the central crystal. All simulations are conducted in a vacuum environment to eliminate interference from scattering effects with air.

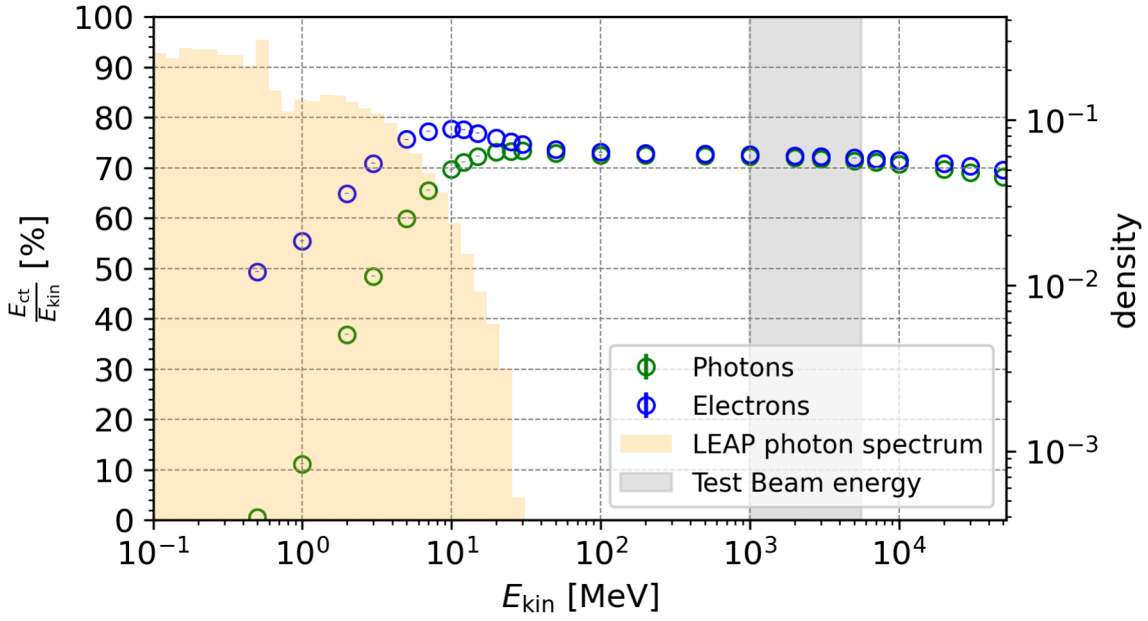

Figure 6.11.: Calorimeter response for single photons and electrons from 0.5 MeV to 50 GeV, illustrating the system's performance across a wide energy range. The expected photon spectrum for the LEAP polarization measurement is shown in orange, while the electron energies of the DESY II Test Beam are represented by the gray band.

In Fig. 6.11, the calorimeter signal E_{ct}, mean over 1000 particles, is shown for single electrons (blue circles) and photons (green circles) over a wide range of energies. The signal is normalized to the kinetic energy of the incoming particles, illustrating the system's response relative to the incoming energy.

The response for electrons and photons increases with the energy of the incoming particles for energies below 30 MeV, then becomes constant for particle energies between 30 MeV to about 10 GeV, before decreasing again at higher energies. The weaker response in the lower energy regime is due to the production threshold of Cherenkov radiation, which was accounted for in the simulated E_{ct}. The difference between the photon and electron responses in the lower energy regime is because photons must

first convert into charged particles through processes such as electron-positron pair production or the photoelectric effect before contributing to Cherenkov light production.
Figure 6.11 also includes an example bremsstrahlungs photon transmission spectrum (shown in orange) as expected from a 30 MeV electron beam (cf. Sec. 3.3.1) which illustrates the photon energy range to be measured with the LEAP calorimeter. This spectrum falls within the nonlinear response region of the detector and thus requires careful investigation. Additionally, the single electron energies of the DESY II Test Beam, ranging from 1 GeV to 5.6 GeV, are shown as a gray band within the calorimeter linear response region. Later, these single electron beams will be utilized to calibrate the calorimeter cells and to benchmark the simulation with actual data.
For particle energies above 10 GeV the energy response decreases due to the longitudinal shower energy leakage. This phenomenon is depicted in Fig. 6.12, which shows the energy deposition within the calorimeter along the beam axis for different incident electron energies across the 45 cm length of the lead glass crystals. Higher energy particles create deeper showers scaling with $ln(E)$, leading to more significant leakage from the back of the calorimeter.

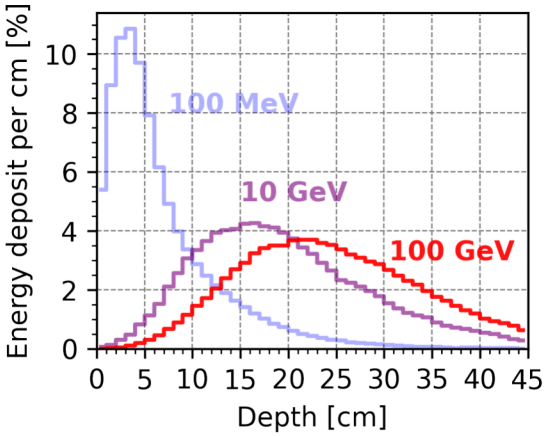

Figure 6.12.: Energy deposition of electrons as a function of depth in the calorimeter. Shown is the energy deposition along the length of the lead glass crystals (45 cm) for incident electrons with energies of 100 MeV, 10 GeV, and 100 GeV.

Influence of the G4PhysicsList

As shown in Fig. 6.11, the detector response is likely nonlinear over the photon energy range expected for LEAP. This nonlinearity can affect the polarization measurement

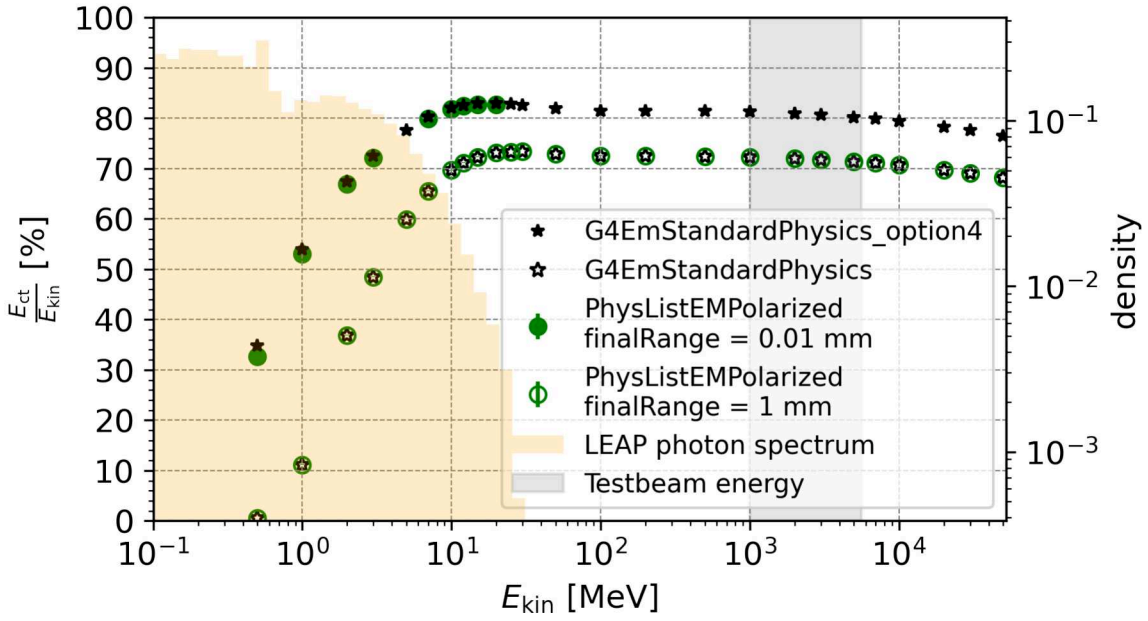

Figure 6.13.: Simulated calorimeter response for single photons from 0.5 MeV to 50 GeV using different `GEANT4` physics lists. The expected photon spectrum for the LEAP polarization measurement is shown in orange, while the electron energies of the DESY II test beam are represented by the gray band.

and needs to be modeled more carefully. Factors such as step size and energy cuts must be carefully considered to simulate the system response, especially for low-energy particles. It is essential to find a balance between accuracy and efficiency since finer granularity in the simulation consumes more time and computational resources. This section will investigate the influence of the chosen physics list on the calorimeter response. Specifically, the `PhysListEMPolarized` physics list, typically used in `leap_sims` simulations for modeling polarization-dependent effects, will be compared to `GEANT4` standard electromagnetic physics lists.

Figure 6.13 shows the simulated detector response for photons using the LEAP specific `PhysListEMPolarized` (green circles), along with the standard physics lists `G4StandardPhysics` (open black stars) and `G4StandardPhysics_option4` (filled black stars). `G4StandardPhysics_option4` is a more precise configuration for electromagnetic processes, using smaller step sizes and lower energy cutoffs, which enhances accuracy at the cost of longer simulation times and will, therefore, be used as the benchmark. The `G4StandardPhysics` and LEAP `PhysListEMPolarized` physics lists perform similarly because both use the default `GEANT4` EM parameter settings. However, `G4StandardPhysics_option4` shows a significantly higher response across the

entire energy range.
The step function, critical for the dynamic calculation of GEANT4 steps in the simulation, was found to play a crucial role in these differences. The final step size, whose default value is 1 mm but is set to 0.01 mm in G4StandardPhysics_option4, significantly impacts the results. By adjusting this parameter in the PhysListEMPolarized physics list, almost similar outcomes to those obtained with G4StandardPhysics_option4 are achieved, as indicated in Fig. 6.13 with green dots. This adjustment allows the LEAP PhysListEMPolarized to match the accuracy of the G4StandardPhysics_option4 while maintaining reasonable simulation times. When comparing the runtimes of the physics lists, the PhysListEMPolarized takes as long as the G4StandardPhysics, whereas the G4StandardPhysics_option4 takes four times as long. Reducing the final step size to 0.01 mm increases the simulation runtime by 2 when using PhysListEMPolarized. This increase is reasonable given the need for extra precision, particularly in the low-energy regime. Thus, using the polarized physics list for all polarimeter simulations, including the calorimeter, is justified.

6.3. Test Beam Operation

In this section, the system test of the LEAP calorimeter at the DESY II Test Beam Facility, as described earlier in Sec. 4.1, will be presented.
The purpose of the calorimeter test encompasses three key objectives: Firstly, it aims to investigate the response of the calorimeter under controlled experimental conditions using a mono-energetic electron beam. Secondly, the test beam serves to perform cross-calibration of the signals from each of the nine cells comprising the crystal and PMT assembly. The aim is to devise a calibration method that takes into account the voltage settings of the PMTs, allowing for individual voltage adjustments for each of the nine PMTs. This approach ensures flexibility to accommodate diverse experimental conditions while preserving the calibration. And thirdly, the test provides the opportunity to benchmark the calorimeter simulation against actual experimental data.
In the experiment, the PMT anode signal is measured using the QDC, as detailed in Sec. 6.1.4. This system provides a QDC value directly proportional to the PMT anode charge and, consequently, to the number of photons reaching the PMT's photocathode. The expected signal exhibits linear scaling with the beam's energy, while its dependence on the applied HV to the PMT follows an exponential pattern.

The signal can be expressed as

$$Q = kEV^{\alpha} \tag{6.3}$$

Where Q represents the measured QDC value, E signifies the beam energy, V denotes the applied voltage to the PMT, and α is a PMT-specific constant (cf. Sec. 4.4).

6.3.1. Setup and Measurements

The LEAP calorimeter was operated for one week (05.06. - 11.06.2023) at the DESY II Test Beam area T24, as introduced in Sec. 4.1.
Figure 6.14 shows a photograph of the area and the experimental setup with its main components. In panel a), a sketch of the beam path is overlaid. The beam enters through a beam collimator with a quadratic aperture of 8x8 mm^2. Additionally, Figure 6.15 provides an illustration of the main components, trigger, and readout chain. Following the collimator, the electron beam traverses two crossed scintillator trigger fingers utilized to trigger the readout chain. Subsequently, the beam enters the beam telescope, comprising six silicon tracker planes. Eventually, the beam enters the calorimeter, positioned on an x-y-stage, facilitating precise alignment with the electron beam at sub-mm precision. The nine calorimeter PMTs were powered by the CAEN

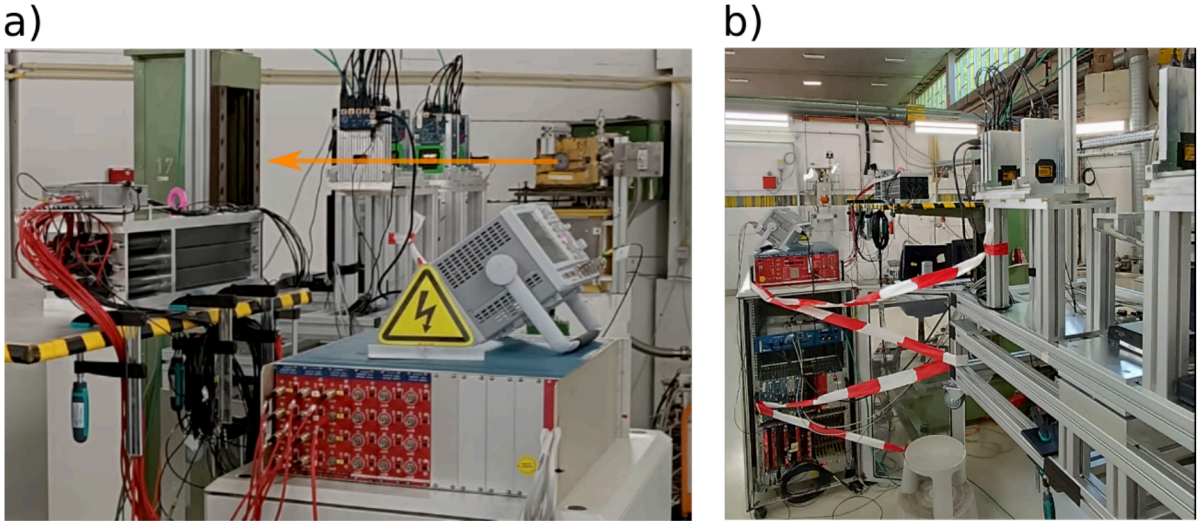

Figure 6.14.: Photograph of the LEAP calorimeter test setup at the DESY II Test Beam. a) Upstream view of the setup with an overlaid sketch of the beam path. The calorimeter mounted on the x-y stage is currently positioned outside the beam path. b) Downstream view of the setup.

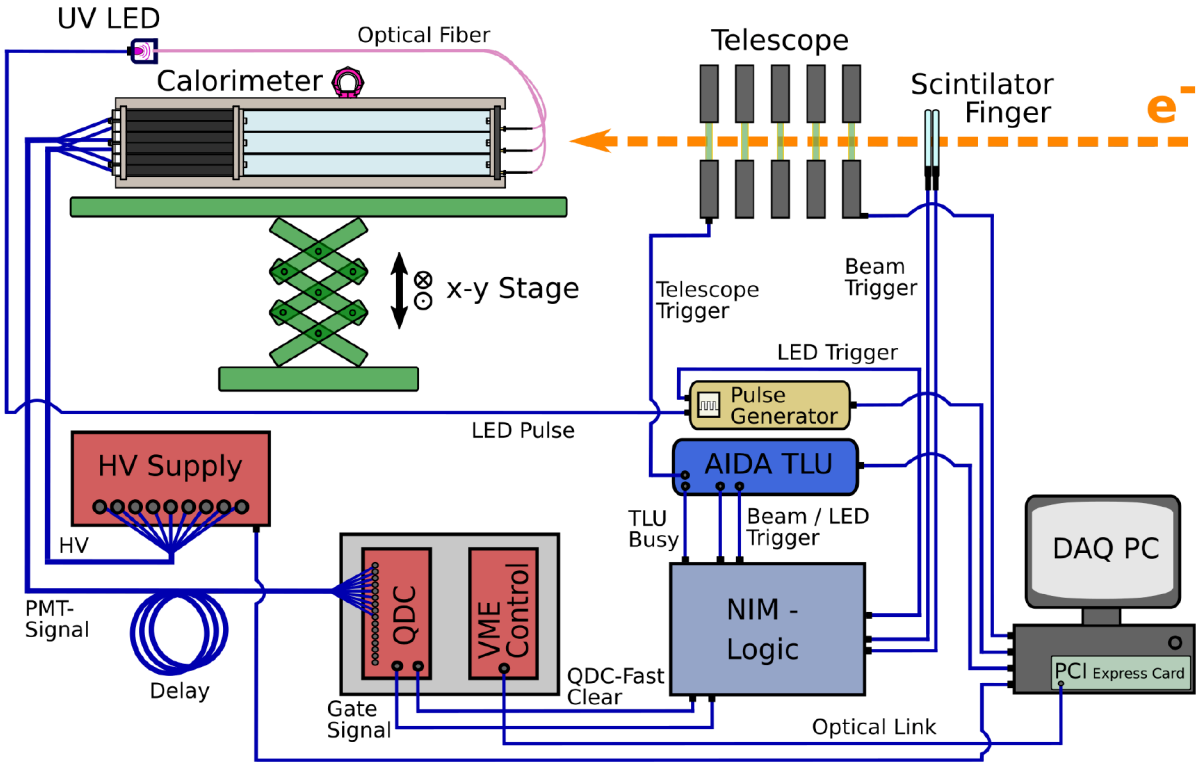

Figure 6.15.: Illustration of the experimental setup for the LEAP calorimeter test at the DESY II Test Beam. The main components of the setup, along with the paths of the trigger and readout signals, are depicted.

SY12 high-voltage system, as detailed in Sec. 6.1.3, connected to the DAQ PC via an RS-232 cable and controlled through the serial port. The PMT signals were transmitted through 15 m long LEMO cables, serving as a delay, to channels 0-8 of the VME QDC module *V965* from CAEN, as described in Sec. 6.1.4. The calorimeter's optical fibers were coupled to a control UV LED to facilitate PMT functionality testing during calorimeter operation. The LED was pulsed by a self-made ARDUINO microcontroller-based nanosecond pulse generator, which was connected to the DAQ PC via USB.
For data acquisition, the `EUDAQ2` software [141] was utilized. A trigger logic was configured to initiate data collection, comprising the logical trigger unit AIDA TLU [142], capable of distributing trigger signals and event numbers to multiple devices within an experiment. Alongside the `EUDAQ2` software, this setup enabled the saving of all detector signals from a single event with the corresponding event number, facilitating data synchronization. An analogue NIM trigger logic was employed to generate the gate signal for the QDC, enabling triggering on beam events using the scintillator trigger finger signals as well as on LED events using the LED trigger from the pulse generator.

Trigger Logic and Data Flow

Figure 6.15 illustrates a schematic of the setup along with the trigger and data flow. The basic concept of the trigger logic is to differentiate between two types of events: beam events, triggered when an electron passes through the scintillator fingers, and LED events, triggered by the LED pulser. The LED events serve two purposes: firstly, to capture data from an LED pulse, and secondly, to gather empty trigger events where neither a beam nor an LED pulse is present, facilitating the measurement of pedestal values for the QDC channels. The scintillator fingers generate a signal upon the passage of electrons. Both signals undergo discriminators before entering a coincidence unit within the NIM logic. The coincidence signal (beam trigger signal) is combined with the LED trigger signal through a logical OR operation. This OR signal is utilized to generate the QDC gate signal. Additionally, both the LED and beam trigger signals trigger the TLU on trigger inputs one and two, respectively, enabling the distinction between beam and LED events. Once triggered, the TLU sends a trigger signal to the telescope to save the telescope data for that event. Upon processing the event, the TLU emits a TLU busy signal to the NIM logic. If this signal is not sent before the next event, the NIM logic generates a QDC-Fast clear signal, clearing the QDC buffer to prevent data desynchronization. This precautionary measure is necessary because the TLU cannot directly generate the gate for the QDC, potentially leading to intrinsic data synchronization issues. Since the TLU requires approximately 100 ns for processing and triggering, the PMT's signals would be lost until the QDC gate is generated, resulting in missed events. All data is collected using the `EUDAQ2` software on the DAQ PC.

Measurement Overview

The calorimeter was aligned using the alignment laser positioned in the test beam area to center the beam on the central crystal, marking the default position where the beam is centered on the entire calorimeter. With the aid of the x-y stage, the calorimeter could be adjusted to center the beam on each of the nine crystals individually. The width of the QDC gate signal was set to 100 ns, and its delay was fine-tuned to coincide with the signals generated by the beam and the LED pulse in the calorimeter.
In Fig. 6.16 a), the gate signal and a PMT signal from one channel of the calorimeter are displayed on an oscilloscope in purple and yellow, respectively. In Fig. 6.16 b), the numbering of the calorimeter cells is shown as it is utilized in the subsequent analysis.

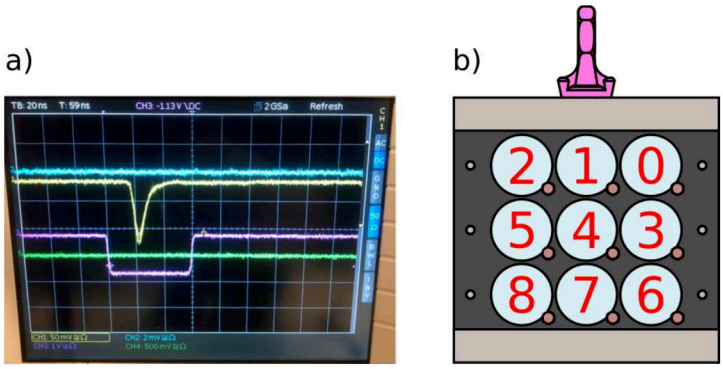

Figure 6.16.: a) Photograph of the oscilloscope showing the gate signal (purple) and the PMT signal (yellow). b) Schematic representation of the front face of the calorimeter, illustrating the numbering of the calorimeter cells.

The following runs were conducted for each calorimeter cell centered on the beam axis:

- **Energy Scan**: Electron energies [1, 1.6, 2, 2.6, 3, 3.6, 4, 4.6, 5, 5.6] GeV were used, with a fixed PMT voltage of 950 V for all PMTs, approximately 10^6 events per run.
- **PMT Voltage Scan**: Voltage steps [700, 750, 800, 850, 900, 950, 1000, 1200] V were varied, with a fixed beam energy of 3 GeV, approximately 10^6 events per run.
- **Between Data Runs**: LED and empty LED trigger runs were conducted, approximately 2×10^4 events per run.

During the empty trigger runs, a QDC gate without a signal (LED pulse or electron beam) was triggered to collect information about the QDC pedestal values and the noise.

6.3.2. Signal Shape and Definition

This section exemplifies the processing and definition of the calorimeter signal. Figure 6.17 illustrates a typical calorimeter signal obtained during a data run.
The figure shows the QDC low-range signal of calorimeter cell 4 (see Fig. 6.16 b)) for 3 GeV electrons and a PMT voltage setting of 950 V. The beam signal is depicted in blue (TLU trigger input 1), while the red signal represents an empty trigger (TLU trigger input 2), taken concurrently to ascertain the QDC channel's pedestal value. The beam signal exhibits a peak at the pedestal position, indicating events where the beam was triggered, however, electrons failed to reach the calorimeter due to

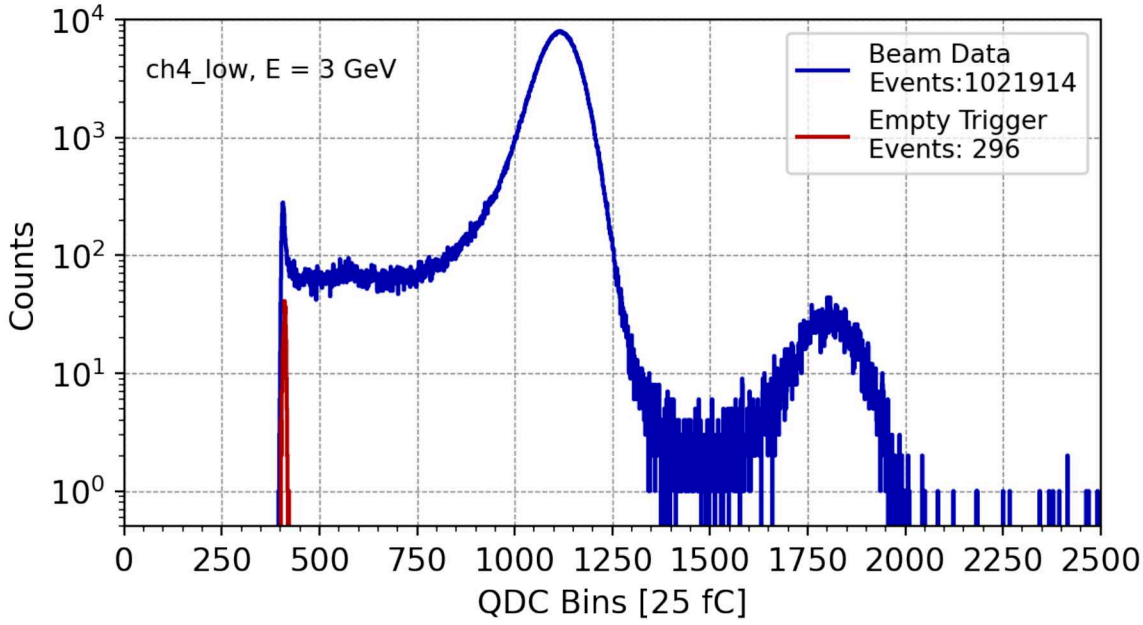

Figure 6.17.: Calorimeter signal of cell 4 recorded during a run with a 3 GeV electron beam and a PMT voltage of 950 V. The blue histogram represents the data collected from the beam, while the red histogram depicts the data collected from empty trigger events during the experiment.

scattering on the scintillator fingers and/or the beam telescope in the beamline. The dominant central peak represents the signal generated by by single electron absorbed in the calorimeter. Although rare, there is a slight possibility of multiple electron events due to the electron beam's production mechanism (cf. Sec. 6.3). The signal of a two-electron event is recognizable in the calorimeter signal, appearing as the last peak in the histogram. These two-electron events are currently not considered for further analysis due to their rare occurrence.

To define the single electron signal, the first step involves subtracting the QDC pedestal of the data, which is obtained by computing the mean value of the empty trigger events, as depicted in Fig. 6.18 a). For the parametrization of the signal, the $mean_{90}$ and rms_{90} were used, representing the mean and standard deviation calculated over only 90 % of the data, as defined in Eq. 6.4 and Eq. 6.5.

$$mean90 = \frac{1}{0.9N} \sum_{i \in \mathcal{S}_{90}} x_i \tag{6.4}$$

$$rms90 = \sqrt{\frac{1}{0.9N} \sum_{i \in \mathcal{S}_{90}} (x_i - mean90)^2} \tag{6.5}$$

Here, x_i denotes a data value, and $\mathcal{S}_{90}$ denotes the subset of data points. Various methods exist for selecting 90 % of the data; however, the one that minimizes the $rms90$ was chosen. This approach excludes highly improbable data points, offering a robust and straightforward method of defining the signal independent of a fit and its fitting range. In Fig. 6.18 b), the example calorimeter signal is depicted with its offset subtracted. The obtained $mean90$ and $rms90$ are represented as black dashed lines and a gray band, respectively, with the red dashed lines marking the 90 % of events included in the calculation. The algorithm that retrieves the $mean90$, and $rms90$ iterates over all histogram bins to find the smallest $rms90$. This ensures the signal definition for single-electron events while excluding empty and two-electron events. Unless otherwise noted, the signals are retrieved using $mean90$ and $rms90$ within this thesis. For convenience, the QDC calorimeter signal will be converted and displayed as the physical charge value Q, representing the measured anode charge of the PMT. This simplifies and enhances comparability when transitioning between the high and low range of the QDC, which have bin sizes of 200 fC and 25 fC, respectively. Root [105, 106], Python, and PyROOT are utilized for data processing and analysis.

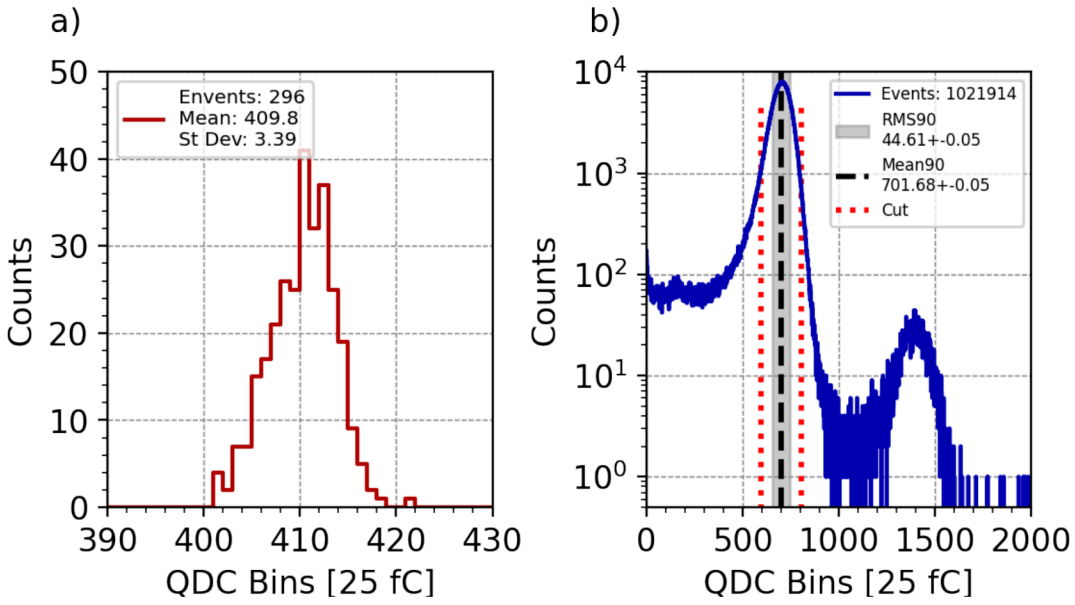

Figure 6.18.: a) Exemplary QDC pedestal of channel 4. b) Calorimeter signal of calorimeter cell 4 for a run with a 3 GeV electron beam and a PMT voltage of 950 V. The signal is defined as $mean90$, shown as black dashed lines, with $rms90$ depicted as a gray band. The red dashed lines indicate the data cut.

6.3.3. System Response

The expected behavior of the calorimeter response, as described by Eq. 6.3, with respect to the beam energy and the PMTs operation voltage needs to be verified. This analysis will be performed individually for the nine calorimeter channels using the energy and voltage scan data.

Energy scans

In Eq. 6.3, it is claimed that the PMT signal scales linearly with the energy of the beam, which will now be verified with the data. For the analyses, runs were selected where shots were aimed at the center of each crystal to ensure consistent conditions across all calorimeter cells. The PMT voltage was maintained at 950 V for all runs under consideration. A linear relationship is anticipated between the PMT anode charge Q_i and the beam energy for each of the nine calorimeter channels.

$$Q_i = a(V_i)E \tag{6.6}$$

Here, a depends on the PMT gain, which depends on the voltage V_i. However, a is assumed to be constant for the current analysis as the data is conducted with fixed voltages V_i. It is important to note that Eq. 6.6 should theoretically have no offset term, as a beam energy of 0 should yield no signal.
Figure 6.19 displays the calorimeter signal for each channel with respect to the electron energy. The signals are determined by the *mean*90 and standard error of the *mean*90 of the respective distribution, as explained in Sec. 6.3.2. The solid lines represent a linear fit $Q = aE + b$ of the respective data points and the obtained fit parameters are presented in Tab. 6.3.
The signals exhibit a clear linear relation with the beam's energy, consistent with our expectations, particularly within the energy ranges considered in this study. The observed differences in slopes among the channels may be attributed to variations in the gain values of the PMTs. Consequently, ensuring signal comparability necessitates cross-calibration, which will be explained in Sec. 6.3.4. Additionally, while the pedestal terms obtained from the fit are not precisely zero, they are insignificant compared to the typical signal strengths, which are in the order of tens of pC. This observation reinforces our assumption that the intercept term is effectively zero. However, a non-zero offset could potentially arise from inadequate QDC pedestal subtraction. Hence,

it may serve as a method to initially identify the correct pedestal values for each QDC channel.

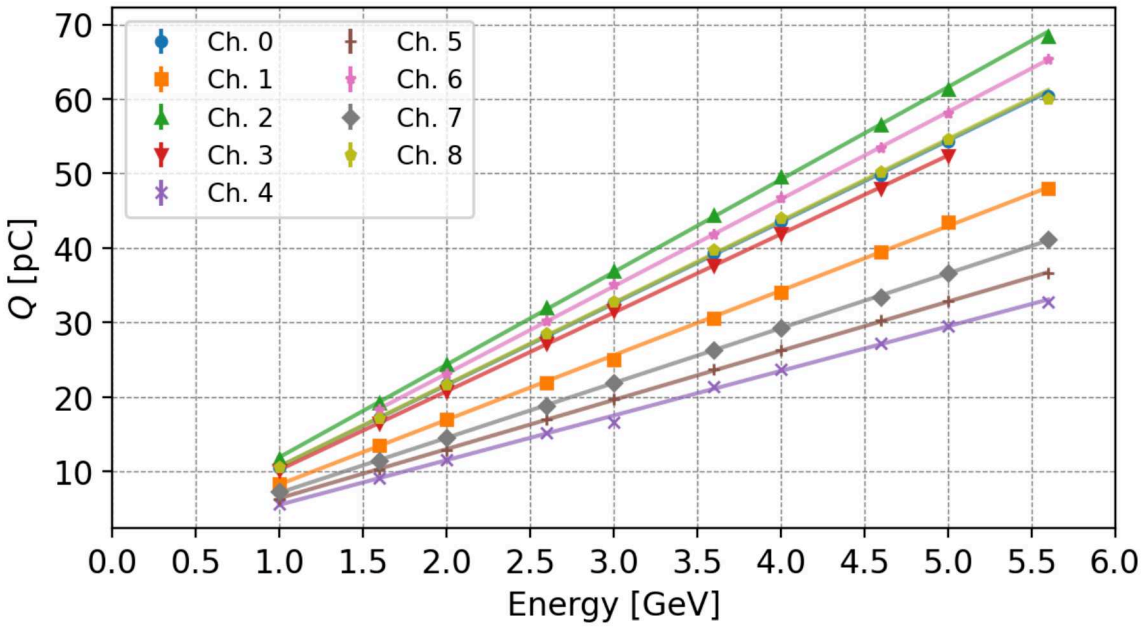

Figure 6.19.: PMT anode charge Q for each crystal at 950 V PMT voltage over the beam energy, along with a linear fit. The errors are purely statistical.

Channel	Slope (a) [pC/GeV]	Intercept (b) [pC]
0	10.93 ± 0.0005	-0.26 ± 0.001
1	8.67 ± 0.0004	-0.39 ± 0.001
2	12.42 ± 0.0006	-0.48 ± 0.002
3	10.54 ± 0.0005	-0.31 ± 0.001
4	6.0 ± 0.0003	-0.36 ± 0.001
5	6.59 ± 0.0002	-0.17 ± 0.001
6	11.7 ± 0.0007	-0.26 ± 0.002
7	7.36 ± 0.0003	-0.19 ± 0.001
8	10.98 ± 0.0005	-0.27 ± 0.002

Table 6.3.: Fit parameters of the linear fit $Q = b + a \cdot E$ of the energy scan data depicted in Fig. 6.19.

Voltage Scan

To examine the signal behavior with respect to the applied PMT voltage, the voltage scan runs from the test beam data were selected where each calorimeter cell was

positioned at the beam center. The voltage was ramped from 750 V to 1200 V, while the beam energy remained fixed at 3 GeV. According to Eq. 6.3, the signal scales with voltage to the power of α, where α represents a PMT-specific constant. For analytical simplicity, the logarithm of Eq. 6.3 is taken; thereby, it becomes apparent that the logarithm of the calorimeter signal Q exhibits linear scaling with the logarithm of the PMT voltage value V:

$$\log(Q/\mathrm{pC}) = \underbrace{\log(k \cdot E/\mathrm{GeV})}_{\beta} + \alpha \cdot \log(V/\mathrm{V}) \tag{6.7}$$

Where β is a constant for a fixed beam energy. Figure 6.20 shows the logarithm of the calorimeter signal ($\log(Q/\mathrm{pC})$) as a function of $\log(V/\mathrm{V})$ for each of the nine calorimeter channels. The voltage values correspond to the calibrated voltages (see Sec. 6.1.3). The data exhibits the expected linear behavior. The solid lines represent linear fits to the data points, and the retrieved fit parameters β and α are presented in Tab. 6.4.

Upon comparing the signals, it is evident that they display consistent behavior but differ in absolute values. They are depicted as parallel lines shifted along the y-axis of the figure, attributed to variations in the absolute gain of the PMTs which may arise due to production-related factors. These discrepancies in the gain of the nine PMTs are also apparent in the energy scan depicted in Fig. 6.19. There, the slopes of the linear fits are larger for PMTs with higher gains, aligning well with the order observed in the voltage scan. Considering the differences in the absolute gain values of the PMTs, calibration is necessary to ensure the comparability of the calorimeter signals. This calibration process will utilize the retrieved fit parameters from the voltage scan, which will be elaborated upon in detail in the subsequent section.

Channel	Slope (α)	Intercept (β)
0	$7.69 \pm 3 \times 10^{-5}$	-49.13 ± 0.00019
1	$7.64 \pm 3 \times 10^{-5}$	-49.08 ± 0.00022
2	$7.64 \pm 3 \times 10^{-5}$	-48.7 ± 0.00018
3	$7.53 \pm 3 \times 10^{-5}$	-48.1 ± 0.00018
4	$7.58 \pm 3 \times 10^{-5}$	-49.07 ± 0.00021
5	$7.68 \pm 3 \times 10^{-5}$	-49.63 ± 0.00022
6	$7.67 \pm 3 \times 10^{-5}$	-48.97 ± 0.00018
7	$7.58 \pm 3 \times 10^{-5}$	-48.8 ± 0.00019
8	$7.7 \pm 3 \times 10^{-5}$	-49.27 ± 0.00019

Table 6.4.: Fit parameters of the linear fit $\log(Q/\mathrm{pC}) = \beta + \alpha \cdot \log(V/\mathrm{V})$ of the voltage scan data depicted in Fig. 6.20

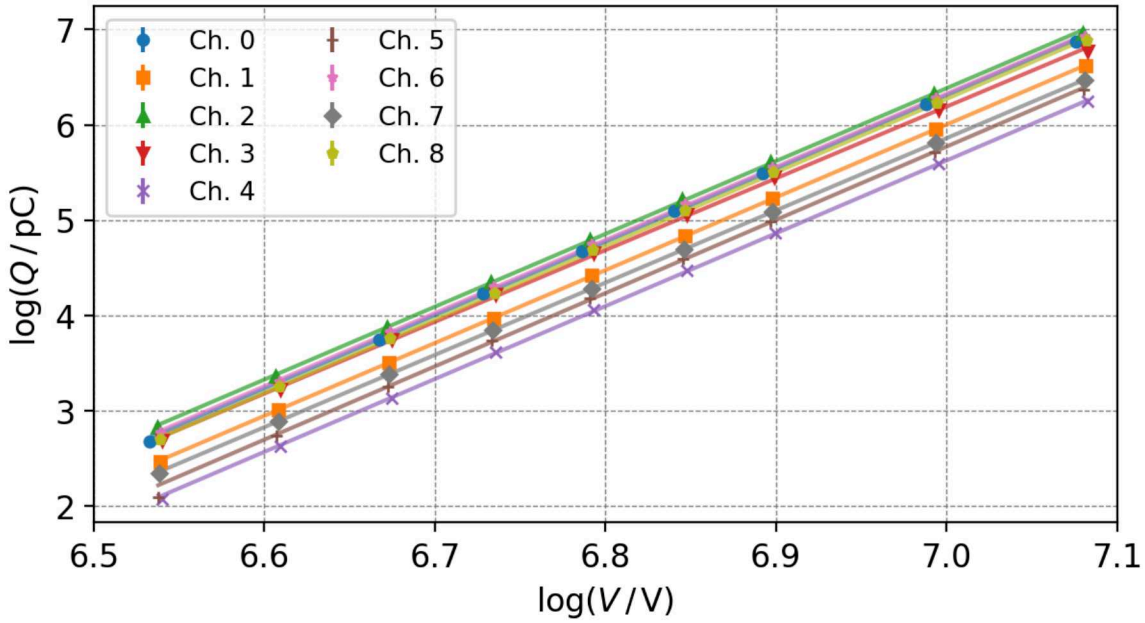

Figure 6.20.: Logarithm of the calorimeter signal (Q) as a function of the logarithm of the applied PMT voltage (V) for each of the nine calorimeter channels. The beam energy was fixed at 3 GeV. The solid lines represent linear fits to the data points.

6.3.4. Cross-Calibration of the Calorimeter Cells

In this analysis phase, the signals recorded by the nine distinct calorimeter cells will be cross-calibrated. A clear understanding of what cross-calibrating signals means will be established. Essentially, this entails aligning the response of each system [PMT+Crystal]$_i$ with that of every other system [PMT+Crystal]$_j$, ensuring that system i shows an equivalent signal to system j when exposed to the same energy deposition. In mathematical terms, the objective is to substitute:

$$Q_i(E, V_i) \longrightarrow Q_j(E, V_j) \tag{6.8}$$

By executing this calibration process, the energy depositions in each system can be directly compared by examining their respective measured signals. Practically, this involves multiplying $Q_i(E, V_i)$ by the calibration coefficients:

$$C_{ij}(V_i, V_j) = \frac{Q_j(E, V_j)}{Q_i(E, V_i)} = \frac{k_j E V_j^{\alpha_j}}{k_i E V_i^{\alpha_i}} = \frac{k_j V_j^{\alpha_j}}{k_i V_i^{\alpha_i}} \tag{6.9}$$

where $C_{ij}(V_i, V_j)$ depends on the known PMT voltages and the corresponding k_i and α_i values. These calibration coefficients can be computed using data from the voltage scans. Utilizing the relationship $\beta = \log(k \cdot E)$, the calibration coefficient is expressed as:

$$C_{ij}(V_i, V_j) = \exp(\beta_j - \beta_i)\frac{V_j^{\alpha_j}}{V_i^{\alpha_i}} \tag{6.10}$$

Here, α and β represent the slopes and the intercept values obtained from the linear fits of the voltage scans (see Tab. 6.4). In practice, unless otherwise specified, the calibration of all calorimeter channels will be standardized to channel 4 at a PMT voltage of 950 V, positioned at the center of the calorimeter. Data from the energy scan (see Fig. 6.19) will be used to verify the calibration procedure, as it was not employed in determining the calibration coefficients and is therefore independent. The energy scan for each of the nine calorimeter cells is depicted in Fig. 6.21, calibrated to the reference channel 4 at 950 V PMT voltage. The relative deviation from the reference is less than 2.5 % for each data point, confirming the successful cross-calibration.

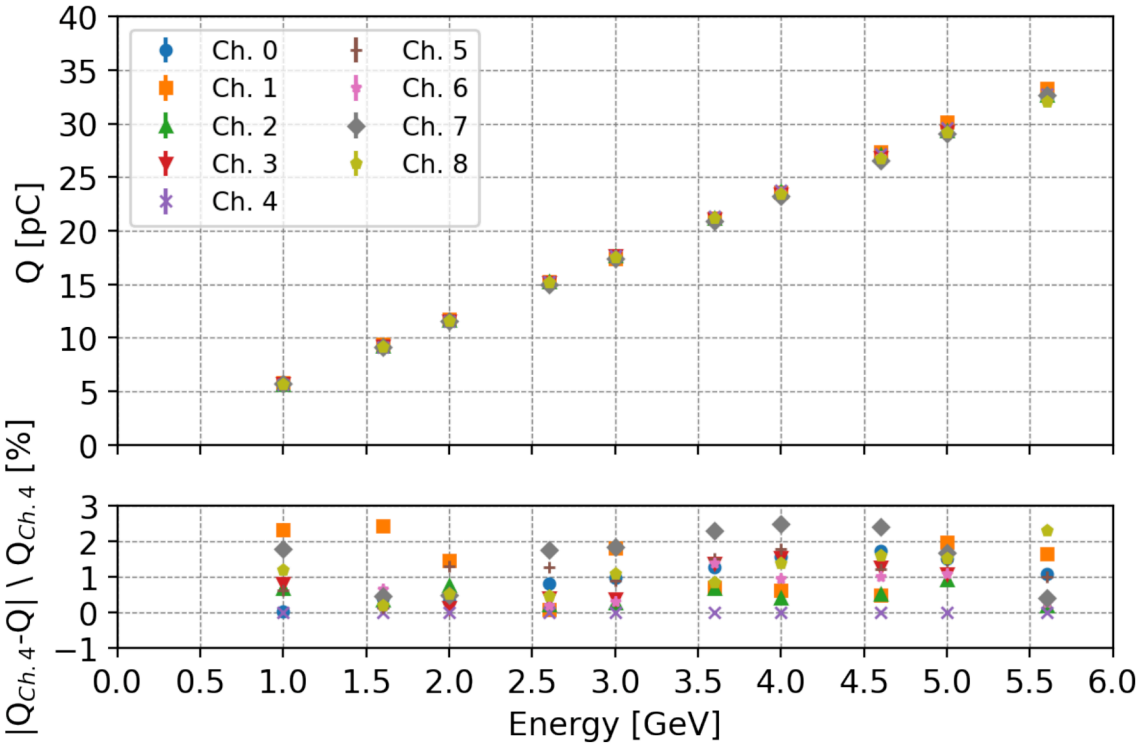

Figure 6.21.: Energy scan of the calorimeter cells (see Fig. 6.19) calibrated to channel 4 at 950 V PMT voltage.

6.3.5. Linearity

The next step is to verify the linearity of the calibrated calorimeter signal with respect to the beam energy. For this purpose, all nine signals from the calorimeter channels will be taken, calibrated with the previously derived calibration coefficients, and summed up to yield the full calorimeter signal.
Figure 6.22 a) shows the signal distributions of the full calorimeter for different electron energies. The signals are normalized to the number of events collected for each run. The dashed black lines indicate the *mean*90 of the respective distributions. In panel b), the *mean*90 of the calorimeter signals is shown as a function of the electron energy along with a linear fit indicated by the solid red line. Within the errors, the data agrees well with the linear fit, as depicted in panel c). This result confirms the anticipated linear response of the system within the GeV energy range of the DESY II Test Beam, as illustrated in Fig. 6.11.

6.3.6. Energy Resolution

The energy resolution of the calorimeter, $\frac{\sigma_E}{\langle E \rangle}$ (see Sec. 2.4.1), can be extracted from the calibrated test beam data.
The distributions of the calorimeter signal measured for electron energies ranging from 1 GeV to 5.6 GeV are depicted in Fig. 6.22 a). By taking the *rms*90 values and dividing them by the corresponding *mean*90 values of the respective distributions, the relative energy resolution is obtained, as shown in Fig. 6.23. The experimental data aligns well with the fit depicted in red, which follows the general parametrization of energy resolution as defined by Eq. 2.18. The stochastic term, $\frac{6.5 \pm 0.1\%}{\sqrt{E\,[GeV]}}$, is reasonable for a lead glass calorimeter which is typically in the order of $\frac{(5-10)\,\%}{\sqrt{E\,[GeV]}}$ [51, 143]. The noise term b, caused by readout electronics and digitization, is measured to be (40 ± 3) MeV. Both terms diminish at higher energies due to their respective energy dependencies. The constant term c, which primarily affects the energy resolution at high energies, is determined to be 0 within an uncertainty of 0.6 % ($0.0 \pm 0.6\%$). The determined energy resolution remains valid as long as most energy is contained within the calorimeter. However, longitudinal leakage becomes more significant for higher energy particles, potentially degrading the energy resolution. Nevertheless, within the LEAP project, numerous low-energy particles in the MeV range are expected to contribute to high total energies; thus, longitudinal leakage will not be a significant issue.

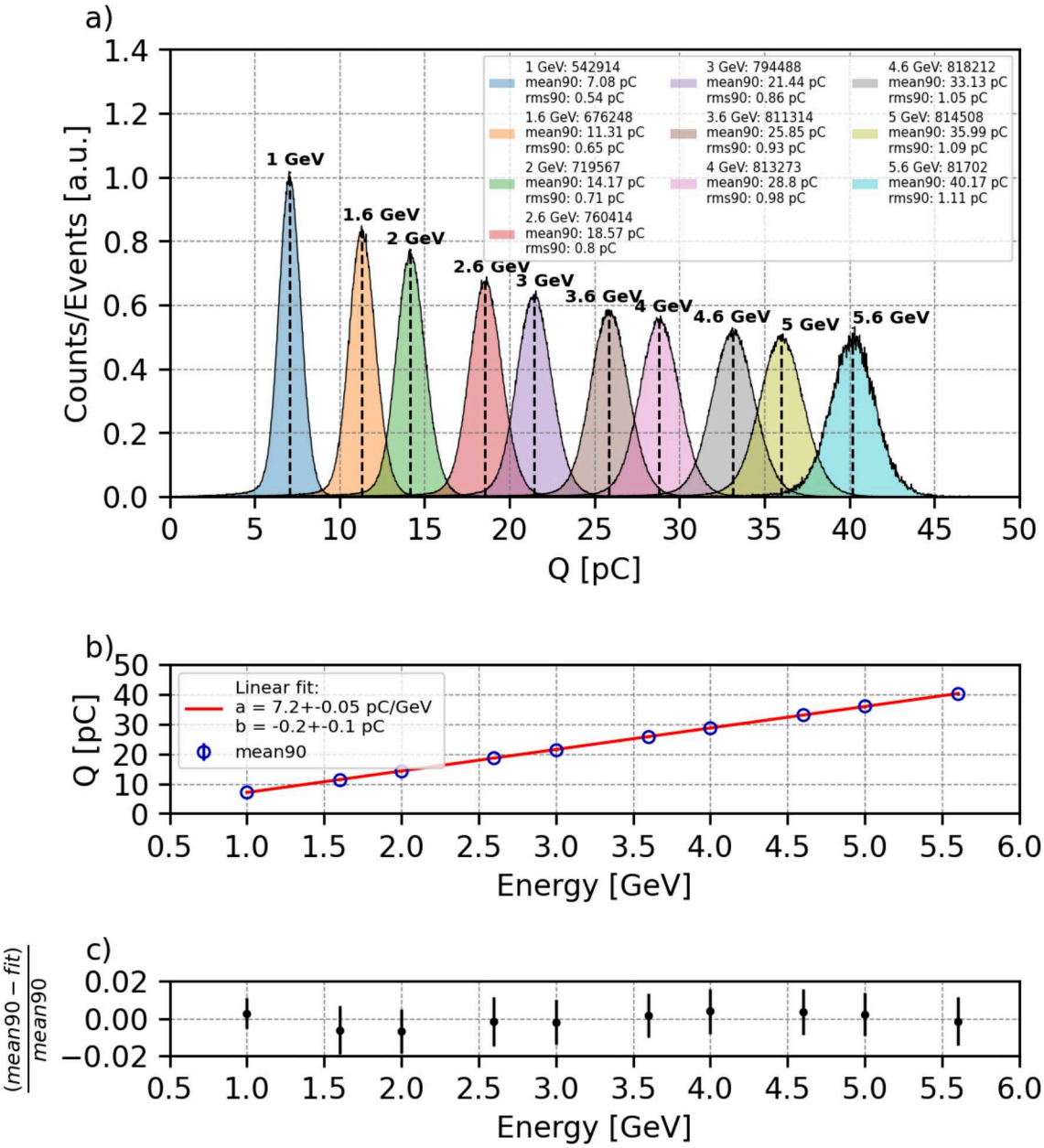

Figure 6.22.: a) Distributions of the calibrated calorimeter signal for each incident electron energy. b) *mean*90 of the signal distributions in a) as a function of the electron energy, with a linear fit shown in red. c) Relative deviation from the linear fit.

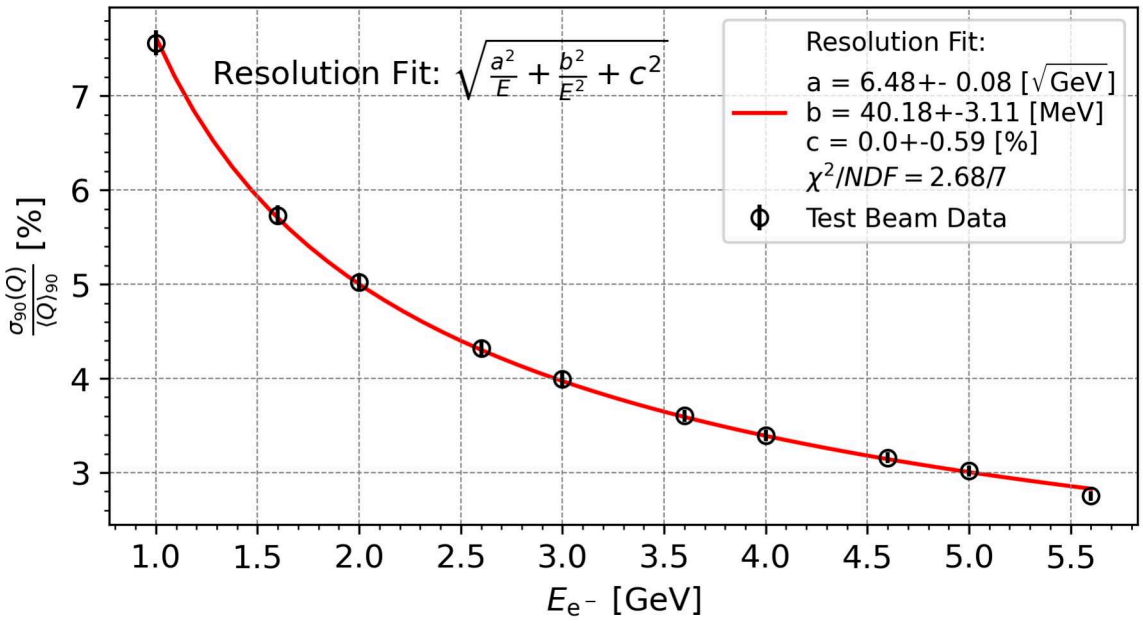

Figure 6.23.: Experimental data of the calorimeter resolution for single electrons from 1 GeV to 5.6 GeV, along with the parameterized resolution fit shown in red.

6.4. Benchmarking the Simulation with the Test Beam Data

To effectively compare simulation data with subsequent experiments, it is crucial to translate the simulated calorimeter signal into the actual physical signal measured by the calorimeter, referred to as the digitized signal. This is achieved by benchmarking the calorimeter simulation against test beam data to derive a transfer function which can then be used to simulate the digitized calorimeter response.
The benchmarking process consists of two main steps. Firstly, the simulated signal E_{ct} which is the deposited energy of charged particles above the Cherenkov threshold as defined in Sec. 6.2.2, is translated into the physical calorimeter signal Q which is a charge value measured in pC. Secondly, the discrepancies between the simulated and real data distributions are identified and quantified. Those discrepancies may be caused by additional statistical fluctuations in Cherenkov light production, the quantum efficiency of the PMTs, and electronic noise from the PMTs and the readout electronics which are not accounted for in the simulation. By comparing the simulation data with the test beam results, these factors can be accounted for, thereby improving the accuracy of the simulated digitized calorimeter response.

6.4.1. Simulation of the Test Beam Setup

For simulating the test beam setup (see Fig 6.15), the beamline of the test beam was included in the `leap_sims` simulation framework, incorporating the telescope and the scintillator trigger fingers. The telescope is modeled as six planes of 0.5 mm thick silicon discs, while the trigger fingers are represented as a 10 mm thick cube of plastic scintillator material positioned along the beam path. A visualization of the simulation geometry is shown in Fig. 6.24. In the simulation, the telescope and scintillator fingers are treated as dummy materials to introduce additional scattering, replicating the test beam conditions.

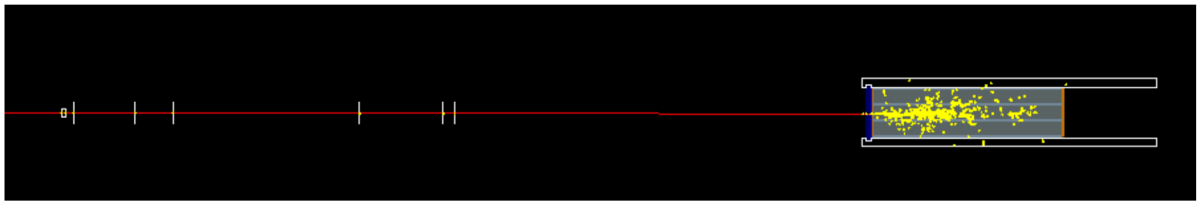

Figure 6.24.: Geometry of the test beam simulation, incorporating the calorimeter, six telescope planes, and scintillator trigger fingers.

For the simulation, a single electron particle gun is positioned at the location of the test beam collimator, 3.7 m upstream of the calorimeter entrance surface, with a square flat beam profile distribution of 8x8 mm^2, corresponding to the collimator opening. The simulation cover electron energies ranging from 1 GeV to 5.6 GeV.
The calorimeter test beam was conducted in test beam area T24, where the exact energy spread of the mono-energetic electrons was not measured. However, the energy spread of test beam area T21 is known to be 158 ± 6 MeV [74], remaining constant across the entire energy range. According to the test beam coordinators [private communication, M. Stanitzki], the energy spread in T24 is expected to be roughly half of that, approximately 80 MeV, and similarly constant over the entire range.
In Fig. 6.25, the simulated calorimeter signal is shown for beam energy spreads of $\sigma_{E,\text{beam}} = 0$ MeV a), 80 MeV b), and 158 MeV c). For each energy setting, one million events were simulated to match the statistics of the actual data. The distributions are normalized to the total number of events to facilitate comparison.
Recalling the discussion on calorimeter energy resolution (see Sec. 2.4.1), the width of the calorimeter signal distribution follows: $\sigma_{\text{calo}} \propto a \cdot \sqrt{E} \oplus b$, where the $\sqrt{E}$ term arises from intrinsic fluctuations in the electromagnetic shower, while the b term represents an energy-independent broadening originating, e.g., from electronic noise. In the case

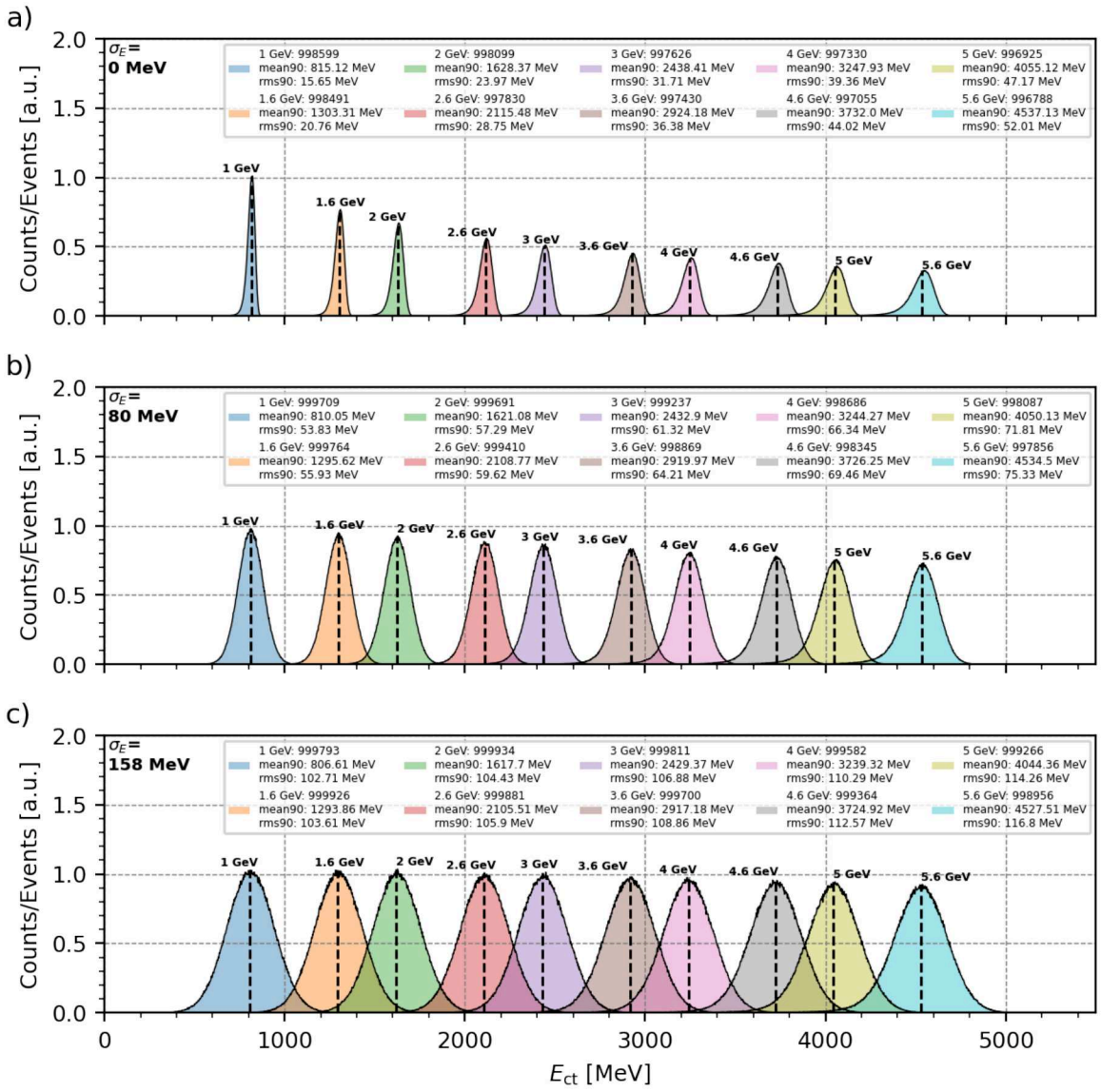

Figure 6.25.: Results of the test beam simulation for electron energies from 1 GeV to 5.6 GeV. The distributions of E_{ct} are shown for beam energy spreads of $\sigma_{E,\text{beam}} = 0$ MeV a), 80 MeV b), and 158 MeV c).

of the test beam data, the b term also includes contributions from the intrinsic energy spread of the test beam itself. The small c term, which becomes dominant only at higher energies, is neglected here.

Looking at the simulation results for $\sigma_{E,\text{beam}} = 0$ MeV (Fig. 6.25 a)), the absence of an initial beam energy spread as well as electronic noise means that the width of the distribution is primarily determined by intrinsic shower fluctuations. As expected from the $\sqrt{E}$ scaling, the absolute width σ_{calo} increases with energy, leading to broader

distributions at higher energies. In the chosen representation, this also causes the peak height to decrease with increasing energy.
When the beam energy spread is set to $\sigma_{E,\text{beam}} = 80$ MeV (Fig. 6.25 b)), the overall width of the signal distribution increases only slightly with beam energy and the height of the distributions decreases only marginally. This indicates that the beam energy spread overshadows the intrinsic shower fluctuations, reducing the relative impact of the energy-dependent broadening seen in panel a).
For $\sigma_{E,\text{beam}} = 158\,\text{MeV}$ (Fig. 6.25 c)), the overall width of the signal distribution remains relatively constant across different energies and the height of the distributions does not change significantly. This suggests that the broadening is now almost entirely determined by the beam energy spread, with only a minor contribution from shower fluctuations.
Comparing these results to the test beam data (see Fig.6.22), it is evident that the data is primarily governed by the $\sqrt{E}$ term. The absolute width increases with energy while the peak height decreases which is most comparable to the simulation without an applied beam energy spread.
Furthermore, when examining the fitted energy resolution (see Fig. 6.23), the extracted b term is found to be approximately 40 MeV. This broadening arises from a combination of the beam energy spread and electronic noise which suggests that the beam energy spread alone is unlikely to exceed this value, as assumed above. Additionally, since both the beam energy spread and electronic noise contribute to the overall broadening in an energy-independent way, it is impossible to separate their individual effects. As the exact beam energy spread in T24 is unknown and cannot be directly measured within the scope of this thesis, it will be neglected in the following discussion.
To benchmark the calorimeter simulation, the simulated signal E_{ct} (defined in Sec. 6.2.2) will be translated into the physical calorimeter signal Q, and the additional broadening of the digitized signal will be estimated by comparing the test beam data to simulations without an applied beam energy spread. This approach suggests that the energy spread of T24 is small compared to noise and other sources of broadening in the digitization process. In the worst case, this leads to an overestimation of the contributions caused, for example, by electronic noise from the calorimeter system itself, resulting in a more conservative estimate of the calorimeter's energy resolution. The details of this benchmarking process will be elaborated in the following sections.

6.4.2. Absolute Calibration

As previously mentioned, the test beam simulation assumed single mono-energetic electron beams without energy spread, which are compared to the actual experimental data. The results are depicted in Fig. 6.25 a), showing distributions for various electron energies with their respective mean values marked by dashed lines. The linear scaling of the simulated calorimeter signal E_{ct} with respect to beam energy, alongside the linear relationship between calorimeter signal and electron energy derived from the test beam data (see Fig. 6.22), forms the basis for translating the E_{ct} signal into the physical calorimeter signal Q [pC]. As the calorimeter signal depends on the applied

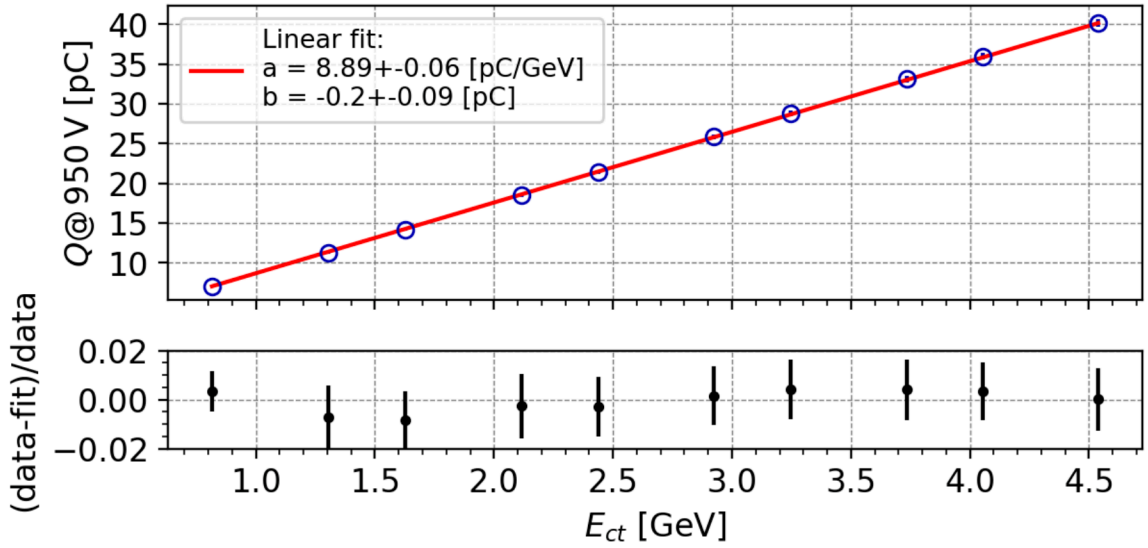

Figure 6.26.: Calibrated calorimeter signal Q as a function of the simulated calorimeter signal E_{ct}. A linear fit is shown in red. The lower section of the graph displays the relative deviation from the linear fit.

PMT voltage, the conversion is based on the default calibration, where the calorimeter signal is referenced to channel 4 at a PMT voltage of 950 V. Figure 6.26 illustrates the linear relation between E_{ct} and the measured calorimeter signal Q. The linear fit of the data, shown in red, indicates a negligible deviation of less than 1 %, as depicted in the lower plot of the figure. The obtained fit parameters, a and b, allow for the conversion of E_{ct} into a physical calorimeter signal Q:

$$Q[\mathrm{pC}] = (8.89 \pm 0.06) \left[\frac{\mathrm{pC}}{\mathrm{GeV}}\right] \cdot E_{\mathrm{ct}}[\mathrm{GeV}] - (0.2 \pm 0.09)[\mathrm{pC}] \tag{6.11}$$

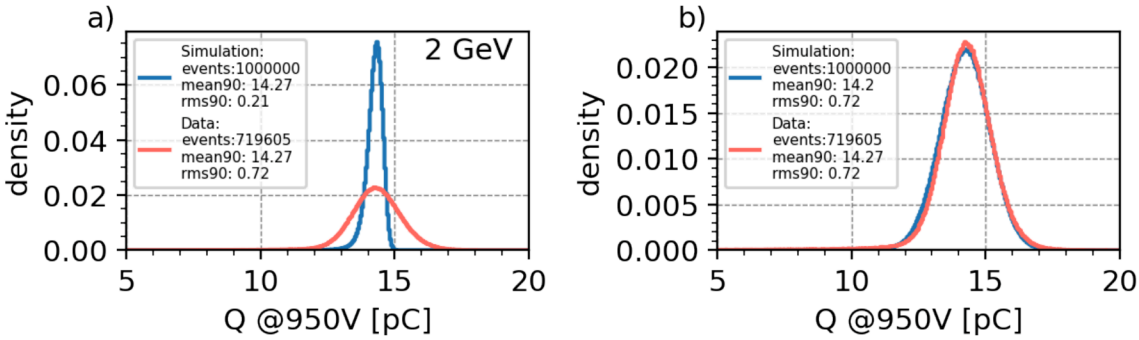

Figure 6.27.: Calibrated calorimeter signal for 2 GeV electrons, alongside the translated simulated distribution a) and the full digitized simulated calorimeter signal b).

6.4.3. Additional Broadening

Figure 6.27 a) displays the calibrated calorimeter signal Q for 2 GeV incident electrons (red histogram) alongside the test beam simulation, converted to pC using Eq. 6.11 (blue histogram). It is apparent that the simulation does not adequately replicate the width of the measured distributions. This discrepancy arises because the simulation stops at the deposited energy of charged particles above the Cherenkov threshold without accounting for additional statistical fluctuations due to Cherenkov light production, the quantum efficiency of the PMTs, and electronic noise which would naturally broaden the distributions. Within the scope of this thesis, the additional contributions from the signal chain, spanning from the deposited energy to the digitized signal, will be assessed by comparing the simulation to the test beam data. This comparison will be discussed in the following sections.
In Fig. 6.28 a), the calorimeter energy resolution, $\frac{\sigma_{90}}{\langle E \rangle_{90}}$, is illustrated for both the test beam data and the simulated calorimeter signal, E_{ct}, covering incident electron energies from 1.6 GeV to 5.6 GeV. Here, σ_{90} and $\langle E \rangle_{90}$ correspond to the $rms90$ and $mean90$ of their respective distributions. As expected, the simulation exhibits a superior energy resolution across the tested energy range, as it does not include noise or additional statistical fluctuations from the digitization chain. To account for this discrepancy, an additional contribution to the width of the distributions, denoted as σ_{diff}, is introduced. This term quantifies the difference between the simplified simulation and the experimental data which must be added in quadrature.

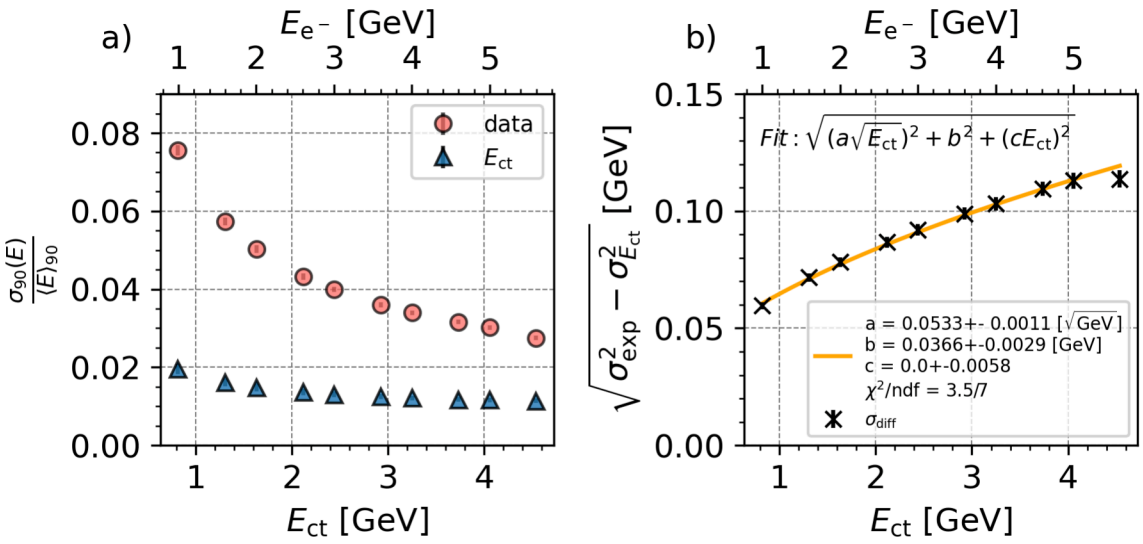

Figure 6.28.: a) Comparison of the experimental and simulated calorimeter energy resolution for incident electron energies from 1 GeV to 5.6 GeV. b) Difference in distribution widths between simulation and test beam data, along with a parameterized resolution fit.

The resulting width, denoted as $\sigma_{\text{digitized}}$, is given by:

$$\sigma^2_{\text{digitized}} = \sigma^2_{E_{ct}} + \sigma^2_{\text{diff}} \tag{6.12}$$

where $\sigma_{E_{ct}}$ represents the intrinsic width of the simulated calorimeter signal, and σ_{diff} accounts for the additional broadening due to discrepancies between the simulation and experimental data. The latter is formulated in Eq. 6.13:

$$\sigma^2_{\text{diff}} = \sigma^2_{\text{exp}} - \sigma^2_{E_{ct}} \tag{6.13}$$

In the context of calorimeter energy resolution, described by Eq. 2.18, σ_{diff} can be parameterized using the coefficients a, b, and c, as expressed in Eq. 6.14:

$$\sigma_{\text{diff}} = \sqrt{\sigma^2_{\text{exp}} - \sigma^2_{E_{ct}}} = \sqrt{(a \cdot \sqrt{E_{ct}})^2 + b^2 + (c \cdot E_{ct})^2} \tag{6.14}$$

Here, a corresponds to the stochastic term, b to the noise term caused by readout electronics, and c to a constant term influenced by factors such as inhomogeneities as well as imperfections in the calorimeter construction.

In Fig. 6.28 b), the σ_{diff} retrieved from the data and the simulation is depicted alongside the fit from Eq. 6.14 which aligns well with the data. As expected, the fit is primarily influenced by the parameters a and b, representing additional stochastic fluctuations and electronic noise that are not accounted for in the simulation. The retrieved fit, along with Eq. 6.12, will be utilized to transition from the simple simulation based on E_{ct} to the level of the digitized signal, facilitating comparison with the actual calorimeter signal.
The translation of a simulated signal E_{ct} to the digitized physical calorimeter signal Q [pC] is briefly outlined as follows: First, the corresponding additional width σ_{diff} is calculated using Eq. 6.14. Subsequently, a random number is drawn from a normal distribution with a mean of E_{ct} and a standard deviation of $\sigma = 1.25 \cdot \sigma_{\text{diff}}$ which will replace the initial E_{ct} value. The factor of 1.25 stems from the fact that the calculations of σ_{diff} are based on $rms90$ values and $\sigma \approx 1.25 \cdot rms90$. The adjusted value of E_{ct} is then translated to the calorimeter signal Q using Eq. 6.11.
In Fig. 6.27 b), the digitized calorimeter signal obtained using this method is shown for the exemplary 2 GeV test beam simulation (blue), demonstrating good agreement with the corresponding distribution from the test beam data (red).

6.5. Calorimeter Suitability for LEAP

This section will explore the performance of the LEAP calorimeter based on simulations incorporating the expected beam parameters of the LEAP experiment. In particular, the expected energy resolution of the calorimeter will be extrapolated to the TeV energy regime, created by multiple MeV, using simulations benchmarked with test beam data. Furthermore, the influence of a potentially non-linear detector response in the low-MeV range – expected due to the Cherenkov threshold of the calorimeter – on the analyzing power and the observed asymmetry, as they would be measured with the LEAP polarimeter, will be evaluated through simulations.

6.5.1. Extrapolated Energy Resolution

Figure 6.29 shows the energy resolution, $\frac{\sigma_{90}}{\langle E \rangle_{90}}$, of the calorimeter, as determined from test beam data of single electrons ranging from 1 GeV to 5.6 GeV, depicted with black circles. Simulation results for mono-energetic single electrons, obtained using the

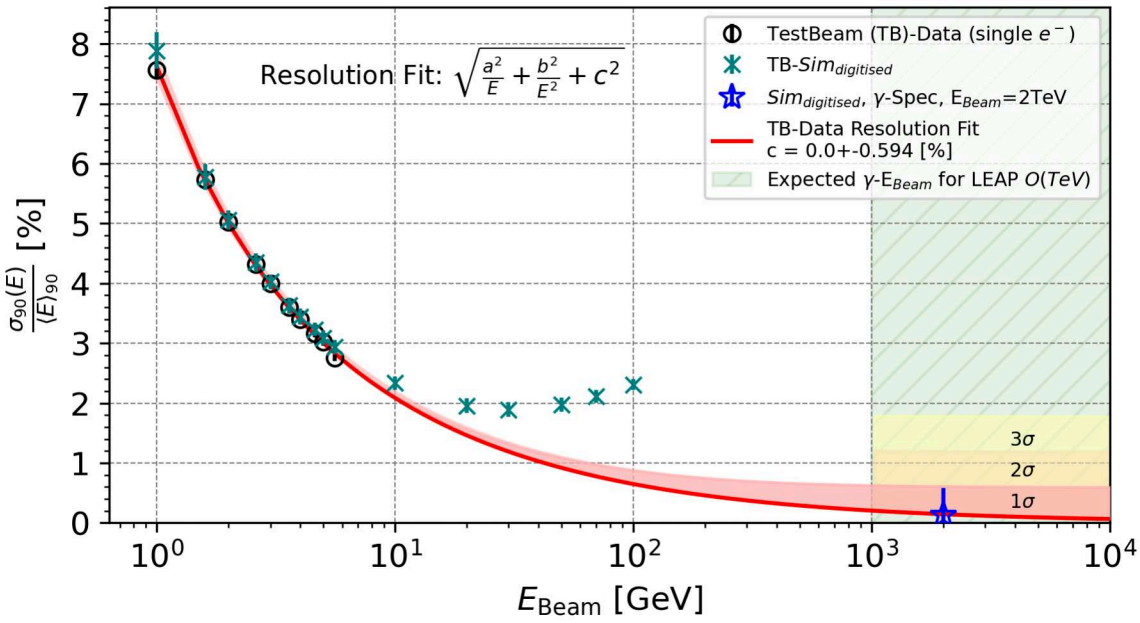

Figure 6.29.: Extrapolation of calorimeter energy resolution to the TeV energy regime expected for LEAP. The test beam data (black circles) is shown along with the digitized test beam simulation (cyan crosses) and the simulated energy resolution for a photon spectrum originating from a 30 MeV electron beam (cf. Fig. 6.30), with a total energy of 2 TeV (blue star). The test beam data is accompanied by a parameterized energy resolution fit (red) extrapolated to TeV energies. The red, orange, and yellow bands represent the 1σ, 2σ, and 3σ error bands of the fit, respectively.

`leap_sims` simulation tool, are shown as cyan crosses. These simulations correspond to the simulated digitized calorimeter signal described in the previous section. The results indicate that the calorimeter's resolution starts to degrade for single-electron energies above 30 GeV which can be attributed to noticeable longitudinal shower energy leakage at these high energies.

For the LEAP project, detecting single high-energy particles is unnecessary. Instead, numerous low-energy (< 100 MeV) photons are expected to contribute to a high total energy beam in the TeV range. For those low photon energies longitudinal shower leakage will not be a significant issue. Although the calorimeter could not be tested under these specific experimental conditions, the energy resolution in the TeV regime for low-energy photon beams, where energy leakage can be neglected, can be estimated by extrapolating the parameterized energy resolution fit from the test beam data and detailed `GEANT4` simulations. In the energy range of the test beam data (1-5.6 GeV), longitudinal leakage is assumed to be negligible.

The fit of the energy resolution, given by Eq. 2.18, is depicted in red and extrapolated to the TeV energy range. In the relevant high-energy regime, the noise and stochastic contributions to the energy resolution are negligible, with the constant term and its associated error dominating. This constant term is determined to be $c = 0.0 \pm 0.6\,\%$. The 1σ error band, resulting from the fit uncertainty, is shown as a light red band, while the 2σ and 3σ error bands for energies greater than 1 TeV are shown as orange and yellow bands, respectively. The simulation results for a photon transmission spectrum originating from a 30 MeV electron beam, qualitatively similar to the one shown in Fig. 6.30, with a total energy of 2 TeV are shown as a blue star. This result shows good agreement with the extrapolated energy resolution based on the test beam data.
Since the precise energy resolution for the desired LEAP beam parameters in the TeV regime cannot be verified with experimental data within the scope of this thesis, a conservative estimate is provided. Based on the extrapolated experimental data, the calorimeter energy resolution is constrained to $\frac{\sigma_{90}}{\langle E \rangle}(\mathrm{TeV}) < 2\,\%$ within a three-sigma confidence interval, establishing an upper bound on the actual resolution. Notably, even with this conservative estimate, the calorimeter meets the required energy resolution of $< 2\,\%$ at TeV-scale total energies for the LEAP project, as introduced in Sec. 3.3.3.

6.5.2. Influence of the Detector Response on the Asymmetry and Analyzing Power

As detailed in Sec. 3.2, the polarization measurement relies on the linear scaling of the photon transmission asymmetry, δ, with the initial electron polarization, expressed as $\delta = A \cdot P_{e^-}^{Fe} \cdot P_{e^-}$, where A denotes the analyzing power and $P_{e^-}^{Fe}$ is the polarization of the electrons in the iron absorber. This section investigates this relation and the influence of the detector response using the `leap_sims` simulation tool.
The basic geometry of the polarimeter simulation used in this section is shown in Fig. 7.2. The energy spectrum of the transmitted photons through the iron absorber of the solenoid magnet, for approximately 1000 electron bunches – each containing 10^5 electrons with an energy of 30 MeV and a longitudinal polarization of $P_{e^-} = 1$ – is shown in Fig. 6.30. The cases where the initial electron polarization is parallel and antiparallel to the polarization of the electrons in the iron are shown in blue and red, respectively. The polarization of the electrons in the iron, $P_{e^-}^{Fe}$, is set to ± 1. The spectra

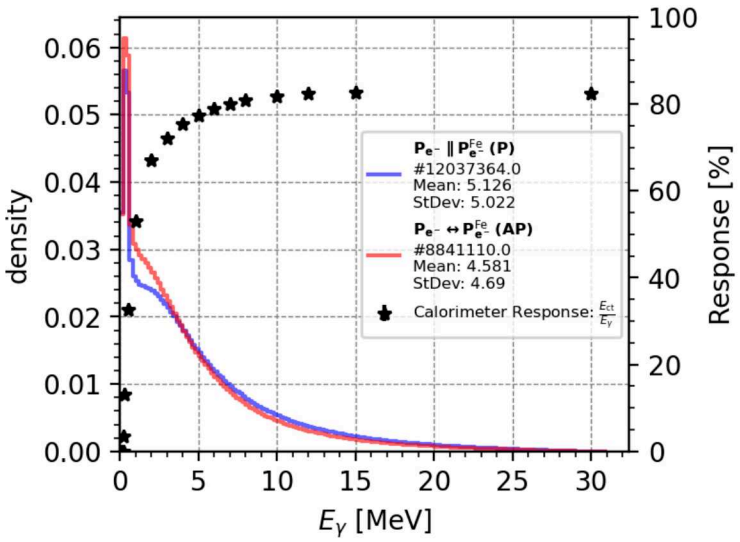

Figure 6.30.: Simulated spectral density of photons transmitted through the 150 mm iron absorber of the LEAP solenoid magnet for a 30 MeV electron beam with $P_{e^-} = 1$. The red and blue spectra represent the cases where the polarization of the beam electrons and the electrons in the iron absorber, $P^{Fe}_{e^-} = \pm 1$, are parallel and antiparallel, respectively. The simulated energy response of the calorimeter is illustrated by black stars.

are detected at the virtual front detector of the calorimeter (see Fig. 6.10), located 9 cm downstream of the solenoid magnet. For simplicity, the simulations were conducted in a vacuum to minimize additional fluctuations due to scattering in air.
Comparing the spectral density for the parallel and antiparallel cases reveals differences not only in the total number of transmitted photons but also in the spectral shape. The simulated detector response as a function of photon energy (see Sec. 6.2.3) is overlaid as black stars in the figure. Since this response varies across the spectrum and the spectral shape changes, it may influence the transmission asymmetry, δ. With the polarization measurement in mind, the most important aspect to verify is the linear relation between the transmission asymmetry and both the initial electron polarization, P_{e^-}, and the polarization of the iron electrons, $\pm P^{Fe}_{e^-}$. This linearity is crucial for the Compton transmission polarimetry method and will be examined in the following.
Figure 6.31 a) shows the simulated asymmetry, calculated over 1000 electron bunches, as a function of the initial electron polarization P_{e^-}. Here, $P^{Fe}_{e^-}$ was set to 1. The asymmetry is calculated for two cases: for the perfect detector with a constant energy response (black rectangles), which is derived from the total photon energy sum E^{sum}_γ detected in the virtual calorimeter front detector, and for the case considering the

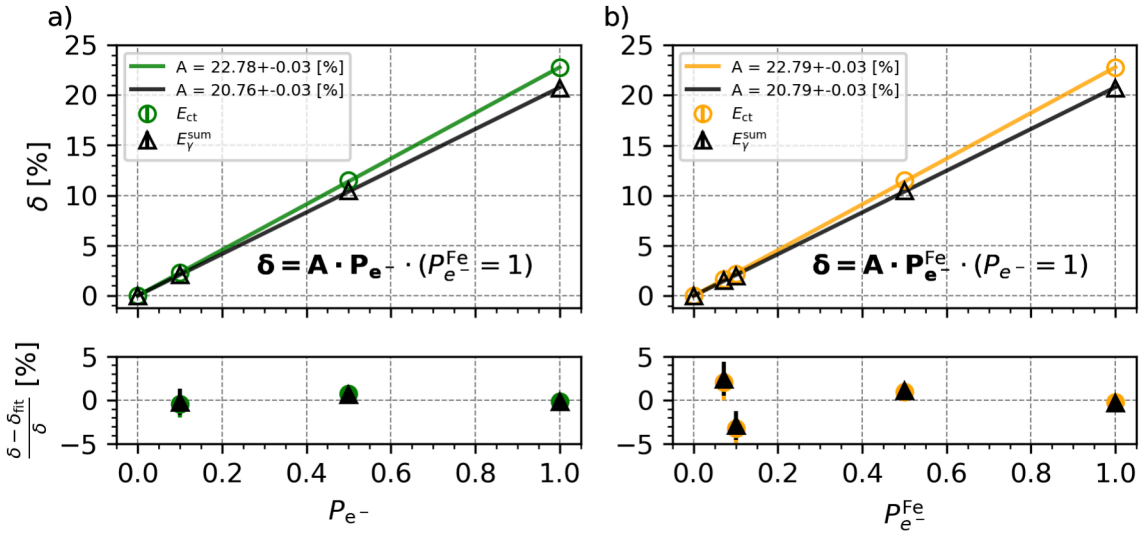

Figure 6.31.: a) Simulated transmission asymmetry δ with respect to the initial electron polarization P_{e^-} of an idealized 30 MeV electron bunch for a 150 mm magnetized iron absorber with $\pm P_{e^-}^{Fe} = 1$. The asymmetry δ is calculated using the calorimeter signal Ect (defined in Sec. 6.2.2), which accounts for the calorimeter's energy response, represented by green circles. Additionally, the asymmetry calculated using the transmitted photon energy sum E_γ^{sum} is shown with black triangles, representing the asymmetry assuming an ideal detector with a constant energy response. The data is fitted with a linear fit. b) Same as a), but the simulated transmission asymmetry with respect to the polarization of the iron electrons $\pm P_{e^-}^{Fe}$ ($P_{e^-} = 1$) is depicted as orange circles.

calorimeter's energy response (green circles), calculated from the calorimeter signal E_{ct}, which takes the Cherenkov production threshold into account and is defined in Sec. 6.2.2. For both cases, the asymmetries scale linearly with P_{e^-}, as indicated by the respective linear fits. The same linear relation between δ and $P_{e^-}^{Fe}$ was found by holding P_{e^-} constant at 1, as displayed in Fig. 6.31 b).

This demonstrates that the non-uniform calorimeter energy response does not affect the polarization measurement. Furthermore, as expected, the simulation shows no difference in the measurement when either the polarization of the electrons or the polarization of the electrons in the iron core is changed.

For the simulations shown in Fig. 6.31a), the initial electron polarization P_{e^-} was kept at 1 and in panel b), the polarization of the iron electrons $|P_{e^-}^{Fe}|$ was fixed at 1. Therefore, the slope of the linear fits yields the analyzing power A of the system, which, in the case of E_{ct}, is approximately 2 % higher compared to the ideal detector case. This increase is due to the stronger suppression of differences in the spectral shape of the

transmission spectra for gamma energies below approximately 10 MeV. The resulting increase in asymmetry can actually be beneficial for the polarization measurement, as it indicates a greater separation of the calorimeter signals for the parallel (P) and antiparallel (AP) cases.
In this thesis, the precise energy response of the calorimeter to MeV photons could not be directly measured and was instead inferred using GEANT4 simulations. These simulations are inherently sensitive to the choice of physics list, as illustrated in Fig. 6.13. This dependency introduces an uncertainty in the determination of the analyzing power of the polarimeter which must be quantified. To address this, the impact of small variations in the detector response – particularly in the low-energy regime (< 10 MeV), where nonlinear behavior is observed – on the analyzing power is investigated in the following.

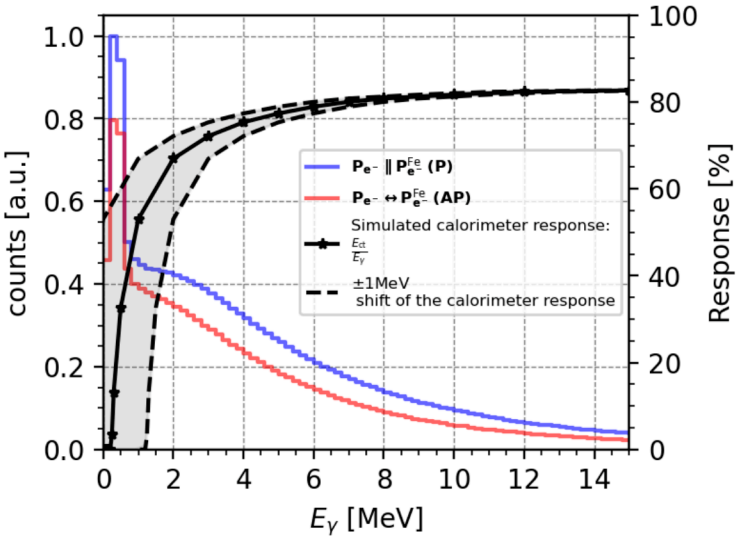

Figure 6.32.: Simulated photon transmission spectra through the 150 mm iron absorber for a 30 MeV electron beam with $P_{e^-} = 1$. The red and blue spectra represent the cases where the polarization of the electrons and the electrons in the iron absorber ($P_{e^-}^{Fe} = \pm 1$) are parallel and antiparallel, respectively. The simulated energy response of the calorimeter is illustrated by the solid black curve. Small variations in the calorimeter response are introduced by shifting the response curve by ± 1 MeV, indicated by the black dashed lines.

The effect on the analyzing power is expected to be most significant at low initial electron energies due to the non-uniform response of the detector in the low-energy range. Therefore, the influence is examined starting with an initial electron energy of 30 MeV – the lowest expected electron energy for LEAP – using the simulated trans-

mission spectra introduced earlier (see Fig. 6.30). Furthermore, small variations in the simulated detector response, based on the standard physics list `PhysListEMPolarized`, are introduced by shifting the response curve by $\pm 1\,\mathrm{MeV}$ along the energy axis.
In Fig. 6.32, the simulated transmission spectra for the aforementioned 30 MeV electron beam are presented for both cases where the electron polarization is parallel (blue histogram, P) and antiparallel (red histogram, AP) to the polarization of the electrons in the iron core. The simulated detector response is overlaid as a solid black line, while the shifted responses are shown as dashed black lines. The analyzing power is computed for all three detector responses by weighting the two transmission spectra (parallel and antiparallel) with the respective energy-dependent detector response. The integrals of these weighted spectra are used to calculate the asymmetry and, consequently, the analyzing power, since $|P_{e^-}| = |P_{e^-}^{Fe}| = 1$, using Eq. 3.9.
For the unshifted response, the analyzing power is calculated to be $A = 21.17\,\%$. For the positively shifted response, $A_{+1\mathrm{MeV}} = 21.67\,\%$, and for the negatively shifted response, $A_{-1\mathrm{MeV}} = 21.01\,\%$. The relative deviation from the nominal analyzing power is determined using the expression $\frac{\Delta A_{\pm 1\mathrm{MeV}}}{A} = \frac{|A - A_{\pm 1\mathrm{MeV}}|}{A}$. This results in relative deviations of $\frac{\Delta A_{+1\mathrm{MeV}}}{A} = 2.17\,\%$ and $\frac{\Delta A_{-1\mathrm{MeV}}}{A} = 0.94\,\%$.
Performing the same analysis for an initial electron energy of 80 MeV – around the actual mean energy during the initial polarimeter commissioning (see Cap. 7) – yields a relative deviation of the analyzing power of $\frac{\Delta A_{+1\mathrm{MeV}}}{A} = 1.48\,\%$ and $\frac{\Delta A_{-1\mathrm{MeV}}}{A} = 0.74\,\%$. As expected, the deviation decreases with increasing initial electron energy, reflecting the nonlinear behavior of the detector response in the low-energy regime.
Based on this analysis, and considering the unknown exact response of the calorimeter, the resulting relative uncertainty in the analyzing power is conservatively estimated to be on the order of 1.5 % to 2.2 % for electron energies of 80 MeV to 30 MeV, respectively. The determination of the response curve of the calorimeter for low-energy photons should be addressed in future studies in order to provide a more accurate estimation of the uncertainties affecting the determination of the analyzing power and, consequently, the polarization measurement.

Chapter 7.

Commissioning of the LEAP Polarimeter

This chapter focuses on the commissioning of the LEAP polarimeter system at the FLARE facility (see Sec. 4.2) through a polarization measurement (see Sec. 3.2) using an unpolarized laser-plasma accelerator (LPA) electron source. Although the generation of polarized electron beams has not yet been achieved, this zero-polarization measurement provides crucial insights into the system's behavior, measurement uncertainties, and systematic effects. These findings will inform future improvements to the polarimeter, beam diagnostics, and the LPA setup for upcoming polarization measurements.

The LPA experiment setup at FLARE is not a turnkey system; rather, it is an evolving platform that undergoes continuous upgrades and modifications to support cutting-edge research. Factors such as laser properties, timing, alignment, and gas target parameters all influence the performance of the LPA system. However, the optimization of the LPA electron beam itself is outside the scope of this thesis. Instead, the focus is on the performance of the polarimeter system, the measurement procedures, and the interplay of diagnostics, all of which are tested using a consistently optimized LPA electron beam provided by Martin Meisel, an expert from the DESY MPA group. Performing an asymmetry measurement with unpolarized electron beams allows the identification of systematic errors that arise due to changes in experimental conditions between the periods during which the asymmetry is calculated. The primary goal of this commissioning process is to evaluate the precision of the asymmetry measurement under the given experimental conditions. Key beam parameters, such as energy and charge and their stability, are studied to estimate the associated measurement errors.

Additionally, the retrieval of electron polarization from asymmetry measurements requires a well-understood analyzing power of the polarimeter system. This chapter also reviews the uncertainties in analyzing power that stem from the retrieved beam conditions and the properties of the polarimeter setup. Furthermore, the polarization result will be discussed, along with estimations for real polarization measurements.

7.1. The LEAP Polarimeter Setup

In this section, the LEAP polarimeter, as set up in the BOND laboratory at the FLAIR facility (see Sec. 4.2), is presented.

7.1.1. Polarimeter Components

The LEAP polarimeter, installed in the beamline of the LPA at the FLARE facility, consists primarily of two main components: an iron-core solenoid magnet and the LEAP lead glass calorimeter, which has been described in detail in Chap. 6.

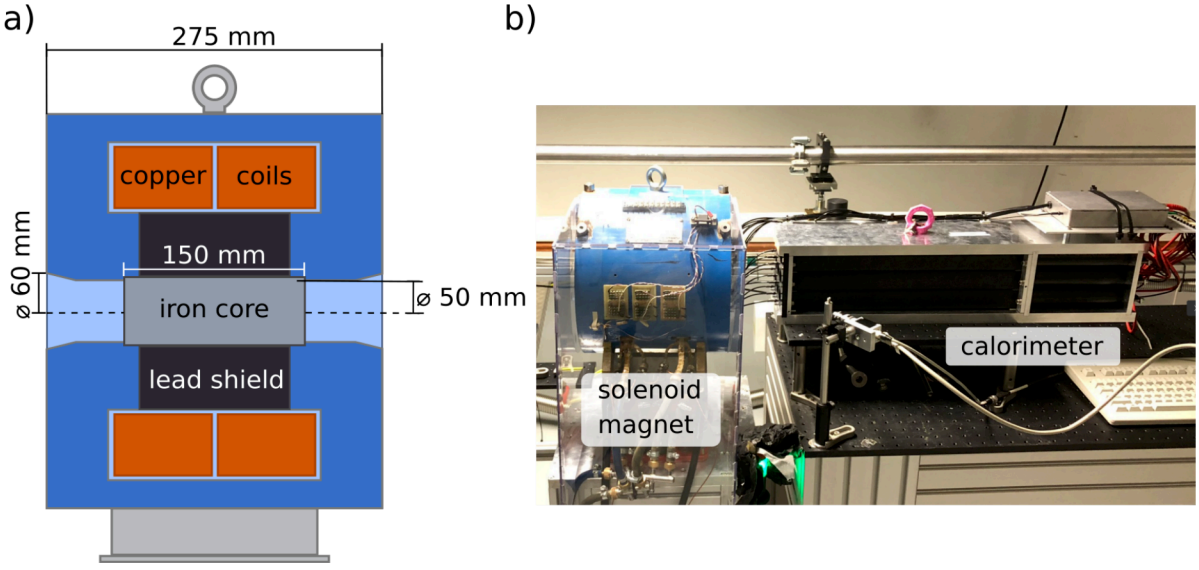

Figure 7.1.: a) Sketch of the solenoid cross-section (adapted from [34]). b) Photograph of the polarimeter setup, incorporating the analyzing solenoid magnet and the LEAP lead glass calorimeter.

A photograph of the polarimeter setup is shown in Fig. 7.1 b). The solenoid magnet used here is a remnant from the E166 experiment [66], where it was employed as a

photon analyzer. Detailed specifications of the magnet, as provided by [66], are listed in Tab. A.2. A sketch of the magnet cross-section is presented in Fig. 3.3 a), illustrating its dimensions. The magnet features a cylindrical iron core with a diameter 50 mm and a length of $L = 150$ mm. The magnet operation current is ± 60 A. The magnetic field was measured during the E166 experiment using several pickup coils surrounding the iron core. The central magnetic field $B_z^{\max}$ was reported to be 2.165 T, with a relative measurement error of 1 %. The average on-axis magnetic field over the entire core length L, $\langle B_z \rangle = 2.040$ T, was modeled using the OPERA-2d code [144]. The electron polarization is reported as $P_{e^-}^{\text{Fe}} = 0.0723 \pm 0.0015$. This polarization was calculated using the equation $P_{e^-}^{\text{Fe}} = 0.03727 \langle B[T] - B_0[T] \rangle$ (Eq. 3.2), where B_0, the magnetic field from the coil current without the iron core, is assumed to be approximately 5 % of B. This reported value of the iron core polarization will be used in this thesis, as the measurement of the magnetic field and the subsequent simulations are beyond its scope, but may be addressed in future studies.

7.1.2. LEAP Polarimeter Simulations using `leap_sims`

In this section, the `leap_sims` (see Sec. 4.5) polarimeter simulations used throughout the chapter will be presented, with a particular focus on the geometry of the polarimeter as implemented in `GEANT4`. Additionally, the performance of the polarimeter will be discussed for both idealized unpolarized and polarized electron beams.

Basic Geometry of the Polarimeter in `leap_sims`

The geometry of the polarimeter, as implemented in `GEANT4`, is shown in Fig. 7.2. It consists of two main components: the solenoid magnet which incorporates an iron yoke, copper coils (modelled as solid copper bulk) and a 150 mm long cylindrical iron core with a diameter of 50 mm (see Fig 7.1 a)), and the LEAP calorimeter which is made up of nine TF1 lead glass crystals housed in an aluminum structure with a PEEK plastic front plate, as introduced earlier in Sec. 6.2.1. In the simulation, the particle gun is typically positioned just before the solenoid entrance, allowing the beam parameters to be set in accordance with the experimental conditions. When the polarimeter simulations are referenced throughout this chapter, further details, such as the particle gun configuration and other specific simulation parameters, will be explained in the relevant sections.

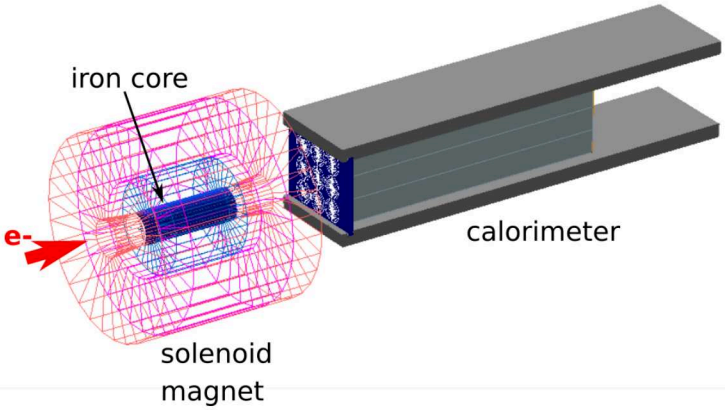

Figure 7.2.: Basic geometry of the LEAP polarimeter as implemented in GEANT4.

Polarimeter Response to Unpolarized Beams

The polarimeter signal is essentially the calorimeter's output, measured by the QDC. In the simulation, the calorimeter signal is defined as E_{ct}, which represents the deposited energy from all charged particles with energy above the Cherenkov threshold, as introduced in Sec. 6.2.2. The signal measured by the calorimeter clearly depends on both the energy and total charge of the electron beam entering the solenoid. In the case of unpolarized beams, the solenoid functions as a simple piece of magnetized iron in the beam path.
When considering the beam charge, the calorimeter signal should, in principle, be proportional to the incident electron beam charge, assuming the system operates in a regime where the PMTs and other components do not saturate. This is because the transmission through the solenoid magnet is independent of the beam charge. However, this linear relationship does not necessarily hold for beam energy due to the energy dependence of cross-sections for electromagnetic processes such as Compton scattering, the photoelectric effect, and pair production (cf. Sec. 2.3.2 and Sec. 3.2.1). To investigate the scaling of the calorimeter signal with respect to the initial electron energy, simulations were conducted using monoenergetic, idealized, unpolarized electron beams with a fixed bunch charge of 0.08 pC (5×10^5 electrons). The simulation geometry closely resembled experimental conditions, with the calorimeter positioned 91 mm downstream of the solenoid magnet. In Figure 7.3, the calorimeter signal,E_{ct} , per electron is shown for incident electron energies ranging from 10 MeV to 150 MeV. Each data point corresponds to the mean value obtained from 1000 simulated bunches, normalized to the number of electrons per bunch. The results demonstrate that

the calorimeter signal does not scale strictly linearly with electron energy, which is expected due to energy-dependent transmission and the nonlinear response of the calorimeter at lower energy levels (see Sec. 6.2.3)

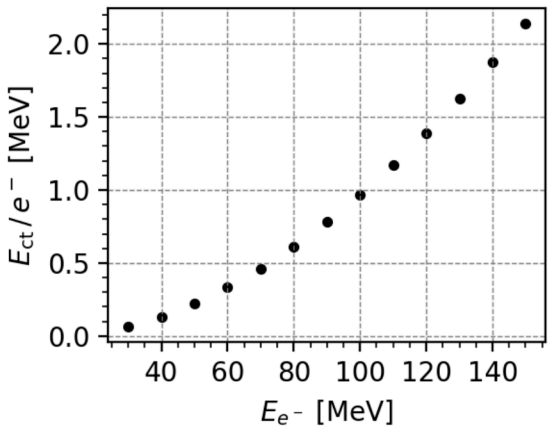

Figure 7.3.: Simulated calorimeter energy response to unpolarized electron beams incident at the solenoid entrance, generated using `leap_sims`. The simulations were performed with idealized monoenergetic beams, each having a fixed bunch charge of 5×10^5 electrons. Each data point represents the mean of 1000 simulated electron bunches, normalized to the number of electrons per bunch. The statistical errors are indicated but are too small to be visible in this representation.

Expected Asymmetries for polarized Beams

This section provides an initial estimate of the analyzing power of the LEAP polarimeter and the corresponding asymmetries expected for polarization measurements using idealized electron beams.

The analyzing power of the LEAP polarimeter for idealized monoenergetic beams in the energy range of 10 MeV to 190 MeV was simulated. For each electron energy, bunches with a fixed charge of 5×10^5 electrons and a polarization of $P_{e^-} = 1$ were modeled. The polarization of the electrons in the iron core was set to $P_{e^-}^{\mathrm{Fe}} = \pm 1$. The analyzing power was determined by calculating the asymmetry between simulations with opposite polarization settings of the iron core. For this calculation, the mean calorimeter signal (E_{ct}) was taken over 1000 simulated bunches for each iron core polarization setting. The resulting analyzing power as a function of electron energy is shown in Fig. 7.4 a) for initial electron energies ranging from 10 MeV to 190 MeV. Figure 7.4 b) displays the expected asymmetries for an initial electron polarization

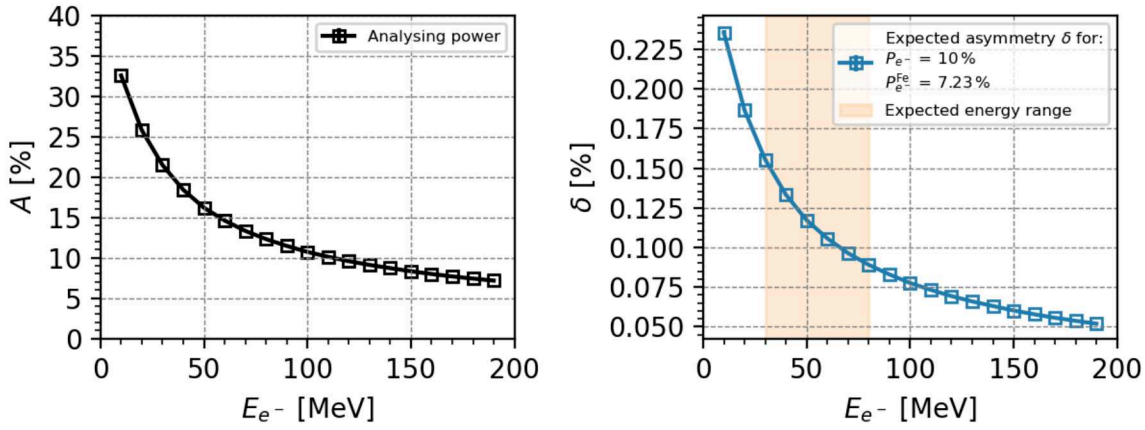

Figure 7.4.: a) Analyzing power for the LEAP polarimeter setup for idealized monoenergetic beams, simulated using `leap_sims`. b) Expected asymmetries for monoenergetic beams, an electron polarization of $P_{e^-} = 10\,\%$ and an iron core polarization of $P_{e^-}^{\mathrm{Fe}} = 7.23\,\%$. The orange band indicates the anticipated energy range for LEAP of 30 MeV to 80 MeV. The statistical errors are indicated but are too small to be visible in this representation.

of $P_{e^-} = 10\,\%$ and an iron core polarization of $P_{e^-}^{\mathrm{Fe}} = 7.23\,\%$. The asymmetries are calculated using the analyzing power from panel a) and Eq. 3.8.
This estimate reveals that, within the anticipated energy range for LEAP (30 MeV to 80 MeV, indicated by the orange band), asymmetries on the order of one per mille can be expected for an initial electron polarization of 10 %.

7.1.3. Calorimeter DAQ and Solenoid Slow Control

The high voltage required to power the calorimeter PMTs was supplied by the SY12 high voltage system, as detailed in Sec. 6.1.3. This system was connected to the DAQ PC via an RS-232 cable and controlled through the serial port. The signals from the calorimeter PMTs were transferred via LEMO cables to the 16-channel charge-sensitive analogue-to-digital converter (QDC) module V965 from CAEN [137] for digitization, as previously described in Sec. 6.1.4. The QDC was integrated into the control system framework DOOCS (cf. Sec. 4.2.3) and the data were saved within the FLARE Facility DAQ which enables the synchronization of all diagnostics based on a common shot number.
The power supply for the solenoid magnet was also integrated into DOOCS. The magnet current could be controlled via a DOOCS graphical user interface (JDDD, cf.

Sec. 4.2.3) panel. Additionally, the "Taskomat" software [145] was used to program a sequence that alternated the magnet polarity (magnet current) between negative and positive values with a specified period and amplitude, which could also be adjusted and controlled within the JDDD panel. In the experiment, a magnet cycle with a duration of approximately 5 min was used, with the magnet current alternating between $\pm$ 60 A. This means the magnet held a current of 60 A for 5 min, then ramped to -60 A and maintained this for 5 min, repeating this cycle. The ramping time from -60 A to 60 A took approximately 12.5 s. The magnet current was also recorded within the DAQ system.

7.2. Full Experimental Setup and Diagnostics

Figure 7.5 depicts an illustration of the experimental setup for commissioning the LEAP polarimeter through a zero polarization measurement at FLARE. The illustration includes the LPA setup, all main diagnostics, and the polarimeter.

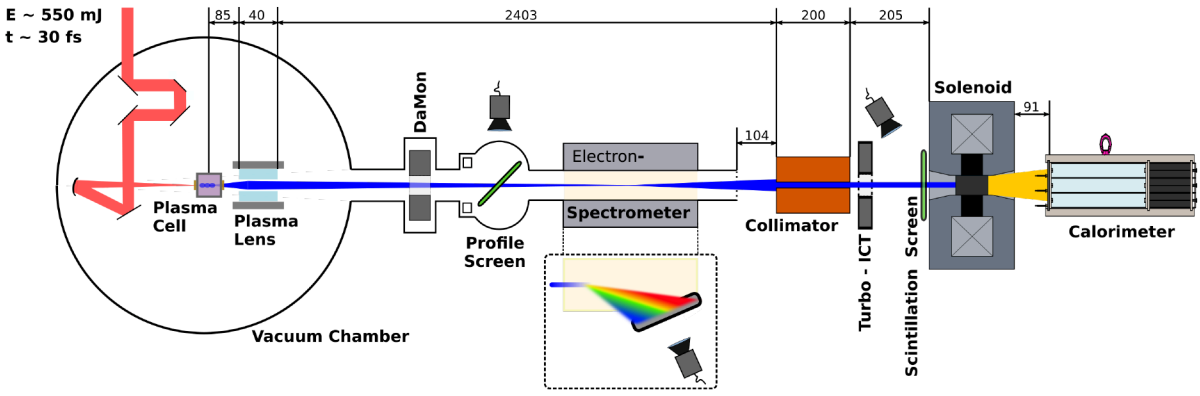

Figure 7.5.: Illustration of the experimental setup of the LPA at FLARE and the LEAP polarimeter, including all main beam diagnostics for the zero polarization measurement.

The driver laser for the LPA is guided from the laser lab to the LPA vacuum interaction chamber, located at the BOND laboratory (see Sec. 4.2.1) which houses the electron source setup. The laser is focused using an off-axis parabola onto the plasma target (a plasma cell) to drive the plasma wave and accelerate electrons injected via ionization injection (cf. Sec. 2.2). The plasma cell was operated with a helium-nitrogen gas mixture. The detailed acceleration scheme is described in [75, 84]. Shortly after the plasma cell, the electron beam is captured and focused by an active plasma lens (APL, see Sec. 4.3).

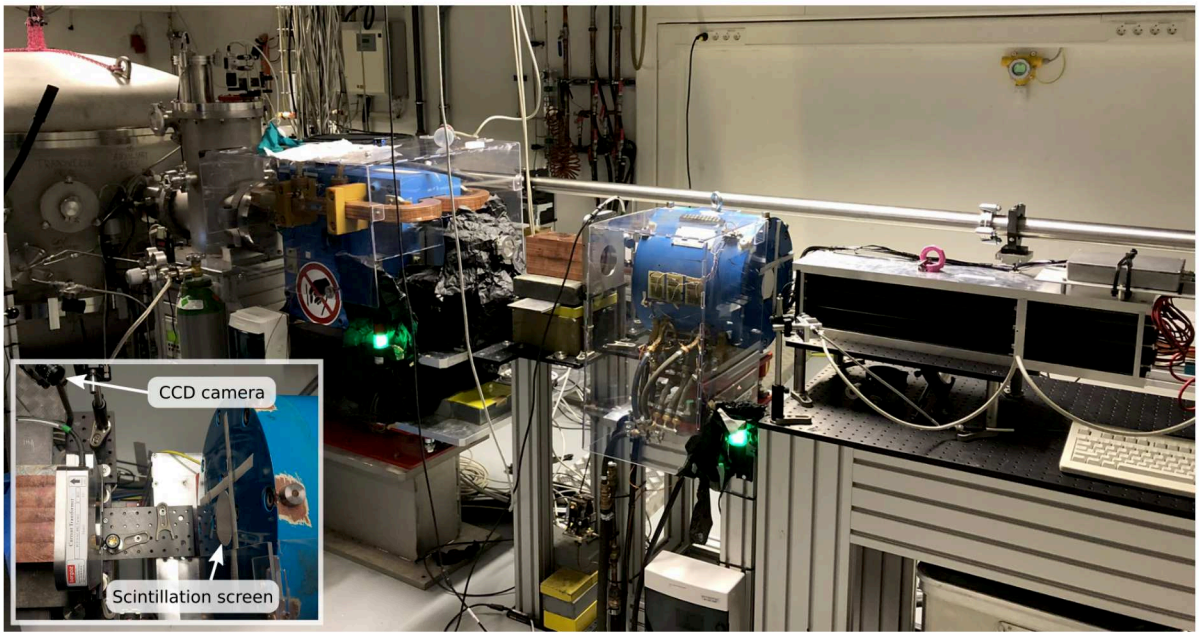

Figure 7.6.: Photograph of the experimental setup of the LPA at FLARE and the LEAP polarimeter for the zero polarization measurement. The inset shows a close-up of the scintillation screen diagnostic for charge monitoring in front of the solenoid entrance.

Upon exiting the interaction chamber, the electron beam charge is measured using the dark current monitor system (DaMon, see Sec. 4.2.2) which allows for a non-invasive absolute charge measurement. After the DaMon system, a scintillator screen can be inserted into the beam path to image the electron beam profile using a CCD camera. This diagnostic was primarily used as a beam monitor during the LPA optimization phase, prior to data collection. Next, a dipole magnet electron spectrometer (see Sec. 4.2.2) can be used to determine the electron beam energy spectrum. The dipole bends the electron beam onto a scintillator screen, where the beam is dumped, making this a destructive measurement method that prevents any further diagnostics downstream. If the spectrometer magnet is turned off, the beam exits the vacuum beamline through a 300 μm aluminum vacuum window and continues propagation in air. A copper collimator, with a cylindrical aperture of 1 mm in diameter, is positioned in the beam path. This collimator serves both as a beam collimator and, in conjunction with the APL, as an energy filter to narrow the electron spectrum exposed to the polarimeter (see Sec. 7.6.2).

A turbo-integrating current transformer (Turbo-ICT, ICT-VAC-082-Turbo2 [146]) was installed to measure the absolute charge transmitted through the collimator. Unfortunately, this measurement was not feasible due to a low signal-to-noise ratio in the

Turbo-ICT data, likely caused by low charge levels near the detection limit of 50 fC and additional noise from the APL operation.
To provide real-time visual feedback of the electron beam at the solenoid entrance, a DRZ-high scintillation screen was installed, covering the solenoid's full aperture. This screen captured the spatial beam profile and fluctuations in beam intensity when imaged with a CCD camera and was used for relative charge measurement and monitoring (see Sec 4.2.2). The LEAP polarimeter was installed about 2.9 m downstream from the electron source. The polarimeter consists of the solenoid magnet and the LEAP lead glass calorimeter, as described in Sec. 7.1. A photograph of the setup in the experimental area is shown in Fig. 7.6.

7.3. Preliminary Adjustments and Calorimeter Operation

In this section, the operation of the calorimeter will be discussed, focusing specifically on the signal definition, the generation and timing of the QDC gate signal, and the adjustment of the working point with respect to potential saturation effects.

7.3.1. Generation and Timing of the QDC Gate Signal

The gate signal for the QDC (cf. Sec. 6.1.4) was generated using simple analogue NIM logic (Nuclear Instrumentation Module). NIM is a standard for analogue logic signals, often used in nuclear and particle physics experiments. A TTL (Transistor-Transistor Logic) trigger from the primary laser trigger circuit was supplied to initiate the QDC gate generation. TTL is a type of digital logic signal with defined voltage levels for "low" and "high" states, commonly used in electronics for triggering and communication between devices.
This TTL trigger was first converted to a NIM signal using a TTL-to-NIM converter unit. The NIM signal was then sent to a NIM coincidence unit, where it coincided with itself. The reason for using this coincidence unit was that it offers an adjustable-length output signal which could be used directly as the QDC gate. The gate width was set to 100 ns. The TTL trigger used to trigger the QDC gate could be digitally delayed with respect to the laser (electron beam), allowing the timing of the QDC gate to be adjusted to coincide with the calorimeter PMT signal. The timing was monitored using an oscilloscope. An oscilloscope event display, showing a PMT signal generated

by an electron beam overlaid with the QDC gate in time, is presented in Fig. 7.7. It should be noted that the PMT signal appears quite small and noisy, suggesting that this snapshot was likely taken for a low-charge beam. However, it demonstrates that the PMT signals lie within the integration time of the QDC, as defined by the gate signal.

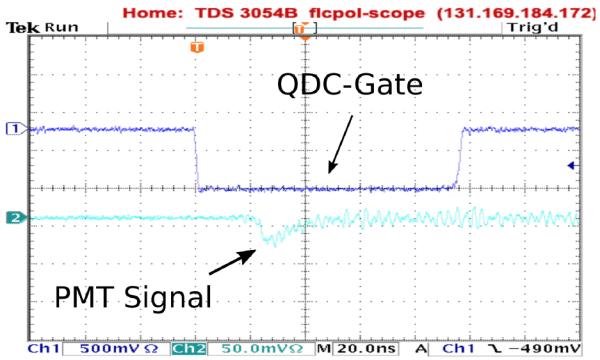

Figure 7.7.: Oscilloscope display showing a PMT signal generated by the electron beam (light blue), overlaid with the 100 ns wide QDC gate signal (dark blue).

7.3.2. Calorimeter Signal Definition

As introduced throughout the thesis in Chap. 6, the calorimeter signal is the PMT signal digitized using the QDC and thus has the physical unit of charge. In this section, the calorimeter signal will be denoted as Q_i, where i represents the index of the respective calorimeter channel, with a total of nine channels. Additionally, the signals from the nine calorimeter channels are typically normalized to the central channel, channel 4, to ensure comparability between them (see Sec. 6.3.4). The QDC signal processing can be summarized in three key steps:

1. **Pedestal subtraction:** The QDC value for each channel is first corrected by subtracting the respective pedestal value which is measured shortly before or after data acquisition.

2. **Charge conversion:** The QDC values are then converted to a physical charge using the conversion factor for the QDC binning: 200 fC for the high range and 25 fC for the low range of the QDC (see Sec. 6.1.4).

3. **Signal normalization:** Finally, the signals are normalized to the central channel (channel 4) using the relationship $Q_i = C_{i,4}(V_i, V_4) \cdot Q'_i$, where Q'_i is the unnormal-

ized signal of channel i, and $C_{i,4}$ represents the calibration coefficient depending on the set voltages of the channels, as defined in Eq. 6.10. A calibration voltage of $V_4 = 950\,V$ was predominantly used, unless otherwise noted, to facilitate comparison with test beam operations (see Sec. 6.3). It should be noted that this calibration voltage does not correspond to the operational voltage of the PMTs which was set to 600 V during this measurement campaign (see Sec. 7.3.3).

In general, when referring to the calorimeter signal Q, the sum of all calibrated channel signals $Q = \sum Q_i$ is implied, unless stated otherwise.

7.3.3. Adjustment of the Calorimeter Working Point

For the experiment, it is essential to operate the calorimeter in a regime where the signal Q scales linearly with the beam intensity. The proper operating point must be found and adjusted before data collection begins to avoid entering a regime where saturation effects occur. There are two ways to adjust the working point: by controlling the beam intensity or by adjusting the gain (HV setting) of the calorimeter PMTs. These settings need to be precisely configured to maintain linearity.
The direct control of the beam charge from the LPA is challenging. However, within the setup (see Fig. 7.5), the applied collimator in the beamline inherently reduces the overall beam charge reaching the polarimeter. Three copper collimators with cylindrical apertures of 1 mm, 5 mm, and 15 mm in diameter were available. The smallest, 1 mm collimator was primarily chosen because, in conjunction with the APL, it acts as an energy filter, narrowing the electron spectrum exposed to the polarimeter (see Sec. 7.6.2). Additionally, it also reduces the beam charge the most among the available collimators. It should be noted that during initial test runs, it became evident that when using the 5 mm or 15 mm collimator, the calorimeter signal was too large, and the QDC was always in saturation despite its high dynamic range, even when applying a very low voltage of 500 V to the PMTs. Even with the chosen 1 mm collimator, the PMT voltage needed to be carefully adjusted to a point where the calorimeter signal scaled linearly with the DRZ scintillator screen signal S_{scint} (defined in Sec. 4.2.2), which is proportional to the beam charge. This linearity was achieved at a PMT voltage of 600 V.
Figure 7.8 shows the correlation between Q and S_{scint} using the 1 mm collimator and an APL discharge voltage of 20 kV. Panel b) presents data for the selected working point of 600 V, compared to a higher voltage setting of 750 V in panel a). In both

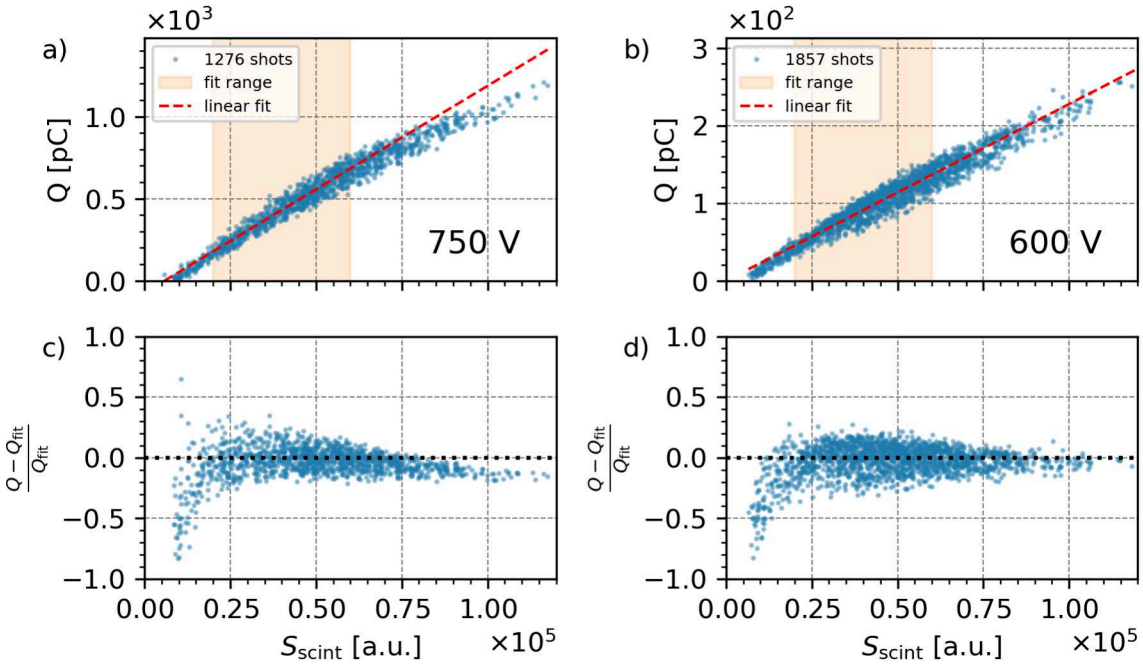

Figure 7.8.: a) Correlation between the calorimeter signal Q and the relative beam charge measurement S_{scint} at a PMT voltage of 750 V, using the 1 mm collimator and an APL discharge voltage of 20 kV. The data is shown with a linear fit (red), and the fit range is indicated by the orange band. b) Same as a), but at a PMT voltage of 600 V. c) and d) show the relative deviation from the linear fit for the 750 V and 600 V data, respectively.

cases, the data shows a correlation, with a linear fit (red) over the same fit range from $S_{\text{scint}} = 20000$ to 60000, indicated by the orange band. It is evident that, at 750 V, the calorimeter signal deviates from linear behavior at high S_{scint} (high beam charges), due to saturation effects in the PMT amplification. This saturation is not present in the 600 V case, as seen in panels c) and d), which display the relative deviation from the linear fit for the 750 V and 600 V runs, respectively.

At low scintillator screen signals ($S_{\text{scint}} < 20000$), regardless of the PMT voltage, Q and S_{scint} deviate from a linear relation. This deviation is likely caused by a non-linear response of the DRZ screen and imaging system at low beam charges, which was not investigated further in this thesis. Therefore, for the following analysis, data with $S_{\text{scint}} < 20000$ will be discarded to ensure accurate correction of beam charge fluctuations in the calorimeter signal (see Sec. 7.5.2).

7.3.4. Influence of the APL Operation on the QDC Pedestal

The QDC pedestal, which represents the base level of dark current flowing during the integration time of the QDC, needs to be measured for each QDC channel to allow for accurate subtraction of this background from the QDC counts that are generated by the PMT signals themselves. It has been observed that this pedestal value is influenced by the use of the APL, likely due to electromagnetic pulses (EMP) caused by the high-voltage discharge. A significant reduction in this influence was achieved by shortening the signal cable length from $\sim$17 m, originally used for signal delay, to $\sim$2 m, as shown in Fig. 7.9. The QDC pedestal for calorimeter channel 4 (corresponding to the central crystal) is shown under three different conditions: with no cables connected to the QDC (dark blue), with $\sim$17 m LEMO cables connecting the PMTs to the QDC (orange), and with $\sim$2 m cables (cyan). The data was acquired consecutively with an APL discharge voltage of 16 kV. The shorter cable length significantly reduced the influence of the APL, suggesting that the longer cables acted as antennas, picking up noise from the EMP. However, reducing the cable length did not completely eliminate

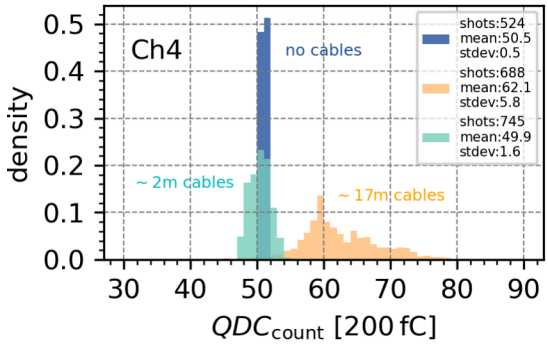

Figure 7.9.: QDC pedestal of channel 4 for different signal cable lengths, demonstrating the influence of APL discharge for an APL setting of 16 kV.

the APL influence on the QDC pedestal. This is further demonstrated in Fig. 7.10 a), where the shift in the pedestal mean value is shown as a function of the APL discharge voltage, using the shortened signal cables. It should be noted that the data presented here were collected on a different day than the data shown in Fig. 7.9. When the APL is activated, the pedestal shifts by about -4 QDC bins, while the standard deviation increases slightly from 0.8 QDC bins to $\sim$1.2, as shown in panel b), compared to when the APL is off. Similar effects were observed in other channels, although the shifts were not always negative. Unfortunately, no consistent pattern could be identified,

warranting further investigation in future studies.
This analysis highlights the importance of measuring the QDC pedestal for each run under consistent experimental conditions to ensure accurate pedestal subtraction and reliable data.

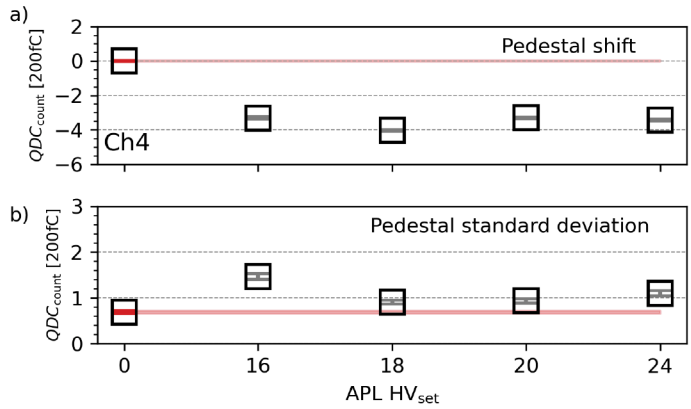

Figure 7.10.: a) Shift in the pedestal mean position for QDC channel 4 with respect to the APL discharge voltage. b) Standard deviations of the pedestal distributions corresponding to the data shown in a). The data was taken with the adjusted signal cable length of 2 m.

7.4. Measurement Overview and Procedures

This section provides an overview of the various measurements conducted during the experiment. The measurements can be classified into three categories: Polarimeter runs, spectrometer runs, and pedestal runs. Throughout the measurement campaign, the LPA operated at a repetition rate of 2 Hz. A detailed run list is provided in the appendix (see Tab. A.1).

Polarimeter runs: The polarimeter runs were the primary data collection periods of the measurement campaign, during which polarimeter data was gathered, and the asymmetry measurement was performed. In these runs, the magnetic current alternated between -60 A and 60 A, with the current held for 5 minutes at each value. The main runs of the campaign were conducted using an APL setting of 20 kV. Additional runs were performed with APL settings of 16 kV, 18 kV, and 24 kV to investigate the calorimeter signal's dependency on the APL setting. Moreover, runs were conducted with the magnet turned off to assess any

potential effects related to the magnetic field switching. During the data runs, the beam charge was measured shot by shot using DaMon and the DRZ-high scintillating screen.

Spectrometer runs: Spectrometer runs were conducted frequently to determine the LPA electron spectrum. Since these measurements are destructive, they could not be performed in parallel with the polarimeter runs on a shot-to-shot basis. The spectrometer dipole magnet was always operated at a current of 180 A. Runs were conducted with the APL turned off to measure the initial LPA electron spectrum. In particular, a long run, lasting around 30 minutes, was performed to estimate the average spectrum and its stability. Additionally, runs with the plasma lens active were conducted, scanning from 14 kV to 24 kV in 0.5 kV increments to investigate the APL's focusing performance.

Pedestal runs: Pedestal runs were performed with the electron beam switched off (laser blocked). These runs were conducted after each polarimeter run under the same conditions to measure the corresponding QDC pedestal, enabling accurate baseline subtraction later. Additionally, the DRZ-high scintillator screen data collected during these runs was used to measure and correct for the background signal (see Sec. 4.2.2), which is primarily caused by ambient light.

7.5. The Beam Charge

An important parameter in this experiment is the beam charge incident on the polarimeter entrance. Variations in beam intensity affect the accuracy of the measurement in two ways. On one hand, large fluctuations increase the statistical uncertainty, reducing the precision of the measurement. However, a more critical issue arises from drifts in the mean beam charge between intervals during which the asymmetry is calculated. These drifts can lead to fake asymmetries (see Sec. 7.7.2) that are not related to polarization, significantly compromising the accuracy of the asymmetry measurement. To address both fluctuations and drifts, it is essential to measure the beam charge on a shot-to-shot basis and adjust the calorimeter signal accordingly. This section discusses how this issue is managed using the diagnostic tools employed in the experiment.

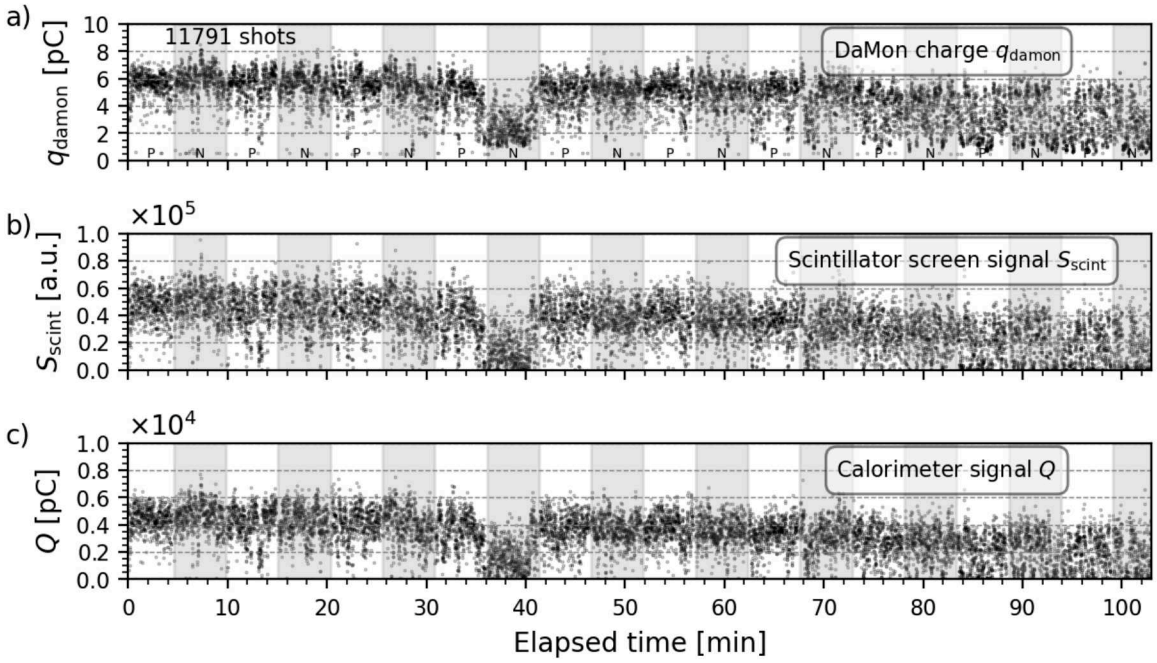

Figure 7.11.: a) DaMon charge measurement during the main polarimeter run 50379 (11791 shots) over elapsed time. b) Measured scintillator screen signal S_{scint} over time. c) Corresponding calorimeter signal Q. The white and gray stripes represent the periods when the solenoid magnet current was set to positive and negative (± 60 A), respectively.

7.5.1. Overview

In this experiment, absolute beam charge measurements were taken before the collimator using the DaMon diagnostic (see Sec. 4.2.2), while relative measurements were performed after the collimator using the DRZ-high scintillator screen (see Sec. 4.2.2), which is located directly in front of the solenoid entrance. These relative measurements provided an indication of the fraction of the beam charge that reached the polarimeter. An absolute charge measurement directly in front of the solenoid magnet was intended using the Turbo-ICT [146], as shown in the experimental setup in Fig. 7.5, but reliable data could not be obtained due to low signal levels, disturbances from the APL discharge, or potentially incorrect operation. Further investigation will be required in future studies.

In Fig. 7.11, the DaMon signal q_{damon} (a), the scintillator screen signal S_{scint} (b), and the calorimeter signal Q (c) for the main polarimeter run 50379, consisting of 11791 shots, are presented over time. The white and grey bands represent the periods when the

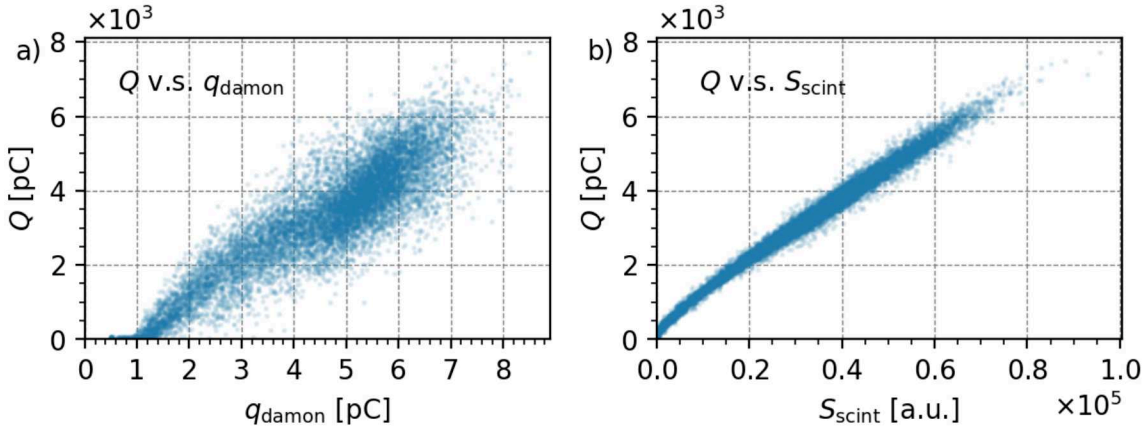

Figure 7.12.: a) Correlation of the calorimeter signal with the overall LPA beam charge as measured by DaMon. b) Correlation of the calorimeter signal Q with the relative beam charge reaching the polarimeter, S_{scint}, as measured by the scintillator screen.

solenoid magnet current was set to positive (P, +60 A) or negative (N, -60 A). The initial beam charge, as measured with the DaMon, shows substantial fluctuations and drifts over the measurement period. When comparing the DaMon signal to S_{scint} and Q, it is evident that both signals closely follow the fluctuations in the overall beam charge. This is expected for S_{scint}, as it is proportional to the beam charge. More importantly, it suggests that the calorimeter signal is primarily influenced by the beam charge. The correlation between the calorimeter signal Q and q_{damon} is shown in Fig. 7.12 a), while Fig. 7.12 b) shows the correlation of Q with S_{scint}. It is clear that the calorimeter signal has a stronger correlation with S_{scint} compared to its correlation with the initial beam charge. This is due to the collimator in the beam path which reduces the beam size and makes pointing instabilities more prominent. Pointing instabilities refer to slight shot-to-shot variations in the alignment of the electron beam as it enters the collimator. Since the collimator has a fixed aperture, any misalignment of the beam can result in a portion of the beam being blocked or scattered. As a result, even if the total beam charge would remain relatively stable, the amount of charge reaching the polarimeter can fluctuate, causing a weaker correlation between the overall beam charge and the calorimeter signal. Therefore, to correct the calorimeter signal for beam charge fluctuations, the scintillator screen signal will be used, as discussed in the following section.

7.5.2. Beam Charge Correction Using the Scintillator Screen

This section discusses the correction of the calorimeter signal Q to account for beam charge fluctuations and drifts, using the scintillator screen signal S_{scint}. The charge-corrected calorimeter signal, denoted as Q_c, is defined as:

$$Q_c = \frac{Q}{\frac{S_{\text{scint}}}{\langle S_{\text{scint}} \rangle}} \tag{7.1}$$

where S_{scint} is the scintillator screen signal and $\langle S_{\text{scint}} \rangle$ is its mean value. In this equation, the calorimeter signal is normalized to the beam charge fluctuations observed in S_{scint}, ensuring that the corrected calorimeter signal retains the unit of physical charge. Before applying the charge correction, the data is preselected to exclude low-quality

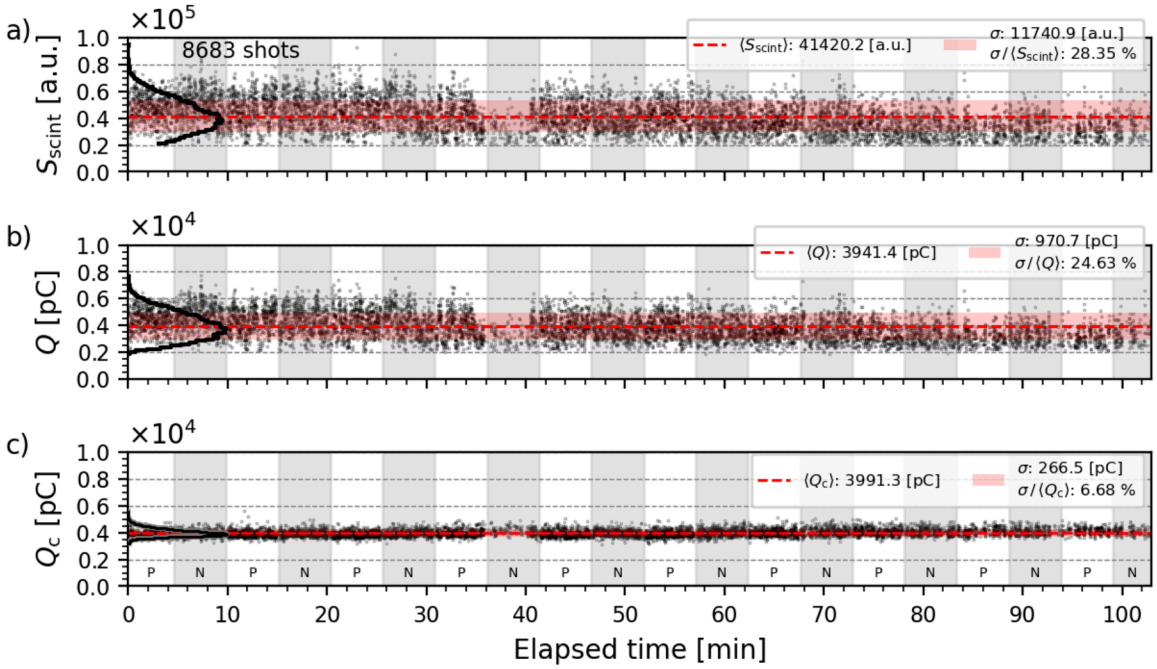

Figure 7.13.: a) Scintillator screen signal S_{scint} over time for the main polarimeter run 50379, after applying data quality cuts that exclude all shots where $q_{\text{damon}} < 3\,\text{pC}$ and $S_{\text{scint}} < 20000$. The red dashed line represents the mean value $\langle S_{\text{scint}} \rangle$, and the red band shows the standard deviation σ. The black line shows the projected distribution of the signal. b) Same as a), but showing the calorimeter signal Q. c) Calorimeter signal after the correction for beam charge fluctuations, referred to as Q_c according to Eq. 7.1, using the measured scintillator screen signal in a). The white and gray stripes indicate periods when the solenoid magnet current was set to positive or negative (± 60,A), respectively.

shots, primarily based on the DaMon signal. Shots with an initial beam charge $q_{\text{damon}} < 3\,\text{pC}$ are excluded. Additionally, to ensure that Q can be accurately calibrated against S_{scint}, the signals must be proportional. As observed during the adjustment of the calorimeter working point, Q is not proportional to S_{scint} for signals below 20000 (see Fig. 7.8 d)). Therefore, shots are excluded where $S_{\text{scint}} < 20000$. These preselection cuts result in the rejection of approximately 25 % of the collected shots in the main dataset.
In Fig. 7.13 a) and b), the scintillator screen signal S_{scint} and the calorimeter signal Q are shown after the applied data cuts (similar to Fig. 7.11). The mean and standard deviation are represented by the red dashed line and red band, respectively. Figure 7.13 c) shows the corresponding charge-calibrated calorimeter signal, Q_{c}, calculated using Eq. 7.1. The corrected signal Q_{c} exhibits significantly improved stability compared to the uncorrected calorimeter signal Q. The relative width of the signal distribution is reduced by nearly a factor of four, decreasing from $\frac{\sigma_Q}{\langle Q \rangle} = 24.63\,\%$ to $\frac{\sigma_{Q_{\text{c}}}}{\langle Q_{\text{c}} \rangle} = 6.68\,\%$
The charge-corrected calorimeter signal Q_{c} will be utilized for the calculation of the asymmetry δ (see Sec. 7.7.3). The subsequent section will examine the limitations of the charge correction process, with particular focus on the residual width observed in the Q_{c} distribution.

7.5.3. Limitations of the Beam Charge Correction

This section discusses the limitations of the beam charge correction method using the scintillator screen signal S_{scint}, with a particular focus on the residual width observed in the distribution of the charge-corrected calorimeter signal Q_{c}.
The fundamental assumption behind the charge correction is that both the calorimeter signal Q and the scintillator signal S_{scint} are influenced by the beam charge q. By normalizing the calorimeter signal using S_{scint}, as shown in Eq. 7.1, the effect of beam charge fluctuations is expected to cancel out. However, other factors may contribute to the observed residual width in the corrected signal.
The scintillator screen signal S_{scint} depends on the beam charge q and its fluctuations Δq, and is further broadened by the resolution of the scintillator screen setup ΔS_{scint} which can be expressed as:

$$\text{Scintillator screen signal} :\rightarrow S_{\text{scint}}(q \pm \Delta q) \pm \Delta S_{\text{scint}} \tag{7.2}$$

In contrast, the calorimeter signal Q depends not only on the beam charge q and its fluctuations Δq, but also on the beam energy E and its fluctuations ΔE. Additionally, the calorimeter signal is broadened by the intrinsic resolution of the polarimeter setup ΔQ which includes factors such as the calorimeter's energy resolution and intrinsic fluctuations in energy transmission through the solenoid's iron core.

$$\text{Calorimeter signal} :\rightarrow Q(q \pm \Delta q, E \pm \Delta E) \pm \Delta Q \tag{7.3}$$

Given these dependencies, the residual width in the corrected signal Q_c could be influenced by three main factors: fluctuations in the beam energy ΔE, the resolution of the scintillator screen setup ΔS_{scint}, and the intrinsic resolution of the polarimeter setup ΔQ.
In Fig. 7.14 a), the distribution of the charge-corrected calorimeter signal Q_c is shown as a black histogram for the main polarimeter run 50379 (previously presented in Fig. 7.13). The figure also includes distributions for a simulated calorimeter signal covering two cases: one neglecting the calorimeter resolution, Q_{sim} (green histogram), and another accounting for it, $Q_{sim,digitized}$ (orange histogram). The results were obtained using the `leap_sims` polarimeter simulation (see Sec. 7.1.2). The simulation was based on 6000 unpolarized electron bunches with a constant charge of 5×10^5 electrons, and an energy spectrum corresponding to an APL setting of 20 kV (see Fig. 7.25). To obtain the simulated calorimeter signal Q_{sim}, the energy deposited in the calorimeter by charged particles above the Cherenkov threshold, E_{ct} (see Sec. 6.2.2), was converted to physical charge using the linear scaling from Eq. 6.11. This was further scaled to match the mean value of Q_c, as the absolute charge incident on the polarimeter is not known. The digitized calorimeter signal $Q_{sim,digitized}$, including the calorimeter's energy resolution, was derived following the procedure described in Sec. 6.4.2.
Starting with the simulation results, the width of the simulated distribution $Q_{sim,digitized}$ resembles the intrinsic resolution of the polarimeter setup ΔQ. The similarity between simulations with and without accounting for the calorimeter's energy resolution demonstrates that this resolution has minimal impact on the intrinsic width of the calorimeter signal ΔQ. This suggests that ΔQ is primarily influenced by factors such as intrinsic fluctuations in energy transmission through the solenoid's iron core.
The comparison of the Q_c distribution with the simulation results reveals that the charge-corrected calorimeter signal is significantly broader than expected from the simulations. This indicates that the intrinsic resolution of the polarimeter setup ΔQ is not the dominant contributor to the residual width and may even be negligible in

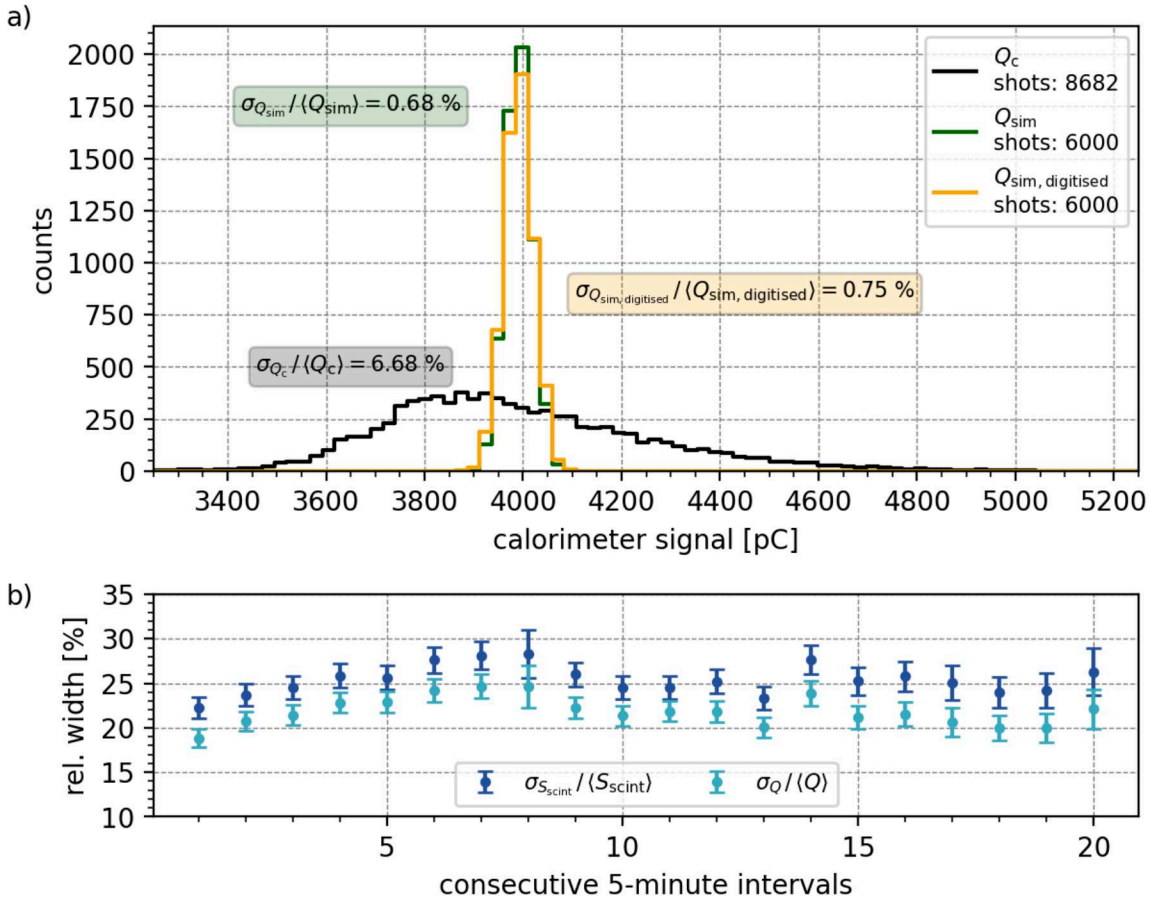

Figure 7.14.: a) Distribution of the charge-corrected calorimeter signal Q_c for the main polarimeter run 50379, shown as a black histogram. The dark green and orange histograms represent simulation expectations using the `leap_sims` polarimeter simulation, with (orange) and without (green) incorporating the calorimeter's energy resolution. b) Relative width of the calorimeter signal Q and the scintillator screen signal S_{scint} for each 5-minute interval of the main data set 50379 (shown as light blue and blue dots, respectively).

this context. This leads to the preliminary conclusion that the width of the charge-corrected calorimeter signal is primarily dominated by fluctuations in the beam energy ΔE and/or the resolution of the scintillator screen setup ΔS_{scint}.
Given that the calorimeter signal depends on both the beam charge q and energy E, one would expect its distribution to exhibit a larger relative width compared to that of the scintillator screen signal. However, the opposite trend is observed. As shown in Fig. 7.13 a) and b), the relative width of the scintillator screen signal $\frac{\sigma_{S_{\text{scint}}}}{\langle S_{\text{scint}} \rangle} = 28.35\,\%$ is greater than that of the calorimeter signal $\frac{\sigma_Q}{\langle Q \rangle} = 24.63\,\%$. This trend is consistent across the dataset when comparing the relative widths for each 5-minute interval, as presented in Fig. 7.14 b). In this figure, the blue dots represent the relative width of the calorimeter signal, while the light blue dots represent the relative width of the scintillator screen signal, showing a clear correlation between the two. These observation suggests that the resolution of the scintillator screen setup plays a key role in the residual width observed in the charge-corrected signal, likely overshadowing the broadening expected from energy fluctuations.
Assuming the contributions from beam energy fluctuations ΔE and the resolution of the polarimeter setup ΔQ are negligible, the difference in relative widths between the calorimeter and scintillator screen signals can primarily be attributed to the scintillator screen resolution. Using this approach, the relative resolution of the scintillator screen setup can be estimated by quadratically subtracting the relative width of the calorimeter signal distribution Q from the relative width of the S_{scint} distribution:

$$\frac{\Delta S_{\text{scint}}}{\langle S_{\text{scint}} \rangle} \approx \sqrt{\left(\frac{\sigma_{S_{\text{scint}}}}{\langle S_{\text{scint}} \rangle}\right)^2 - \left(\frac{\sigma_Q}{\langle Q \rangle}\right)^2} = \sqrt{(0.2835)^2 - (0.2463)^2} \approx 0.14 \tag{7.4}$$

Thus, the relative resolution of the scintillator screen is estimated to be approximately 14 %.
Under these assumptions, the relative width of the charge-corrected calorimeter signal Q_c would be expected to match the estimated relative resolution of the scintillator screen setup. However, the observed relative width of Q_c is $\frac{\sigma_{Q_c}}{\langle Q_c \rangle} = 6.68\,\%$ which is about half of the expected value. This discrepancy is not entirely surprising, given the low statistics, unstable beam properties, and the fact that the signal distributions are approximately Gaussian, though not perfectly (see Fig. 7.13).
Another possible explanation for this discrepancy, as well as the difference between the relative spreads of Q and S_{scint} (see Fig.7.14) is the assumption of an anti-correlation between the beam energy and charge fluctuations. Further investigation is needed to

confirm or rule out this possibility. However, it is worth mentioning that a positive correlation between energy and charge was observed by Simon Bohlen et al. [65] in a study using the same LPA setup with a similar acceleration scheme.
This analysis suggests that the effectiveness of the charge correction is primarily influenced by the resolution of the charge measurement in front of the solenoid. A future study could address improving this measurement resolution to optimize the charge correction procedure.

7.6. The Beam Energy

For the polarization measurement, precise knowledge of the beam energy – specifically, the energy spectrum of the beam entering the polarimeter – is crucial for several reasons. The measurement relies on the polarization-dependent transmission of bremsstrahlung photons through a magnetized iron absorber, where the transmission probability is influenced by photon energy due to the energy dependence of Compton scattering (see Sec. 3.2). Therefore, the initial electron energy spectrum not only affects the observed transmission asymmetry but must also be characterized accurately to simulate the analyzing power of the system, which is essential for reconstructing the initial electron polarization.
Furthermore, although the calorimeter signal is primarily influenced by the beam charge and its fluctuations (see Sec. 7.5), variations in beam energy can also affect the calorimeter signal in a similar way. These energy fluctuations can introduce additional statistical uncertainties and also cause fake asymmetries (cf. Sec. 7.7.2) due to changes in the average energy between measurement intervals where the asymmetry is calculated. In the current LEAP setup, the beam energy spectrum cannot be measured simultaneously with the polarization measurement, making shot-to-shot energy corrections impossible. Therefore, a narrow, stable, and well-characterized energy spectrum is essential for reliable polarization measurements.
In the current experimental setup (see Fig. 7.5), the APL, in conjunction with the collimator, not only captures and collimates the beam but also acts as an energy filter due to its energy-dependent focal length (see Sec. 4.3). As a result, it shapes the actual energy spectrum that reaches the polarimeter. This filtering effect is beneficial for generating a narrower, more stable energy spectrum and selecting the peak energy by adjusting the APL's focusing strength. This section summarizes the quantitative

characteristics of this energy filtering effect, accessing the shape and overall stability of the energy spectrum.

7.6.1. LPA Energy Spectrum

To access the initial LPA electron spectrum, a dipole electron spectrometer was utilized (see Sec. 4.2.2). The spectrometer data consists of images captured by a CCD camera which recorded the energy-dispersed electron beam on the spectrometer screen. These raw images were calibrated to an absolute energy axis using the Python tool `espec_analysis` [86], developed by Rob Shallo. For a detailed explanation of the calibration process, refer to [84].

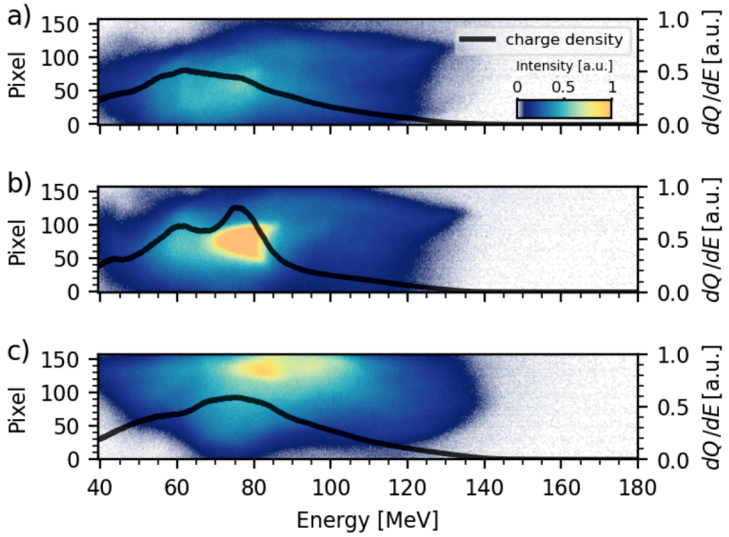

Figure 7.15.: Energy-calibrated spectrometer images from three consecutive shots: a), b), and c). The image intensity values correspond to the beam charge within a given energy band. The corresponding energy spectra (charge density) are represented as black lines.

Figure 7.15 a), b), and c) show energy-calibrated spectrometer images from three consecutive shots. These images display the energy-dispersed electron beam, where pixel intensity corresponds to the number of electrons within a given energy band along the x-axis. Due to the non-linear relationship between the detector coordinates and electron energy (see Fig. 4.5 d)), each pixel width corresponds to a different energy band. The black line represents the integrated pixel values normalized by the individual pixel energy bandwidth revealing the energy spectrum of the electron beam $\frac{dQ}{dE}$.

To be noted, the presented energy spectra are not corrected for additional broadening effects arising from beam divergence, pointing, scattering in the exit window of the spectrometer's beam pipe, and the resolution of the spectrometer's imaging system. All these effects potentially smear the appearance of the electron beam on the spectrometer's screen and therefore contribute to the intrinsic broadening of the spectra retrieved with the dipole spectrometer. These effects are described in more detail and have been investigated on this LPA by Simon Bohlen; for more details, refer to his work [75]. Nevertheless, the impact of these effects is considerably small compared to the beam energy itself, as demonstrated in Figure 4.22 of Bohlen's dissertation, and will, therefore, not be addressed in the context of this work.
From Fig. 7.15, it is evident that there can be significant fluctuations between shots due to the complexity of the acceleration process. Since the electron spectrometer measurement is destructive and cannot be conducted during the polarimeter data runs, an extended spectrometer run (50281) over approximately 30 minutes, containing 3386 consecutive shots, was analyzed. This dataset is used to estimate the average energy spectrum and assess the overall stability of the beam energy. To filter out shots with

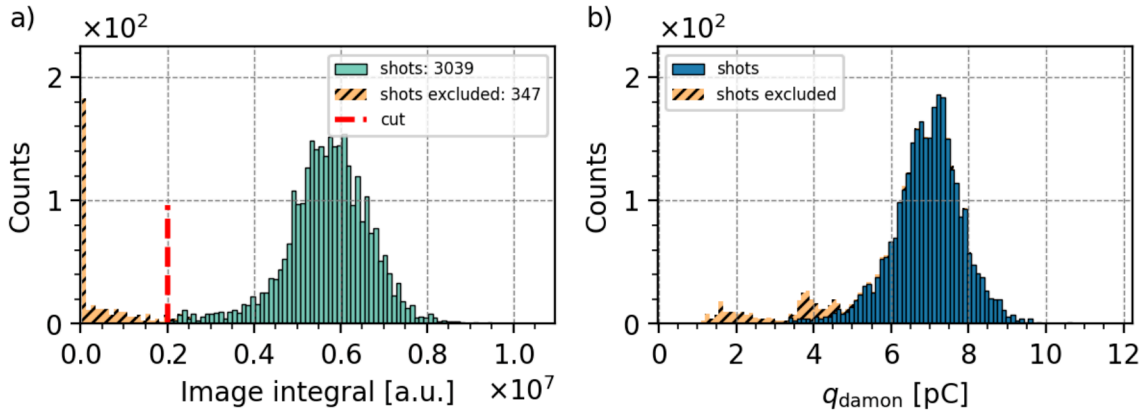

Figure 7.16.: a) Distribution of the integrated pixel values of the spectrometer images (image integral) from 3386 consecutive shots. A quality cut at $> 0.2 \cdot 10^7$, indicated by the red dashed line, was applied. The cyan histogram represents the retained shots, while the orange histogram shows the rejected ones. b) Distribution of the measured DaMon beam charge, with the rejected data based on the image integral cut from a) shown in orange.

low-quality beams – specifically those with low charge or beams that failed to reach the spectrometer screen due to large pointing instabilities – data cuts were applied based on the integrated pixel values of the spectrometer images (image integral). Figure 7.16 shows the distribution of the image integral for 3386 consecutive shots. An integral

cut of $> 0.2 \cdot 10^7$, indicated by the red dashed line, was applied to discard empty or low-charge shots. This cut resulted in the rejection of approximately 10 % of the collected data, as shown by the orange histogram. In Fig. 7.16 b), the overall beam charge for the considered shots is presented, demonstrating that the applied integral cut already includes the general 3 pC quality threshold for the DaMon charge (q_{damon}), as introduced earlier in Sec. 7.5.

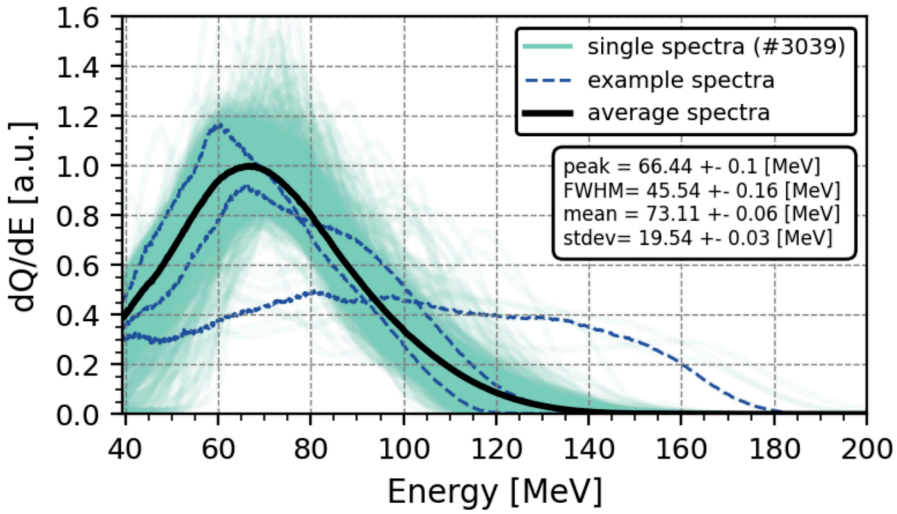

Figure 7.17.: Average electron spectrum (solid black line) over 3039 shots, with all individual spectra overlaid in cyan. Three individual shots are highlighted with blue dashed lines to emphasize the significant fluctuations.

In Fig. 7.17, the average electron spectrum over the remaining 3039 shots is shown as a solid black line, with all individual spectra overlaid in cyan. Additionally, three representative single-shot spectra are highlighted with dashed blue lines. The spectra are normalized by their integrals to allow for easier comparison of their shapes, eliminating shot-to-shot charge variations. In plasma acceleration research, the peak energy and full width at half maximum (FWHM) are commonly used to parameterize the energy spectra [75]. Given the significant fluctuations in spectral shape, the mean energy and its standard deviation are also considered. The retrieved average spectrum shows a peak energy of 66.44 ± 0.1 MeV, with an FWHM of 45.54 ± 0.16 MeV, indicating a broad energy spectrum with a spread of nearly 70 %. The average mean energy is slightly higher, at 73.11 ± 0.06 MeV, with an average standard deviation of 19.54 ± 0.03 MeV.

In Fig. 7.18 a), all remaining spectra of run 50281 are displayed in a waterfall plot, arranged in consecutive order over the elapsed time. Each vertical line corresponds

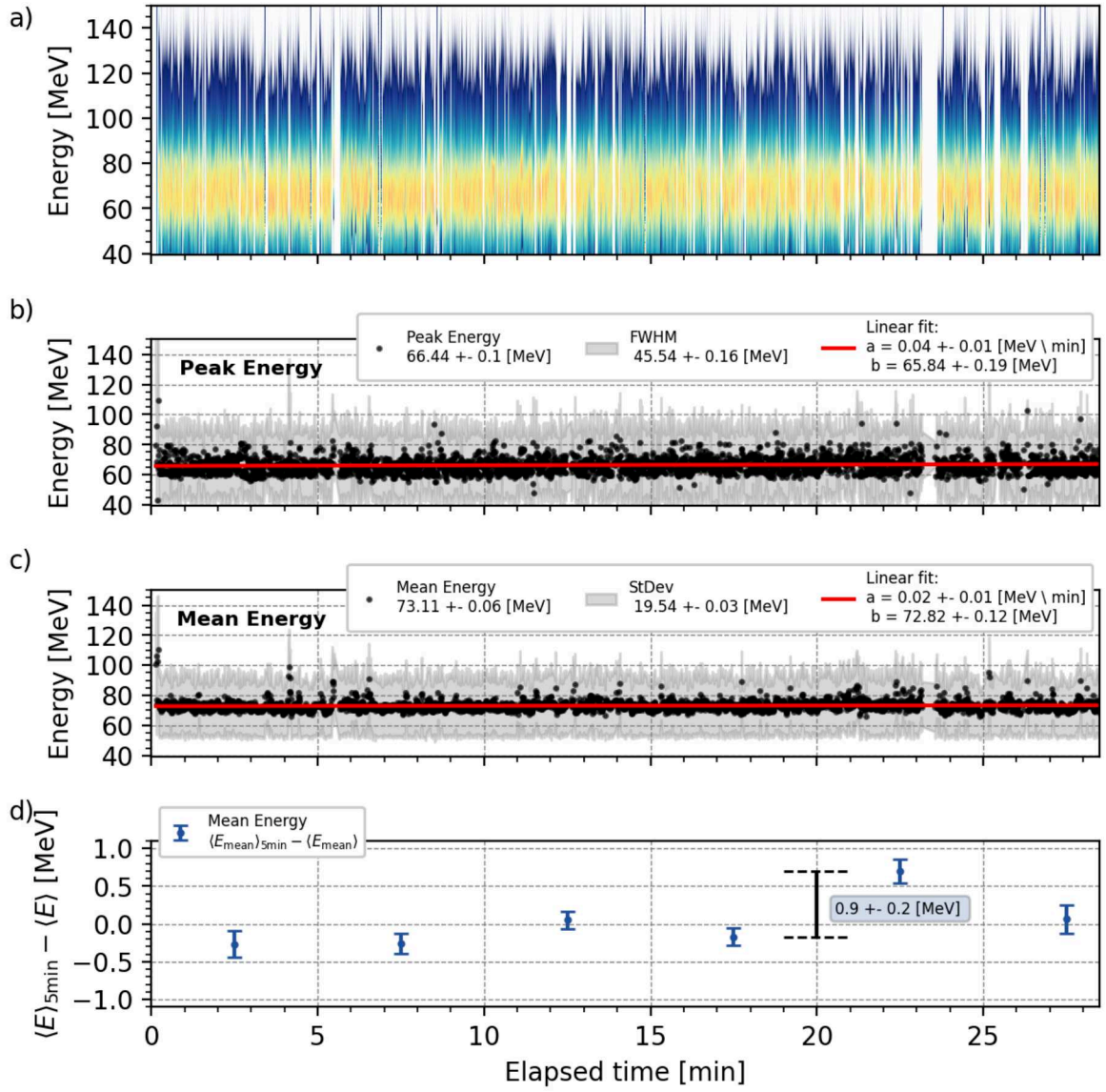

Figure 7.18.: a) Waterfall plot displaying the spectra of 3039 shots in consecutive order over the elapsed time. Spectra are normalized by their integrals for comparability. b) Peak energies of each individual shot and the corresponding FWHM are represented by black dots and a grey band, with a linear fit of the peak energies shown in red. c) Same as b), but with mean energies and standard deviations of the individual spectra. d) Deviation of the mean spectral energy, averaged over consecutive 5-minute intervals, from the overall mean energy.

to the retrieved energy spectrum for the respective shot, normalized by its integral to facilitate comparison. In Fig. 7.18 b), the peak energies of each shot and their corresponding FWHM are shown as black dots and a gray band, respectively. A linear fit of the peak energies, shown in red, indicates no significant drift over the half-hour observation period. The same trend is observed for the mean energies of the individual spectra, as shown in Fig. 7.18 c), where the mean energy is plotted over time, with the standard deviation of the spectra displayed as a gray band.
In the experiment, during the polarimeter runs (see Sec. 7.4), the magnet current was switched from negative to positive every 5 minutes to calculate asymmetries over these intervals. Therefore, the stability of the energy spectra over each magnet cycle is crucial for ensuring accurate asymmetry measurements. In Fig. 7.18 d), the deviation of the mean spectral energy, averaged over consecutive 5-minute intervals, from the overall mean energy is shown. The mean energy exhibits a maximum deviation of approximately 1 MeV between intervals.
To obtain an estimated value for the possible resulting fake asymmetry due to the observed energy drifts, the mean energies of the intervals with the largest deviations, 72.9 MeV and 73.8 MeV, are converted to the calorimeter signal E_{ct} using the simulated polarimeter energy response to unpolarized electrons (see Fig. 7.3). This yields $E_{\mathrm{ct}} = 0.509$ an $E_{\mathrm{ct}} = 0.519$, obtained through linear interpolation of the corresponding data points. Using these values, the fake asymmetry is estimated to be around $\delta_E \approx |1.3|$ %, as calculated from Eq. 3.9. This would already be more than ten times larger than the expected asymmetry of $\delta \sim 0.1$ % which is anticipated for an idealized beam with 10 % polarization (see Sec. 7.1.2), as expected for LEAP.
This underlines the importance of employing the APL and collimator as an energy filter for stabilization which will be evaluated in the following section.

7.6.2. APL and Collimator as Energy Filter

The plasma lens exhibits an energy-dependent focal length, causing electrons across the broad LPA electron spectrum to be focused at different positions along the z-axis. Consequently, the collimator in the beamline serves two main purposes: firstly, in conjunction with the plasma lens, it selects a certain fraction of the energy spectrum, thereby acting as an energy filter; secondly, it collimates the beam, ensures a consistent incident position on the polarimeter and reduces the overall charge delivered to the polarimeter.

To determine the transmitted energy spectrum through the collimator, and thus the energy spectrum that reaches the polarimeter, linear beam transport matrix calculations will be employed, as introduced in Sec. 4.3.2. These calculations allow the beam waist along the beam path to be computed, with the transport matrix defined as follows:

$$\begin{aligned}\begin{pmatrix} R_{11}(E,I) & R_{12}(E,I) \\ R_{21}(E,I) & R_{22}(E,I) \end{pmatrix} = &\begin{pmatrix} 1 & D \\ 0 & 0 \end{pmatrix} \\ &\times \begin{pmatrix} \cos\left(\sqrt{k(E,I)}L_{APL}\right) & \frac{1}{\sqrt{k}}\sin\left(\sqrt{k(E,I)}L_{APL}\right) \\ -\sqrt{k(E,I)}\sin\left(\sqrt{k(E,I)}L_{APL}\right) & \cos\left(\sqrt{k(E,I)}L_{APL}\right) \end{pmatrix} \\ &\times \begin{pmatrix} 1 & d \\ 0 & 0 \end{pmatrix}\end{aligned} \tag{7.5}$$

Here, $d = 85\,\text{mm}$ is the distance from the plasma source to the APL, D is the distance after the APL, $L_{APL} = 40\,\text{mm}$ is the length of the APL (cf. Fig. 7.5) and $k(I,E)$ is the energy- and APL current-dependent focusing strength, as defined in Eq. 4.6. According to Eq. 4.17, the RMS beam size σ at a given distance D after the APL can be calculated as::

$$\sigma_D^2(E,I) = R_{11}^2(E,I,D)\beta_0\varepsilon - 2R_{11}(E,I,D)R_{12}(E,I,D)\alpha_0\varepsilon(E) + R_{12}^2(E,I,D)\gamma_0\varepsilon \tag{7.6}$$

Here, α_0, β_0, and γ_0 are the Twiss parameters at the electron source, and ε is the geometric emittance. For the calculations, a symmetric beam profile is assumed, meaning the x and y phase space coordinates are identical. The initial beam properties at the plasma source are assumed to be $\sigma_0 = 1\,\mu\text{m}$, $\alpha_0 = 0$, and a normalized emittance of $\varepsilon_{\text{norm}} = 1\,\mu\text{m}$. The geometric emittance ε can be calculated using Eq. 4.13, while the Twiss parameters β_0 and γ_0 can be determined using $\beta_0 = \frac{\sigma_0}{\varepsilon}$ and $\gamma_0 = \frac{1+\alpha_0^2}{\beta_0}$, as outlined in Sec. 4.3.2.

To perform the matrix calculations, the energy- and current-dependent focusing strength of the APL needs to be determined. This will be done in order to calculate the energy transfer function of the APL and collimator setup, enabling the estimation of the electron spectrum at the entrance of the polarimeter. First, the APL current will be retrieved, and the resulting focusing strength will be compared with the actual observed performance, using spectrometer data for validation. Once this comparison

has been made, the energy transfer function will be defined and calculated, based on the APL current settings.

APL Current

In this section, the measurement and retrieval of the APL current, introduced by the APL discharge, will be outlined. For further details, a comprehensive description of the APL discharge setup can be found in [85].
The current passing through the plasma is measured utilizing an inductive coil (Person Current Monitor 6595) at the ground cable of the APL electrode, yielding an output of $0.5\,\frac{V}{A}$. This signal is attenuated via a 60 dB attenuator and digitized employing an ADC with a conversion factor of $\frac{1}{27600}\left[\frac{\mathrm{V}}{ADC_{\mathrm{count}}}\right]$. The precise signal attenuation introduced by the BNC cable and the 60 dB attenuator between the pickup coil and the ADC was assessed utilizing a square pulse, 10 Hz with an amplitude of 5 V, generated by a pulse generator and subsequently measured using an oscilloscope. The total attenuation was determined to be $\frac{5.66\,\mathrm{mV}}{4.96\,\mathrm{V}} \approx \frac{1}{876}$. The APL current can be derived from the ADC count via the conversion:

$$I_{\mathrm{APL}} = 2 \cdot 876 \cdot \frac{1}{27600}\left[\frac{\mathrm{V}}{ADC_{\mathrm{count}}}\right] \cdot \frac{1}{0.5}\left[\frac{\mathrm{A}}{\mathrm{V}}\right] \cdot ADC_{\mathrm{count}} \tag{7.7}$$

The additional factor of 2 arises here from the pickup coil to BNC characteristics. In the experiment, the voltage value of the APL discharge was set to adjust the APL current and, consequently, the focusing strength of the APL. The set voltage value will be utilized to denote the APL setting.
In Fig. 7.19 a), an exemplary current profile of the APL discharge is presented for an APL setting of 16 kV. The profile exhibits a first pulse with a plateau and a secondary pulse which is merely a reflection of the first one. Since the electron bunch length is on the order of a few femtoseconds and thus short compared to the discharge profile, each shot can be attributed a constant current value. A signal from a photodiode is employed to ascertain the current observed by the electron beam, assuming the electron beam timing coincides with the laser timing. The diode signal was recorded using the same ADC and is illustrated in Fig. 7.19 a) as red dashed lines. Since the diode indicates the laser timing in the laser lab, it necessitates a delay of 120 ns to synchronize with the timing in the LPA chamber, represented here as a solid red line. Consequently, the current value perceived by the electron beam corresponds to the time when the delayed diode signal peaks.

In Fig. 7.19 b), the mean value and standard deviation of the derived APL current are shown for four different data runs, corresponding to APL high voltage settings of 16 kV, 18 kV, 20 kV and 24 kV. The data clearly demonstrate that the APL current scales linearly with the voltage setting. For the most commonly used APL setting of 20 kV, the APL current was measured at 423 A with a standard deviation of 3 A, based on approximately 12000 consecutive shots.

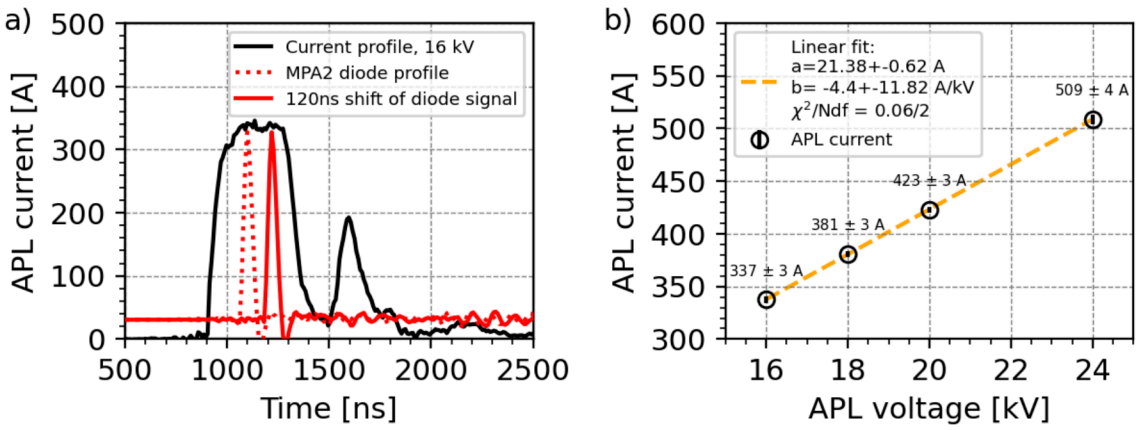

Figure 7.19.: a) APL discharge current (black) and diode timing signal (red). b) Measured APL current I for four different APL settings.

Focusing Strength of the APL

The focusing strength of the APL is linearly related to the discharge current and can be calculated using the measured APL current I, as described in Eq. 4.6. With this the energy dependent beam size along the beam path can be calculated using Eq. 7.6. In this section, the calculated APL focusing performance will be validated by comparing it with the actual observed performance, as derived from the spectrometer data. In the following discussion, the APL's performance will be characterized based on the discharge current, since the focusing strength of the APL depends on it. The measured APL current will be denoted as I, while I_{eff} will represent the current required for calculations to match the actual observed APL focusing performance.
To measure the APL focusing performance relative to I, spectrometer data was collected from an APL scan ranging from 14 kV to 24 kV in 0.5 kV steps, with approximately 50 shots per step. An exemplary spectrometer image is shown in Fig. 7.20 a), demonstrating the beam focused onto the screen with the APL operating at 19 kV. Un-

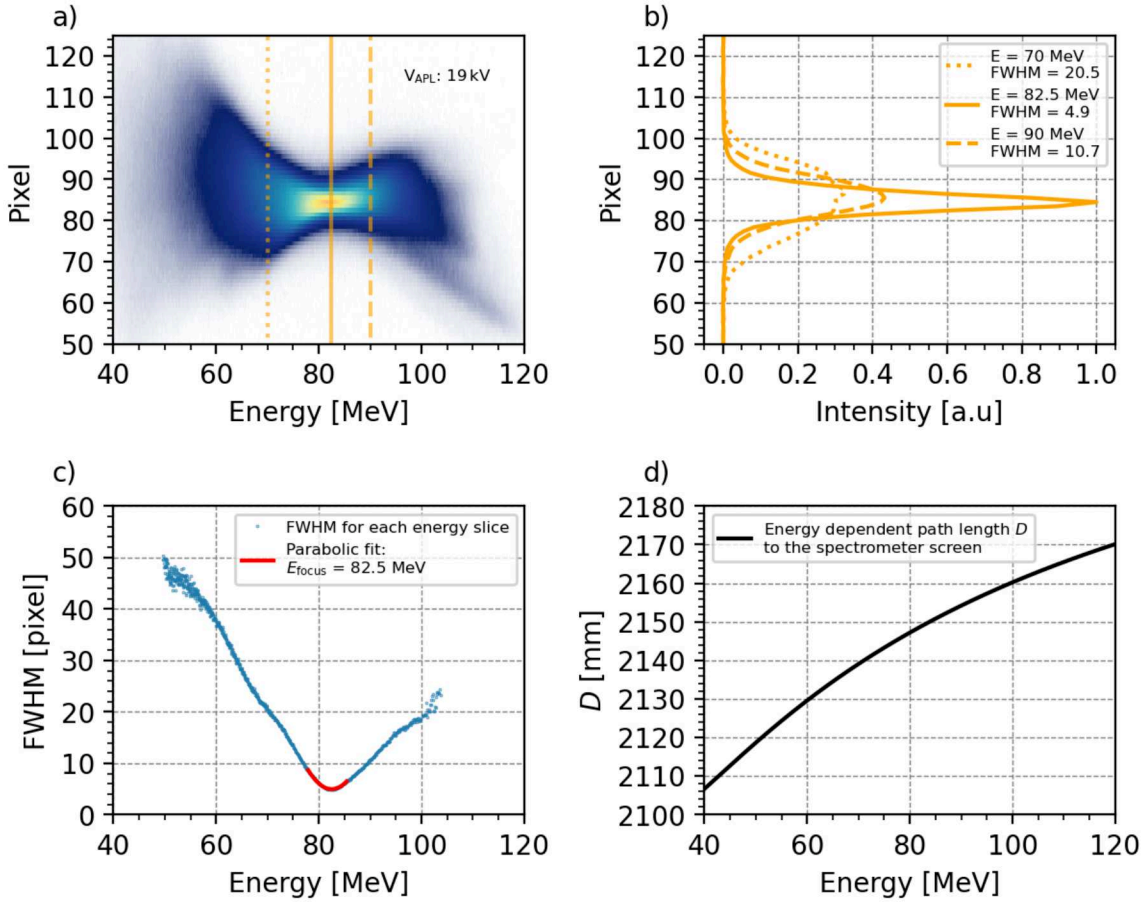

Figure 7.20.: a) Example of a single-shot spectrometer image for a focused electron beam with an APL setting of 19 kV. b) Lineouts of the spectrometer energy slices at three different positions, marked in orange in a). c) FWHM of each energy slice with a parabolic fit to determine the focused energy. d) Simulated energy-dependent drift length D from the end of the APL to the spectrometer screen for a dipole current of 180 A (simulations performed by Martin Meisel [85]).

like spectrometer images for shots where the APL is off (see Fig. 7.15), the image with the APL in operation displays a butterfly-like shape, with a distinct beam waist. This pattern results from the combination of beam dispersion by the spectrometer dipole magnet and symmetric focusing by the APL. The energy in focus for the respective APL setting appears as the waist of the butterfly figure on the spectrometer screen. To determine the waist of the figure and, therefore, the energy in focus, the FWHM of each lineout of the image along the energy axis is utilized. Figure 7.20 b) shows the lineouts for three different energy slices, marked with dashed orange lines in panel a). Panel c) shows the FWHM for each energy slice along the energy axis, clearly revealing the waist and the focused energy. A parabolic fit (shown in red) is applied to the data

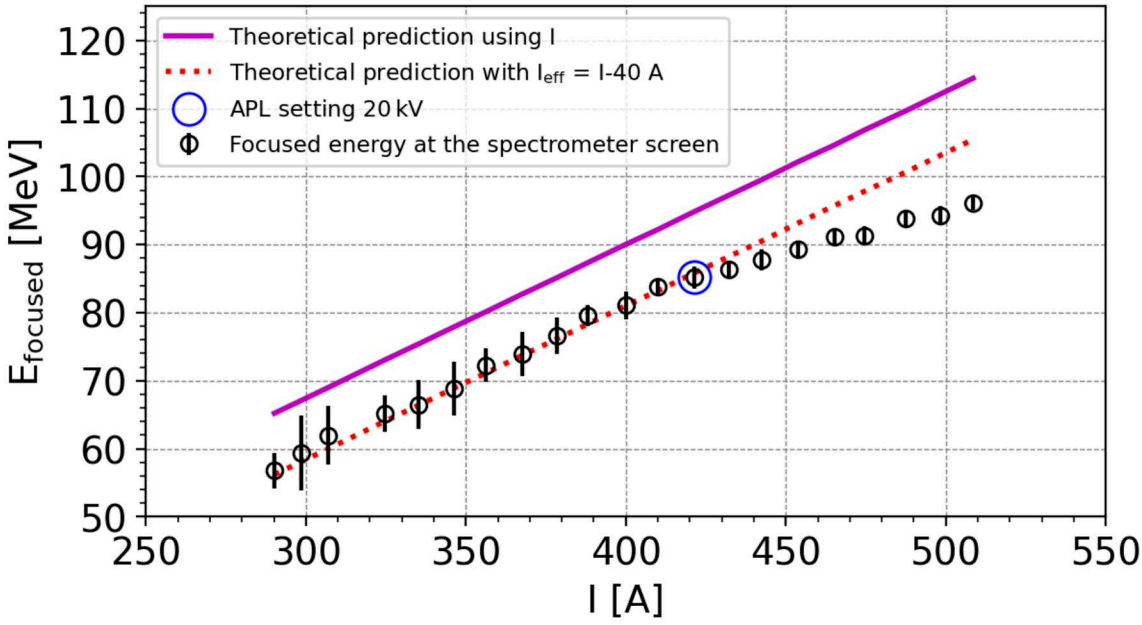

Figure 7.21.: Focused energy on the spectrometer screen with respect to the APL current. The black dots show the data retrieved using the spectrometer images. The purple solid line show theoretical prediction. The red dashed line show the theoretical prediction for a corrected APL current I_{eff} = I - 40 A. The blue circle marks the predominately used APL setting of 20 kV.

around the minimum to determine the focused energy. This process is repeated for all calibrated spectrometer images captured during the APL scan. The determined mean values of the energy focused onto the spectrometer screen for each scanned APL current I are represented by black circles in Fig. 7.21. The purple solid line illustrates the theoretical prediction calculated using Eq. 7.6, with the measured discharge current I, the energy-dependent beam path D of the electrons from the exit of the APL to the spectrometer screen, as displayed in Fig. 7.20 d), and Eq. 7.6.

The energies observed in focus on the spectrometer screen (black circles) for a given APL current are lower than the calculated energies predicted to be in focus for the same current. This suggests that the actual focusing strength is weaker than expected. Since the APL current scales linearly with the focusing strength, it can be concluded that the measured APL current is higher than the effective APL current I_{eff}. To illustrate this, the red dashed line represents the calculated focused energies using an effective current, with $I_{\text{eff}} = I - 40\,A$. Using the effective current, the calculations align well with the data up to an APL setting of 20 kV (marked with a blue circle). Beyond this point, the data shows some saturation effects that are not yet understood and

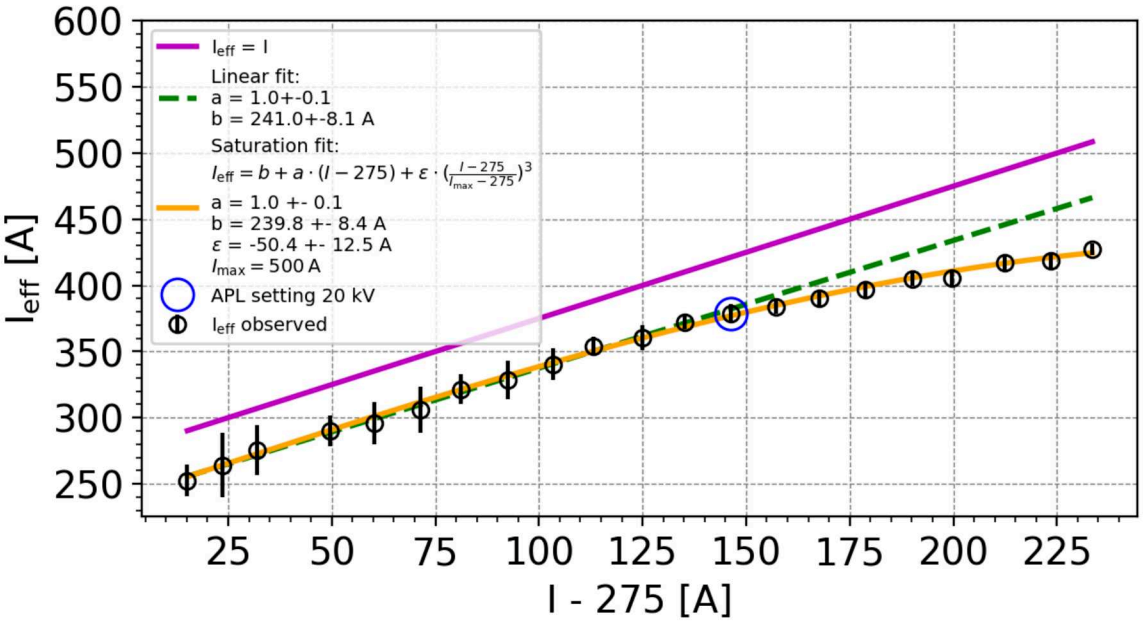

Figure 7.22.: APL effective current I_{eff} with respect to the measured APL current I. The data is fitted (including the first 13 data points) with a linear fit, represented by the dashed green line. The orange line shows a fit to the entire dataset, referred to as the saturation fit in the legend. The purple line shows the case of $I_{\text{eff}} = I$, for comparison. The blue circle marks the predominantly used APL setting of 20 kV.

may be addressed in a future study. For the subsequent analysis, the conversion from the measured APL current I to the effective APL current I_{eff} – observed through spectrometer data – will be determined to enable more accurate APL beam transport calculations. From the observed energy in focus on the spectrometer screen for a given measured APL current (see Fig. 7.21), the corresponding I_{eff} can be retrieved using Eq. 7.6 and the energy-dependent electron drift length to the screen, as shown in Fig. 7.20 d).

The retrieved I_{eff} is depicted with respect to the measured current I in Fig. 7.22, where the I axis is arbitrary shifted by -275 A to fit the data just across the relevant regions of the APL discharge. The purple solid line represents the estimation of $I_{\text{eff}} = I$, and the blue circle marks the APL setting of 20 kV. The effective current shows a linear relation to the measured I, with a constant offset indicated by a linear fit of the first 13 data points, showing a slope of one. To account for the data, including the saturation above 420 A, a linear fit is applied, suppressed by a cubic term:

$$I_{\text{eff}}[\text{A}] = b + a \cdot (I - 275)[\text{A}] + \epsilon \cdot \left(\frac{(I - 275)[\text{A}]}{(I_{\text{max}} - 275)[\text{A}]} \right)^3 \tag{7.8}$$

where the saturation parameter ϵ indicates the deviation of $I_{\text{max}} = 500\,A$ from the linear fit. The saturation fit is drawn as orange solid line. Both the linear and saturation fit yield similar parameters for a and b, as noted in the figure's legend. Unless stated otherwise, in the following the retrieved fit parameters a, b and ϵ from the saturation fit (Eq. 7.8) will be used to calculate I_{eff} for modeling the APL's focusing performance.

Transmission Function

Assuming a beam with a Gaussian spatial beam profile, the beam width $\sigma(E, I, z)$ along the beam path can be calculated using Eq. 7.6. Figure. 7.23 illustrates the calculated beam width for the experimental setup, starting from the plasma cell and extending along the beam path to the collimator, for five different energies. For the calculation, the APL current is fixed at $I_{\text{eff}} = 378\,\text{A}$, corresponding to the effective APL current for an APL setting of 20 kV. The APL capillary is depicted in orange, while the solid copper bulk of the collimator, featuring a cylindrical aperture of 1 mm, is shown in light gray.

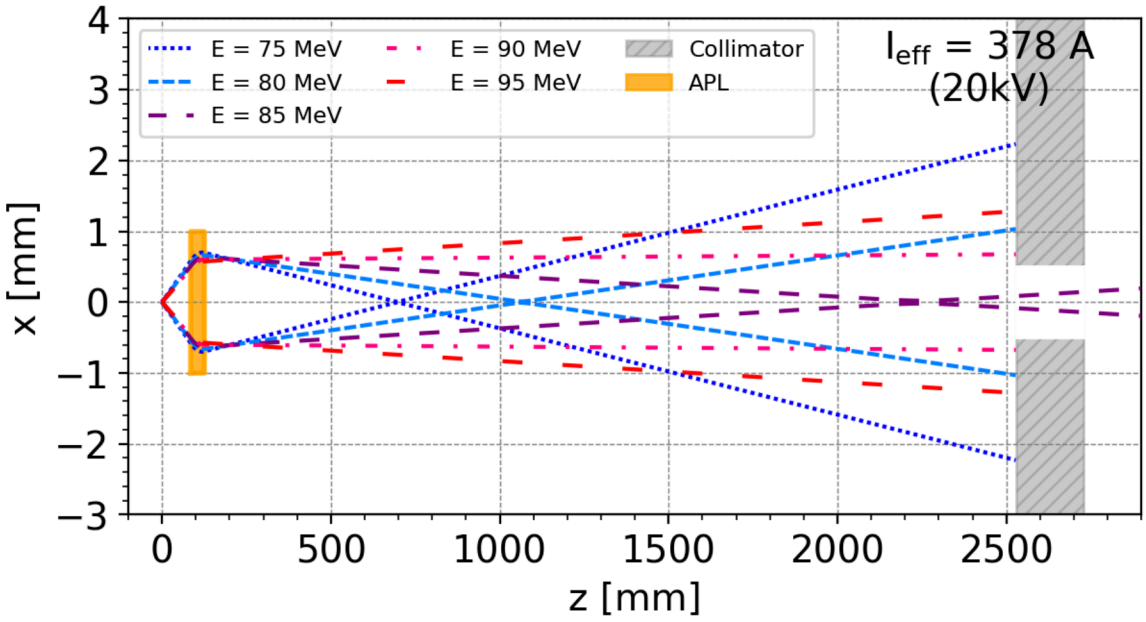

Figure 7.23.: Beam envelope along the z-axis for the APL setting of 20 kV (I_{eff} = 378 A) for different beam energies. The APL capillary and the collimator copper bulk are depicted in orange and light gray, respectively.

The results clearly demonstrate that the focal length is highly sensitive to changes in energy, with the focus shifting along the z-axis toward the collimator as the energy increases. Beyond a certain energy, the focusing strength of the APL becomes insufficient to converge the beam, resulting in beam divergence. This energy-dependent focal length leads to variations in beam size at the collimator entrance, as depicted in Fig. 7.24 a). Consequently, the transmission through the collimator also becomes energy-dependent, as different parts of the energy spectrum are either transmitted or suppressed, depending on the degree of clipping by the collimator aperture.

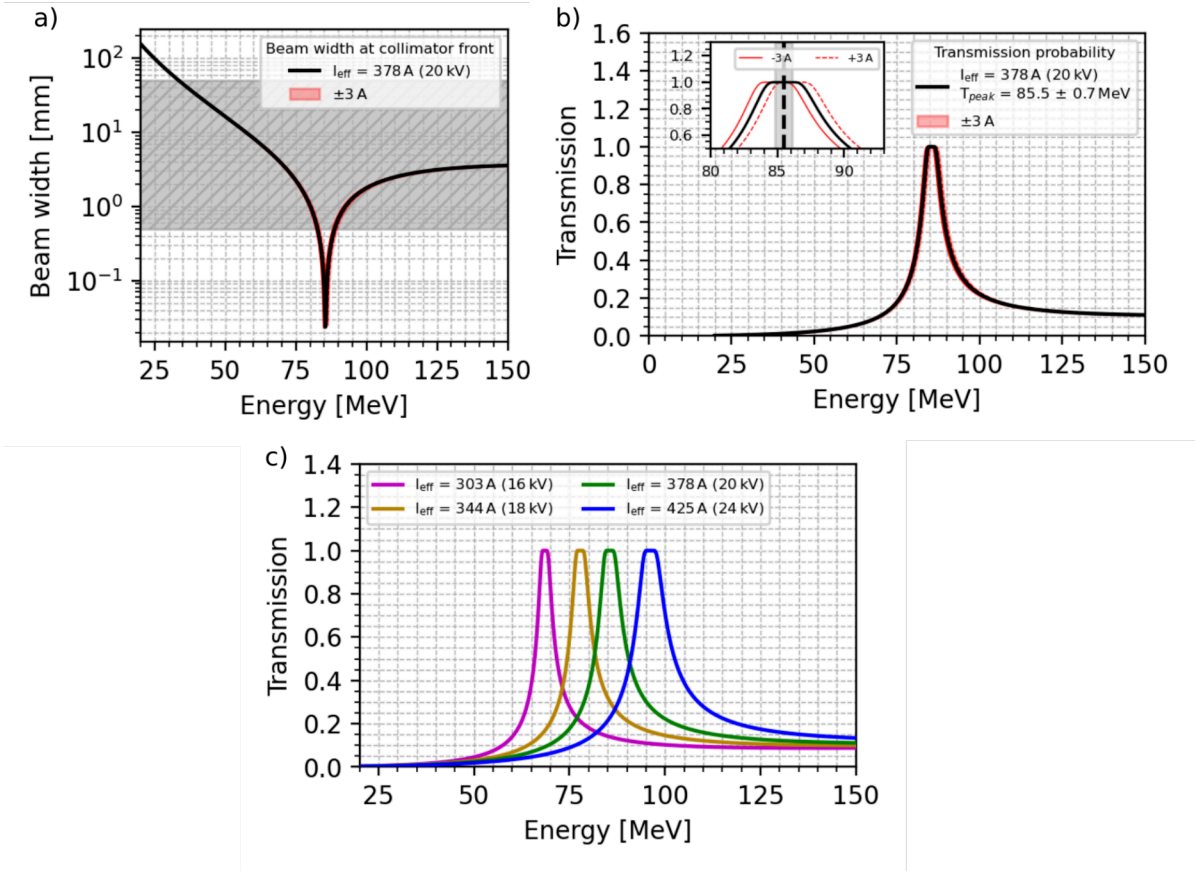

Figure 7.24.: a) Beam size at the front plane of the collimator for an APL setting of 20 kV ($I_{\text{eff}} = 378$ A). The gray area represents the solid copper bulk of the collimator. b) Calculated transmission probability, shown as a solid black line. The red band denotes the influence due to a APL current variation of ± 3 A. The inset provides a close-up view of the transmission peak. c) Transmission probability for four different APL settings (16 kV, 18 kV, 20 kV and 24 kV) as applied in the experiment.

To quantify this filtering or energy suppression effect, a simple model is employed. It is assumed that all beam electrons entering the collimator aperture pass through it unobstructed, while those outside the aperture are stopped at the front surface of the

solid copper bulk of the collimator. Based on this assumption the fraction of the beam transmitted through the collimator, relative to the initial beam, can be expressed as

$$T(\sigma(E,I,z),r) = \frac{\int_{-\infty}^{\infty} f(x)\cdot \exp\left(-\frac{x^2}{2\sigma^2}\right)\, dx}{\int_{-\infty}^{\infty} \exp\left(-\frac{x^2}{2\sigma^2}\right)\, dx} \tag{7.9}$$

where $f(x)$ is defined as:

$$f(x) = \begin{cases} 1 & \text{for } -r \leq x \leq r \\ 0 & \text{else} \end{cases} \tag{7.10}$$

Here, σ represents the energy- and APL current-dependent beam size at the z-position of the collimator entrance plane (Eq. 7.6), while r denotes the radius of the collimator's aperture. Since the beam size at the collimator front depends on the energy and the applied APL current, $T(E,I)$ becomes a function of E and I and will henceforth be referred to as the energy transmission probability.

Figure 7.24 b) shows the calculated transmission probability as a function of electron energy for an effective APL current of 378 A (20 kV setting) represented by the solid black line. The transmission curve exhibits a narrow shape peaking at around 85 MeV. Fluctuations in the APL current, estimated at approximately ± 3 A (see Fig. 7.19 b)), introduce slight shifts in the transmission curve, visualized by the red band. A close-up of the transmission peak is provided in the inset figure, were the ± 3 A variation is indicated by red dashed lines. These current fluctuations result in a peak transmission shift of ± 0.7 MeV.

For the transmission model, the beam size at the collimator front was used, as electrons outside the aperture at this position are definitively blocked. One could argue that the beam divergence (cf. Fig. 7.23) over the length of the collimator ($L_c = 200$ mm) could result in additional electron loss, even for electrons initially within the aperture. However, this effect is relatively small compared to the influence of the APL current. For instance, using the beam size at the collimator's center position for the calculation of T results in a shift of approximately 0.1 MeV of the transmission peak which is considered negligible. The influence of APL current uncertainties on the transmission function, and consequently on the transmitted electron spectrum, is accounted for in the analyzing power of the polarimeter [34], as discussed in Sec. 7.7.4.

In Fig. 7.19 c), the transmission function is shown for different APL currents corresponding to APL settings of 16 kV, 18 kV, 20 kV, and 24 kV, visualizing the shift of the

transmission probability with respect to the applied APL current. This energy- and APL current-dependent transmission allows for the selective filtering of a narrower portion of the broad initial LPA spectrum which will be discussed in the next section.

7.6.3. Electron Transmission Spectra

As outlined earlier, the APL and collimator in the beamline influence the LPA energy spectrum that reaches the polarimeter. Since no direct measurement of the energy spectrum entering the polarimeter after the collimator was available, this section aims to estimate the transmitted spectrum using the previously introduced energy- and APL current-dependent transmission model (see Sec. 7.6.2) which will be validated to some extent by comparing it to the signals observed in the LEAP calorimeter.

Expected Energy Spectrum at the Polarimeter

The energy and APL current-dependent transmission through the collimator can be calculated using Eqs. 7.9 and 7.6. To compute the energy-dependent transmission probability for various APL settings used in the experiment, the effective APL current I_{eff} is employed. The relation between the measured APL current, as shown in Fig. 7.19 b), and I_{eff} is given by Eq. 7.8. To retrieve the transmitted energy spectrum, the initial LPA energy spectrum, measured with the electron spectrometer, is weighted with the calculated transmission function, as shown in Fig. 7.24.
Figure 7.25 shows the resulting transmitted energy spectra for the APL settings of 16 kV, 18 kV, 20 kV, and 24 kV alongside with the fundamental LPA spectrum. The fundamental spectrum used here corresponds to the average energy spectrum depicted in Fig. 7.17 a). It is evident that the peak energy transmitted through the collimator scales well with the APL current. Additionally, the spectrum's FWHM is reduced by a factor of 5 to 10, highlighting the potential of the APL in conjunction with the collimator in narrowing the spectral width and tuning the energy peak for experimental purposes. While these results are based on calculations using simple assumptions, such as Gaussian beam profiles, a more accurate investigation could involve direct measurement of the post-collimator spectrum using an electron spectrometer, potentially complemented by particle tracking simulations (e.g., PIC simulations) to model the transmission through the collimator more precisely. However, this is beyond the scope of this thesis.

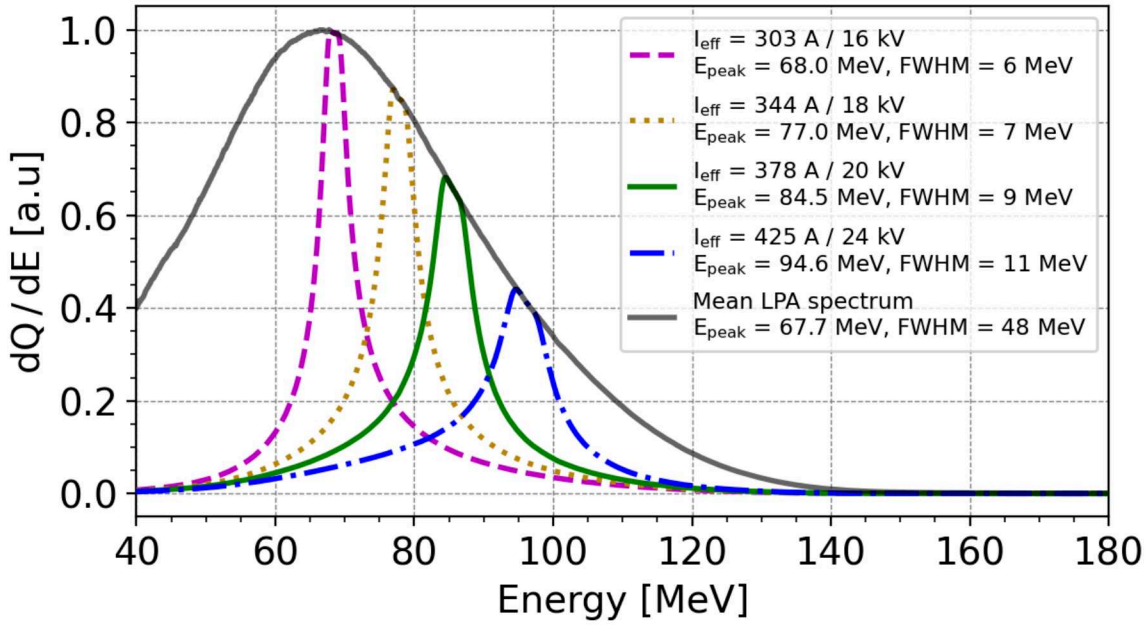

Figure 7.25.: Estimated transmitted energy spectrum through the collimator for four different APL settings.

The combined effect of the APL filtering and the collimator likely not only improves the spectral shape but also enhances stability, thanks to the selective nature of the process. To quantify this, the transfer function for an APL setting of 20 kV will be applied to the 3039 initial electron spectra of the long spectrometer run (50281), as shown in Fig. 7.17. The resulting estimated electron spectra entering the polarimeter are displayed in Fig. 7.26 a), with the average spectrum represented by a black line, while the individual spectra are shown in cyan. Additionally, three single spectra are marked with blue dashed lines, in a manner similar to Fig. 7.17. The deviation of the mean energy, averaged over a 5-minute interval, from the overall mean is depicted in Fig. 7.26 b). In this instance, the largest variation in mean energy between two consecutive 5-minutes intervals is approximately 0.3 MeV, representing an improvement by a factor of about 3 compared to the energy deviation observed without energy filtering (see Fig. 7.18 d)).

For an estimation of the resulting fake asymmetry due to energy drift between intervals, the mean energies of the intervals with the largest deviations, 84.1 MeV and 84.7 MeV, are used (similar to Sec. 7.6.1). These correspond to simulated detector signals of $E_{ct} = 0.681$ MeV and $E_{ct} = 0.686$ MeV ,respectively , obtained through linear interpolation of the simulated polarimeter energy response to unpolarized electron beams (see Fig. 7.3). Based on these E_{ct} values, the fake asymmetry is estimated

to be approximately $\delta_E \approx |0.4|\,\%$. While this represents a significant improvement compared to the fake asymmetry estimated without energy filtering (see Sec. 7.6.1), it remains considerably larger than the expected asymmetry of $\delta \sim 0.1\,\%$ which is anticipated for an idealized electron beam with approximately 10 % polarization (see Sec. 7.1.2).
Although this analysis provides an initial estimate of the potential fake asymmetry due to beam energy drifts during this experimental campaign, it highlights the importance of improving the energy stability of LPA electron beams to pave the way for reliable polarization measurements in the future.

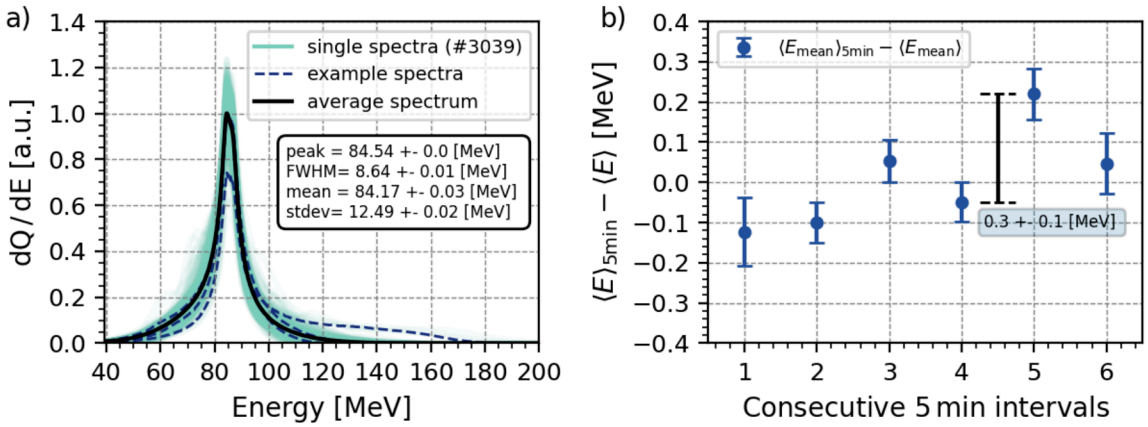

Figure 7.26.: a) Average shape of the expected electron spectrum (solid black line) entering the polarimeter for an APL setting of 20 kV, calculated from 3039 consecutive initial LPA spectra, with all individual spectra overlaid in cyan. b) Deviation of the spectral mean, averaged over consecutive 5-minute intervals, from the overall average mean energy.

Validation of the Electron Transmission Spectra

In this section, the calorimeter signals are analyzed across various APL settings to investigate and partially validate the spectral filtering effects produced by the combination of the APL and the collimator. According to polarimeter simulations using the `leap_sims` tool, the calorimeter signal scales with the energy of electrons incident on the polarimeter solenoid surface as shown in Fig. 7.3. Due to this energy dependence, the calorimeter signal is expected to correlate with shifts of the energy spectrum.
Fig. 7.27 a) shows the correlation between the calorimeter signal Q and the DRZ-high scintillator screen signal S_{scint} for the four APL settings: 16 kV (purple), 18 kV (yellow),

20 kV (green), and 24 kV (blue). Comparing the different APL settings, shots with identical beam charge (S_{scint}) exhibit higher calorimeter signals, as expected, due to the shift in the transmitted energy spectrum (see Fig. 7.25). By normalizing the calorimeter signal Q by the relative beam charge S_{scint}, the energy scaling effect becomes more evident, allowing a more quantitative assessment of the energy-dependent shift, as shown in Fig. 7.27 b). Only shots with DaMon charge greater than 3 pC and $S_{\text{scint}} > 20000$ were considered. Notably, a higher mean value of the respective distributions, indicated by the dashed black lines, corresponds to an APL setting with increased energy. To further validate the transmission spectra, the experimentally observed

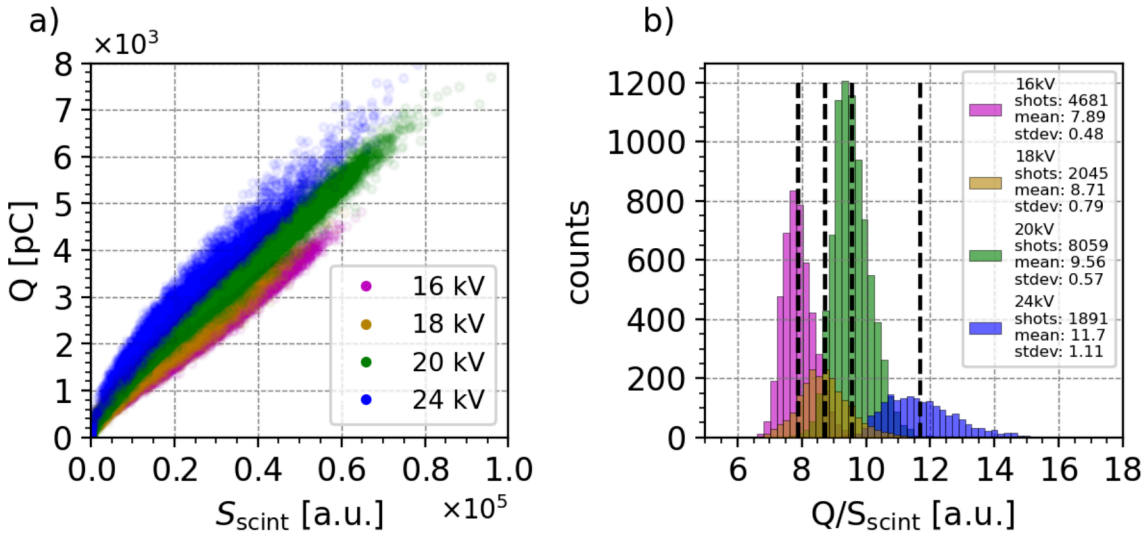

Figure 7.27.: a) Correlation of calorimeter signal Q and DRZ-high scintillator screen signal S_{scint} for APL settings of 16 kV, 18 kV, 20 kV, and 24 kV, shown in purple, yellow, green, and blue, respectively. b) Calorimeter signal normalized by beam charge $\frac{Q}{S_{\text{scint}}}$ for the four different APL settings.

energy-dependent shift of the calorimeter signal is compared to `leap_sims` polarimeter simulation results. In the simulations, unpolarized electron beams with a fixed bunch charge of of 0.08 pC (5×10^5 electrons) and an energy spectrum corresponding to the retrieved transmission spectra for the respective APL settings, as shown in Fig 7.25, are used. A total of 1000 electron bunches were simulated for each APL setting.
Figure 7.28 a) shows the mean of the normalized calorimeter signal as a function of the mean of the simulated calorimeter signal E_{ct} (defined in Sec. 6.2.2). The respective signal distributions corresponding to the different APL settings are shown along the x- and y-axes. Up to an APL setting of 20 kV, the data aligns well with the simulation expectations, as indicated by the linear fit (red dashed line). However, for the 24 kV

setting, the signals deviate from this proportionality. This discrepancy could be explained by the saturation observed in the effective APL current I_{eff} which occurs for APl setting above 20 kV (see Fig. 7.22), as the transmission spectra were calculated following this saturation. In Fig. 7.28 b), similar to Fig. 7.28 a), the observed calorimeter signal is shown as a function of the simulation expectation. However, in this case, the energy spectra used for the simulation were calculated based on the assumption of purely linear behavior of the APL current I_{eff}, as indicated by the dashed green line in Fig. 7.22. Under this assumption, the calorimeter's energy response aligns with simulation expectations across all APL settings. This suggests that the apparent saturation in APL focusing performance may not be inherent to the APL itself, but rather an artifact of the energy measurement or analysis of the spectrometer data. This issue will require further investigation in future studies. Nevertheless, for this thesis, this effect is not critical, as the predominant APL setting during the experiment was 20 kV, and the saturation is primarily relevant for settings above 20 kV (see Fig. 7.22). In summary, the proportionality observed between the calorimeter energy scaling in the simulation and experiment supports and reinforces the validity of the calculated energy transmission spectra for APL settings $\leq$ 20 kV, as displayed in Fig. 7.25.

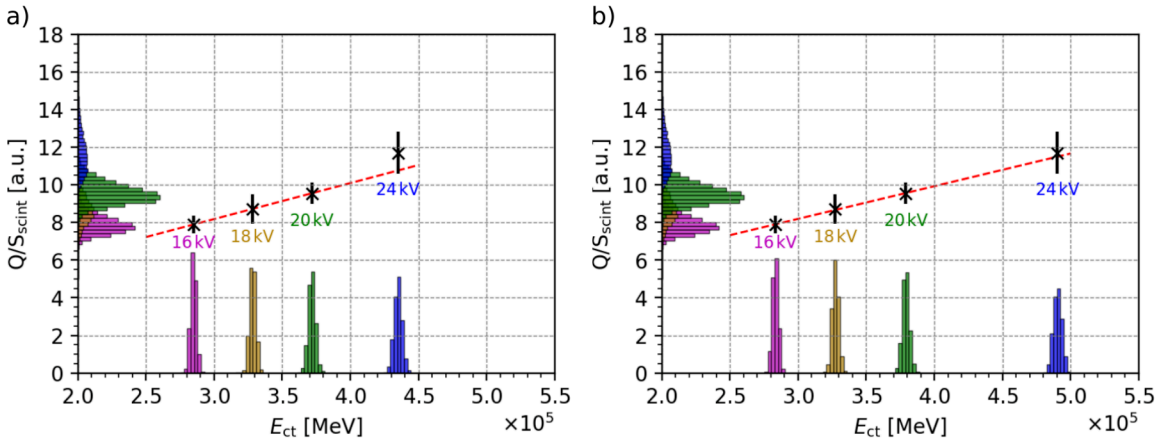

Figure 7.28.: a) Charge-normalized calorimeter signal $\frac{Q}{S_{\text{scint}}}$ vs. `leap_sims` simulation expectations for four different APL settings (16 kV, 18 kV, 20 kV, and 24 kV). The simulations were conducted using 1000 bunches per APL setting with unpolarized electrons and a fixed bunch charge of 5×10^5 electrons, incorporation the APL-dependent energy spectrum shown in Fig. 7.25. The respective signal distributions are shown on the x- and y-axes. b) Same as a), where the energy spectra used for the simulation are calculated based on the assumption of purely linear behavior of the APL current I_{eff} (dashed green line in Fig. 7.22).

7.7. Polarization Measurement

Based on the gained understanding of the calorimeter performance and the achieved level of control of the main beam parameters, we can now turn to the actual polarization measurement. Since the polarized source could not be completed on the timescale of this thesis, the target is to measure zero polarization, which is particularly sensitive to any kind of fake asymmetries and thus a very important system test. The degree of electron polarization can be calculated using Eq. 3.8, where the analyzing power A and its expected error due to beam conditions and fluctuations need to be derived from detailed simulations. The asymmetry δ will be calculated from the measured calorimeter signal with respect to the magnet polarization. The following sections will present the analysis of the asymmetry measurement, the determination of the analyzing power under the experimental conditions of this campaign, and the resulting polarization calculation with its corresponding precision. The results will be discussed to identify the largest sources of uncertainty in the polarization measurement, in order to define future improvements and pave the way for accurate real polarization measurements.

7.7.1. Asymmetry Calculation

The asymmetries are derived from pairs of consecutive magnet current periods with opposite polarities. In general, for one cycle and a general measured quantity X (e.g., the calorimeter signal Q), the asymmetry is defined as:

$$\delta = \frac{\langle X \rangle_{\mathrm{P}} - \langle X \rangle_{\mathrm{N}}}{\langle X \rangle_{\mathrm{P}} + \langle X \rangle_{\mathrm{N}}}. \tag{7.11}$$

where $\langle X \rangle_{\mathrm{P}}$ and $\langle X \rangle_{\mathrm{N}}$ are the mean values of the signal X for the positive (P, +, 60 A) and negative (N, -,-60 A) period of the magnet current, respectively. Following statistical error propagation, the statistical error is given by:

$$\Delta\delta = \frac{2\langle X \rangle_{\mathrm{P}} \cdot \langle X \rangle_{\mathrm{N}}}{\left(\langle X \rangle_{\mathrm{P}} - \langle X \rangle_{\mathrm{N}}\right)^2} \cdot \sqrt{\left(\frac{\Delta\langle X \rangle_{\mathrm{P}}}{\langle X \rangle_{\mathrm{P}}}\right)^2 + \left(\frac{\Delta\langle X \rangle_{\mathrm{N}}}{\langle X \rangle_{\mathrm{N}}}\right)^2} \tag{7.12}$$

where ΔX_{N} and ΔX_{N} are the uncertainties of the mean values for the positive and negative current periods, respectively.

7.7.2. Impact and Considerations of Fake Asymmetries

In general, for a polarization measurement with the LEAP polarimeter, the asymmetry is calculated using the measured calorimeter signal $\langle Q \rangle$ according to Eq. 7.11 between intervals where the magnet current is positive (P, +) and negative (N, -), respectively. Therefore, any variation in $\langle Q \rangle$ between the P and N cycles that is unrelated to polarization effects will introduce a fake asymmetry δ_{F}. These variations may be caused by initial beam properties, such as drifts in beam energy or charge, or by other effects that correlate with the magnet polarity and influence Q. All of these factors contribute to systematic uncertainties due to the introduction of fake asymmetries in the measurement.
To understand how the polarization-induced asymmetry δ_{p} combines with a fake asymmetry, a generic case is first considered where $\langle Q \rangle_{\pm}$ is proportional to $T_{\pm}$, the polarization-dependent transmission, and an additional quantity $F_{\pm}$:

$$\langle Q \rangle_{\pm} \sim F_{\pm} \cdot T_{\pm} \tag{7.13}$$

Here, $F_{\pm} = F \pm \Delta F$ represents a quantity (e.g., beam charge) that changes between the P and N intervals by a small variation ΔF. By substituting this expression into Eq. 7.11, the measured asymmetry δ_{Q} is given by:

$$\delta_{\mathrm{Q}} = \frac{\delta_{\mathrm{p}} + \delta_{\mathrm{F}}}{1 + \delta_{\mathrm{p}}\delta_{\mathrm{F}}} \tag{7.14}$$

where $\delta_{\mathrm{p}} = \frac{T_+ - T_-}{T_+ + T_-}$ is the asymmetry due to polarization-dependent transmission, which is of interest, and $\delta_{\mathrm{F}} = \frac{\Delta F}{F}$ represents the fake asymmetry.

Given the stability of the LPA beam during this measurement campaign, the initial beam conditions – specifically the charge and energy, as evaluated in Sec. 7.5 and Sec. 7.6 – are expected to be the most significant sources of systematic errors due to fake asymmetries. Assuming that both the beam energy E and the beam charge q differ simultaneously between the P and N intervals (i.e., $\langle E \rangle_+ \neq \langle E \rangle_-$ and $\langle q \rangle_+ \neq \langle q \rangle_-$) and Q being proportional to E for small changes ΔE. These changes introduce asymmetries in both beam charge and energy, given by $\delta_q = \frac{\langle q \rangle_+ - \langle q \rangle_-}{\langle q \rangle_+ + \langle q \rangle_-}$ and $\delta_E = \frac{\langle E \rangle_+ - \langle E \rangle_-}{\langle E \rangle_+ + \langle E \rangle_-}$, respectively. Since these asymmetries are unrelated to electron polarization, they contribute to a fake asymmetry. In this case, the fake asymmetry can be expressed as $\delta_{\mathrm{F}} = \frac{\delta_q + \delta_E}{1 + \delta_q \delta_E}$ which is analogous to Eq. 7.14.

Substituting this back into Eq. 7.14, the following expression is obtained:

$$\delta_Q = \frac{\delta_\mathrm{p} + \delta_q + \delta_E + \delta_\mathrm{p}\delta_q\delta_E}{1 + \delta_\mathrm{p}\delta_q + \delta_\mathrm{p}\delta_E + \delta_q\delta_E} \tag{7.15}$$

Assuming all asymmetries are small, the measured asymmetry δ_Q can be simplified by considering only the terms linear in δ, i.e.

$$\delta_Q \approx \delta_\mathrm{p} + \delta_q + \delta_E. \tag{7.16}$$

This implies that all fake asymmetries are expected to add linearly to the true asymmetry associated with polarization effects.
Within this measurement campaign, the beam charge – specifically the relative beam charge incident on the polarimeter, S_scint – was measured on a shot-to-shot basis using a scintillation screen (see Sec. 4.2.2). It was shown to be useful to normalize the calorimeter signal Q to the observed charge fluctuations on a shot-to-shot basis using S_scint. The resulting charge-fluctuation-corrected signal Q_c is discussed in detail in Sec. 7.5.2. Therefore, using Q_c for the asymmetry calculation is expected to eliminate possible fake asymmetries, δ_q, associated with drifts in the beam charge. However, since the beam energy in this experiment is not known on a shot-to-shot basis and, therefore, cannot be corrected, fake asymmetries due to beam energy drifts are still expected. These are estimated in Sec. 7.6.3 to potentially be on the order of a few per mille (e.g., $\delta_E \approx 0.4\,\%$). This implies that for this measurement campaign, where $\delta_p = 0$ due to the unpolarized beam, the asymmetry obtained using the charge-corrected calorimeter signal is expected to be dominated by the asymmetry caused by beam energy fluctuations, i.e., $\delta_{Q_\mathrm{c}} \approx \delta_E$, assuming that the main sources of fake asymmetries are beam charge and energy. This will be further assessed in the following section.

7.7.3. Measured Asymmetry

This section discusses and interprets the measured asymmetry from the main polarimeter run 50379. It should be noted that no polarization-dependent asymmetry is expected to be measured, as the beam is unpolarized. Any observed asymmetry is, therefore, considered a fake asymmetry and regarded as a systematic error of the measurement. The asymmetry will be calculated using the charge-normalized calorimeter signal Q_c (see Sec. 7.5.2) and compared to the asymmetries derived from

the raw calorimeter signal Q and the scintillator screen signal S_{scint}.
Figure 7.29 a) shows Q_c for each shot over the elapsed time of the main polarimeter run, identical to Fig. 7.13, where Q and S_{scint} are also presented. Again, the same quality cuts were applied, rejecting shots with beam charges q_{damon} less than 3 pC and shots where $S_{\text{scint}} < 20000$, as discussed in previous sections. Additionally, one negative interval was excluded due to an initial laser energy drop, leading to fewer valid shots in this period, marked by a gap around minute 40. Shots taken during the magnet ramping phase (approximately 30 seconds) were also excluded. The white

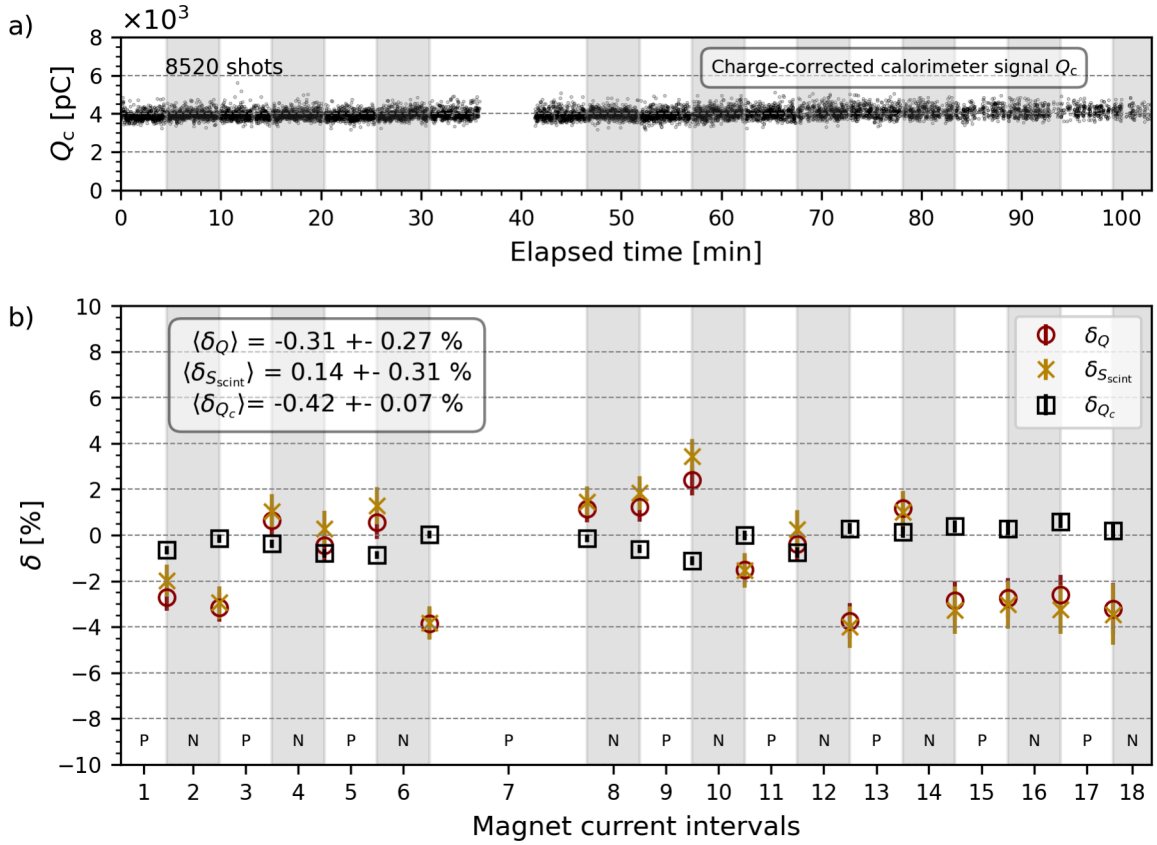

Figure 7.29.: a) Beam charge-corrected calorimeter signal Q_c for each shot considered for the main polarimeter run 50379. The white and grey bands represent the $\sim$5 min intervals where the solenoid current was set to +60 A (P) and -60 A (N), respectively. b) Calculated asymmetries for each interval using the charge-corrected calorimeter signal Q_c (black squares) compared with asymmetries calculated from the raw calorimeter signal Q (red circles) and the scintillator screen signal S_{scint} (yellow stars). Mean asymmetries $\langle\delta\rangle$ are shown with associated statistical errors, calculated using Eq. 7.11 and Eq. 7.12, incorporating data from all P and N intervals.

and grey bands indicate the periods where the magnet current was set to +60 A and -60 A, respectively. The final dataset contains 8520 shots. Figure 7.29 b) displays the asymmetry δ_{Q_c} for the charge-corrected calorimeter signal in black squares for each P-N and N-P magnet current interval, calculated using Eq. 7.11. The red circles represent the asymmetry δ_Q from the raw calorimeter signal, while the yellow crosses represent the asymmetry $\delta_{S_{\text{scint}}}$ from the scintillator screen signal. Statistical errors for the data points were calculated using Eq. 7.12.

Both δ_Q and $\delta_{S_{\text{scint}}}$ show significant fluctuations throughout the run, with asymmetry values reaching up to $\pm 4\,\%$. A strong correlation between δ_Q and $\delta_{S_{\text{scint}}}$ is observed, consistent with the assumption that the calorimeter signal is largely influenced by the beam charge. In contrast, the charge-corrected asymmetry δ_{Q_c} exhibits significantly reduced fluctuations and is markedly smaller than both δ_Q and $\delta_{S_{\text{scint}}}$.

The mean asymmetries for the entire dataset were calculated using Eq. 7.11, with associated errors from Eq. 7.12, incorporating data from all P and N intervals. The results are $\langle \delta_{Q_c} \rangle = -0.42 \pm 0.07\,\%$, $\langle \delta_Q \rangle = -0.31 \pm 0.27\,\%$, and $\langle \delta_{S_{\text{scint}}} \rangle = 0.14 \pm 0.31\,\%$. The asymmetries for the raw calorimeter signal, $\langle \delta_Q \rangle$, and the scintillator screen signal, $\langle \delta_{S_{\text{scint}}} \rangle$, are consistent with zero, given their large fluctuations and uncertainties. However, in the charge-corrected case $\langle \delta_{Q_c} \rangle$, the asymmetry deviates from zero by 6σ. As expected, the statistical uncertainty of $\langle \delta_{Q_c} \rangle$ is significantly reduced compared to $\langle \delta_Q \rangle$ and could potentially decrease further with improved resolution of the charge measurement in front of the polarimeter (cf. Sec. 7.5.3).

Comparing the mean asymmetries, it is evident that $\langle \delta_Q \rangle \approx \langle \delta_{S_{\text{scint}}} \rangle + \langle \delta_{Q_c} \rangle$. Assuming that other systematic effects are negligible, $\langle \delta_{Q_c} \rangle$ can be attributed to a fake asymmetry caused by beam energy drifts (Eq. 7.16), as discussed in the previous section. The fact that the retrieved asymmetry is comparable to the potential fake asymmetry caused by energy drifts, $\delta_E \approx 0.4\,\%$, as estimated in Sec. 7.6.3 based on the exemplary spectrometer run 50281, further supports this assumption.

To further investigate this, a similar analysis was performed on run 50282, which had the same APL setting of 20 kV, but with the magnet current off. Figure 7.30 shows the results, following the same structure as Fig. 7.29. Panel a) shows the charge-corrected calorimeter signal Q_c for the 3601 considered shots of the data set, with data grouped into positive and negative intervals, mimicking the 5-minute intervals from the polarization measurements. Panel b) shows the calculated asymmetries for these intervals. Similar trends are observed in both the magnet-off run and the main polarimeter run. The asymmetry δ_Q closely follows the incident charge asymmetry $\delta_{S_{\text{scint}}}$. The resulting mean asymmetries for this run are $\langle \delta_{Q_c} \rangle = -0.27 \pm 0.14\,\%$, $\langle \delta_Q \rangle = 0.29 \pm 0.37\,\%$, and

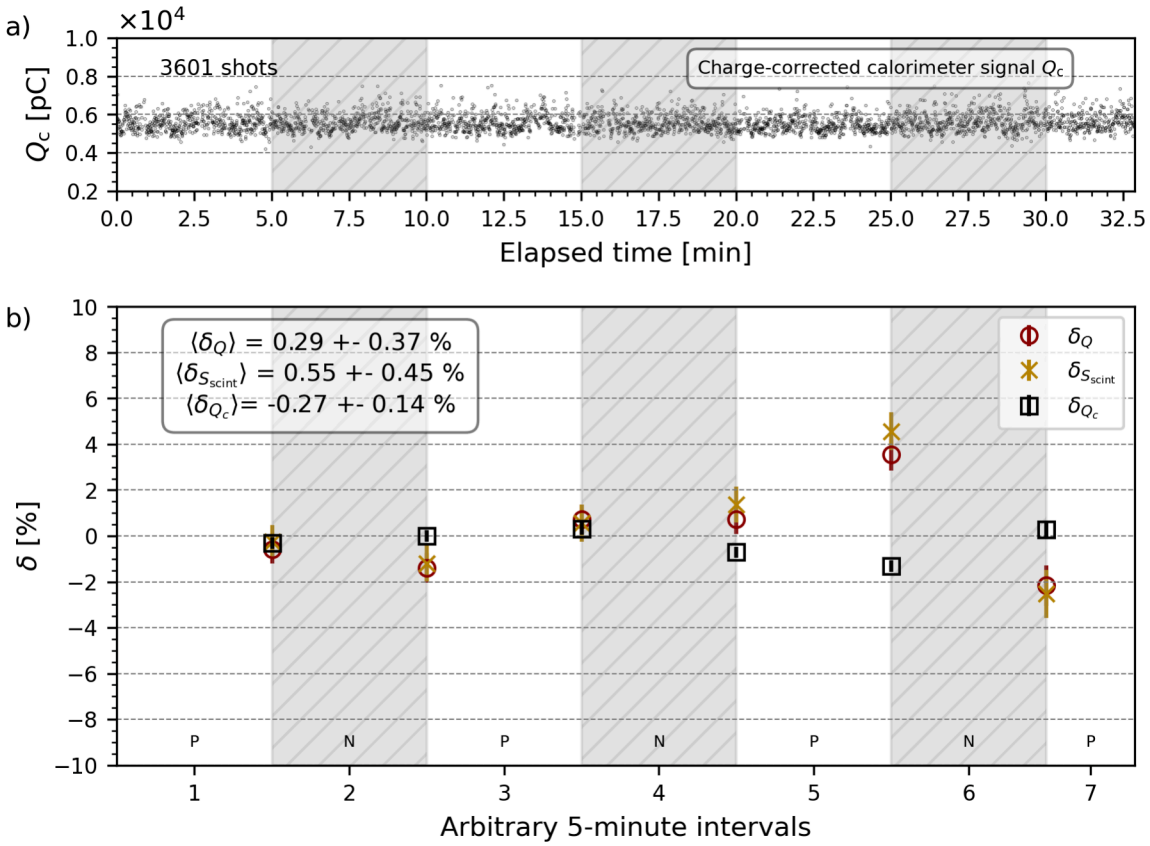

Figure 7.30.: a) Beam charge-corrected calorimeter signal Q_c for the 3601 shots of run 50282, where the magnet was off. The white and hatched gray bands represent the artificial assignment to the solenoid current's positive and negative 5-minute intervals. b) Asymmetries for the assigned intervals based on the charge-corrected calorimeter signal Q_c (black squares), the raw calorimeter signal Q (red circles), and the scintillator screen signal S_{scint} (yellow stars). Mean asymmetries $\langle\delta\rangle$ are presented with associated statistical errors, calculated using Eqs. 7.11 and 7.12, incorporating all data as assigned to P and N intervals.

$\langle\delta_{S_{scint}}\rangle = 0.55 \pm 0.45\,\%$. The non-vanishing $\langle\delta_{Q_c}\rangle$ remains consistent with the main polarimeter run, and the relation $\langle\delta_Q\rangle \approx \langle\delta_{S_{scint}}\rangle + \langle\delta_{Q_c}\rangle$ holds true. This suggests that no significant asymmetries arise due to the change in magnetic field alone.

Across all datasets, the trends remain consistent, as summarized in Tab. 7.1. A non-vanishing δ_{Q_c} most likely arises from asymmetries in the LPA beam energy, which could not be corrected for in this experimental campaign and are considered the leading systematic error. For future experiments, focusing on stabilizing the beam energy is recommended to minimize this effect.

Run	V_{APL} [kV]	Solenoid	Number of shots: P/N	$\langle\delta_{\mathrm{Q}}\rangle$ [%]	$\langle\delta_{\mathrm{Sscint}}\rangle$ [%]	$\langle\delta_{Q_c}\rangle$ [%]
50282	20	off	1926/1675	0.29 ± 0.37	0.55 ± 0.45	-0.27 ± 0.14
50285	24	off	1291/1008	0.64 ± 0.47	0.34 ± 0.64	0.35 ± 0.24
50288	16	off	1550/1499	1.57 ± 0.46	1.40 ± 0.51	0.17 ± 0.15
50379	20	on	4513/4007	-0.31 ± 0.27	0.14 ± 0.31	-0.42 ± 0.07
50414	16	on	2627/2945	0.97 ± 0.32	1.38 ± 0.36	-0.40 ± 0.10
50418	18	on	1187/1460	-0.32 ± 0.42	-0.49 ± 0.48	0.05 ± 0.20
50422	20	on	805/1204	-1.95 ± 0.53	-1.89 ± 0.61	-0.07 ± 0.14

Table 7.1.: Mean asymmetries $\langle\delta_Q\rangle$, $\langle\delta_{S_{\mathrm{scint}}}\rangle$ and $\langle\delta_{Q_c}\rangle$ with associated statistical uncertainties calculated using Eqs. 7.11 and 7.12, for different polarimeter runs taken in the experiment. For runs where the magnet was off, data were assigned artificially to positive and negative solenoid current intervals in 5-minute segments, starting with a positive interval. Shot numbers refer to the number of shots in the positive (P) and negative (N) intervals after applying data cuts ($q_{\mathrm{damon}} < 3\,\mathrm{pC}$ and $S_{\mathrm{scint}} < 20000$). The gray band indicates the main polarimeter run 50379, as shown in Fig. 7.29.

7.7.4. Determination of the Analyzing Power

Generally, for an actual polarization measurement, the analyzing power of the polarimeter system must be precisely known in order to translate the measured asymmetry into the actual polarization of the electron beam. The analyzing power acts as a scaling factor that quantifies the system's asymmetry response for a 100 % polarized electron beam and a 100 % polarized iron absorber (see Sec. 3.2). This section discusses the determination of the analyzing power along with its associated uncertainty for the LEAP polarimeter setup under the experimental conditions of this measurement campaign.

Detailed `leap_sims` polarimeter simulations (cf. Sec. 7.1.2) were conducted to determine the central value of the analyzing power and the associated uncertainties under the given experimental conditions [34]. These simulations were performed using 100 % polarized electron beams ($P_{e^-} = 1$) and 100 % polarization of the electrons in the solenoid's iron absorber ($P_{e^-}^{\mathrm{Fe}} = \pm 1$). In the simulation, the polarization in the iron core is flipped, and the analyzing power (asymmetry) was calculated, based on the simulated calorimeter signal E_{ct} (defined in Sec. 6.2.2), between simulations with identical input parameters but opposite $P_{e^-}^{\mathrm{Fe}}$. For a detailed description of the analysis methodology, refer to [34].

The input parameters for the simulations include the beam and geometrical parameters as measured during the experimental campaign (listed below). The central value of the analyzing power was determined by incorporating these experimental parameters

into the simulations. Systematic uncertainties in the analyzing power were estimated by varying the simulation input parameters within ranges corresponding to the precision of the experimental measurements. The key experimental parameters and their associated uncertainties considered in this analysis are:

Energy spectrum: The energy spectra used for the analysis of the analyzing power were derived within this work (see Sec. 7.6). The average electron spectrum incident on the polarimeter, corresponding to an APL setting of 20 kV (see Fig. 7.26 a)), was utilized in the simulation to determine the central value of the analyzing power. Variations in the mean energy were introduced based on the uncertainty of the APL current measurement, $\Delta I_{\mathrm{APL}} = \pm 3\,\mathrm{A}$ (see Fig. 7.19 b)), which directly affects (shifts) the electron spectrum transmitted through the collimator (cf. Sec. 7.6.3).

Beam spot size: The rms beam size of the electron beam at the entrance of the solenoid, used in this study, was measured to be $0.74 \pm 0.02\,\mathrm{mm}$ using the scintillation screen setup [34].

Position of the calorimeter relative to the beam axis: The calorimeter was assumed to be centered on the beam axis, with $x = y = 0 \pm 2\,\mathrm{mm}$, based on the measurement precision achieved using a measuring tape.

Distance between the solenoid and the calorimeter: The distance between the solenoid magnet and the calorimeter was measured to be $91 \pm 2\,\mathrm{mm}$, using a measuring tape.

Figure 7.31 summarizes the main results of the simulation study, which is part of the dissertation of J. Popp [34]. Panel a) shows the analyzing power derived for the average values of the experimental parameters, denoted as A_0, alongside the analyzing power from simulations that account for different uncertainties in the experimental parameters as listed above. Panel b) presents the relative deviation from the central value A_0 due to the variations in the here considered parameters.
For the average values of experimental parameters, the analyzing power was determined to be $A_0 = 11.737 \pm 0.004\,\%$, where the error corresponds to the Monte Carlo statistical error. It is evident that the uncertainty on the mean energy (determined by the APL current) has the largest impact on the analyzing power, as expected, due to its energy dependence (see Fig. 3.6).
In addition to uncertainties arising from the aforementioned experimental conditions, another significant contribution to the precision of the analyzing power simulation

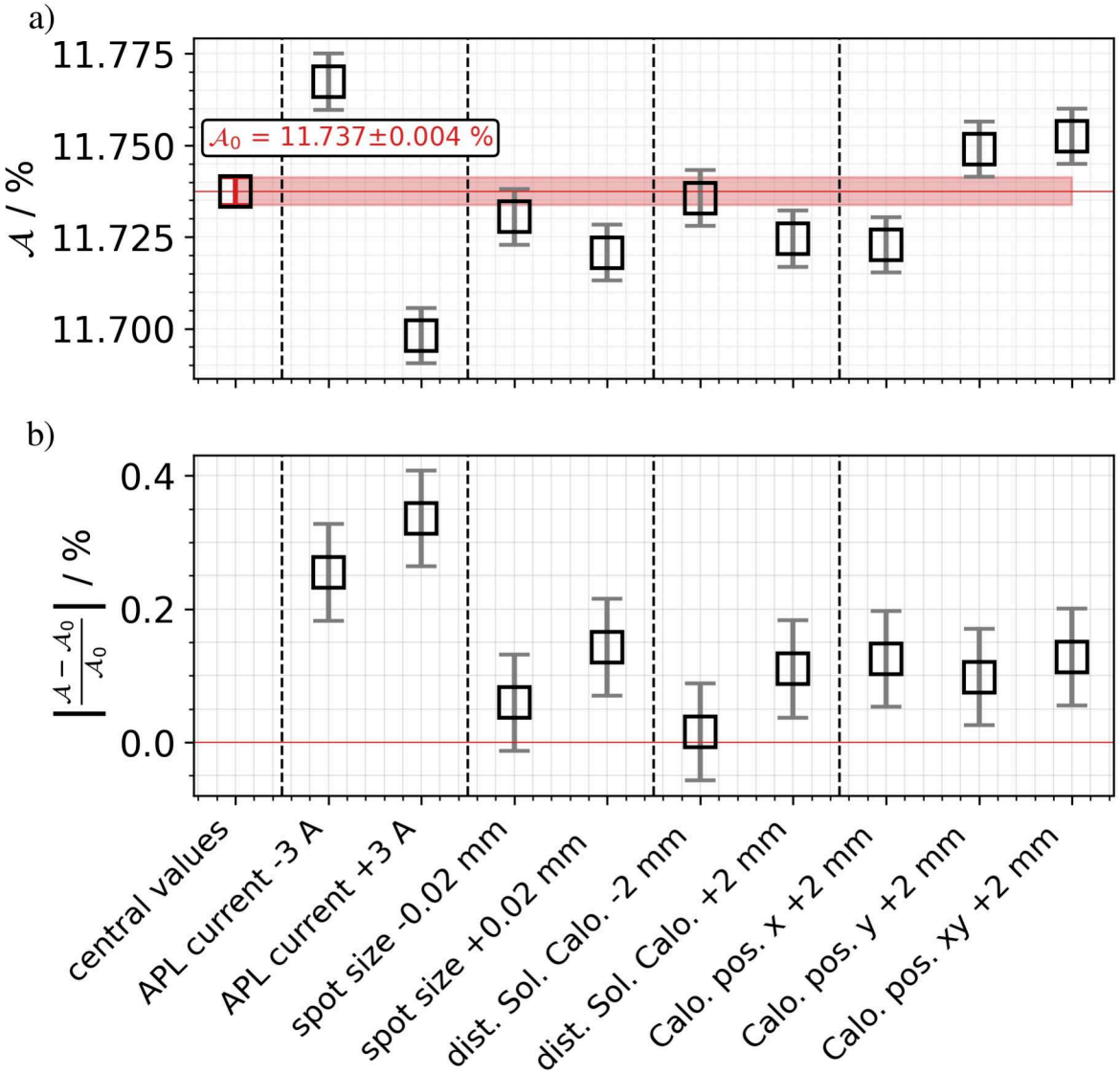

Figure 7.31.: Analyzing power as derived from `leap_sims` simulations for varying beam and setup parameters, as measured during the experimental campaign. The central value A_0 corresponds to fixed initial beam and setup conditions. The lower plot shows the relative deviation from the central value A_0 arising from the variations of the experimental parameters within their uncertainties [34].

stems from the uncertainty in the calorimeter's response to low-energy particles (<10 MeV), as estimated in Sec. 6.5.2 of this work. Due to the nonlinearity of the energy response in the low-energy regime, the influence decreases at higher electron energies. At approximately 80 MeV, the calorimeter response introduces a relative error of about $\frac{\Delta A}{A} \sim 1.5\,\%$, as detailed in Sec. 6.5.2.

The total uncertainty in the analyzing power is calculated as the quadratic sum of individual contributions:

$$\begin{aligned}\frac{\Delta A}{A} &= 0.034\,\% \;\rightarrow \text{Monte Carlo error}\\ &\oplus 0.34\,\% \;\rightarrow \text{Central value of energy spectrum (APL current)}\\ &\oplus 0.14\,\% \;\rightarrow \text{Beam spot size}\\ &\oplus 0.11\,\% \;\rightarrow \text{Distance between solenoid and calorimeter}\\ &\oplus 0.13\,\% \;\rightarrow \text{Calorimeter } x-y \text{ position}\\ &\oplus 1.5\,\% \;\rightarrow \text{Calorimeter energy response}\\ &= 1.55\,\%\end{aligned}$$

The results indicate that the uncertainty is primarily dominated by the calorimeter's response to low-energy particles, which decreases for higher electron energies. Therefore, it is recommended that future studies further investigate the calorimeter response to improve accuracy in analyzing power estimation.
Nevertheless, the analyzing power of the LEAP polarimeter setup under the conditions of this measurement campaign is estimated to be:

$$A = 11.74 \pm 0.18\,\% \tag{7.17}$$

7.7.5. Determination of the Electron Polarization

In this section, the general procedure for polarization retrieval will be demonstrated based on the results of this zero-polarization measurement campaign. According to Eq. 3.8, the electron polarization can be calculated as:

$$P_{e^-} = \frac{\delta_\mathrm{m}}{A \cdot P_{e^-}^{\mathrm{Fe}}}. \tag{7.18}$$

where δ_m is the measured asymmetry, A is the analyzing power, and $P_{e^-}^{\mathrm{Fe}}$ is the polarization of the electrons in the iron absorber. The uncertainty in the polarization, ΔP_{e^-}, can be expressed as:

$$\Delta P_{e^-} = \frac{\delta_\mathrm{m}}{A \cdot P_{e^-}^{\mathrm{Fe}}} \cdot \sqrt{\left(\frac{\Delta\delta_\mathrm{m}}{\delta_\mathrm{m}}\right)^2 + \left(\frac{\Delta A}{A}\right)^2 + \left(\frac{\Delta P_{e^-}^{\mathrm{Fe}}}{P_{e^-}^{\mathrm{Fe}}}\right)^2} \tag{7.19}$$

Using the measured asymmetry from the main polarimeter run (50379), $\delta_{\mathrm{m}} = \langle \delta_{Q_{\mathrm{c}}} \rangle = -0.42 \pm 0.07\,\%$ ($\frac{\Delta\delta_{\mathrm{m}}}{\delta_{\mathrm{m}}} = 16.7\,\%$), the analyzing power $A = 11.74 \pm 0.18\,\%$ ($\frac{\Delta A}{A} = 1.6\,\%$), as discussed in the previous section, and the polarization of the electrons in the iron absorber $P_{e^-}^{\mathrm{Fe}} = 7.23 \pm 0.15\,\%$ ($\frac{\Delta P^{\mathrm{Fe}} e^-}{P^{\mathrm{Fe}} e^-} = 2.1\,\%$) from [66], the electron polarization is calculated as:

$$|P_{e^-}| = 49.5 \pm 8.4\,\% \tag{7.20}$$

The polarization is inconsistent with zero even within the uncertainty, which is unsurprising given the context. The large absolute value of the derived polarization is attributed to the significant measured asymmetry, δ_{m}, which is most likely associated with a fake asymmetry in the calorimeter signal caused by energy drifts that could not be corrected, as discussed previously in Sec. 7.7.3. This result demonstrates how asymmetries can scale to seemingly significant polarization values that are, in this case, contributions from systematic errors. Once more, this underlines that achieving reliable polarization measurements in future experiments requires improving the stability of the beam energy to minimize potential fake asymmetries induced by energy drifts, δ_E.

Referring to the uncertainty of the reconstructed polarization, it is evident that it is primarily constrained by the uncertainty in the measured asymmetry, which, in turn, is generally affected by limited statistics and fluctuations in beam energy and charge. Since charge fluctuations have been corrected for in this experiment, the uncertainty is most likely affected by the resolution of the charge measurement at the polarimeter entrance, as discussed in Sec. 7.5.3.

The following section will generally assess how different sources of uncertainty, particularly fluctuations in the electron beam charge and energy, impact the precision of a realistic polarization measurement based on the results from this campaign.

7.8. Considerations and Estimations towards Real Polarization Measurements

In this section, the requirements and considerations for achieving a real polarization measurement will be discussed. Specifically, a performance estimation of the electron polarization measurement and its associated statistical uncertainties will be provided concerning the stability of the initial beam.

According to Eq. 7.19, the relative error of the reconstructed electron polarization can be expressed as:

$$\frac{\Delta P_{e^-}}{P_{e^-}} = \sqrt{\left(\frac{\Delta A}{A}\right)^2 + \left(\frac{\Delta P_{e^-}^{\mathrm{Fe}}}{P_{e^-}^{\mathrm{Fe}}}\right)^2 + \left(\frac{\Delta \delta_{\mathrm{m}}}{\delta_{\mathrm{m}}}\right)^2} \tag{7.21}$$

This error is influenced by the uncertainties in the measured asymmetry, the polarization of electrons in the iron core, and the analyzing power. The relative error of the measured asymmetry, according to Eq. 7.12, is given by:

$$\frac{\Delta \delta_{\mathrm{m}}}{\delta_{\mathrm{m}}} = \frac{1}{\delta_{\mathrm{m}}} \cdot \underbrace{\frac{2 \cdot \langle Q \rangle_{\mathrm{P}} \cdot \langle Q \rangle_{\mathrm{N}}}{(\langle Q \rangle_{\mathrm{P}} - \langle Q \rangle_{\mathrm{N}})^2}}_{\approx \frac{1}{2}} \cdot \sqrt{\left(\frac{\Delta \langle Q \rangle_{\mathrm{P}}}{\langle Q \rangle_{\mathrm{P}}}\right)^2 + \left(\frac{\Delta \langle Q \rangle_{\mathrm{N}}}{\langle Q \rangle_{\mathrm{N}}}\right)^2} \tag{7.22}$$

where $\langle Q \rangle_{\mathrm{P,N}}$ represent the mean calorimeter signals for the positive and negative magnet current intervals over which the asymmetry is calculated. Given the expected small asymmetries, the first factor in Eq. 7.22 can be approximated as 0.5, even for $P_{e^-} \approx 1$.

Now considering the error in the measured signal $\frac{\Delta \langle Q \rangle}{\langle Q \rangle}$ which is primarily influenced by four factors: The first is the **intrinsic resolution of the polarimeter σ_{Pol}**, which accounts for the inherent width of the calorimeter signals caused by statistical fluctuations in the transmission through the solenoid analyzing core and the resolution of the calorimeter itself. The latter has been found to have a minor effect and is likely negligible (see Sec. 7.5.3). The second and third factors are the **beam charge and beam energy fluctuations**, denoted as σ_q and σ_E, respectively. Variations in beam charge and energy lead to a broadening of the calorimeter signal and, therefore, contribute to the overall measurement uncertainty. It should be noted that σ_q can also be interpreted as the resolution of the charge measurement system itself since shot-by-shot charge measurements allow for corrections of beam charge fluctuations at the calorimeter signal level, as detailed in Sec. 7.5.2, leaving the resolution of the charge measurement system as the remaining source of uncertainty. The fourth factor, the **number of measurement shots N**, naturally improves the statistical precision of the measurement. With this, the relative error of the calorimeter signal can be expressed as:

$$\frac{\Delta \langle Q \rangle}{\langle Q \rangle} = \frac{1}{\sqrt{N}} \cdot \sqrt{\sigma_{Pol}^2 + \sigma_E^2 + \sigma_q^2} \tag{7.23}$$

By substituting Eq. 7.23 into Eq. 7.22, the relative error of the measured asymmetry becomes:

$$\frac{\Delta\delta_{\mathrm{m}}}{\delta_{\mathrm{m}}} = \underbrace{\frac{1}{\delta_m}}_{A\cdot P_{e^-}\cdot P_{e^-}^{\mathrm{Fe}}} \cdot \frac{1}{\sqrt{2\cdot N}} \cdot \sqrt{\sigma_{Pol}^2 + \sigma_E^2 + \sigma_q^2}. \tag{7.24}$$

Finally, by substituting Eq. 7.24 into Eq. 7.21, the uncertainty of the electron polarization is obtained as a function of the number of shots per magnet cycle, N, as well as the polarimeter resolution σ_{Pol} and the overall charge and energy stability, σ_q and σ_E, of the initial beam:

$$\frac{\Delta P_{e^-}}{P_{e^-}} = \sqrt{\left(\frac{\Delta A}{A}\right)^2 + \left(\frac{\Delta P_{e^-}^{\mathrm{Fe}}}{P_{e^-}^{\mathrm{Fe}}}\right)^2 + \left(\frac{1}{A\cdot P_{e^-}\cdot P_{e^-}^{\mathrm{Fe}}} \cdot \frac{1}{\sqrt{2\cdot N}} \cdot \sqrt{\sigma_{Pol}^2 + \sigma_E^2 + \sigma_q^2}\right)^2}. \tag{7.25}$$

Based on Eq. 7.25, the requirements for beam stability will be assessed in relation to the necessary number of shots needed to achieve the desired statistical precision in the polarization measurement. For this discussion, an anticipated electron polarization of $P_{e^-} = 0.1$, expected for LEAP, is assumed. Furthermore, the analyzing power is taken to be equivalent to the value obtained from the zero-polarization measurement campaign, $A = 11.74 \pm 0.18\,\%$ ($\frac{\Delta A}{A} = 1.6\,\%$), as outlined in Sec. 7.7.4. The polarization of the electrons in the iron core is assumed to be $P_{e^-}^{\mathrm{Fe}} = 7.23 \pm 0.15\,\%$ ($\frac{\Delta P_{e^-}^{\mathrm{Fe}}}{P_{e^-}^{\mathrm{Fe}}} = 2.1\,\%$), as discussed in Sec. 7.1.

In Fig. 7.32 a) the expected relative precision on the polarization measurement is shown as a function of the total number of shots, $2N$, for three different cases of the therm $\sigma_{Pol} \oplus \sigma_E \oplus \sigma_q$ in Eq. 7.25. The orange line represents the case based on the conditions observed during this initial measurement campaign, where $\sigma_{Pol} \oplus \sigma_E \oplus \sigma_q \approx 6.68\,\%$ corresponds to the relative width of the measured distribution of the charge-normalized calorimeter signal Q_c, as shown in Fig. 7.14. To achieve a relative precision of 20 %, approximately $1.5 \cdot 10^5$ shots would be required, as indicated by the black dashed lines. Even if the technical maximum repetition rate of 10 Hz for the LPA used in the experiment were achieved (while the typical rate is only 1–2 Hz), the measurement would still take over four hours, making it experimentally impractical.

The blue line represents the case of nearly ideal beam conditions, where energy and charge fluctuations are assumed to be on the order of one per mill. Under these conditions, the dominant contribution to the uncertainty comes from the polarimeter resolution, which was estimated through simulations to be approximately $\sigma_{Pol} = 0.75\,\%$,

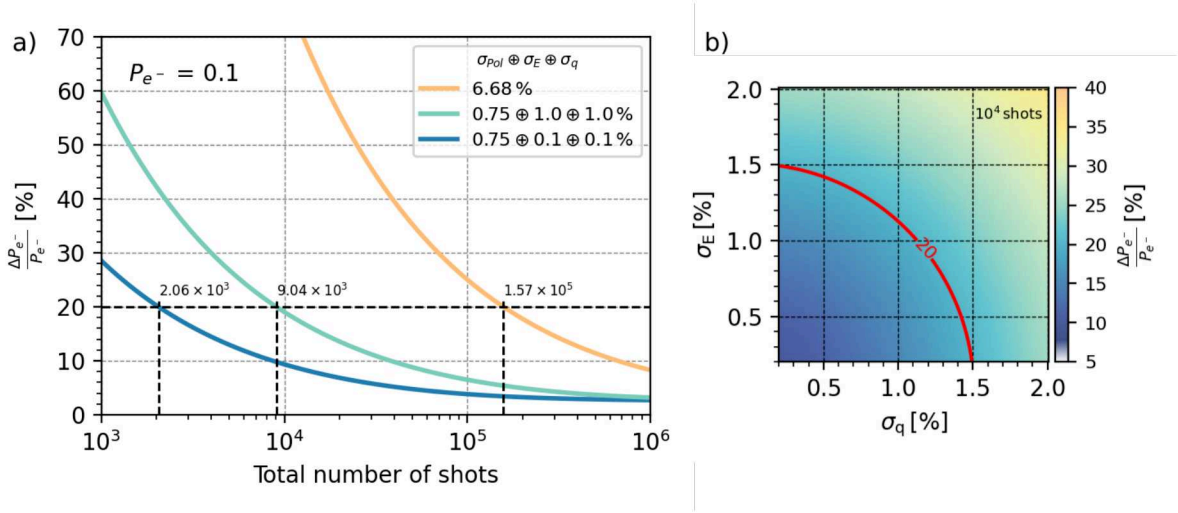

Figure 7.32.: a) Estimated precision of the polarization measurement as a function of the total number of shots, assuming an anticipated electron polarization of $P_{e^-} = 10\%$. Results are shown for three cases of $\sigma_{\mathrm{Pol}} \oplus \sigma_E \oplus \sigma_q$ (Eq. 7.25), where σ_{Pol} represents the intrinsic resolution of the polarimeter, and σ_E and σ_q denote the energy and charge fluctuations of the initial electron beam, respectively. The black dashed lines indicate the expected number of shots required to achieve a precision of 20 % in the retrieved polarization. b) Precision of the polarization measurement as a function of σ_E and σ_q, assuming a fixed sample of 10^4 shots. The red line marks the 20 % precision threshold.

as shown in Fig. 7.14. With this, about $2 \cdot 10^3$ shots would be required to achieve a precision of 20 %. This corresponds to a measurement time of roughly three minutes (at 10 Hz), highlighting the high intrinsic performance of the LEAP polarimeter setup. The asymptotic behavior of the curve at high shot numbers arises from the precision limits of the analyzing power and the polarization of electrons in the iron core, as these do not scale with the shot number. Since these factors become the dominant sources of uncertainty at sufficiently high shot counts (around 10^5), this suggests that the measurement is primarily influenced by the statistical uncertainty of the asymmetry rather than by the precision of the analyzing power and the iron core polarization.
The cyan line represents the case where the contributions from beam charge and energy fluctuations, as well as the polarimeter resolution, are all approximately equal at around 1 %. Under these conditions, about 10^4 shots would be required to achieve a statistical precision of better than 20 % in the polarization measurement. Again, assuming the technical maximum repetition rate of 10 Hz for the LPA used in this experimental campaign, this would correspond to a measurement time of about 15 minutes, which appears reasonable. Furthermore, in Fig. 7.32 b), the precision of the polarization measurement under these assumed conditions is shown as a function

of energy and beam fluctuations for a total of 10^4 shots. The red curve marks the 20 % precision threshold. This indicates that both energy and charge stability should be at the level of approximately 1 % or better to enable a reasonable polarization measurement.

The required energy stability may already be achievable using energy filtering techniques, such as a plasma lens in combination with a collimator, as applied in the measurement campaign presented in this thesis, though this still requires further investigation.

In general, the estimated requirement for energy stability appears feasible, given that LPA beams with shot-to-shot energy stability and relative energy spreads at the percent and sub-percent level have been demonstrated in recent experiments investigating beam control and stabilization using machine learning techniques [147, 148]. Additionally, simulation studies suggest that even lower energy spreads and shot-to-shot stability, in the sub-0.1 % range, are achievable using additional energy compression schemes [149, 150]. In contrast, the charge stability observed in the aforementioned studies is lower, on the order of approximately 10 %. However, since charge fluctuations could already be corrected for, as demonstrated in this experiment, achieving a sufficient precision of ~ 1 % on the relative charge measurement seems reasonable using charge diagnostics such as DaMon and ICTs in future experiments.

Furthermore, it is evident that the measurement precision strongly depends on the number of shots taken during the experiment, which is practically limited by the typically low repetition rates of LPAs. However, the development of high-repetition-rate laser-plasma accelerators, such as the kHz-scale KALDERA system at DESY [151], is pushing these limits and would naturally benefit the polarization measurement presented here.

Improvements on the polarimeter side are also worth considering. For instance, increasing the core length of the solenoid magnet can enhance the analyzing power (see Fig. 3.6), which would, in turn, reduce the overall uncertainty, as shown in Eq. 7.25. Additionally, a more detailed investigation of the calorimeter response to low-energy particles could help reduce the uncertainty in the analyzing power simulations, as discussed in Sec. 6.5.2.

So far, the statistical precision has been discussed. As shown in the previous section, the measurement is affected by fake asymmetries arising from beam intensity drifts, introducing a systematic error. Naturally, these effects become less significant as the overall stability of LPA beams improves. As previously demonstrated, beam charge drifts may not be a major issue, as the calorimeter signal can be corrected using

shot-to-shot charge measurements. However, in the case of beam energy drifts, if fake asymmetries remain an issue despite improved overall beam energy stability, non-invasive shot-to-shot energy measurements would be desirable to correct for potential drifts. Such a measurement could potentially be implemented using machine learning techniques by monitoring critical LPA laser parameters [147].
The above estimations and considerations emphasize that, with rapidly advancing LPA technology and research, reliable polarization measurements using Compton transmission polarimetry are becoming increasingly feasible.

Chapter 8.

Conclusion

Polarized particle beams are essential for many particle and nuclear physics experiments that investigate spin-dependent processes, and novel plasma accelerator concepts show great potential for enabling more compact and cost-efficient experimental designs. However, the acceleration of polarized beams using plasma-based methods has not yet been demonstrated.
The LEAP project at DESY serves as a proof-of-principle experiment, aiming to demonstrate polarized laser-plasma acceleration (LPA) for the first time, utilizing a pre-polarized plasma source and Compton transmission polarimetry for electron beam polarization measurement. Thus, showcasing the generation and transport of polarized beams using a plasma-based accelerator. Within this thesis, three key aspects of the LEAP project have been addressed, focusing on the development and implementation of the experimental realization.

A key step toward preparing the pre-polarized plasma source – and thus enabling polarized LPA – is the generation of a UV dissociation laser, required for the photodissociation of HCl molecules to produce polarized electrons. Within this work, a feasibility study was conducted to investigate whether the fourth harmonic of the LPA driver laser can be generated using cascaded second harmonic generation with two beta-barium borate crystals to produce the required UV dissociation laser. This approach ensures the necessary synchronization with the LPA driver laser. The achieved energy conversion efficiency of $\eta_{\omega \to 4\omega} \approx 0.8\,\%$ was found to be sufficient to meet the requirements of the UV dissociation laser for LEAP. Future work should focus on the experimental demonstration of HCl dissociation using a pulse generated with this method, further advancing the development of the pre-polarized plasma source.

With respect to the development of a Compton transmission polarimeter for polarization measurement within LEAP, a homogeneous lead-glass Cherenkov calorimeter was designed and built as an integral part of the polarimeter in this thesis.
The calorimeter was tested and calibrated using single electrons from the DESY II Test Beam Facility. The analysis demonstrated an energy resolution of $\frac{\sigma_E}{\langle E \rangle} < 2\,\%$ at TeV-scale total energies, which is sufficient for its application within the LEAP polarimeter. `GEANT4` simulations indicate a nonlinear response for low-energy particles (<10 MeV). The uncertainty of this response has been shown to impact the accuracy of the analyzing power simulation, introducing a relative uncertainty of $\sim 1.5\,\%$ on the analyzing power. Further measurements of the calorimeter response at low energies could improve precision.

A first operational polarization measurement using an unpolarized LPA electron beam was conducted to commission the LEAP polarimeter setup, consisting of a solenoid magnet and the lead-glass Cherenkov calorimeter. The gathered insights into system behavior, operation procedures, and key sources of uncertainty under real experimental conditions pave the way for future polarization measurements.
The LEAP polarimeter was successfully integrated and operated at the FLARE facility at DESY, where initial polarization measurement data were collected. The analyzing power under the given experimental conditions was determined through simulations to be $A = 11.74 \pm 0.18\,\%$ ($\frac{\Delta A}{A} = 1.6\,\%$) with the dominant uncertainty arising from the calorimeter's nonlinear energy response, as stated above. However, at the current stage of the project, this uncertainty is not considered a significant limitation.
The asymmetry measurement was found to be significantly influenced by electron beam conditions, particularly fluctuations and drifts in beam energy and charge, both of which introduce statistical and systematic uncertainties. Charge-related uncertainties were shown to be reducible using shot-to-shot non-invasive charge diagnostics, though this approach remains limited by the precision of charge measurement. Since energy fluctuations could not be monitored simultaneously with the polarization measurement on a shot-by-shot basis, addressing associated uncertainties was not feasible. In particular, beam energy drifts were identified as the most plausible source of the observed fake asymmetries, which are unrelated to beam polarization. However, non-invasive procedures for energy monitoring are being developed [147], offering great potential for solutions to current challenges.
An extrapolation of uncertainties for a real polarization measurement further emphasizes the importance of improving beam stability and control. Achieving a shot-to-

shot energy and charge stability of 1 % would enable a polarization measurement of $P = 10\,\%$ with a relative precision of 20 % within 20 minutes, assuming the current maximum repetition rate of 10 Hz for the LPA. Further improving stability to the 0.1 % level could reduce this measurement time to about three minutes. This also highlights the significant benefits of higher repetition rates for polarization measurements. Encouragingly, recent advances in LPA technology regarding beam stability and diagnostics [147, 148], as well as ongoing research on high-repetition-rate LPAs [151], demonstrate great potential for successfully applying Compton transmission polarimetry in future LPA experiments.

Appendix A.

Appendices

A.1. Run Overview

Run Type	Date 2024	Time	Run Number	V_{APL}[kV]	Solenoid
Spectrometer	15. Dec.	15:16-15:44	50281	off	off
Polarimeter	15. Dec.	15:47-16:20	50282	20	off
Polarimeter	15. Dec.	16:26-16:49	50285	24	off
Polarimeter	15. Dec.	17:17-17:37	50288	16	off
Spectrometer	18. Dec.	13:41-13:52	50377	[14:24:0.5]	off
Polarimeter	18. Dec.	13:55-15:38	50379	20	on
Polarimeter	20. Dec.	10:51-12:03	50414	16	on
Polarimeter	20. Dec.	13:12-14:15	50418	18	on
Polarimeter	20. Dec.	14:40-15:27	50422	20	on

Table A.1.: Overview of the data collected during the operational polarization measurement campaign at the LPA at FLARE and analyzed within this thesis.

A.2. Solenoid Magnet Specifications

Table A.2.: Specification parameters of the polarimeter solenoid magnet as provided in [66]

Parameter	value
overall length	275 mm
overall diameter	320 mm
iron core length	150 mm
iron core diameter	50 mm
length of internal Pb absorber	125 mm
overall mass	195 kg
number of coils	2
coil length	86 mm
coil inner diameter	152 mm
coil outer diameter	248 mm
number of turns per coil	175
conductor dimensions	4 x 4 mm
coolant bore diameter	2.5 mm
water cooling circuits	4
water flow rate	˜2 l/min
operating current	$\pm$ 60 A
power	1.37 kW
current reversal time	12.5 s
time between reversals	5 min
Field $B_z^{\max}$ at center	2.165 T
on-axis mean field at center	2.040 T
air field B_0 at center	0.100 T
$\langle P_{e^-}^{Fe} \rangle$ (on axis)	0.0723 $\pm$ 0.0723 T

A.3. TF1 Lead Glass Data Sheet

LYTKARINO OPTICAL GLASS FACTORY, JSC

ЛЗОС LZOS

TF1
glass type

n_e 1.652188	υ_e 33.62	$n_{F'} - n_{C'}$ 0.019397
n_d 1.647665	υ_d 33.87	$n_F - n_C$ 0.019120

Class of bubbles	Viscosity temperature				
	η [Poise]	$10^{14.5}$	10^{13}	10^{10}	10^{8}
1	t [°C]	375	455	530	605

Relative partial dispersion deviations from the 'Normal Line'

	i – F'	g – F'	F' - e	F' - r
ΔP	+0.008	+0.0004	+/-0	-0.0004
Δ υ_e	+0.9	+0.3	+/-0	+0.5
	i – F	**g – F**	**F - e**	**F – r**
ΔP	+0.009	+0.0006	+/-0	-0.0003
Δ υ_d	+0.9	+0.3	+/-0	+0.5

Stress optical coefficient B [nm·cm^{-1} / kp·cm^{-2}], λ=550nm	Thermal conductivity			
	-50°C	0°C	+20°C	+50°C
2.60	0.55	0.60	0.63	0.65

Optical density increment on irradiation

Initial density D_0 [cm^{-1}]	Radiation dose [R]	Optical density increment Δ D [cm^{-1}]
0.055	$1 \cdot 10^4$	0.090
	$1 \cdot 10^5$	0.60

Young's modulus E [kp · mm^{-2}]	Shear modulus G [kp·mm^{-2}]	Coefficient of linear thermal expansion $\alpha_{20/t} \cdot 10^7$ [°C]		Chemical resistance	
				Stain resistance	
				Group	II
5470	2229				
Poisson's ratio μ	**Density ρ [g · cm^{-3}]**	+20 ÷ -60°C	+20 ÷ +120°C	**Weather resistance**	
0.227	3.86	82	86	**Group**	A

Refractive indices

λ [nm]	n	
312.6	-	-
334.1	-	-
365.0	i	1.70022
404.66	h	1.68229
435.83	g	1.672451
479.99	F'	1.662347
486.13	F	1.661196
546.07	e	1.652188
587.56	d	1.647665
589.29	D	1.647500
643.85	C'	1.642950
656.27	C	1.642076
706.52	r	1.63901
768.2	-	1.63602
852.1	-	1.63289
1013.9	-	1.62862
1128.6	-	1.62638
1395.1	-	1.62232
1529.6	-	1.62054
1813.1	-	1.61691
1970.1	-	1.61487
2249.3	-	1.61102
2325.4	-	1.60991

Dispersion coefficients

$\nu_h = \frac{n_h - 1}{n_i - n_g}$	24.6
$\nu_e = \frac{n_e - 1}{n_{F'} - n_{C'}}$	33.62
$\nu_d = \frac{n_d - 1}{n_F - n_C}$	33.87
$\nu_D = \frac{n_D - 1}{n_F - n_C}$	33.86
$\nu_{1529.6} = \frac{n_{1529.6} - 1}{n_{1013.9} - n_{2249.3}}$	35.3

Internal transmittance

λ [nm]	τ_i (s=10mm)	τ_i (s=25mm)
280	-	-
300	-	-
320	-	-
340	-	-
360	-	-
380	0.840	0.647
400	0.960	0.903
420	0.977	0.944
440	0.983	0.958
460	0.988	0.971
480	0.991	0.978
500	0.993	0.983
520	0.995	0.987
540	0.996	0.990
560	0.996	0.990
580	0.996	0.990
600	0.995	0.987
620	0.994	0.985
640	0.994	0.985
660	0.994	0.985
680	0.995	0.987
700	0.995	0.987
750	0.997	0.993
800	0.998	0.995
900	0.997	0.993
1000	0.997	0.993
1050	0.997	0.993
1100	0.997	0.993
1200	0.996	0.990
1300	0.997	0.993
1400	0.993	0.983
1500	0.993	0.983

Refractive indices at laser wavelengths

λ [nm]	n
350.7	-
356.4	-
488.0	1.66085
514.0	1.65656
520.8	1.65555
530.0	1.65427
568.2	1.64964
632.8	1.64378
647.1	1.64272
694.3	1.63970
890.0	1.63172
1060.0	1.62767

Relative partial dispersions

Δ n	$\frac{\Delta n}{n_{F'} - n_{C'}}$	$\frac{\Delta n}{n_F - n_C}$
312.6 – 334.1	-	-
334.1 - i	-	-
i - h	0.924	0.938
h - g	0.5073	0.5146
g – F	0.5803	0.5886
g – F'	0.5209	0.5285
F - e	0.4644	0.4711
F - D	0.7061	0.7163
F' - e	0.5237	0.5313
d - D	0.0085	0.0086
D - C	0.2796	0.2837
e – C'	0.4763	0.4832
e - C	0.5213	0.5289
C' - r	0.203	0.206
C - r	0.158	0.160
r – 852.1	0.316	0.320
852.1 – 1013.9	0.220	0.223
1013.9 – 1128.6	0.115	0.117
1128.6 – 1395.1	0.210	0.213
1395.1 – 1529.6	0.092	0.093
1529.6 – 1813.1	0.187	0.189
1813.1 – 1970.1	0.105	0.107
1970.1 – 2249.3	0.198	0.201
2249.3 – 2325.4	0.057	0.058

Radiation resistant analogue glass type-

TF101

Figure A.1.: Data sheet of the optical properties of TF1 type lead glass as provided by the LYTKARINO OPTICAL GLASS FACTORY via email.

List of figures

List of tables

Bibliography

[1] C. A. Aidala et al. “The spin structure of the nucleon”. *Rev. Mod. Phys.* 85 (2 2013), pp. 655–691. DOI: 10.1103/RevModPhys.85.655.

[2] G. Moortgat-Pick et al. “Polarized positrons and electrons at the linear collider”. *Physics Reports* 460.4 (2008), pp. 131–243. DOI: https://doi.org/10.1016/j.physrep.2007.12.003.

[3] A. A. Sokolov and I. M. Ternov. “Synchrotron Radiation”. *Soviet Physics Journal* 10.10 (1967), pp. 39–47. DOI: 10.1007/BF00820300.

[4] D. T. Pierce, F. Meier, and P. Zürcher. “Negative electron affinity GaAs: A new source of spin-polarized electrons”. *Applied Physics Letters* 26 (12 1975), pp. 670–672. DOI: 10.1063/1.88030.

[5] J. Grames and M. Poelker. “Polarized Electron Sources”. *Polarized Beam Dynamics and Instrumentation in Particle Accelerators: USPAS Summer 2021 Spin Class Lectures*. Ed. by F. Méot et al. Cham: Springer International Publishing, 2023, pp. 261–284. DOI: 10.1007/978-3-031-16715-7_11.

[6] E. Esarey, C. B. Schroeder, and W. P. Leemans. “Physics of laser-driven plasma-based electron accelerators”. *Rev. Mod. Phys.* 81 (3 2009), pp. 1229–1285. DOI: 10.1103/RevModPhys.81.1229.

[7] B. Foster, R. D’Arcy, and C. A. Lindstrøm. “A hybrid, asymmetric, linear Higgs factory based on plasma-wakefield and radio-frequency acceleration”. *New Journal of Physics* 25 (9 2023), p. 093037. DOI: 10.1088/1367-2630/acf395.

[8] J. Vieira et al. “Polarized beam conditioning in plasma based acceleration”. *Physical Review Special Topics - Accelerators and Beams* 14 (7 2011), p. 071303. DOI: 10.1103/PhysRevSTAB.14.071303.

[9] M. Wen, M. Tamburini, and C. H. Keitel. “Polarized Laser-WakeField-Accelerated Kiloampere Electron Beams”. *Physical Review Letters* 122 (21 2019), p. 214801. DOI: 10.1103/PhysRevLett.122.214801.

[10] H. C. Fan et al. "Control of electron beam polarization in the bubble regime of laser-wakefield acceleration". *New Journal of Physics* 24 (8 2022), p. 083047. DOI: 10.1088/1367-2630/ac8951.

[11] Y. Wu et al. "Polarized electron-beam acceleration driven by vortex laser pulses". *New Journal of Physics* 21 (7 2019), p. 073052. DOI: 10.1088/1367-2630/ab2fd7.

[12] S. Bohlen et al. "Colliding pulse injection of polarized electron bunches in a laser-plasma accelerator". *Phys. Rev. Res.* 5 (3 2023), p. 033205. DOI: 10.1103/PhysRevResearch.5.033205.

[13] T. P. Rakitzis et al. "Spin-polarized hydrogen atoms from molecular photodissociation". *Science* 300 (5627 2003), pp. 1936–1938. DOI: 10.1126/science.1084809.

[14] A. Hützen et al. "Polarized proton beams from laser-induced plasmas". *High Power Laser Science and Engineering* 7 (2019), p. 16. DOI: 10.1017/hpl.2018.73.

[15] J. Kessler. *Polarized Electrons*. 2nd. Berlin, Heidelberg: Springer, 1985. DOI: 10.1007/978-3-662-02434-8.

[16] F. Méot et al. *Polarized Beam Dynamics and Instrumentation in Particle Accelerators*. Particle Acceleration and Detection. Cham, Switzerland: Springer Nature Switzerland AG, 2023. DOI: 10.1007/978-3-031-16715-7.

[17] E. Hecht. *Optik*. 5th ed. Oldenbourg Wissenschaftsverlag München, 2009. ISBN: 978-3-486-58861-3.

[18] E. Gianfelice-Wendt. "Self-polarization in Storage Rings". *Proceedings of 23rd International Spin Physics Symposium – SPIN2018*. Vol. 346. PoS, 2019, p. 013. DOI: 10.22323/1.346.0013.

[19] D. P. Barber et al. "High spin polarization at the HERA electron storage ring". *Nuclear Inst. and Methods in Physics Research, A* 338 (2-3 1994), pp. 166–184. DOI: 10.1016/0168-9002(94)91311-0.

[20] D. P. Barber et al. "The first achievement of longitudinal spin polarization in a high energy electron storage ring". *Physics Letters B* 343 (1-4 1995), pp. 436–443. DOI: 10.1016/0370-2693(94)01465-0.

[21] C. K. Sinclair et al. "A high intensity polarized electron source for the stanford linear accelerator". *AIP Conference Proceedings* 35.1 (1976), pp. 424–431. DOI: 10.1063/1.30984.

[22] C. Y. Prescott et al. "Parity non-conservation in inelastic electron scattering". *Physics Letters B* 77 (3 1978), pp. 347–352. DOI: 10.1016/0370-2693(78)90722-0.

[23] K. Aulenbacher et al. "The MAMI source of polarized electrons". *Nuclear Instruments and Methods in Physics Research, Section A: Accelerators, Spectrometers, Detectors and Associated Equipment* 391 (3 1997), pp. 498–506. DOI: 10.1016/S0168-9002(97)00528-7.

[24] W. Hillert, M. Gowin, and B. Neff. "The 50 kV inverted source of polarized electrons at ELSA". *AIP Conference Proceedings* 570.1 (2001), pp. 961–964. DOI: 10.1063/1.1384233.

[25] C. K. Sinclair et al. "Development of a high average current polarized electron source with long cathode operational lifetime". *Physical Review Special Topics - Accelerators and Beams* 10 (2 2007), p. 023501. DOI: 10.1103/PhysRevSTAB.10.023501.

[26] C. Adolphsen et al. *The International Linear Collider Technical Design Report - Volume 3.II: Accelerator Baseline Design*. 2013. URL: https://arxiv.org/abs/1306.6328.

[27] S. Weinberg. *The Quantum Theory of Fields, Volume 1: Foundations*. Cambridge, U.K.: Cambridge University Press, 1995. Chap. 2.5. DOI: 10.1017/CBO9781139644167.

[28] T. Tajima and J. M. Dawson. "Laser Electron Accelerator". *Phys. Rev. Lett.* 43 (4 1979), pp. 267–270. DOI: 10.1103/PhysRevLett.43.267.

[29] D. Strickland and G. Mourou. "Compression of amplified chirped optical pulses". *Optics Communications* 56 (3 1985), pp. 219–221. DOI: 10.1016/0030-4018(85)90120-8.

[30] F. F. Chen. *Introduction to Plasma Physics and Controlled Fusion*. 3rd ed. Springer Cham, 2018. DOI: 10.1007/978-3-319-22309-4.

[31] V. Malka et al. "Principles and applications of compact laser-plasma accelerators". *Nature Physics* 4 (6 2008), pp. 447–453. DOI: 10.1038/nphys966.

[32] J. M. Dawson. "Nonlinear electron oscillations in a cold plasma". *Physical Review* 113 (2 1959), pp. 383–387. DOI: 10.1103/PhysRev.113.383.

[33] A. Pukhov and J. Meyer-ter-Vehn. "Laser wake field acceleration: The highly non-linear broken-wave regime". *Applied Physics B: Lasers and Optics* 74 (4-5 2002), pp. 355–361. DOI: 10.1007/s003400200795.

[34] J. Popp. "Polarimetry of Laser Plasma Accelerated Electron Beams". PhD thesis. Hamburg: University of Hamburg, 2025.

[35] S. Bulanov et al. "Particle injection into the wave acceleration phase due to nonlinear wake wave breaking". *Phys. Rev. E* 58 (5 1998), R5257–R5260. DOI: 10.1103/PhysRevE.58.R5257.

[36] E. Oz et al. "Ionization-Induced Electron Trapping in Ultrarelativistic Plasma Wakes". *Phys. Rev. Lett.* 98 (8 2007), p. 084801. DOI: 10.1103/PhysRevLett.98.084801.

[37] K. Schmid et al. "Density-transition based electron injector for laser driven wakefield accelerators". *Phys. Rev. ST Accel. Beams* 13 (9 2010), p. 091301. DOI: 10.1103/PhysRevSTAB.13.091301.

[38] A. Buck et al. "Shock-Front Injector for High-Quality Laser-Plasma Acceleration". *Phys. Rev. Lett.* 110 (18 2013), p. 185006. DOI: 10.1103/PhysRevLett.110.185006.

[39] E. Esarey et al. "Electron Injection into Plasma Wakefields by Colliding Laser Pulses". *Phys. Rev. Lett.* 79 (14 1997), pp. 2682–2685. DOI: 10.1103/PhysRevLett.79.2682.

[40] J. Faure et al. "Controlled injection and acceleration of electrons in plasma wakefields by colliding laser pulses". *Nature* 444 (7120 2006), pp. 737–739. DOI: 10.1038/nature05393.

[41] Particle Data Group Collaboration. "Review of Particle Physics". *Phys. Rev. D* 110 (3 2024), p. 030001. DOI: 10.1103/PhysRevD.110.030001.

[42] C. Leroy and P.-G. Rancoita. *Principles of Radiation Interaction in Matter and Detection*. 2nd ed. World Scientific Publishing Co., 2009. ISBN: 981-281-827-8.

[43] R. Wigmans. *Calorimetry: Energy Measurement in Particle Physics*. 2nd ed. Oxford University Press, 2017. DOI: 10.1093/oso/9780198786351.001.0001.

[44] K. W. McVoy. "Circular Polarization of Bremsstrahlung from Polarized Electrons in Born Approximation". *Phys. Rev.* 106 (4 1957), pp. 828–829. DOI: 10.1103/PhysRev.106.828.

[45] H. Olsen and L. C. Maximon. "Photon and electron polarization in high-energy bremsstrahlung and pair production with screening". *Physical Review* 114 (3 1959), pp. 887–904. DOI: 10.1103/PhysRev.114.887.

[46] R. Barday et al. "Compton transmission polarimeter for a very precise polarization measurement within a wide range of electron currents". *Journal of Physics: Conference Series* 298 (1 2011), p. 012022. DOI: 10.1088/1742-6596/298/1/012022.

[47] S. B. Gunst and L. A. Page. "Compton scattering of 2.62-Mev gamma rays by polarized electrons". *Physical Review* 92 (4 1953), pp. 970–973. DOI: 10.1103/PhysRev.92.970.

[48] H. Schopper. "Measurement of Circular Polarization of γ-Rays". *Nuclear Instruments* 3.3 (1958), pp. 158–176. DOI: 10.1016/0369-643X(58)90018-5.

[49] W. R. Nelson, H. Hirayama, and D. W. O. Rogers. *The EGS4 Code System*. Tech. rep. SLAC-265. Menlo Park, CA: Stanford Linear Accelerator Center (SLAC), 1985.

[50] W. Heitler. *The Quantum Theory of Radiation*. Oxford: Clarendon Press, 1954.

[51] H. Kolanoski and N. Wermes. *Teilchendetektoren - Grundlagen und Anwendungen*. 1st ed. Springer Spektrum Berlin, Heidelberg, 2016. DOI: 10.1007/978-3-662-45350-6.

[52] C. W. Fabjan and F. Gianotti. "Calorimetry for particle physics". *Rev. Mod. Phys.* 75 (4 2003), pp. 1243–1286. DOI: 10.1103/RevModPhys.75.1243.

[53] C. K. Sinclair. "Electron beam polarimetry". *AIP Conference Proceedings* 451.1 (1998), pp. 23–39. DOI: 10.1063/1.57045.

[54] K. Aulenbacher et al. "Precision electron beam polarimetry for next generation nuclear physics experiments". *International Journal of Modern Physics E* 27 (7 2018), p. 1830004. DOI: 10.1142/S0218301318300047.

[55] M. Büscher et al. "Generation of polarized particle beams at relativistic laser intensities". *High Power Laser Science and Engineering* 8 (2020), e36. DOI: 10.1017/hpl.2020.35.

[56] T. P. Rakitzis. "Pulsed-laser production and detection of spin-polarized hydrogen atoms". *ChemPhysChem* 5 (10 2004), pp. 1489–1494. DOI: 10.1002/cphc.200400108.

[57] D. Sofikitis et al. "Nanosecond control and high-density production of spin-polarized hydrogen atoms". *EPL* 81 (6 2008), p. 68002. DOI: 10.1209/0295-5075/81/68002.

[58] D. Sofikitis et al. "Highly Nuclear-Spin-Polarized Deuterium Atoms from the UV Photodissociation of Deuterium Iodide". *Physical Review Letters* 118 (23 2017), p. 233401. DOI: 10.1103/PhysRevLett.118.233401.

[59] D. Sofikitis et al. "Ultrahigh-Density Spin-Polarized H and D Observed via Magnetization Quantum Beats". *Physical Review Letters* 121 (8 2018), p. 233401. DOI: 10.1103/PhysRevLett.121.083001.

[60] A. K. Spiliotis et al. "Ultrahigh-density spin-polarized hydrogen isotopes from the photodissociation of hydrogen halides: new applications for laser-ion acceleration, magnetometry, and polarized nuclear fusion". *Light: Science & Applications* 10.1 (2021), p. 35. DOI: 10.1038/s41377-021-00476-y.

[61] B. Friedrich and D. Herschbach. "Polarization of molecules induced by intense nonresonant laser fields". *Journal of Physical Chemistry* 99 (42 1995), pp. 15686–15693. DOI: 10.1021/j100042a051.

[62] A. K. Spiliotis et al. "Depolarization of spin-polarized hydrogen via collisions with chlorine atoms at ultrahigh density". *Chemical Physics Impact* 2 (2021). Absorption model paper, p. 100022. DOI: 10.1016/j.chphi.2021.100022.

[63] M. Glass-Maujean, H. Frohlich, and J. A. Beswick. "Experimental evidence of an interference between photodissociation continua". *Physical Review Letters* 61 (2 1988), pp. 157–160. DOI: 10.1103/PhysRevLett.61.157.

[64] L. Drescher et al. "Extreme-ultraviolet spectral compression by four-wave mixing". *Nature Photonics* 15 (4 2021), pp. 263–266. DOI: 10.1038/s41566-020-00758-8.

[65] S. Bohlen et al. "Stability of ionization-injection-based laser-plasma accelerators". *Physical Review Accelerators and Beams* 25 (3 2022), p. 031301. DOI: 10.1103/PhysRevAccelBeams.25.031301.

[66] G. Alexander et al. "Undulator-based production of polarized positrons". *Nuclear Instruments and Methods in Physics Research Section A:Accelerators, Spectrometers, Detectors and Associated Equipment* 610.2 (2009), pp. 451–487. DOI: https://doi.org/10.1016/j.nima.2009.07.091.

[67] G. Blume et al. "A Compton transmission polarimeter for DC and SRF electron photo-injectors". *Nuclear Instruments and Methods in Physics Research, Section A: Accelerators, Spectrometers, Detectors and Associated Equipment* 1062 (2024), p. 169224. DOI: 10.1016/j.nima.2024.169224.

[68] T. Omori et al. "Efficient propagation of polarization from laser photons to positrons through compton scattering and electron-positron pair creation". *Physical Review Letters* 96 (11 2006), p. 114801. DOI: 10.1103/PhysRevLett.96.114801.

[69] T. Zwart et al. "Transmission Polarimetry at MIT Bates". *AIP Conference Proceedings* 675.1 (2003), pp. 1011–1015. DOI: 10.1063/1.1607286.

[70] C. Weinrich. "The transmission Compton polarimeter of the A4 experiment". *The European Physical Journal A* 24 (S2 2005), pp. 129–130. DOI: 10.1140/epjad/s2005-04-030-2.

[71] K. T. McDonald. "Use of a Transmission Polarimeter for a Nonmonochromatic Photon Beam". Unpublished manuscript. 2008. URL: https://kirkmcd.princeton.edu/accel/polarimetry.pdf.

[72] K. Ogawa et al. "A Test of Lead Glass Shower Counters". *Japanese Journal of Applied Physics* 23 (7R 1984), p. 897. DOI: 10.1143/JJAP.23.897.

[73] M. Y. Balatz et al. "The lead-glass electromagnetic calorimeter for the SELEX experiment". *Nuclear Instruments and Methods in Physics Research, Section A: Accelerators, Spectrometers, Detectors and Associated Equipment* 545 (1-2 2005), pp. 114–138. DOI: 10.1016/j.nima.2005.01.328.

[74] R. Diener et al. "The DESY II test beam facility". *Nuclear Instruments and Methods in Physics Research, Section A: Accelerators, Spectrometers, Detectors and Associated Equipment* 922 (2019), pp. 265–286. DOI: 10.1016/j.nima.2018.11.133.

[75] B. Simon. "Mearuserment of electrom parameter using thomson scattering". PhD thesis. Universitaet Hamburg, 2020.

[76] D. Lipka et al. "Dark Current Monitor for the European XFEL". *Proceedings of DIPAC2011, Hamburg, Germany*. JACoW, 2011, pp. 572–574. URL: https://bib-pubdb1.desy.de/record/90975/files/weoc03.pdf.

[77] D. Lipka, J. Lund-Nielsen, and M. Seebach. "Resonator for Charge Measurement at REGAE". *Proceedings of IBIC2013, Oxford, UK*. JACoW, 2013, pp. 872–875. URL: https://accelconf.web.cern.ch/IBIC2013/papers/wepf25.pdf.

[78] M. Optonix. *DRZ Screens*. Accessed 2024. URL: http://www.mcio.com/Products/drz-screens.aspx.

[79] R. Morlotti et al. "Intrinsic conversion efficiency of X-rays to light in Gd2O2S : Tb3+ powder phosphors". *Journal of Luminescence* 72-74 (1997), pp. 772–774. DOI: 10.1016/S0022-2313(96)00330-4.

[80] G. G. Stokes. "On the change of refrangibility of light". *Philosophical Transactions of the Royal Society of London* 142 (1852), pp. 463–562. DOI: 10.1098/rstl.1852.0022.

[81] Y. C. Wu et al. "Note: Absolute calibration of two DRZ phosphor screens using ultrashort electron bunch". *Review of Scientific Instruments* 83 (2 2012), p. 026101. DOI: 10.1063/1.3681442.

[82] J. P. Schwinkendorf et al. "Charge calibration of DRZ scintillation phosphor screens". *Journal of Instrumentation* 14 (9 2019), P09025. DOI: 10.1088/1748-0221/14/09/P09025.

[83] M. C. Downer et al. "Diagnostics for plasma-based electron accelerators". *Reviews of Modern Physics* 90 (3 2018), p. 035002. DOI: 10.1103/RevModPhys.90.035002.

[84] C. Varma. "Generation and Characterization of Electron Beams from a Laser-driven Plasma Accelerator". MA thesis. Deutsches Elektronen-Synchrotron, 2023.

[85] M. Marin. "Tunable narrowband thomson source based on a laser-plasma accelerator". PhD thesis. Universitaet Hamburg, 2023.

[86] R. Shallo et al. *espec analysis tool*. Accessed 2024. URL: https://gitlab.desy.de/mpa4/espec_analysis.

[87] DESY. *DOOCS - The Distibuted Object-Oriented Control System Framework*. Accessed 2024. URL: https://doocs.desy.de.

[88] E. Sombrowski et al. "JDDD: A Java DOOCS Data Display for the XFEL". *Proceedings of ICALEPCS07, Knoxville, Tennessee, USA*. JACoW Publishing, 2007, pp. 43–45. URL: https://accelconf.web.cern.ch/icalepcs07/papers/mopb05.pdf.

[89] W. K. Panofsky and W. R. Baker. "A focusing device for the external 350-Mev proton beam of the 184-inch cyclotron at Berkeley". *Review of Scientific Instruments* 21 (5 1950), pp. 445–447. DOI: 10.1063/1.1745611.

[90] J. V. Tilborg et al. "Active Plasma Lensing for Relativistic Laser-Plasma-Accelerated Electron Beams". *Physical Review Letters* 115 (18 2015), p. 184802. DOI: 10.1103/PhysRevLett.115.184802.

[91] C. A. Lindstrøm et al. "Emittance Preservation in an Aberration-Free Active Plasma Lens". *Physical Review Letters* 121 (19 2018), p. 194801. DOI: 10.1103/PhysRevLett.121.194801.

[92] J. H. Röckemann et al. "Direct measurement of focusing fields in active plasma lenses". *Physical Review Accelerators and Beams* 21 (12 2018), p. 122801. DOI: 10.1103/PhysRevAccelBeams.21.122801.

[93] E. D. Courant and H. S. Snyder. "Theory of the alternating-gradient synchrotron". *Annals of Physics* 3 (1 1958), pp. 1–48. DOI: 10.1016/0003-4916(58)90012-5.

[94] H. Wiedemann. *Particle Accelerator Physics I - Basic Principles and Linear Beam Dynamics*. 2nd ed. Springer Berlin, Heidelberg, 2003. DOI: 10.1007/978-3-662-03827-7.

[95] L. Goldberg. "Laser-Based Discharge Ignition for Capillary Waveguides". MA thesis. Universität Hamburg, 2013.

[96] PHOTONIS. *Photomultiplier Tubes Catalogue*. Accessed 2024. URL: https://hallcweb.jlab.org/DocDB/0008/000809/001/PhotonisCatalog.pdf.

[97] Hamamatsu Photonics. *Photmultiplier Tubes - Basics and Applications*. Accessed 2025. URL: https://www.hamamatsu.com/content/dam/hamamatsu-photonics/sites/documents/99_SALES_LIBRARY/etd/PMT_handbook_v4E.pdf.

[98] J. Popp and F. Stehr. *leap_sims: A Simulation Framework for Polarimeter Studies*. Accessed 2024. URL: https://github.com/JennPopp/leap_sims.

[99] S. Agostinelli et al. "GEANT4 - A simulation toolkit". *Nuclear Instruments and Methods in Physics Research, Section A: Accelerators, Spectrometers, Detectors and Associated Equipment* 506 (3 2003), pp. 250–303. DOI: 10.1016/S0168-9002(03)01368-8.

[100] J. Allison et al. "Geant4 developments and applications". *IEEE Transactions on Nuclear Science* 53 (1 2006), pp. 270–278. DOI: 10.1109/TNS.2006.869826.

[101] J. Allison et al. "Recent developments in GEANT4". *Nuclear Instruments and Methods in Physics Research, Section A: Accelerators, Spectrometers, Detectors and Associated Equipment* 835 (2016), pp. 186–225. DOI: 10.1016/j.nima.2016.06.125.

[102] Geant4 Collaboration. *Geant4 Homepage*. Accessed 2024. URL: https://geant4.web.cern.ch.

[103] Geant4 Collaboration. *Physics Reference Manual*. Release 11.3 (2024), Accessed 2024. URL: https://geant4-userdoc.web.cern.ch/UsersGuides/PhysicsReferenceManual/fo/PhysicsReferenceManual.pdf.

[104] Geant4 Collaboration. *Book For Application Developers*. Release 11.3 (2024), Accessed 2024. URL: https://geant4-userdoc.web.cern.ch/UsersGuides/ForApplicationDeveloper/fo/BookForApplicationDevelopers.pdf.

[105] R. Brun and F. Rademakers. "ROOT - An object oriented data analysis framework". *Nuclear Instruments and Methods in Physics Research, Section A: Accelerators, Spectrometers, Detectors and Associated Equipment* 389 (1-2 1997), pp. 81–86. DOI: 10.1016/S0168-9002(97)00048-X.

[106] ROOT Team. *ROOT - Data Analysis Framework Homepage*. Accessed 2024. URL: https://root.cern/.

[107] CERN. *CERN Homepage*. Accessed 2024. URL: https://home.cern/.

[108] DESY. *NAF Documentation*. Accessed 2024. URL: https://docs.desy.de/naf/.

[109] *HTCondor Manual*. Center for High Throughput Computing, University of Wisconsin-Madison, Accessed 2024. URL: https://htcondor.readthedocs.io/en/latest/.

[110] Amplitude. *Synchronization*. Accessed 2024. URL: https://amplitude-laser.com/add_ons/pulse-management/synchronization/.

[111] T. R. Schibli et al. "Attosecond active synchronization of passively mode-locked lasers by balanced cross correlation". *Optics Letters* 28 (11 2003), pp. 947–949. DOI: 10.1364/ol.28.000947.

[112] Y. Kobayashi et al. "Long-term optical phase locking between femtosecond Ti:sapphire and Cr:forsterite lasers". *Optics Letters* 30 (18 2005), pp. 2496–2498. DOI: 10.1364/ol.30.002496.

[113] H. Keller-Rudek et al. "The MPI-Mainz UV/VIS Spectral Atlas of Gaseous Molecules of Atmospheric Interest". *Earth System Science Data* 5.2 (2013), pp. 365–373. DOI: 10.5194/essd-5-365-2013.

[114] G. Wang et al. "High-Efficiency Frequency Conversion in Deep Ultraviolet with a $KBe_2BO_3F_2$ Prism-Coupled Device". *Applied Optics* 47.3 (2008), pp. 486–488. DOI: 10.1364/AO.47.000486.

[115] X. Zhang et al. "Widely Tunable and High-Average-Power Fourth-Harmonic Generation of a Ti:Sapphire Laser with a $KBe_2BO_3F_2$ Prism-Coupled Device". *Optics Letters* 34.9 (2009), pp. 1342–1344. DOI: 10.1364/OL.34.001342.

[116] T. Kanai et al. "Watt-Level Tunable Deep Ultraviolet Light Source by a KBBF Prism-Coupled Device". *Optics Express* 17.10 (2009), pp. 8696–8703. DOI: 10.1364/OE.17.008696.

[117] R. Jiang et al. "Tunable vacuum ultraviolet laser based spectrometer for angle resolved photoemission spectroscopy". *Review of Scientific Instruments* 85 (3 2014), p. 033902. DOI: 10.1063/1.4867517.

[118] D. Cyranoski. "Materials science: China's crystal cache". *Nature* 457 (7232 2009), pp. 953–955. DOI: 10.1038/457953a.

[119] C. Chen et al. "A New-Type Ultraviolet SHG Crystal——β-BaB_2O_4". *Scientia Sinica (Series B)* 28.3 (1985).

[120] D. N. Nikogosyan. *Nonlinear optical crystals: A complete survey*. Springer New York, NY, 2005. DOI: 10.1007/b138685.

[121] J. Ringling et al. "Tunable femtosecond pulses in the near vacuum ultraviolet generated by frequency conversion of amplified Ti:sapphire laser pulses". *Optics Letters* 18 (23 1993), pp. 2035–2037. DOI: 10.1364/ol.18.002035.

[122] R. W. Boyd. *Nonlinear Optics*. 3rd ed. Elsevier, 2008. ISBN: 978-0-12-369470-6.

[123] S. Augst et al. "Tunneling ionization of noble gases in a high-intensity laser field". *Physical Review Letters* 63 (20 1989), pp. 2212–2215. DOI: 10.1103/PhysRevLett.63.2212.

[124] A. Kramida et al. NIST Atomic Spectra Database (ver. 5.12), [Online]. Available: https://physics.nist.gov/asd [2024, November 22]. National Institute of Standards and Technology, Gaithersburg, MD. 2024.

[125] E. Optics. Accessed 2023. URL: https://eksmaoptics.com/out/media/EKSMA_Optics_Thin_BBO_Crystals.pdf.

[126] FASTLITE. *Wizzler*. Accessed 2023. URL: https://fastlite.com/produits/wizzler-ultrafast-pulse-measurement/.

[127] T. Oksenhendler et al. "Self-referenced spectral interferometry". *Applied Physics B: Lasers and Optics* 99 (1-2 2010), pp. 7–12. DOI: 10.1007/s00340-010-3916-y.

[128] FASTLITE. *Dazzler: Ultrafast pulse shaper*. Accessed 2024. URL: https://fastlite.com/produits/wizzler-ultrafast-pulse-measurement/.

[129] F. Verluise et al. "Amplitude and phase control of ultrashort pulses by use of an acousto-optic programmable dispersive filter: pulse compression and shaping". *Optics Letters* 25 (8 2000), pp. 575–577. DOI: 10.1364/ol.25.000575.

[130] Y. Tamaki, M. Obara, and K. Midorikawa. "Second-Harmonic Generation from Intense, 100-fs Ti:Sapphire Laser Pulses in Potassium Dihydrogen Phosphate, Cesium Lithium Borat and β-Barium Metaborate". *Japanese Journal of Applied Physics* 37.9R (1998), p. 4801. DOI: 10.1143/JJAP.37.4801.

[131] F. Binon et al. "Hodoscope multiphoton spectrometer GAMS-2000". *Nuclear Inst. and Methods in Physics Research, A* 248 (1 1986), pp. 86–102. DOI: 10.1016/0168-9002(86)90501-2.

[132] M. R. Adams et al. "Radiation damage studies of cerium-doped radiation-resistant lead glass detectors". *Nuclear Inst. and Methods in Physics Research, A* 238 (2-3 1985), pp. 333–340. DOI: 10.1016/0168-9002(85)90470-X.

[133] Oak Ridge Associated Universities - Museum of Radiation and Radioactivity. *Leaded Glass for Shields*. Accessed 2024. URL: https://orau.org/health-physics-museum/collection/lichtenberg/glass/leaded.html.

[134] D. Ryckbosch. "The HERMES RICH detector on behalf of HERMES collaboration". *Nuclear Instruments and Methods in Physics Research, Section A: Accelerators, Spectrometers, Detectors and Associated Equipment* 433 (1-2 1999), pp. 98–103. DOI: 10.1016/S0168-9002(99)00356-3.

[135] Tektronix. *AFG 3102*. Accessed 2024. URL: https://www.tek.com/en/datasheet/afg3000-series.

[136] CAEN. *V6533*. Accessed 2024. URL: https://www.caen.it/products/v6533/.

[137] CAEN. *V965*. Accessed 2024. URL: https://www.caen.it/products/v965/.

[138] CAEN. *SY127 HIGH VOLTAGE SYSTEM*. Accessed 2024. URL: https://groups.nscl.msu.edu/nscl_library/manuals/caen/sy127.pdf.

[139] FLUKE. *79 Series II Multimeter*. Accessed 2024. URL: https://dam-assets.fluke.com/s3fs-public/79_26___smeng0300.pdf.

[140] CAEN. *VME–PCI Optical Link Brige V2718, Technical Information Manual*. Accessed 2025. URL: https://www.users.ts.infn.it/~rui/univ/Acquisizione_Dati/Manuals/CAEN%20V2718%20rev11.pdf.

[141] Y. Liu et al. "EUDAQ2 - A flexible data acquisition software framework for common test beams". *Journal of Instrumentation* 14 (10 2019), P10033. DOI: 10.1088/1748-0221/14/10/P10033.

[142] P. Baesso, D. Cussans, and J. Goldstein. "The AIDA-2020 TLU: A flexible trigger logic unit for test beam facilities". *Journal of Instrumentation* 14 (9 2019), P09019. DOI: 10.1088/1748-0221/14/09/P09019.

[143] OPAL Collaboration. "The OPAL detector at LEP". *Nuclear Instruments and Methods in Physics Research Section A: Accelerators, Spectrometers, Detectors and Associated Equipment* 305.2 (1991), pp. 275–319. DOI: 10.1016/0168-9002(91)90547-4.

[144] Dassault Systemes. *OPERA-2D*. Accessed 2024. URL: https://www.3ds.com/de/produkte-und-services/simulia/produkte/opera/.

[145] L. Fröhlich et al. "Taskomat & Taskolib: A Versatile, Programmable Sequencer for Process Automation". *Proceedings of PCaPAC2022, Dolní Brežany, Czech Republic*. JACoW Publishing, 2022, pp. 94–97. DOI: 10.18429/JACoW-PCaPAC2022-FRO11.

[146] B. Intrumentation. *Turbo-ICT Users Manuel*. Accessed 2024. URL: https://www.bergoz.com/wp-content/uploads/Turbo-ICT-manual-3-1-1.pdf.

[147] M. Kirchen et al. "Optimal Beam Loading in a Laser-Plasma Accelerator". *Phys. Rev. Lett.* 126 (17 2021), p. 174801. DOI: 10.1103/PhysRevLett.126.174801.

[148] S. Jalas et al. "Bayesian Optimization of a Laser-Plasma Accelerator". *Physical Review Letters* 126 (10 2021), p. 104801. DOI: 10.1103/PhysRevLett.126.104801.

[149] S. A. Antipov et al. "Design of a prototype laser-plasma injector for an electron synchrotron". *Physical Review Accelerators and Beams* 24 (11 2021), p. 111301. DOI: 10.1103/PhysRevAccelBeams.24.111301.

[150] A. F. Pousa et al. "Energy Compression and Stabilization of Laser-Plasma Accelerators". *Physical Review Letters* 129 (9 2022), p. 094801. DOI: 10.1103/PhysRevLett.129.094801.

[151] MPL at DESY. *KALDERA*. Accessed 2025. URL: http://mpl.desy.de/kaldera#mpl-kaldera-head.

[152] A. Buckley. *The hepthesis LaTeX class*.

[153] OpenAI. *ChatGPT (Version GPT-4)*. large language model, Accessed 2025. URL: https://openai.com/chatgpt.

[154] Grammarly Inc. *Grammarly*. writing assistant, Accessed 2025. URL: https://www.grammarly.com.

Acknowledgements

Now, this work finally comes to an end, and I am grateful for all the things I have learned and how I have grown as a person over the last years. I think of all the people without whom this endeavor would not have been possible, and I want to take the time to thank all of them. If you don't find yourself here, I might have forgotten, and I sincerely apologize!:)

First, I want to thank **Jenny** for the grate supervision and for always helping me whenever I got stuck. A big thank you also to **Kris**, who did the same. And, of course, **Gudi** and all the other members of my committee for reviewing my work.

A special thank you to **Jennifer** – we truly went through this together! Thank you for the countless discussions, support over the years, work-related and beyond. We made it!

I would also like to thank my wonderful colleagues in **SLB** and **FTX**, it has been a great pleasure working with you all. I especially enjoyed being part of this group, particularly the nice lunch breaks, amusing ourselves and collectively wondering about the surprises the canteen had in store for us each day. My gratitude also goes to all my fellow PhD students and friends for the great times we shared, especially the legendary Friday night dinners. A special shout-out to **Louis**, **Antonios**, **Ivo**, **Tangui**, and my DESY mentor **Stefan**, you were always hands-on when it came to test beam preparations, organization, and so much more. I truly appreciate all the time and effort you invested to make this work possible. Furthermore, I want to thank **Karsten** and his team for their excellent work in constructing our calorimeter.

Of course, I also want to express my gratitude to the **MPA** group and its former members, especially **Simon**, **Martin**, and **Song**, for their great support and the time we spent together in the lab conducting my final experiments. A big thank you as well to everyone who worked behind the scenes.

Timo, **Annabel**, and **Jenn**, thank you for all the fun we had. You made DESY a special place for me beyond work, especially with our adventures around the large campus, always on the hunt for the best blackberry bushes in summer. More importantly, thank

you for becoming such great friends.
A huge thank you to my friends **Lorenz**, **Marius**, **Adrian**, **Jakob**, and **Laura** for being part of everything. And, of course, to all my university friends, with whom I first started exploring physics, especially **Simon** and **Ruben**, who were always there whenever a theoretical perspective was needed.
Last but certainly not least, I want to thank my family: my "mother-in-law", **Stefanie**, for her encouragement; my brother, **Johannes**, and his family for all the fruitful discussions; and especially my parents, **Helga** and **Kurt**, for their unconditional support. And of course to **Anne**, thank you for your love, for always having my back and for your constant encouragement, especially during the stressful and challenging times on this journey – honestly, I probably owe you half of my title! ;) I am so grateful to have you by my side.

Colophon

This thesis was made in LaTeX 2_ε using the "hepthesis" class [152].

Large Language Models and AI-based writing assistants, such as ChatGPT [153] and Grammarly [154], have been used for linguistic refinement, specifically for grammar correction and stylistic improvements, but not for content generation.

Eidesstattliche Versicherung/ Declaration of Oath

Hiermit versichere ich an Eides statt, die vorliegende Dissertationsschrift selbst verfasst und keine anderen als die angegebenen Hilfsmittel und Quellen benutzt zu haben.

Sofern im Zuge der Erstellung der vorliegenden Dissertationsschrift generative Künstliche Intelligenz (gKI) basierte elektronische Hilfsmittel verwendet wurden, versichere ich, dass meine eigene Leistung im Vordergrund stand und dass eine vollständige Dokumentation aller verwendeten Hilfsmittel gemäß der Guten wissenschaftlichen Praxis vorliegt. Ich trage die Verantwortung für eventuell durch die gKI generierte fehlerhafte oder verzerrte Inhalte, fehlerhafte Referenzen, Verstöße gegen das Datenschutz- und Urheberrecht oder Plagiate.

Hamburg, 22. Mai 2025

Felix Paul Georg Stehr